Magnetometry of Magnetic Nanoparticles with $\mathbf{YBa_2Cu_3O_{7\text{-}x}}$ nanoSQUIDs

Dissertation
der Mathematisch-Naturwissenschaftlichen Fakultät
der Eberhard Karls Universität Tübingen
zur Erlangung des Grades eines
Doktors der Naturwissenschaften
(Dr. rer. nat.)

vorgelegt von
Martin Johannes Hack
aus Tettnang

Tübingen
2025

Gedruckt mit Genehmigung der Mathematisch-Naturwissenschaftlichen Fakultät
der Eberhard Karls Universität Tübingen.

Tag der mündlichen Qualifikation: 29.07.2025
Dekan: Prof. Dr. Thilo Stehle
1. Berichterstatter: Prof. Dr. Dieter Kölle
2. Berichterstatter: Prof. Dr. Yonathan Anahory

Mm-noom-ba-deh
Doom-boom-ba-beh
Doo-boo-boom-ba-beh-beh

Pressure pushin' down on me
Pressin' down on you, no man ask for
Under pressure that brings a building down
Splits a family in two, puts people on streets
Mm-ba-ba-beh, mm-ba-ba-beh
Dee-day-da, ee-day-da
That's okay

That's the terror of knowing what this world is about
Watchin' some good friends screamin', "Let me out"
Pray tomorrow gets me higher
Pressure on people, people on streets

Da-da-da, mm-mm
Da-da-da-ba-bum
Okay

Chippin' around, kick my brains 'round the floor
These are the days it never rains but it pours
Ee-doh-ba-buh, ee-da-ba-ba-bop
Mm-bo-bop, beh-lup
People on streets, ee-da-dee-da-day
People on streets, ee-da-dee-da-dee-da-dee-da ...

Freddie M.

Contents

Acronyms

CNT	Carbon Nano Tube
ESD	ElectroStatic Discharge
EuS	Europium(II) sulfide
FIB	Focused Ion Beam
FLL	Flux-Locked Loop
Ga-FIB	Gallium-Focused Ion Beam
IVC	Current-Voltage-Characteristic
Ne-FIB	Neon-Focused Ion Beam
RCSJ	Resistively and Capacitively Shunted Junction
SEM	Scanning Electron Microscope
SQUID	Superconducting QUantum Interference Device, see 2.3
STO	$SrTiO_3$
YBCO	$YBa_2Cu_3O_{7\text{-x}}$, see 2.4

Abstract

This thesis explores the development and application of high-temperature superconducting quantum interference devices (SQUIDs) based on $YBa_2Cu_3O_{7-x}$ (YBCO) for the magnetometry of individual magnetic nanoparticles. For this application, the fabrication of grain boundary YBCO SQUIDs was optimised, involving both a microstructuring step using optical lithography and argon ion milling, and a subsequent nanopatterning step using focused ion beam (FIB) techniques. To improve patterning accuracy and increase device quality and yield, an enhanced lithography alignment strategy and optimised mask designs were developed. In addition to conventional gallium-FIB processing, a novel approach based on neon-FIB milling was employed, enabling higher resolution structuring.

Due to the high critical temperature and magnetic field resilience of YBCO, the fabricated nanoSQUIDs allowed measurements at temperatures up to 31 K and magnetic fields up to 400 mT. Two types of magnetic nanoparticles were investigated: iron (Fe) nanowires embedded in carbon nanotubes and europium sulfide (EuS) nanodiscs.

The magnetic switching behaviour of Fe nanowires was studied over a temperature range of 4 K to 31 K, and the switching fields were found to follow a thermally activated reversal model. EuS nanodiscs with diameters ranging from 200 nm to 700 nm were investigated at temperatures from 15 mK to 20 K and magnetic fields up to 150 mT. The 700 nm discs exhibited vortex-like magnetisation behaviour and Curie temperatures around 18 K, in good agreement with micromagnetic simulations and thin-film properties. However, the 200 nm disc showed degradation, revealing the critical impact of fabrication with FIB milling.

In addition to the nanoparticle studies, this thesis demonstrates the successful implementation of the novel vector-substrate approach to realise YBCO-based grain boundary Josephson junctions on a sapphire substrate. An epitaxially grown bicrystalline $SrTiO_3$ (STO) membrane was released from its original growth substrate using a water-soluble sacrificial layer and transferred onto a sapphire substrate. Subsequent epitaxial growth of a YBCO thin film resulted in a bicrystalline film on the STO-sapphire stack. Part of this thesis included the microfabrication and electrical characterisation of functional Josephson junctions in this novel heterostructure.

Zusammenfassung

Diese Arbeit befasst sich mit der Entwicklung und Anwendung hochtemperatur superconducting quantum interference devices (SQUIDs) auf Basis von $YBa_2Cu_3O_{7-x}$ (YBCO) zur Magnetometrie einzelner magnetischer Nanopartikel. Für diese Anwendung wurde die Herstellung von YBCO-SQUIDs mit Korngrenzen Josephson Kontakten optimiert. Dies umfasste sowohl einen Mikrostrukturierungsschritt mittels optischer Lithographie und Argonionen-Ätzen als auch eine nachgelagerte Nanostrukturierung mittels fokussiertem Ionenstrahl (FIB). Zur Verbesserung der Strukturierungsgenauigkeit sowie der Qualität und Ausbeute der SQUIDs wurden ein verbessertes Lithographie-Ausrichtungsverfahren sowie optimierte Maskendesigns entwickelt. Neben der konventionellen Strukturierung mit Gallium-FIB kam erstmals auch ein neuartiger Ansatz mit Neon-FIB zum Einsatz, der eine höher aufgelöste Bearbeitung ermöglicht.

Dank der hohen Sprungtemperatur und der Magnetfeldtoleranz von YBCO erlaubten die hergestellten nanoSQUIDs Messungen bei Temperaturen bis zu 31 K und Magnetfeldern bis zu 400 mT. Zwei Typen magnetischer Nanopartikel wurden untersucht: Eisen (Fe) Nanodrähte eingebettet in Kohlenstoffnanoröhren sowie Europiumsulfid (EuS) Nanodiscs.

Das magnetische Umschaltverhalten der Fe-Nanodrähte wurde im Temperaturbereich von 4 K bis 31 K analysiert; die gemessenen Schaltfelder folgen einem thermisch aktivierten Umschaltmodell. EuS-Nanodiscs mit Durchmessern zwischen 200 nm und 700 nm wurden im Temperaturbereich von 15 mK bis 20 K und bei Magnetfeldern bis zu 150 mT untersucht. Die 700 nm Discs zeigten ein wirbelartiges Magnetisierungsverhalten und eine Curie-Temperatur von etwa 18 K, was gut mit mikromagnetischen Simulationen und Dünnschichteigenschaften übereinstimmt. Die 200 nm Disc wies hingegen eine deutliche Degradierung auf, was den kritischen Einfluss der FIB-Strukturierung aufzeigt.

Neben der Untersuchung magnetischer Nanopartikel wird in dieser Arbeit auch die erfolgreiche Umsetzung des neuartigen Vector-Substrat-Ansatzes zur Realisierung von YBCO basierten Korngrenzen-Josephson-Kontakten auf einem Saphirsubstrat vorgestellt. Eine epitaktisch gewachsene bikristalline $SrTiO_3$-Membran (STO) wurde mittels einer wasserlöslichen Opferschicht vom ursprünglichen Wachstumssubstrat gelöst und auf ein Saphirsubstrat übertragen. Das anschließende epitaktische Wachsen eines YBCO Dünnfilms führte zu einem bikristallinen, supraleitenden Dünnfilm auf dem STO-Saphir-Stapel. Im Rahmen dieser Arbeit wurden funktionale Josephson-Kontakte in dieser neuartigen Heterostruktur mikrostrukturiert und elektrisch charakterisiert.

Use of Artificial Intelligence Tools

In accordance with the current *Guidelines on the Use of Generative AI Tools* issued by the University of Tübingen[1], and initial recommendations formulated by the German Research Foundation (DFG)[2], parts of this thesis were stylistically improved with the support of artificial intelligence (AI) tools.

The DFG explicitly states: *“In view of its considerable opportunities and development potential, the use of generative models in the context of research work should by no means be ruled out”, says the paper: “However, certain binding framework conditions will be required in order to ensure good research practice and the quality of research results.” Here, too, the standards of good research practice generally established in science and the humanities are fundamental.*

To optimise the text for a consistent style, LaTeX formatting, and grammatical correctness, a custom version of GPT based on the GPT-4 model (as of 2024) was employed[3]. The structure, scientific content, and argumentation of the texts were entirely specified and verified by the author to prevent plagiarism and hallucination.

ScholarGPT[4] was partially used to support literature research.

Additionally, DeepL Write and DeepL Translator[5] were employed at selected points to translate and refine formulations between German and English. All content, structure, scientific conclusions, and critical evaluations presented in this thesis are the sole responsibility of the author. No parts of the experimental data, scientific interpretations, or critical discussions were generated, modified, or influenced by AI tools.

---

[1] University of Tübingen: *Guidelines on the Use of Generative AI Tools*, available at `https://uni-tuebingen.de/en/research/support/good-scientific-practice/guidelines-on-generative-ai/` [Accessed 26.04.2025]

[2] DFG Press Release: *Dealing with Generative Models in Research Contexts*, available at `https://www.dfg.de/en/news/news-topics/announcements-proposals/2023/info-wissenschaft-23-72` [Accessed 26.04.2025]

[3] A custom GPT assistant, optimised for physics thesis writing and LaTeX support, based on OpenAI’s GPT-4 technology. Developed and configured by the author using the OpenAI platform: `https://platform.openai.com/` and `https://chatgpt.com/` [Accessed 26.04.2025]

[4] ScholarGPT is a research-focused AI model developed to assist in literature searches and technical summaries. See: `https://chatgpt.com/g/g-kZ0eYXlJe-scholar-gpt` [Accessed 26.04.2025]

[5] DeepL Translator and DeepL Write: AI-based tools for translation and stylistic text improvement. Available at `https://www.deepl.com/` [Accessed 26.04.2025]

Chapter 1.

Introduction

SQUIDs are among the most sensitive and versatile tools for detecting ultra-weak magnetic fields [1]. In recent decades, substantial progress in their fabrication has significantly broadened their application range.[2]–[7]

SQUIDs operate based on fundamental quantum mechanical principles, including flux quantisation and the Josephson effect, allowing them to resolve tiny local magnetic fields from magnetic nanoparticles with spin sensitivities below $1\,\mu_B/\sqrt{\mathrm{Hz}}$.[8]–[11] Their extreme sensitivity has made them indispensable across a wide range of scientific disciplines, including condensed matter physics, bio-magnetism, and quantum technologies.

A particularly promising development in this field is the advancement of nanoSQUIDs based on high-temperature superconductors such as YBCO.[1] Due to their elevated critical temperature and robust magnetic field tolerance, these sensors can operate in liquid nitrogen, providing significant practical advantages over conventional low-T_c devices. This makes YBCO-based nanoSQUIDs ideal candidates for investigating the magnetic behaviour of individual nanoscale objects, including magnetic nanoparticles such as nanowires and nanodiscs.

The study of magnetic nanoparticles is of fundamental and technological interest, as their magnetic properties are governed by quantum phenomena, domain wall motion, vortex formation, and exchange interactions.[12]–[15] They play a critical role in a variety of emerging applications, ranging from magnetic data storage and spintronic devices to biomedical diagnostics.[16], [17] Yet, due to their minute magnetic moments and complex switching behaviour, single-particle characterisation remains highly challenging. Other important measurement techniques in the field of nanoscale magnetometry include magnetic resonance imaging [18], magneto-optical methods based on nitrogen-vacancy (NV) centres in diamond [19]–[21], the use of CNTs as spin detectors [22], and Hall sensors [23]. NanoSQUIDs offer a distinct advantage as they can reach quantum-limited sensitivity [9], [24]. Their high magnetic sensitivity and direct detection of stray magnetic fields render them uniquely suited for probing the magnetisation dynamics of individual nanoparticles, including switching fields, vortex formation, and thermal stability [25]–[29].

This thesis is dedicated to the fabrication, optimisation, and application of YBCO-based nanoSQUIDs for the investigation of individual magnetic nanoparticles under varying temperature and magnetic field conditions. The study addresses both fundamental questions in nanoscale magnetism and technological challenges in the development of ultra-sensitive cryogenic magnetic sensors. At its core, this work aims to improve the performance and versatility of high-temperature superconducting nanoSQUIDs, and to apply them to the characterisation of two quantum-relevant magnetic systems: Fe nanowires encapsulated in CNTs, and EuS nanodiscs structured via FIB milling. Leveraging the advantages of YBCO—such as its high critical temperature of approximately 90 K and its ability to sustain large magnetic fields—nanoSQUIDs fabricated in this work were operated at fields up to 300 mT and temperatures as high as 31 K, opening new measurement regimes.

Chapter 2 provides a concise introduction to the theoretical background, while Chapter 3 gives an overview of the materials and methods used in this thesis. Chapter 4.1 presents the fabrication of nanoSQUIDs, which were patterned using both Ga-FIB and Ne-FIB techniques. The latter allows for ultra-precise definition of Josephson junctions while potentially reducing fabrication-induced damage. In addition, a novel platform based on a freestanding oxide transfer method enabled the growth of superconducting YBCO films on sapphire substrates. Successful fabrication and characterisation of functioning Josephson junctions on these membranes is demonstrated in Chapter 4.2. These technical developments significantly expand the range of substrates compatible with epitaxial YBCO growth, overcoming traditional constraints and enabling more flexible device integration.

To enable single-particle magnetometry, nanopositioning techniques were developed to place magnetic particles with nanometre-scale precision onto the active area of the nanoSQUID. Two types of magnetic nanoparticles were investigated: Fe nanowires and FIB-fabricated EuS nanodiscs. Chapter 4.3 focuses on Fe nanowires. Temperature-dependent measurements of magnetisation switching revealed thermally activated reversal via the curling mode, consistent with domain wall nucleation. From these measurements, the domain wall energy barrier was extracted. In Chapter 4.4, EuS nanodiscs of various sizes were fabricated and studied across a wide temperature range. The observed saturation behaviour and Curie temperatures showed excellent agreement with thin film properties and simulations, confirming the formation of magnetic vortex states and demonstrating that above a critical disc size, intrinsic material properties were preserved despite FIB structuring and subsequent edge damage.

These results establish the feasibility of single-particle magnetometry with YBCO nanoSQUIDs under realistic experimental conditions. The combination of high spatial resolution, thermal robustness, and magnetic sensitivity opens the door to a wide range of future applications in nanomagnetism, quantum materials research, and hybrid quantum systems. Ultimately, this thesis not only demonstrates the potential of YBCO nanoSQUIDs as powerful tools for fundamental studies of magnetic nanoparticles but also introduces key methodological advances in their fabrication, integration, and operation. The findings contribute to the growing field of superconducting quantum sensors and provide a solid foundation for future developments in spintronics, nanoscale magnetometry, and quantum technologies.

Chapter 2.

Fundamentals

The theoretical background presented in this chapter is based on the textbooks *Festkörperphysik* by Rudolf Gross and Achim Marx [30], *Superconductivity* by Reinhold Kleiner and Werner Buckel [31], and *The SQUID Handbook* by John Clarke and Alex I. Braginski [3] and the reviews *High-temperature superconducting quantum interference devices* by Dieter Koelle [1] et al. and *NanoSQUIDs: Basics & recent advances* by Maria José Martínez-Pérez and Dieter Koelle [11].

2.1. Fundamentals of Superconductivity

The superconducting state is a macroscopic quantum state exhibiting physical phenomena, including current transport without resistance, flux quantisation, and the expulsion of external magnetic fields from the superconducting material. This section introduces the fundamental effects underlying superconductivity, based on the physics presented by Kleiner and Buckel. [31].

2.1.1. Superconducting State and Flux Quantisation

The superconducting state is characterised by the resistance free current transport through a superconductor. This phenomenon was microscopically explained in 1957 by the BCS theory [32], [33], which attributes the effect to the formation of Cooper pairs. If a superconducting material is cooled below its critical temperature, Cooper pair formation occurs. The Cooper pairs result from an effective attractive interaction between electrons mediated by electron–phonon coupling. Cooper pairs consist of two electrons with opposite spin $\vec{s}$ and opposite canonical momentum $\vec{p} = \hbar\vec{k}$. Due to their bosonic nature (total spin $S = 0$), Cooper pairs can be described by a single macroscopic wavefunction. The state at position $\vec{r}$ and time t is given by:

$$\Psi(\vec{r}, t) = \Psi_0(\vec{r}, t) \cdot e^{i\varphi(\vec{r},t)} = \sqrt{n_s(\vec{r}, t)}\, e^{i\varphi(\vec{r},t)} \tag{2.1.1}$$

where n_s denotes the Cooper pair density and φ is the phase.

The transport of supercurrent is described as a collective shift of the centre-of-mass of all Cooper pairs in $\vec{k}$-space. The absence of electrical resistance can be understood in terms of the conservation of the total momentum of the Cooper pair condensate: only scattering events that preserve the centre-of-mass momentum are allowed, and such processes are exceedingly improbable due to the large number of correlated electrons.

Let us now consider a superconducting current circulating in a closed ring. This leads to the phenomenon of fluxoid quantisation. To guarantee that the wave function is unique in a closed path inside the superconductor, the phase can only vary by multiples of 2π. This condition leads to:

$$\oint \vec{\nabla}\varphi d\vec{l} = 2\pi n = \oint \vec{k} d\vec{l} \tag{2.1.2}$$

From the canonical momentum of the Cooper pairs $p_{\mathrm{can}} = p_{\mathrm{kin}} + p_{\mathrm{field}}$ follows:

$$\hbar\vec{k} = m_s\vec{v}_s + q_s\vec{A} = \hbar\vec{\nabla}\varphi$$

with m_s the mass, q_s the charge, and $\vec{v}_s$ the velocity of the Cooper pairs, and $\vec{A}$ the magnetic vector potential:

$$\vec{\nabla}\varphi = \frac{m_s\vec{v}_s + q_s\vec{A}}{\hbar} \tag{2.1.3}$$

From the supercurrent density $\vec{j}_s$, the velocity follows as:

$$\vec{v}_s = \frac{\vec{j}_s}{n_s q_s}$$

Substituting into Equation 2.1.2 leads to:

$$2\pi n = \oint \vec{\nabla}\varphi d\vec{l} = \oint \left(\frac{m_s\vec{v}_s + q_s\vec{A}}{\hbar} \right) = \oint \left(\frac{m_s\vec{j}_s}{n_s q_s \hbar} + \frac{q_s\vec{A}}{\hbar} \right) d\vec{l} \tag{2.1.4}$$

The magnetic flux enclosed by the ring is Φ with:

$$\vec{B} = curl\vec{A} = \int curl\vec{A} df = \oint \vec{A} d\vec{l} = \Phi$$

yielding:

$$2\pi n = \frac{m_s}{n_s q_s \hbar} \oint \vec{j} d\vec{l} + \frac{q_s}{\hbar}\Phi \tag{2.1.5}$$

Using $\hbar = h/2\pi$, the London penetration depth $\lambda_L = \sqrt{m_s/(n_s q_s^2 \mu_0)}$, and $q_s = 2e$, one obtains the fluxoid quantisation condition:

$$n\Phi_0 = \mu_0 \lambda_L^2 \oint \vec{j} d\vec{l} + \Phi \tag{2.1.6}$$

In the limit of a sufficiently thick superconducting ring, the supercurrent density is exponentially small, reducing the flux quantisation condition to

$$\Phi = n\frac{h}{2e} = n\Phi_0 \tag{2.1.7}$$

with the magnetic flux quantum $\Phi_0 = h/(2e) \approx 2.07 \cdot 10^{-15}\,\mathrm{V\,s}$.

2.1.2. Meissner–Ochsenfeld Effect and London Penetration Depth

We now extend the derivation of flux quantisation to the case of a bulk superconductor without a closed loop or hole. In such a case, the macroscopic wavefunction remains non-zero throughout the superconducting body. The line integral in Equation 2.1.4 can be continuously contracted to a point, until it vanishes. This implies that $n = 0$, and the fluxoid quantisation condition is reduced to:

$$\mu_0 \lambda_L^2 \oint \vec{j}_s d\vec{l} = -\Phi = -\int \vec{B} d\vec{f} \tag{2.1.8}$$

Applying Stokes' theorem yields the second London equation in differential form:

$$curl\vec{j}_s = -\frac{q_s^2 n_s}{m_s} \vec{B} = -\frac{1}{\mu_0 \lambda_L} \vec{B} \tag{2.1.9}$$

From this equation, we obtain an expression for the surface current density $\vec{j}_s$, which is responsible for the expulsion of magnetic fields from the superconducting material:

$$\vec{j}_s = \frac{B(z)}{\mu_0 \lambda_L}$$

Combining the second London equation with Ampère's law leads to a differential equation for the magnetic field inside the superconductor:

$$\Delta \vec{B} = \frac{\vec{B}}{\lambda_L^2} \tag{2.1.10}$$

Assuming that an external magnetic field is applied perpendicular to the surface of a semi-infinite superconductor, the solution to this equation is an exponential decay of the magnetic flux density into the material:

$$B_z = B_0 \, e^{-x/\lambda_L} \tag{2.1.11}$$

This means that the magnetic field decays exponentially within the superconductor on the length scale of the London penetration depth λ_L, which is defined as:

$$\lambda_L = \sqrt{\frac{m_s}{\mu_0 n_s q_s^2}}$$

As a result, the superconductor expels magnetic fields from its interior, behaving as a perfect diamagnet. This phenomenon is known as the **Meissner–Ochsenfeld effect**.

Type-I and Type-II Superconductors

The previous derivation of the Meissner–Ochsenfeld effect relied on the assumption that the macroscopic wavefunction remains finite throughout the superconducting material. Only under this condition is the contraction of the line integral in Equation 2.1.4 valid.

But what happens if a superconductor contains non-superconducting regions and is exposed to an external magnetic field?

The characteristic length scale over which the amplitude of the macroscopic wavefunction can vary, thus maintaining superconductivity, is known as the coherence length ξ. The London penetration depth λ_L describes how far an external magnetic field can penetrate into a superconductor. The ratio $\kappa = \frac{\lambda_L}{\xi}$ determines whether the formation of a normal–superconductor boundary is energetically favourable.

Type-I superconductors are characterised by a small λ_L and a large ξ, corresponding to $\kappa < \frac{1}{\sqrt{2}}$. For these materials, the energy gain from forming a normal–superconductor boundary is insufficient to sustain superconductivity in a magnetic field. As a result, the magnetic field is completely expelled from the interior of the material (Meissner phase) up to a critical field B_c, beyond which superconductivity breaks down abruptly and the material reverts to the normal conducting state.

Type-II superconductors, on the other hand, have a large penetration depth and a small coherence length, such that $\kappa > \frac{1}{\sqrt{2}}$. In this case, the formation of a normal–superconductor boundary is energetically favourable.

Upon applying a small magnetic field, the material initially behaves like a Type-I superconductor and expels all flux (Meissner phase). However, above the first critical field B_{c1}, magnetic flux begins to penetrate the material in quantised flux tubes, so called Abrikosov vortices, forming the so-called Shubnikov phase (Figure 2.1 a). Each vortex carries a single flux quantum Φ_0 and contains a normal-conducting core, around which screening supercurrents circulate. A schematic illustration of this vortex structure is shown in Figure 2.1 b.

If the material contains defects or inhomogeneities, vortices tend to be pinned at these non-superconducting regions, which is energetically favourable. As the external magnetic field increases, more vortices enter the material, and their density increases. Eventually, pinned vortices may become mobile due to vortex–vortex interactions or thermal activation, leading to sudden flux motion. These flux jumps can manifest as discontinuities in magnetisation curves, such as those shown in Figure 2.2.

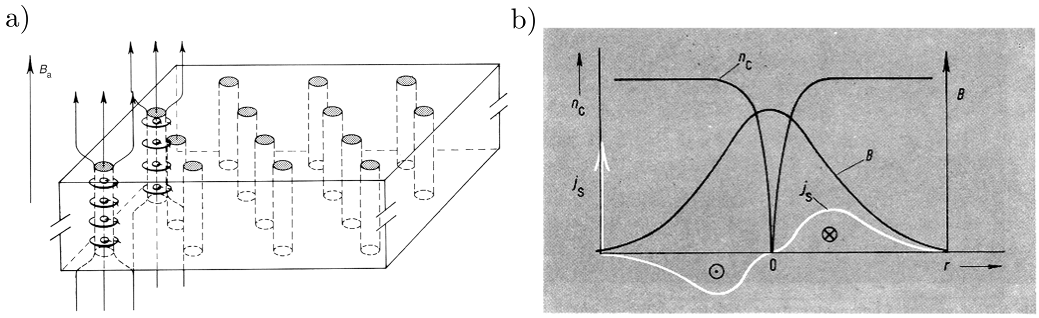

Figure 2.1.: Adapted from Kleiner and Buckel [31]. (a) Schematic depiction of the Shubnikov phase. (b) Cross-sectional sketch of a vortex, showing Cooper-pair density n_C, magnetic flux density B, and supercurrent density j_S.

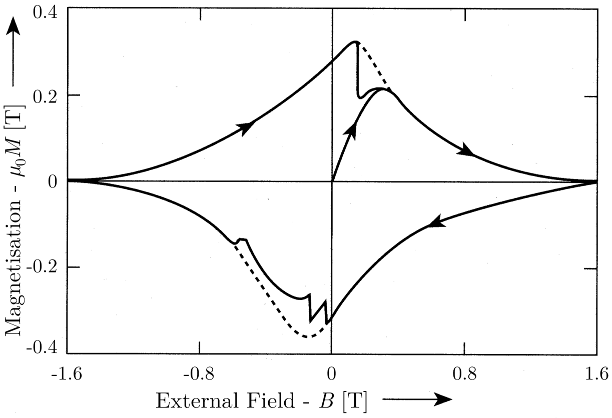

Figure 2.2.: Adapted from Kleiner and Buckel [31]. Complete magnetisation cycle of a Pb-Bi alloy. The dashed curve indicates the expected behaviour in the absence of flux jumps.

When the second critical field B_{c2} is reached, the normal–superconductor boundary becomes energetically unfavourable, the superconducting state is destroyed entirely, and the material becomes entirely normal-conducting throughout.

2.2. Josephson Junctions

This section introduces Josephson junctions, which form the fundamental building blocks of SQUIDs. Beyond their use in quantum interference devices, Josephson junctions are versatile superconducting components. Due to their highly precise and quantised voltage response under microwave irradiation, they were used in metrology to define the volt within the International System of Units (SI) until 2019 [34][31] and are still an important voltage standard [35].The following subsections cover the basic principles, the RCSJ model, and the behaviour of Josephson junctions in magnetic fields. The information presented here is taken from Clarke and Braginski[3] and Gross and Marx [30]. The exact derivations are described there in detail.

2.2.1. Basic Principle

A Josephson junction consists of two weakly coupled superconductors, for instance separated by a thin barrier. This barrier can be made of either a normal-conducting or insulating material, but must be sufficiently thin such that the macroscopic wavefunctions of the superconductors overlap. As a result, Cooper pairs can tunnel in case of an insulating barrier via the quantum tunnelling effect, allowing a supercurrent I_S to flow between the two superconductors. This current is described by the first Josephson equation:

$$I_S = I_0 \sin(\delta) \tag{2.2.1}$$

Here, I_0 is the critical current of the junction, in other words the maximum supercurrent carried by Cooper pairs that can flow across the barrier before single electrons (here referred to a quasiparticles) tunnel through the barrier as well, consequently generating a voltage across the junction. δ is the gauge-invariant phase difference between the macroscopic wavefunctions of the superconductors.

If a voltage U is applied across the junction, the phase difference evolves in time. This relationship is described by the second Josephson equation:

$$\dot{\delta} = \frac{2\pi}{\Phi_0} U \tag{2.2.2}$$

As $\dot{\delta}$ changes, the voltage over the barrier changes as well.

2.2.2. Resistively and Capacitively Shunted Junction Model

The Resistively and Capacitively Shunted Junction (RCSJ) model provides a description of the dynamics of a Josephson junction. In this model, the total current through the junction is treated as a parallel combination of four currents, as illustrated in Figure 2.3(a):

- the supercurrent $I_S = I_0 \sin(\delta)$ flowing through a Josephson element,
- the quasiparticle (resistive) current $I_{qp} = \frac{U}{R}$ through a shunt resistor R,
- the displacement current $I_d = C\dot{U}$ through a self-capacitance C, caused by changing the voltage U, and
- a thermal noise current $I_N(t)$ due to a thermal noise in the resistor R at finite temperature T.

With Kirchhoff's law, the total current is thus given by:

$$I + I_N(t) = I_0 \sin(\delta) + \frac{U}{R} + C\dot{U} \tag{2.2.3}$$

Substituting the second Josephson relation (2.2.2), this becomes:

$$I + I_N = I_0 \sin(\delta) + \frac{\Phi_0}{2\pi}\frac{1}{R}\dot{\delta} + \frac{\Phi_0}{2\pi} C\ddot{\delta} \tag{2.2.4}$$

This second-order differential equation cannot be solved analytically in general but offers a useful analogy: It resembles the equation of motion for a particle in a tilted washboard potential, as shown in Figure 2.3(b,c). This mechanical analogy aids the intuitive understanding of junction dynamics.

In this picture, the phase difference δ corresponds to the position of a fictitious particle. Its velocity is $\dot{\delta}$, the junction capacitance C corresponds to the mass, and the friction coefficient corresponds to the conductance $1/R$. The applied current I corresponds to an external force that tilts the potential.

If the tilt is strong enough, the local minima of the potential vanish, and the particle begins to move. This motion corresponds to a finite voltage across the junction. When the tilt is reduced, two dynamical regimes are distinguished:

In the overdamped case, the particle stops immediately once the tilt is removed, due to strong damping. This occurs when the capacitance (mass) or the resistance (1/damping) is small.

In the underdamped case, the particle continues to move across multiple potential wells, resulting in a hysteretic current–voltage (IV) characteristic. This behaviour arises for high R and/or large C.

The nature of the damping is characterised by the Stewart–McCumber parameter:

$$\beta_c = \frac{2\pi}{\Phi_0} I_0 R^2 C \tag{2.2.5}$$

A hysteresis is observed when $\beta_c > 1$.

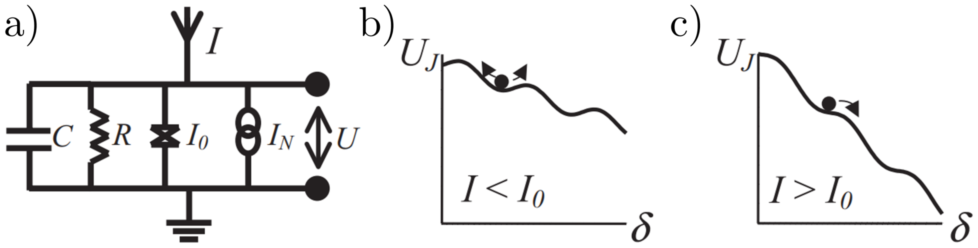

Figure 2.3.: Adapted from Clarke and Braginski [3]. (a) Equivalent circuit of a Josephson junction in the RCSJ model. (b) Tilted washboard potential for $I < I_0$. (c) For $I > I_0$, the particle escapes the local minimum, leading to finite voltage.

2.2.3. Josephson Junctions in a Magnetic Field

When a Josephson junction is subjected to an external magnetic field, it influences the local supercurrent density J_s of the Josephson junction. In this section, we consider the simple case of a short and narrow junction, to be more precise, the Josephson junction needs to be smaller than the Josephson penetration depth λ_J:

$$\lambda_J \equiv \sqrt{\frac{\Phi_0}{2\pi\mu_0 t_B J_c}} \tag{2.2.6}$$

Here, J_c is the maximal Josephson supercurrent density, $t_B = d + \lambda_{L1} + \lambda_{L2}$ is the effective magnetic thickness, including the barrier thickness d and the London penetration depths λ_{L1} and λ_{L2} of the adjacent superconducting electrodes. λ_J represents the characteristic length scale over which magnetic fields are screened within the junction.

Figure 2.4(a) illustrates a Josephson junction exposed to an external magnetic field B_y. The super current density is given by

$$J_s(y,z,t) = J_c(y,z)\sin\left(\frac{2\pi}{\Phi_0} t_B B_y z + \varphi_0\right) = J_c(y,z)\sin(kz + \varphi_0) \tag{2.2.7}$$

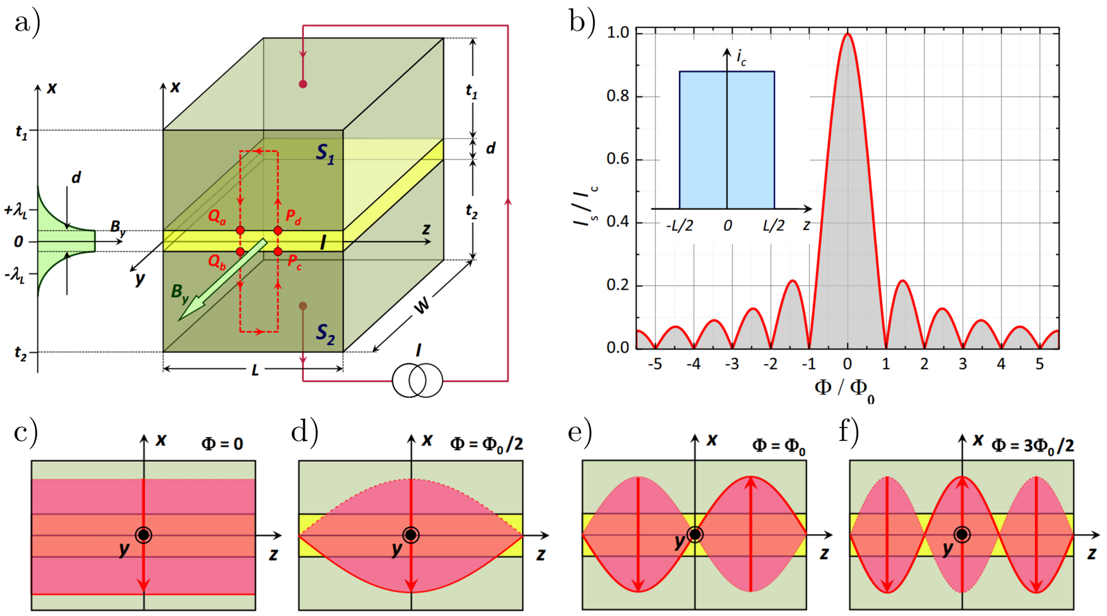

Figure 2.4.: Adapted from Gross and Marx [30]. (a) Josephson junction in an external magnetic field B_y, with supercurrent flowing in the x-direction. The exponential decay of magnetic field strength in the superconductor is shown on the left. (b) Maximum supercurrent $I_s^m(B_y)$ as a function of applied magnetic field. The inset shows the integral of $J_c(y, z)$, illustrating the analogy to Fraunhofer diffraction at a slit. (c–f) Spatial distribution of the supercurrent density in the junction for different values of magnetic flux Φ.

therefore, the supercurrent density J_s oscillates sinusoidally along the z-direction with an oscillation period of $\lambda_z = \frac{2\pi}{k} = \frac{\Phi_0}{t_B B_y}$. This implies that a single flux quantum Φ_0 penetrates the junction over one full oscillation period. The spatial variation of the supercurrent density for different values of total magnetic flux is illustrated in Figure 2.4(c–f).

The current flowing through the junction can be calculated by integrating the maximal current density in the direction of the applied field:

$$i_c(z) = \int_{-\frac{W}{2}}^{\frac{W}{2}} J_c(y, z)\, dy \tag{2.2.8}$$

and integrating in z-direction:

$$I_s(B_y) = \int_{-\frac{L}{2}}^{\frac{L}{2}} i_c(z)\, \sin(kz + \phi_0)\, dz \tag{2.2.9}$$

If $J_c(y, z)$ is spatially uniform, then the integrated current density $i_c(z)$ is constant within the junction width $-L/2 \leq z \leq +L/2$ and zero elsewhere. This corresponds to a rectangular or slit-like current distribution.

As a result, the magnetic field dependence of the maximum Josephson current $I_s^m(B_y)$

takes the form of a Fraunhofer diffraction pattern, analogous to the diffraction of light through a single slit of width L (Figure 2.4).

$$I_s^m(\Phi) = I_\mathrm{c} \left| \frac{\sin\left(\frac{kL}{2}\right)}{\frac{kL}{2}} \right| = I_\mathrm{c} \left| \frac{\sin\left(\pi \frac{\Phi}{\Phi_0}\right)}{\pi \frac{\Phi}{\Phi_0}} \right| \tag{2.2.10}$$

Here, the magnetic flux through the junction is $\Phi = B_y t_B L$, and $I_\mathrm{c} = i_c L$.

The first zero of the diffraction pattern corresponds to the case shown in Figure 2.4 d), where the current densities in the two halves of the junction flow in opposite directions and cancel each other. This destructive interference of the supercurrents is a direct analogue of optical diffraction at a single slit.

2.3. Superconducting Quantum Interference Devices

This section introduces the sensors used in this work to detect magnetic field variations caused by magnetic nanoparticles, and explains their working principles. The information presented here is taken from Koelle et al. [1] Clarke and Braginski [3], Gross and Marx [30] and Martínez-Pérez and Koelle [11]. The exact derivations are described there in detail.

2.3.1. Basic Principle

The SQUIDs used in this thesis are dc-SQUIDs, which consist of a superconducting loop interrupted by two Josephson junctions, as shown in Figure 2.5. When a current I flows through the SQUID, it splits into two partial currents:

$$I = I_1 + I_2. \tag{2.3.1}$$

As described in Chapter 2.1.1, the fluxoid quantisation causes an additional circulating current J in response to an applied magnetic flux through the loop. Using the RCSJ model, the partial currents are given by the sum of the supercurrent, quasiparticle current, and displacement current through each junction:

$$I_1 = \frac{I}{2} + J = I_{0,1}\sin(\delta_1) + \frac{\Phi_0}{2\pi R_1}\dot{\delta}_1 + \frac{\Phi_0}{2\pi} C_1 \ddot{\delta}_1 + I_{N,1}, \tag{2.3.2}$$

$$I_2 = \frac{I}{2} - J = I_{0,2}\sin(\delta_2) + \frac{\Phi_0}{2\pi R_2}\dot{\delta}_2 + \frac{\Phi_0}{2\pi} C_2 \ddot{\delta}_2 + I_{N,2}, \tag{2.3.3}$$

with $I_{N,1}$ and $I_{N,2}$ being independent Nyquist noise currents. The phase differences δ_1 and δ_2 are related by:

$$\delta_2 - \delta_1 = \frac{2\pi}{\Phi_0}\Phi_\mathrm{tot}, \tag{2.3.4}$$

where $\Phi_\mathrm{tot} = \Phi_\mathrm{ext} + LJ$ is the total magnetic flux through the SQUID loop.

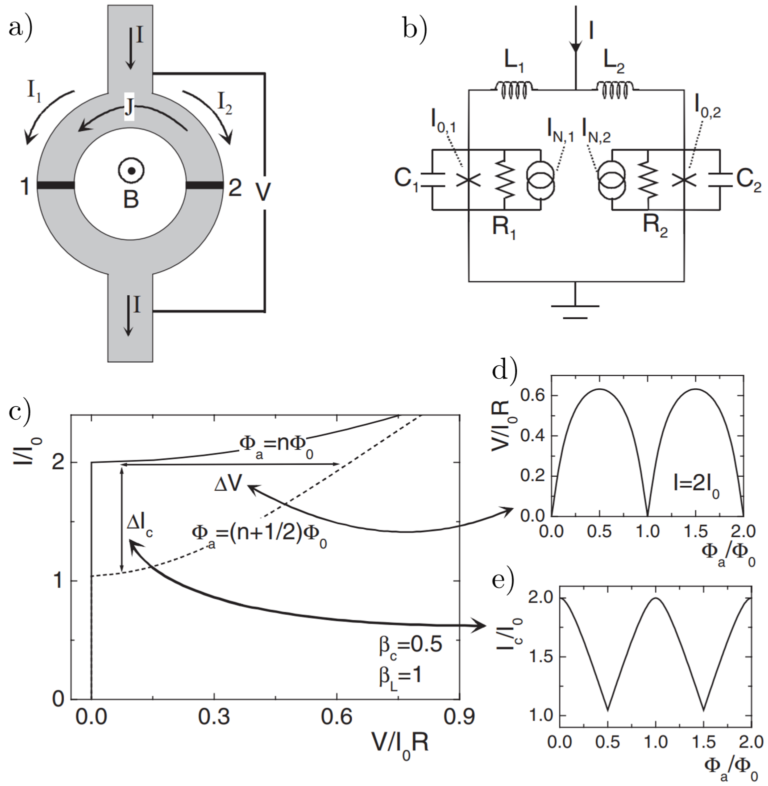

Figure 2.5.: Adapted from Chesca, Kleiner, Koelle, Chapter 2 *SQUID Theory* in Ref. [3]. (a) Schematic design of a dc-SQUID. (b) Equivalent circuit based on the RCSJ model. (c) Current-voltage characteristic, (d) $V(\Phi_0)$ modulation, and (e) $I_c(\Phi_0)$ modulation for $\beta_L = 1$ and $\beta_c = 0.5$.

The flux due to the external magnetic field contributes with $\Phi_{\text{ext}} = BA_{\text{eff}}$ and the inductance of the SQUID ring to itself from the circulating current J can be seen as $L = L_1 + L_2$ with each term containing geometric and kinetic contributions.

To further analyse the equations, we normalise current to I_0, resistance to R, voltage to I_0R, magnetic flux to Φ_0, and time to $\tau = \frac{\Phi_0}{2\pi I_0 R} = \omega_c^{-1}$. Furthermore, we find the average I_0,R and C, and the respective asymmetry parameters α.

$$I_0 = \frac{I_{0,1} + I_{0,2}}{2}, \quad \alpha_I = \frac{I_{0,2} - I_{0,1}}{I_{0,2} + I_{0,1}}, \tag{2.3.5}$$

$$R = \frac{2R_2R_1}{R_2 + R_1}, \quad \alpha_R = \frac{R_2 - R_1}{R_2 + R_1}, \tag{2.3.6}$$

$$C = \frac{C_1 + C_2}{2}, \quad \alpha_C = \frac{C_2 - C_1}{C_2 + C_1} \tag{2.3.7}$$

With these substitutions, the system of Langevin-type equations becomes:

$$\frac{i}{2} + j = (1 - \alpha_I)\sin\delta_1 + (1 - \alpha_R)\dot{\delta_1} + \beta_c(1 - \alpha_C)\ddot{\delta_1} + i_{N,1}, \tag{2.3.8}$$

$$\frac{i}{2} - j = (1 + \alpha_I)\sin\delta_2 + (1 + \alpha_R)\dot{\delta_2} + \beta_c(1 + \alpha_C)\ddot{\delta_2} + i_{N,2}, \tag{2.3.9}$$

$$\delta_2 - \delta_1 = 2\pi\left(\phi_{\text{ext}} + \frac{1}{2}\beta_L j\right), \tag{2.3.10}$$

where the Stewart-McCumber parameter is analogue to Equation 2.2.5:

$$\beta_c = \frac{2\pi}{\Phi_0} I_0 R^2 C, \tag{2.3.11}$$

and the screening parameter is given by:

$$\beta_L = \frac{2LI_0}{\Phi_0}. \tag{2.3.12}$$

In general, these equations must be solved numerically. An example is shown in Figure 2.5(c–e) for $\beta_L = 1$ and $\beta_c = 0.5$. For certain limiting cases, further simplifications are possible. In the static, noise-free, symmetric case with small inductance ($\beta_L \ll 1$), the equations reduce to:

$$\frac{i}{2} + j = \sin\delta_1, \quad \frac{i}{2} - j = \sin\delta_2, \quad \delta_2 - \delta_1 = 2\pi\phi_{\text{ext}}. \tag{2.3.13}$$

From these expressions it follows:

$$i = \sin\delta_1 + \sin\delta_2 = \sin\delta_1 + \sin(\delta_1 + 2\pi\phi_{\text{ext}}). \tag{2.3.14}$$

Introducing the substitution $\gamma = \delta_1 + \pi\phi_{\text{ext}}$, the equation becomes:

$$i = 2\sin\gamma \cdot \cos(\pi\phi_{\text{ext}}). \tag{2.3.15}$$

For subcritical current values, the phase γ will adjust so this equation is fulfilled. Therefore, the maximum current is obtained for $\sin\gamma = \pm 1$, resutling in $i_c = 2\,\|\cos(\pi\phi_{\text{ext}})\|$ or:

$$I = 2I_0 \cdot \left|\cos\left(\frac{\pi\Phi_{\text{ext}}}{\Phi_0}\right)\right|. \tag{2.3.16}$$

This periodic dependence of the critical current on magnetic flux—known as SQUID modulation—is the basis for highly sensitive magnetic flux measurements.

Figure 2.6 shows numerical simulations of the critical current I_{c} as a function of the external magnetic flux Φ_{ext} for different values of β_L. Additionally, the modulation period $\Delta I_{\text{c}}/I_{c,\text{max}}$ is plotted as a function of β_L. These results illustrate that in realistic scenarios, the minimum critical current $I_{c,\text{min}}$ does not vanish completely and for $\beta_L = 1$, the minimum critical current is approximately $0.5\, I_{c,\text{max}}$.

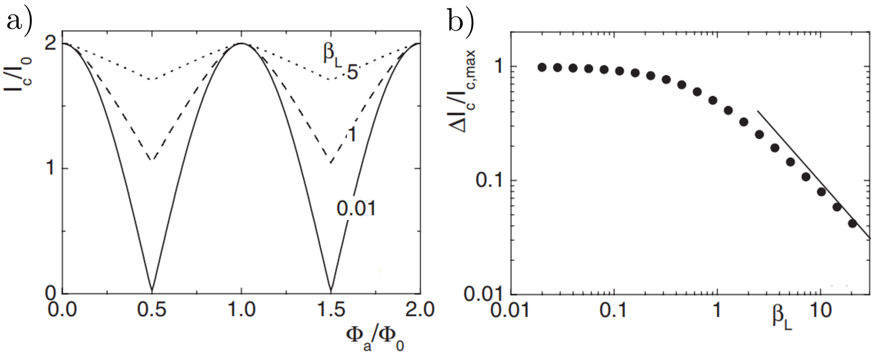

Figure 2.6.: Adapted from Chesca, Kleiner, Koelle, Chapter 2 *SQUID Theory* in Ref. [3]. (a) Critical current I_c vs. Φ_ext for different β_L. (b) Modulation depth $\Delta I_\mathrm{c}/I_{c,\mathrm{max}}$ as a function of β_L. The solid line corresponds to the function β_L^{-1}.

2.3.2. SQUID Electronics

The SQUID is typically operated with a bias current I_b slightly above its critical current I_c. Due to the Josephson effect, a voltage V is induced across the device, which is modulated periodically by the externally applied magnetic flux Φ_ext. This voltage modulation, periodic in the magnetic flux quantum Φ_0, is illustrated in Figure 2.7a. The slope at the steepest point of the $V(\Phi_\mathrm{ext})$ curve defines the flux-to-voltage transfer function V_Φ.

$$V_\Phi = \frac{dV}{d\Phi} \tag{2.3.17}$$

In open loop mode, the SQUID is biased at the steepest point, called the working point, and small variations $\delta\Phi$ in the applied flux result in a linear voltage response. However, for larger external flux, the nonlinearity of the periodic transfer function prevents a direct quantitative evaluation. To extend the linear range and ensure robust operation, a flux-locked loop (FLL) mode is commonly employed.

In a FLL, the SQUID gets biased and the resulting voltage gets matched by a voltage V_b. This way a working point W is defined and the output voltage is $V_f = 0$. Once flux gets coupled into the SQUID, this induces an voltage, which is amplified, integrated and fed back via a feedback resistance R_f to a coil with the mutual inductance M_f, thereby compensating the input flux and maintaining the SQUID at its working point W. This feedback mechanism linearises the output effectively converting the SQUID into a linear flux-to-voltage sensor. The resulting feedback voltage V_f is proportional to the external flux Φ_ext.

$$\Delta\Phi = \frac{M_f}{R_f} V_f \tag{2.3.18}$$

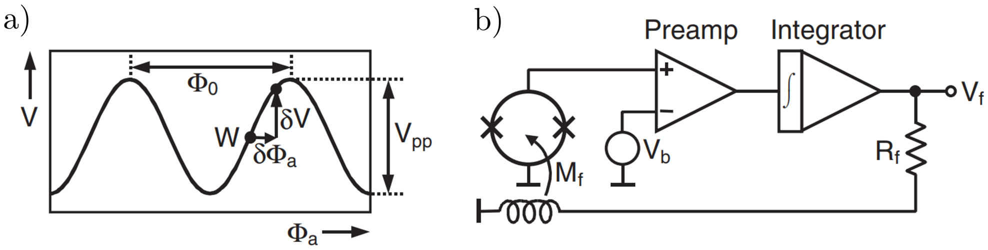

Figure 2.7.: Adapted from Drung, Mück, Chapter 4 *SQUID Theory* in Ref. [3]. (a) Voltage V vs. Φ_{ext} characteristic with working point W. (b) Schematic of a typical FLL circuit. The SQUID is biased via I_b, and the output voltage is regulated by a feedback through R_f and mutual inductance M_f to keep the SQUID at its operating point.

2.3.3. Noise Characteristics of SQUIDs

SQUIDs are among the most sensitive magnetic flux detectors. However, their ultimate performance is limited by intrinsic and extrinsic noise sources. In general, the noise spectrum of a SQUID can be separated into frequency-independent white noise and frequency-dependent $1/f$ noise.

White Noise

The frequency-independent white noise, primarily caused by Johnson-Nyquist noise, which originates from dissipative quasiparticle currents in the Josephson junctions or shunt resistors. It defines the white noise floor of the SQUID and dominates at higher frequencies.

For $\beta_C < 1$, $\beta_L > 0.4$, and $\Gamma\beta_L < 0.1$, the flux noise spectral density is approximately given by:

$$S_\Phi \approx 4(1+\beta_L)\frac{\Phi_0 k_B T L}{I_0 R} \tag{2.3.19}$$

For SQUIDs with $\beta_L \approx 1$, this expression simplifies to:

$$S_\Phi \approx 16 k_B T L^2/R \tag{2.3.20}$$

Other sources of white noise include shot noise and quantum noise, both typically below the Johnson-Nyquist noise level.

$1/f$ Noise

At low frequencies, the noise spectrum is typically dominated by $1/f$ noise. This component arises from temporal fluctuations in the critical current and resistance of the Josephson junctions, as well as from the motion of Abrikosov vortices. Such vortices may hop between pinning sites under the influence of thermal activation or magnetic stimulation. The spectral noise density follows as:

$$S(f) \propto \frac{k_B T}{f} \tag{2.3.21}$$

This low-frequency noise severely limits sensitivity for slowly varying signals.

YBCO-based devices exhibit particularly strong $1/f$ noise contributions. This is primarily attributed to thermally activated hopping of flux vortices at grain boundaries and within intragranular pinning sites. As the pinning energy is highly sensitive to crystalline quality, the fabrication of high-quality epitaxial films is critical to suppress vortex dynamics and minimise $1/f$ noise in YBCO.

2.3.4. Spin Sensitivity

A crucial figure of merit for SQUID-based magnetometry of nanoscale magnetic systems is the spin sensitivity $S_\mu^{1/2}$. It defines the minimum detectable magnetic moment and is typically expressed in units of $\mu_B/\sqrt{\mathrm{Hz}}$, with the Bohr magneton μ_B. The spin sensitivity depends on two key parameters: the root mean square noise $S_\Phi^{1/2}$ of the SQUID and the coupling factor ϕ_μ between the magnetic moment and the SQUID loop.

$$S_\mu^{1/2} = \frac{S_\Phi^{1/2}}{\phi_\mu} \tag{2.3.22}$$

The coupling factor ϕ_μ describes how effectively a magnetic moment $\vec{\mu}$ at position $\vec{r}_\mu$ and orientation $\hat{e}_\mu = \vec{\mu}/|\vec{\mu}|$ couples magnetic flux into the SQUID loop. It is given by:

$$\phi_\mu(\vec{r}_\mu, \hat{e}_\mu) = -\frac{\hat{e}_\mu \cdot \vec{B}(\vec{r}_\mu)}{J} \tag{2.3.23}$$

Here, $\vec{B}(\vec{r}_\mu)$ is the magnetic flux density generated by the current J from the SQUID at the location of the magnetic moment. In practice, ϕ_μ is usually determined numerically, taking into account the exact SQUID geometry, the position and orientation of the particle, and the screening currents in the superconducting loop. Optimisation of ϕ_μ through device geometry and precise positioning of the magnetic particle is essential to approach single-spin sensitivity. Reported values for state-of-the-art YBCO nanoSQUIDs reach spin sensitivities down to a few $\mu_B/\sqrt{\mathrm{Hz}}$ at 4.2 K [24], [36].

2.4. The High-Temperature Superconductor YBCO

This section provides a brief overview of the high temperature superconductor YBCO, which was used throughout this thesis. The fabrication was carried out in collaboration within the research group. For further technical details, the reader is referred to the doctoral thesis by Katja Wurster [37] and the review of Koelle et al. [1].

YBCO belongs to the class of high-temperature cuprate superconductors. It is a type-II superconductor and belongs to the unconventional superconductors. Table 2.1 summarises key material parameters reported in the literature.[38]–[41]

Table 2.1.: Properties of the high-temperature superconductor YBCO, adapted from literature.[38]–[41]

Parameter	Value
Critical temperature T_c	92 K
Crystal structure	Orthorhombic
Lattice constants	$a = 0.3821\,\mathrm{nm},\ b = 0.3885\,\mathrm{nm},\ c = 1.1676\,\mathrm{nm}$
Coherence length ξ_{ab}, ξ_c	1.6 nm, 0.3 nm
Critical field $B_{c2,\perp(0)}$	110 T
Critical field $B_{c2,\parallel(0)}$	240 T

The short coherence length in YBCO, on the order of a few nanometres, reflects the sensitivity of its superconducting properties to crystalline defects. Even atomic-scale imperfections can suppress superconductivity locally.

As a result, the fabrication of high-quality YBCO thin films is technically demanding. The films used in this work were grown using pulsed laser deposition. In this technique, a high-energy laser is rastered across a stoichiometric target, generating a plasma plume via localised surface ablation. This plume, consisting of a mixture of high-energy ions and atoms, is decelerated by a background process gas—typically oxygen—and crystallises on a heated substrate. The crystallographic orientation of the substrate dictates the crystallographic orientation growth of the grown layer. This type of growth is called epitaxial growth.

Given the short coherence length of YBCO, substrate properties are critical for the quality of the resulting film. The substrates used in this work were strontium titanate ($SrTiO_3$, STO) and magnesium oxide (MgO). Compared to the average in-plane lattice constant of YBCO ($a_{\mathrm{YBCO}} = 0.3853\,\mathrm{nm}$), STO with $a_{\mathrm{STO}} = 0.3868\,\mathrm{nm}$ offers a good lattice match with a relative mismatch of only 1.33%. In contrast, MgO has a larger lattice constant of $a_{\mathrm{MgO}} = 0.4212\,\mathrm{nm}$, corresponding to a mismatch of 8.52%, which requires additional growth optimisation to achieve high-quality YBCO layers.[38], [40]–[42]

These substrates were chosen because they are also commercially available as bicrystals. In a bicrystal substrate, two single crystals are joined together with a defined grain boundary, where the crystal orientation changes. When a YBCO layer is epitaxially grown on such a substrate, this crystallographic discontinuity is translated into the YBCO film. Due to the extremely short coherence length, this grain boundary can act as a weak link and effectively form a Josephson junction. This principle is discussed in more detail in the following sections.

Grain Boundary Josephson Junctions in YBCO

Grain boundary Josephson junctions are key elements in YBCO-based superconducting devices. These junctions are typically fabricated using bicrystal substrates with predefined misorientation angles, which create a grain boundary in the epitaxially grown superconducting film. [43] The misorientation angle strongly influences the critical current density j_c. In YBCO, j_c decreases exponentially with increasing misorientation angle $> 10\,\mathrm{deg}$. This behaviour is commonly attributed to a combination of grain boundary faceting and the d-wave symmetry of the superconducting order parameter. Additional factors, such as increased barrier thickness or disorder at the boundary, further contribute to the suppression of the supercurrent.

Due to the extremely short coherence length in YBCO, the microscopic quality of the grain boundary plays an important role in junction performance. As a result, key figures of merit such as the product I_0R often vary by ±20% even among nominally identical junctions on the same chip.

The fabrication process of grain boundary Josephson junctions involves the epitaxial deposition of YBCO on the bicrystal substrate, followed by patterning via optical lithography or FIB milling. The junctions are commonly covered with a thin gold layer, typically 20–60 nm thick. This gold layer serves several purposes: it acts as a resistive shunt, provides mechanical and chemical protection during processing, and shields the junction from ambient degradation such as moisture-induced oxygen loss. The presence of the shunt also influences the junction dynamics and modifies the effective damping.

YBCO grain boundary Josephson junctions are widely employed in superconducting applications, particularly in nanoSQUIDs. Their high critical temperature T_c and resilience to magnetic fields are their key advantages over conventional low-T_c materials.

FIB milling is often used to refine grain boundary Josephson junctions, enabling the creation of nanobridges with lateral dimensions below 100 nm and precisely controlled electrical characteristics [44].

YBCO on Sapphire – A New Approach Using Freestanding Membranes to Overcome Epitaxial Growth Limitations

As outlined in the previous section, the choice of substrate is crucial for the successful epitaxial growth of superconducting YBCO thin films. However, this requirement severely limits the integration of YBCO with conventional semiconductor materials such as silicon, where the crystallographic mismatch prevents high-quality film growth.

A promising solution to this challenge was introduced with the development of the water-soluble material $\mathrm{Sr_3Al_2O_6}$, which enables the fabrication of freestanding oxide membranes.[45] These membranes allow for the transfer of epitaxially grown layers onto a wide range of substrates, thus decoupling the constraints of epitaxial growth from the final device architecture. A detailed discussion of this technique is provided in Wang et al. [46] ant the PhD thesis's by Katja Wurster [37] and Yu-Jung Wu [47].

As part of a collaboration with the group of Prof. Mannhart at the Max Planck Institute for Solid State Research in Stuttgart, YBCO-based Josephson junctions were successfully fabricated on sapphire substrates using this membrane-transfer approach. The implementation and performance of these junctions are described in detail in Chapter 4.2.

2.5. Magnetic Nanoparticles

Magnetic nanoparticles exhibit unique physical properties due to their size being comparable to characteristic magnetic length scales, such as magnetic domain size or the exchange length. This makes them ideal model systems for studying fundamental magnetisation processes, including magnetisation reversal, thermal activation, and the interplay of anisotropy and shape effects. In this work, two classes of magnetic nanoparticles were studied: Fe nanowires encapsulated in CNTs, and EuS nanodiscs. Fe nanowires and their reversal model was previously investigated by Schwarz et al. [24] and Martínez-Pérez et al. [48], while the EuS discs can be compared to investigations from Martínez-Pérez et al. [49], Aguilar-Pujol et al. [50] or García-Pons et al. [51]. The theory of micromagnetic models described in the following are taken from Skomski [52].

Theory of micromagnetism

The reversal of magnetisation in ferromagnetic nanoparticles can be described by different theoretical models, depending on their size and geometry. For small single-domain particles, the Stoner–Wohlfarth model predicts a coherent rotation of the magnetisation vector. It assumes strong exchange coupling between all atomic spins, resulting in uniform rotation of the magnetisation under an external magnetic field. Despite its simplicity, the model captures key phenomena such as the angular dependence of magnetisation curves, coercivity, and spin-reorientation transitions. It is widely used to interpret hysteresis curves of micromagnets and serves as a starting point for understanding magnetic switching processes.[52]

The model accurately describes magnetic behaviour in very small particles, typically with radii below 10 nm, where magnetisation reversal remains coherent. For larger particles, the magnetisation configuration and its reversal is governed by the competition between Zeeman energy, magnetostatic self-energy $\mu_0 M_s^2$, exchange energy, and anisotropy energy. The exchange stiffness A is a parameter that quantifies the strength of the exchange energy. Similarly, K_1 represents the anisotropy constant, describing the anisotropy energy per unit volume, except in cases where surface anisotropy dominates.

To estimate the behaviour of micromagnetic systems, two fundamental length scales are commonly considered: the exchange length and the wall-width parameter. The wall-width parameter describes the thickness of domain walls separating regions of different magnetisation orientation. It also defines the spatial scale over which magnetisation responds to local perturbations such as defects or thermal fluctuations. The wall width varies from about one nanometre in extremely hard magnetic materials to several hundred nanometres in very soft magnetic materials.

The wall-width parameter is given by:

$$\delta_w = \sqrt{\frac{A}{K_1}} \tag{2.5.1}$$

where A is the exchange stiffness and K_1 is the uniaxial anisotropy constant.

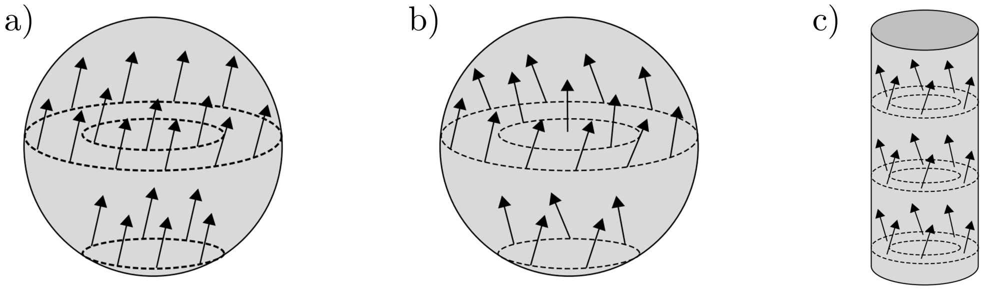

Figure 2.8.: Adapted from Skomski [52]. Sketches of magnetisation reversal types: (a) Coherent rotation, (b) curling in a sphere, and (c) curling in a cylinder.

The exchange length characterises the balance between exchange and magnetostatic energy, and defines the characteristic length scale over which magnetisation remains uniform. It determines, for example, the transition from coherent rotation to curling-type reversal. The exchange length is given by:

$$l_{\text{ex}} = \sqrt{\frac{2A}{\mu_0 M_s^2}} \tag{2.5.2}$$

where A is the exchange stiffness and M_s is the saturation magnetisation.

Micromagnetic theory predicts the critical diameter above which curling becomes energetically favourable as:

$$d_c^{\text{wires}} \approx 7.3\, l_{\text{ex}}, \quad d_c^{\text{spheres}} \approx 10.2\, l_{\text{ex}} \tag{2.5.3}$$

In Figure 2.8, the difference between coherent rotation and curling-type reversal is illustrated. Figure 2.8(a) shows the case of uniform magnetisation rotation as described by the Stoner–Wohlfarth model. Figure 2.8(b) demonstrates the non-uniform curling mode in a spherical geometry, where spins rotate in concentric loops to minimise magnetostatic energy. Figure 2.8(c) shows curling in a cylindrical nanowire, which closely resembles the geometry of the Fe nanowires studied in this work.

Thermally Activated Switching and Temperature Dependence

At finite temperature, the magnetisation reversal becomes a stochastic process governed by thermal activation over an energy barrier. This leads to a broadening of the switching field distribution and a shift of the mean switching field to lower values. The escape rate from the metastable magnetisation state follows an Arrhenius law [53]:

$$\tau(T, H) = \tau_0 \exp\left(\frac{U(H)}{k_B T}\right) \tag{2.5.4}$$

Here, τ is the average switching time, τ_0 the attempt time, $U(H)$ the field-dependent anisotropy energy barrier, T the temperature, and k_B the Boltzmann constant.

Close to the zero-temperature switching field H_{sw}^0, the barrier can be approximated by:

$$U(H) = U_0 \left(1 - \frac{H_{\mathrm{sw}}}{H_{\mathrm{sw}}^0}\right)^{1/\alpha} \tag{2.5.5}$$

The exponent α depends on the reversal mode: $\alpha = 1.5$ for coherent rotation, and $\alpha = 2$ for curling-type switching. In the present case, values of $\alpha \approx 2$ support the curling mode scenario.

Kurkijärvi Model

To describe the temperature dependence of the switching field more quantitatively, the Kurkijärvi model is used.[49], [53]–[55] It relates the observed switching field H_{sw} to the temperature and sweep rate v of the external field:

$$H_{\mathrm{sw}} = H_{\mathrm{sw}}^0 \left\{ 1 - \left[\frac{k_B T}{U_0} \ln \left(\frac{k_B T H_{\mathrm{sw}}^0}{\alpha \tau_0 U_0 v \left(1 - \frac{H_{\mathrm{sw}}}{H_{\mathrm{sw}}^0}\right)} \right) \right]^{1/\alpha} \right\} \tag{2.5.6}$$

This expression allows the extraction of the energy barrier U_0 and attempt time τ_0 by fitting to temperature-dependent switching field measurements.

Curie Temperature and Temperature Dependence of Magnetisation

Magnetic properties of materials are generally temperature-dependent. A key feature of ferromagnetic systems is the vanishing of spontaneous magnetisation above a critical temperature known as the Curie temperature T_C. At $T > T_C$, thermal excitations overcome the interatomic exchange interactions, leading to a transition from an ordered ferromagnetic to a disordered paramagnetic state.

In a classical picture, increasing temperature leads to randomisation of spin orientations due to thermal fluctuations. From a quantum-mechanical perspective, thermal excitation enables population of spin states with $S_z < S$, reducing the net magnetisation.

The underlying mechanism responsible for ferromagnetic order in most materials is the interatomic exchange interaction. This exchange energy is typically on the order of $J \sim 0{,}01\,\mathrm{eV}$ between neighbouring atomic spins. The magnitude of J determines the robustness of magnetic ordering and thus sets the scale of the Curie temperature.

In mean-field models, each atomic spin is considered to be subjected to an effective exchange field generated by its surrounding neighbours. This simplification leads to an analytical expression for the temperature dependence of the magnetisation and provides an estimate for $T_C \propto zJ$, with the number of interacting neighbours z. Although mean-field theory tends to overestimate the actual Curie temperature, it captures the qualitative features of the phase transition.

Material Properties Fe nanowires and EuS nanodisc

The magnetic properties of the Fe nanowire and EuS nanodisc investigated in this work are summarised in Table 2.2.

Fe nanowires encapsulated in CNTs exhibit a high saturation magnetisation and strong shape anisotropy. The Fe core typically forms a high-quality single-crystalline structure as reported by Banerjee et al. [55]. Nanowires with a diameter > 24nm, the reversal process is expected to be governed by curling mode. The anisotropy field of the nanowires $H_k \approx 1.1\,\mathrm{T}$ is dominated by shape anisotropy, with the crystalline contribution being negligible [55].

EuS, in contrast, is a soft ferromagnetic insulator with low coercivity and a Curie temperature around 18–19 K [50]. It belongs to the class of isotropic Heisenberg ferromagnets and can be grown as thin films suitable for spin transport studies. EuS exhibits relatively low saturation magnetisation and high Gilbert damping.

In addition EuS exhibits several key functionalities that make EuS a suitable candidate for coupling it to superconductors and create spintronic structures. [57]–[61]

EuS has the ability to induce a strong magnetic proximity effect in adjacent superconductors. When coupled to a superconductor such as aluminium (Al), EuS can produce an effective internal exchange field that spin-splits the superconducting density of states (DOS), even in the absence of an external magnetic field.

EuS also acts as an efficient spin-filtering barrier. Due to its spin-dependent band structure and ferromagnetic order, it preferentially transmits one spin orientation over the other during electron tunnelling.

A major advantage of EuS-based devices is their ability to operate in a spin-split state without requiring an external magnetic field. The spontaneous magnetisation of EuS below its Curie temperature provides an intrinsic exchange field to the adjacent superconductor.

This proximity-induced spin splitting opens pathways for zero-field spintronics, spin-filtered superconductivity, and spin-valves.

Table 2.2.: Magnetic properties of the Fe nanowire and EuS nanodisc used in this work.

Parameter	**Fe**	**EuS**	**Unit**
Saturation magnetisation M_{sat}	1.75 [56]	1.16 [50]	MA/m
Exchange stiffness A_{ex}	21 [56]	0.16 [56]	pJ/m
Exchange length l_{ex}	3.3	0.43	nm
Curie temperature T_C	1044 [56]	18 [50]	K

Chapter 3.

SQUID and Magnetic Nanoparticle Fabrication and Measurement Setups

This chapter presents the materials and methods employed in this thesis. It includes the fabrication process of YBCO-based SQUIDs, the placement of magnetic nanoparticles, and the experimental setups used for characterisation and measurements. The focus here is to provide an overview of the key steps and parameters relevant to the fabrication and measurement processes. Specific innovations, process optimisations, and detailed results are discussed in the respective results chapters.

3.1. Fabrication of YBCO SQUIDs: From Thin Film to Device

Lithography and FIB milling are the central techniques in micro- and nanofabrication that enables precise structuring of high quality thin films for superconducting devices. The fabrication process begins with the epitaxial deposition of high-quality YBCO thin films using pulsed laser deposition. These films are then structured via optical lithography to define structures such as a thin bridge over the grain boundary, bond pads, basically the coarse layout for a SQUID. Argon ion beam etching (Ar-IBE) to transfer the defined structures into the YBCO thin film. After an initial electrical characterisation of the thereby resulting grain boundary Josephson junction, the structure is further refined using FIB nanopatterning. The precise nanopatterning of a hole, a modulation line and narrowing of the Josephson junction result in a fully functioning SQUID device. An example of a fully patterned SQUID is shown in Figure 3.2 in Chapter 3.2.1. Further details regarding the design and fabrication optimisation are provided in Chapter 4.1.

3.1.1. Optical Lithography

Optical lithography is employed to define the microscopic structures on the YBCO thin films using a UV-light-sensitive photoresist. In this work, two different systems were used to expose the resist: the Karl Suss MA/BA6 mask aligner, which uses conventional chrome masks, and the µMLA Tabletop Maskless Aligner (Heidelberg Instruments), which transfers CAD-designed patterns directly into the resist using a laser. The minimum feature size is limited by the wavelength of the light source, with features down to 2 µm being reliably patterned.

The full process consists of the following steps:

- **Surface Cleaning:** The sample surface is cleaned using acetone and isopropanol to remove organic contaminants. It is then dried with a nitrogen stream.
- **Photoresist Spin Coating:** A layer of positive photoresist (e.g. ma-P 1215) is deposited using a spin coater to achieve a uniform thickness.
- **Soft Baking:** The coated substrate is baked on a hot plate at 90 °C for 3 minutes to evaporate residual solvents and improve adhesion.
- **Mask Alignment and Exposure:** The resist-coated sample is aligned to the grain boundary using either the mask aligner or the µMLA system, followed by exposure to UV light.
- **Development:** The exposed resist is developed in an appropriate developer solution to reveal the pattern.
- **Hard Baking:** The developed sample is post-baked at 90 °C for 5 minutes to improve resist stability and adhesion during subsequent etching steps.

Optical lithography is essential for defining larger device components such as contact pads, bridges, alignment markers for FIB processing, and coarse patterning of the SQUID layout.

3.1.2. Etching

Etching techniques are essential for structuring thin films after lithographic patterning, enabling selective material removal with high precision. Various etching methods exist, including wet chemical etching and plasma-based techniques such as reactive ion etching (RIE) and ion beam etching (IBE). In this thesis, the YBCO thin films were structured using Ar-IBE.

Ar-IBE is a purely physical etching process in which argon atoms are ionised and accelerated towards the sample under vacuum conditions. Upon impact, these ions ablate the material. This technique is especially favourable for YBCO, as it avoids the introduction of water or reactive gases, which could otherwise degrade the superconducting properties by altering oxygen stoichiometry.

A drawback of Ar-IBE is the heat generated during the etching process, which can lead to unwanted thermal effects such as oxygen loss near the surface. To mitigate this, the etching is performed in periodic cycles to allow for cooling between sputtering intervals.

The typical etching parameters used in this work are:

- Chamber pressure: 4.20×10^{-4} mbar
- Ion energy: 400 eV
- Beam current: 20 mA

- Shutter duty cycle: 10 s closed, 5 s open

This approach enables directional, anisotropic etching with high edge fidelity, essential for accurate definition of a thin bridge crossing the grain boundary and bond pads for a SQUID.

3.1.3. Precharacterisation of Grain Boundary Bridges

The initially fabricated sensor structures consist of bond pads and a single superconducting bridge across the grain boundary. This bridge contains one large (few µm wide) grain boundary Josephson junction and serves as a precursor to the final SQUID structure. Before proceeding to further nanopatterning steps, it is beneficial to precharacterise the bridge in order to assess key electrical properties of the YBCO film and junction.

This characterisation provides important parameters such as the critical current resistance product (I_0R) and helps evaluate the uniformity and quality of the Josephson junctions across the chip. The precharacterisation step is essential for monitoring the fabrication process up to this point—from film deposition to lithographic patterning and etching.

The characterisation is performed via four-point measurements at cryogenic temperatures. A magnetic field is applied parallel to the Josephson junction (perpendicular to the thin film plane) to tune and suppress the critical current of the junction. Typical measurements include:

- Current–voltage characteristics (IVC) at zero field
- $I_\mathrm{c}(B)$ curves for both positive and negative bias current I_b
- IV curves under externally applied magnetic field to suppress I_c
- Optional: IV curves at different B
- Voltage versus magnetic field $V(B)$ curves at different I_b

These measurements are typically carried out in a cryogenic transport setup. Details on the electrical transport measurements are provided in Chapter 3.1.5.

3.1.4. Nano-Patterning

To define the final nanoscale geometry of the SQUIDs, FIB milling was used. FIB is a high-precision technique that enables local material removal by directing a focused beam of high-energy ions—typically gallium (Ga) or neon (Ne), with $20 - 30\,\mathrm{keV}$—onto the sample. This method is especially suited for nanostructuring YBCO devices, as it allows for feature sizes down to 50 nm to be reliably patterned.

Key challenges that arise during FIB processing include edge damage and ion implantation, both of which can degrade superconducting properties.

General Considerations

To avoid electrostatic charging during FIB milling, the sample is mounted on an aluminium holder and electrically grounded using a strip of carbon tape. Precise focusing of the ion beam is essential for accurate patterning. For this purpose, the alignment markers defined during the optical lithography step are useful. These markers have a well-defined position relative to the bridge and allow for pre-alignment of the ion beam and performing test cuts near the target area. Test cuts of holes and crosses help to precisely focus the ion beam.

One of the critical steps in nanoSQUID fabrication is the identification of the grain boundary in the substrate, as it defines the location of the Josephson junction. Details on grain boundary identification are provided in Chapter 4.1.1.

To minimise damage to the superconducting bridge, the ion beam should not be scanned over areas that are not intended to be removed. This reduces the risk of unwanted modifications, including oxygen loss and edge amorphisation.

Ga-FIB Milling

To obtain the desired nanoscale geometries and milling depth, a series of test cuts are performed prior to the main milling step. The primary parameters used for Ga-FIB milling are:

- Acceleration voltage: 30 kV
- Beam current: 10–30 pA

In general, lower beam currents reduce edge damage but require longer milling times. Since long milling processes can suffer from sample drift, a compromise must be found between resolution and process stability. For most structures, a milling duration of approximately 10 minutes provides a good balance between precision and reliability.

To avoid oxygen depletion in the YBCO, the milling strategy is designed such that the ion beam starts from the centre of the area to be retained and proceeds outward. This method ensures that the exposed edges of the superconducting film are passivated by redeposited material from subsequent milling steps. This self-passivation helps preserve the superconducting properties at the nanobridge edges.

In this thesis, the dual-beam FIB/SEM systems *FEI Strata DB235* from the research and service facility LISA+[1], *Zeiss Crossbeam 550L* from the Tübingen Structural Microscopy core facility (TSM)[2], and *FEI Helios Nanolab 650* from the Laboratorio de Microscopías Avanzadas (LMA) in Zaragoza[3] were used. These systems offer the ad-

---

[1] LISA+ is a research and service facility within the infrastructure of the University of Tübingen, details at `https://uni-tuebingen.de/en/research/research-infrastructure/lisa/` [Accessed 26.04.2025]

[2] TSM coordinates the existing resources in electron microscopy of the Departments of Biology and Earth Sciences at the University of Tübingen, details at `https://uni-tuebingen.de/en/research/research-infrastructure/tuebingen-structural-microscopy-tsm/` [Accessed 26.04.2025]

[3] LMA is an initiative at the University of Zaragoza focusing on nanofabrication and characterisation of materials, details at `https://lma.unizar.es/en/` [Accessed 26.04.2025]

vantage that the abrasive Ga-FIB ion beam can be aligned with a scanning electron microscope (SEM), enabling precise positioning of the ion beam without damaging the sample and allowing detailed imaging of the milling process.

Ne-FIB Milling

Neon FIB milling follows a similar strategy to Ga-FIB. As a novel approach explored in this thesis, it is still in its early stages of development and requires further investigation. Initial observations suggest that Ne ions enable more precise and cleaner patterning, with feature sizes down to 50 nm being reliably achievable. However, it is advisable to avoid milling large areas, as the Ne-FIB process is significantly slower than Ga-FIB. Prolonged milling appears to induce local swelling of the substrate. Therefore, Ne-FIB is currently best suited for precision cuts and fine tuning of nanoscale geometries rather than large-area structuring.

Further technical details regarding Ne-FIB milling can be found in Timur Weber's PhD thesis.[62] In this thesis, the helium/neon ion microscope system *Zeiss ORION Nanofab* from the research and service facility LISA+ was used. Unlike the dual-beam systems, the ORION Nanofab is a single-beam microscope, requiring careful manual positioning to accurately align the ion beam at the intended patterning location on the sensitive thin film.

3.1.5. Electrical Transport Measurements on SQUIDs

Transport measurements are a fundamental aspect in the characterisation of SQUIDs. The main goal of these measurements is to assess the superconducting properties of the YBCO nanoSQUIDs and to ensure that their electrical characteristics meet the requirements for high-sensitivity magnetometry.

The operating principle of SQUIDs is based on the Josephson effect, which is described in detail in Chapter 2.3. Four-point transport measurements are used to characterise the current–voltage behaviour, and both an external magnetic field and a local modulation line are used to apply magnetic flux to the SQUID loop. The fundamental transport measurements include:

- **IV Characteristics:** The IVC of the SQUID reveal the critical current I_c, resistance R, and the shape of the curve. Comparison to the RCSJ model provides insight into junction quality and the presence of excess current or hysteresis.
- **Critical Current vs Magnetic Field:** The critical current I_c is modulated by either an external magnetic field B or a current through an on-chip modulation line I_{mod}. The resulting $I_\mathrm{c}(B)$ or $I_\mathrm{c}(I_{mod})$ curves reveal information about junction asymmetry, the screening parameter β_L, and the presence of trapped flux. The modulation period of $I_\mathrm{c}(I_{mod})$ is important for the evaluation of the SQUID in FLL operation.
- **Voltage vs Modulation Current Family:** A family of $V(I_{mod})$ curves at different fixed bias currents I_b is recorded. These curves reveal the periodic voltage

response of the SQUID to applied flux. They can be used to determine the voltage modulation amplitude and damping parameter β_C.

- **Voltage vs Bias Current Family:** This family consists of multiple $V(I_b)$ curves recorded at various values of I_{mod}. These measurements are similar to the Voltage vs Modulation Current Family and allow and provide additional insight into the junction damping. At minimum and maximum I_c, selected IV curves are of particular interest, since they provide a good overview of the junction performance.
- **Noise Measurements:** The frequency-dependent voltage noise spectrum provides information about the intrinsic noise performance of the SQUID and quality of the YBCO thin film. Although noise characterisation is crucial for highly sensitive magnetometry, it is not the focus of this work and is therefore not discussed in detail here.

The transport measurements are carried out in a cryogenic setup described in the next section.

3.1.6. Measurement Setups

This section describes the experimental setups used to electrically characterise the SQUIDs and magnetic nanoparticle systems. Depending on the specific requirements—such as temperature, magnetic field, or noise sensitivity—different setups were employed. In total, three primary measurement environments were available: a compact ^{4}He transport setup, a high-field ^{3}He setup in Tübingen, and a ^{3}He/^{4}He dilution refrigerator system from *BLUEFORS* in QMAD[4] in Zaragoza.

Instituto de Nanociencia y Materiales de Aragón Zaragoza, Spain

Electrical Setup

Two electronic systems were available: a custom-built in-house setup and a commercial SQUID electronic system from `Magnicon`. All transport measurements were performed using a four-point measurement configuration, even though the SQUID electronic has a more complex wiring scheme, which is described in more detail in Robin Hutt's Master thesis. [63]

In the in-house setup, a low-noise, battery-powered current source is used to bias the device, and the resulting voltage drop is amplified at room temperature before being digitised via a data acquisition card. The operation of the current source and reading of the data acquisition card is done by the `GoldExi` software[5].

In the `Magnicon` SQUID electronics, the bias and modulation current source as well as the voltage readout are fully integrated into the hardware. The system is capable

---

[4] Quantum Materials and Devices (QMAD) is a research group from the Physics of materials and nanosystems department in the Instituto de Nanociencia y Materiales de Aragón (INMA) in Zaragoza, Spain. María José (Pepa) Martínez-Pérez and her team is part of this group.

[5] Program written by Edward Goldobin. Further details are available at `https://www.geocities.ws/goldexi/links.htm` [Accessed 06.04.2025]

of operating the SQUID in a FLL mode at MHz bandwidth. Data acquisition can be performed via `GoldExi`, `LabVIEW`, or custom `python` scripts.

Transport Setup

The simplest and most efficient measurement setup is the so-called transport setup. Chips are mounted and wirebonded onto a sample holder equipped with an integrated copper coil capable of applying magnetic fields in the mT range. This holder is mounted on a dipstick, which includes an RC filter board and LC feedthrough filters. The chip environment is enclosed within a copper shield acting as a Faraday cage, surrounded by a cryoperm shield to reduce magnetic interference.

The entire dipstick is immersed directly into a transport dewar filled with liquid helium. The complete setup is placed inside an electromagnetic shielding chamber. This configuration enables fast and straightforward measurements, typically within a few hours, with relatively low helium consumption.

High-Field Setup

For high-field and variable-temperature measurements in Tübingen, the so-called high-field setup was used. The configuration is shown in Figure 3.1a. The sample chips are mounted and wirebonded onto a sample holder attached to a copper block, which is screwed onto the base of the so-called 300 mK dipstick. Details of the dipstick design and cooling mechanism can be found in Julian Linek's Master thesis.[64]

The sample resides in vacuum and is thermally coupled to a sophisticated closed-cycle cooling system that uses ^{3}He condensation and evaporation to reach base temperatures down to 300 mK. A resistive heater is used to control the temperature. The entire dipstick is inserted into a liquid helium cryostat containing a superconducting magnet system capable of generating magnetic fields of several Tesla. Compensation coils allow precise alignment of the field with respect to the sample. The `vectorramp` control software, developed by Carsten Spanheimer, enables precise field control.[65]

The advantages of this setup are the ability to reach high magnetic fields and perform measurements over a wide range of variable temperature. However, it requires several days of preparation, consumes a considerable amount of liquid helium, and poses challenges in electromagnetic shielding.

Dilution Refrigerator Setup

For ultra-low temperature and high-field measurements in Zaragoza, a dilution refrigerator setup was used. An image of the setup is shown in Figure 3.1b. The dilution refrigerator (Bluefors) provides continuous cooling to temperatures below 15 mK through the dilution of a ^{3}He–^{4}He mixture in a closed-loop environment.

The system includes a three-axis vector superconducting magnet capable of generating several Tesla in arbitrary directions. Chips are mounted and wirebonded onto a sample holder, which is directly connected to the fridge's cold plate. Electrical connections run to the top of the fridge, where a `Magnicon` SQUID electronic system can be connected.

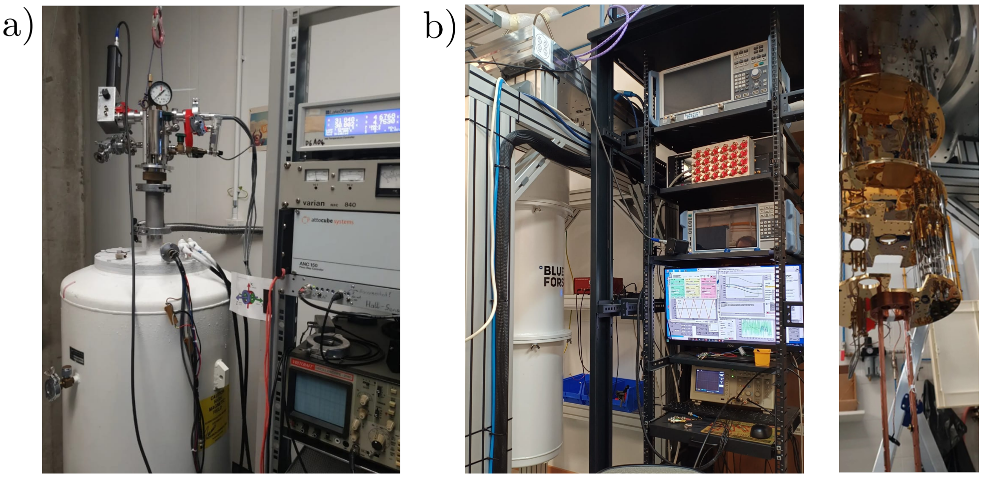

Figure 3.1.: (a) Photograph of the high-field setup in Tübingen. (b) Images of the dilution refrigerator setup in Zaragoza, shown both open and closed.

The main advantages of this setup are its extremely low base temperature and large, precisely oriented magnetic fields. Since the system is closed-loop, no liquid helium is required during operation. However, the cooling system of the setup consumes a significant amount of electrical power and has a long turnaround time: sample mounting, cooling, measurements, and warm-up together take several days.

3.2. Fabrication and Placement of Nanoparticles

3.2.1. Fe Nanowires in Carbon Nanotubes

This section describes the placement of CNTs encapsulating Fe nanowires, produced by collaborators at IFW Dresden. The CNT placement procedure follows a similar approach to that described by the Master thesis by Leon Koch.[66] The step by step procedure of the placement can be seen in Figure 3.2.

To measure magnetisation reversal in these Fe nanowires, an external magnetic field must be applied parallel to the nanowire axis. I_c suppression is minimised by applying the external field perpendicular to the Josephson junction barrier plane. Furthermore, CNTs were placed on the opposite side of the modulation line (marked in magenta). This approach prevents the CNT from being placed too far away from the sensitive region of the SQUID, thereby reducing the risk of a low coupling factor.

The placement was performed at IFW Dresden by Thomas Wiek and Thomas Mühl using a nanomanipulation system (Thermo Scientific EasyLift) integrated into the vacuum chamber of a dual-beam FIB-SEM system (Thermo Scientific Helios 5 CX).

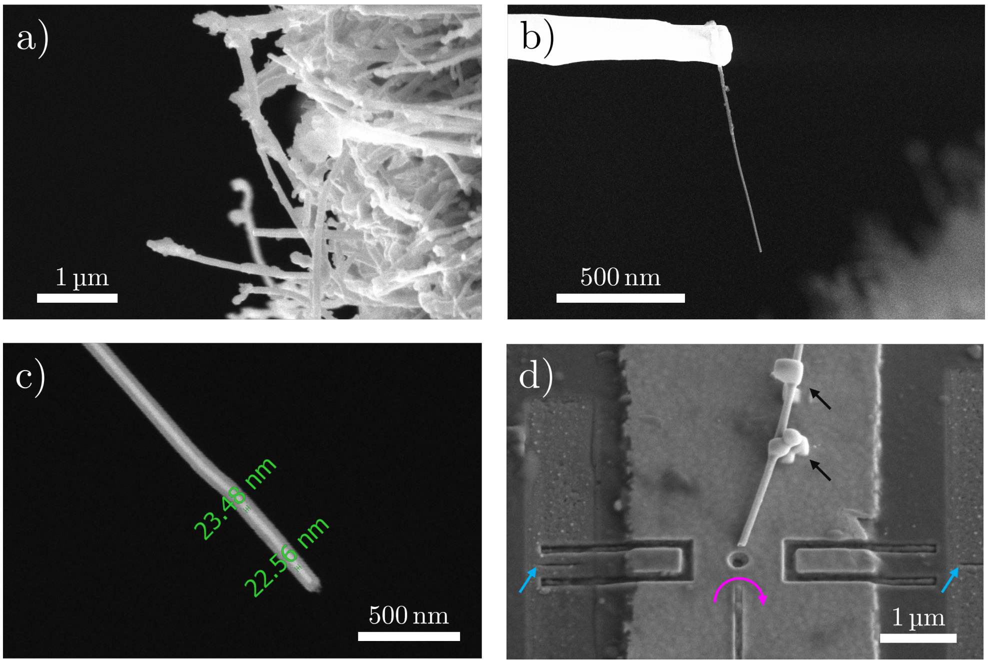

Figure 3.2.: SEM images showing Fe nanowire placement on a SQUID. SEM images were taken by Thomas Wiek and Thomas Mühl in the IFW Dresden. (a) A dense forest of CNTs containing Fe nanowires as grown. (b) A selected CNT is attached to the nanomanipulator using Pt deposition and separated from the forest. (c) Close-up of a suspended CNT. With no background, both the Fe core and CNT shell are clearly distinguishable, allowing diameter estimation. (d) SEM image at 35° tilt showing the CNT positioned on the SQUID. The CNT is fixed with local Pt deposits (black arrows). The modulation line is marked by a magenta arrow, that depicts a modulation current. The grain boundary is highlighted by blue arrows.

3.2.2. EuS Nanodisc Placement

The fabrication and placement of EuS nanodiscs was carried out by the group of María José (Pepa) Martínez-Pérez in Zaragoza. A 40 nm thick EuS film was grown on a free-standing Si_3N_4 membrane by collaborators from the Materials Physics Center in San Sebastián. Using FIB milling, nanodiscs were patterned and transferred onto the SQUIDs by Isabel Rivas and Carolina del Río.

The process begins with patterning the EuS nanodiscs directly into the thin film. Cuts through the membrane define the nanodisc like a stencil or "kit card" structure. The entire chip is then flipped, and an OmniProbe nanomanipulator is connected to the rear of the membrane via electron-beam-induced Pt deposition. Surrounding structures are removed with FIB, releasing the disc for transfer.

The disc is then transported and positioned onto the SQUID. Once aligned, it is fixed in place using local Pt deposition, and finally detached from the manipulator using FIB. This method enables precise placement with nanometre resolution and ensures good magnetic coupling.

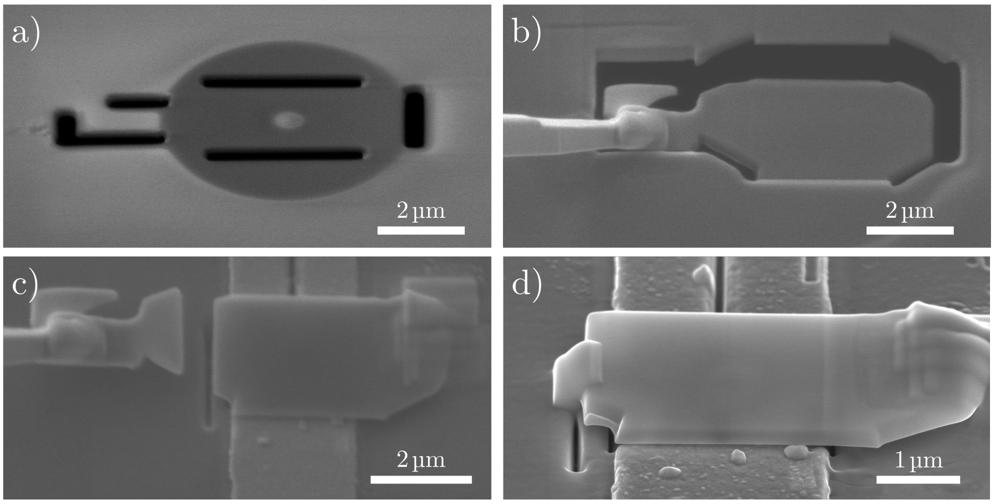

Figure 3.3.: SEM images showing EuS nanodisc fabrication and placement. SEM images were taken by Isabel Rivas in the LMA Zaragoza. (a) An EuS disc is patterned by FIB into a 40 nm film on a Si_3N_4 membrane. Cuts through the membrane prepare the disc for removal. (b) The sample is flipped. An Omniprobe is attached from behind using Pt deposition. The disc is freed by additional FIB milling. (c) The disc is transported and positioned on the SQUID and fixed by Pt deposition. The attachment to the Omniprobe is cut by FIB. (d) SEM image at 52° tilt showing the EuS nanodisc placed on the SQUID. It is fixed by Pt depositions on both sides.

Chapter 4.

YBCO-SQUIDs: fabrication, characterisation and application

This chapter presents and discusses the advancements made in the fabrication, optimisation, and application of YBCO based SQUIDs. These devices were developed and tailored to meet the high-sensitivity requirements for the magnetic characterisation of nanoparticles.

This chapter consists four sections, that can be divided into two themes: theme (I) comprises Chapter 4.1 and 4.2, which address the fabrication and characterisation of SQUIDs, and theme (II) comprises Chapter 4.3 and 4.4, which address the applications of SQUIDs in nanoparticle studies. Theme I is dedicated to an in-depth examination of the methodologies employed in the development and optimisation of YBCO-based SQUIDs. It encompasses a comprehensive analysis of novel techniques employed in thin-film and substrate processing, along with a detailed investigation of the electric transport properties of these devices. Theme II illustrates the utilisation of these devices in the magnetic characterisation of two nanoparticle systems, thereby offering insights into their physical behaviour under various external fields and temperatures.

The main findings of this chapter are presented as follows:

- **Fabrication and Optimisation of YBCO-Based SQUIDs:** The successful development and characterisation of high-quality YBCO-based SQUIDs are presented, with results demonstrating their sensitivity and robustness for the nanoparticle studies presented in Chapter 4.3 and 4.4.

- **Vector Substrate Fabrication:** A novel fabrication approach for YBCO microstructures, based on the transfer of a oxide membrane to a substrate is presented. Although these structures were not directly applied to nanoparticle characterisation, they provide valuable insights into a novel fabrication technique of grain boundary YBCO SQUIDs.

- **Magnetic Properties of Fe Nanowires:** Temperature-dependent magnetic properties of Fe nanowires embedded in CNTs are presented. The results extend on previous studies, providing a deeper understanding of the magnetisation reversal mechanism of these nanowires.

- **Magnetic Properties of EuS Nanodiscs:** Magnetometry measurements on EuS nanodiscs are discussed, highlighting the differences between different disc diameters. The results contribute to a more comprehensive understanding of their magnetic behaviour and potential applications.

This chapter ties together advancements in SQUID fabrication with their application in nanoparticle characterisation. The results not only demonstrate the effectiveness of the developed devices but also offer critical insights into the magnetic properties of the studied nanoparticles. These findings form the foundation for further research and potential technological applications.

4.1. Fabrication and Optimisation of YBCO based SQUIDs for Magnetic Nanoparticle Measurements

This section provides an overview of the fabrication and characterisation of the YBCO SQUIDs used for the measurement of magnetic nanoparticles later in this thesis.

Chapter 4.1.1 presents the unique challenges of fabricating high-quality SQUIDs, based on grain boundary Josephson junctions. Chapter 4.1.2 presents the properties of the SQUID devices used in this work in a summary table that offers an overview of the devices' key characteristics.

The SQUIDs used for the characterisation of Fe nanowires embedded in CNTs is described in the Chapter 4.1.3. It begins with an initial pre-characterisation of the fabricated microbridges. This is followed by a detailed analysis of the SQUID devices, both before and after the placement of the nanoparticles.

In the subsequent Chapter 4.1.4, the SQUIDs developed for measurements of EuS nanodiscs are presented. Particular attention is given to the temperature dependence of their properties in the range of 15 mK to 20 K.

An innovation in this work is the use of Ne-FIB technology for SQUID fabrication, presented in the Chapter 4.1.6. While Ga-FIB methods are conventionally employed, this study compares the properties of SQUIDs fabricated using Ga-FIB and Ne-FIB approaches.

The Chapter 4.1.7 concludes with a discussion of the results, summarising the key findings and insights gained from the fabrication and characterisation processes. These results are the basis for the application of the SQUID devices in subsequent nanoparticle studies.

4.1.1. Challenges during Fabrication

The fabrication of grain boundary based SQUIDs from YBCO thin films is a multi-step process, involving pulsed laser deposition, optical lithography, and FIB milling. These steps are schematically summarised in Figure 4.1.

The process begins with the epitaxial growth of a YBCO thin film by pulsed laser deposition on a bicrystal substrate, which defines the grain boundary (magenta dotted line) that forms a Josephson junction. To protect the YBCO thin film from environmental degradation and during further processing, the surface is coated in situ with a gold layer by electron-beam evaporation.

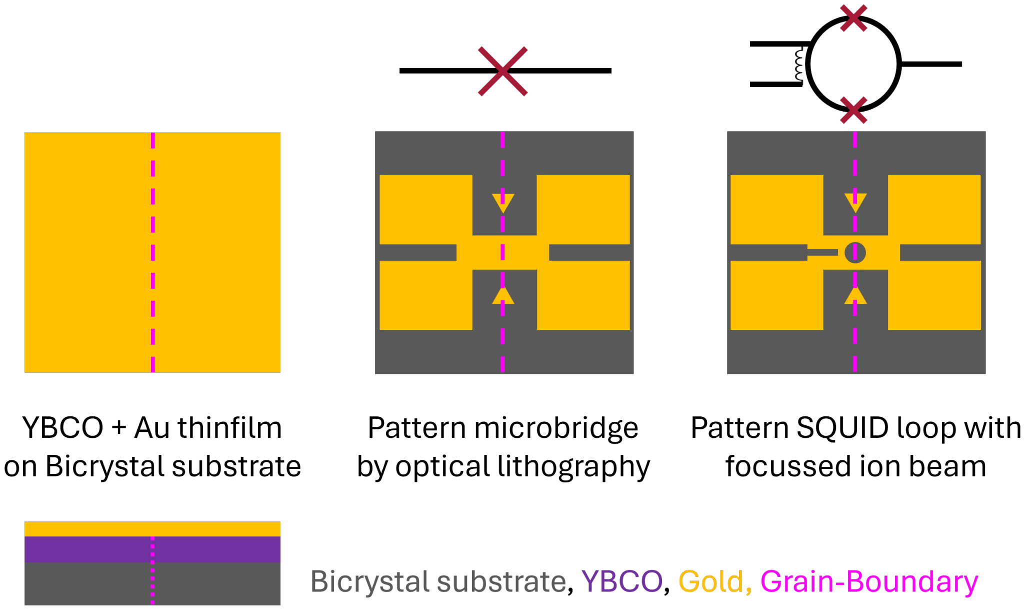

Figure 4.1.: Schematic of the fabrication process from a YBCO thin film to a nanopatterned SQUID. The YBCO thin film is epitaxially grown on a bicrystal substrate by pulsed laser deposition, transferring the grain boundary (magenta dotted line) into the film. A protective gold layer is deposited, followed by optical lithography to define a microbridge with bond pads and markers, resulting in a single Josephson junction. FIB milling then defines the SQUID structure with two Josephson junctions and an integrated modulation line for flux coupling. The circuit diagram depicts the Josephson junctions by a red cross and the modulation line with a coil.

The subsequent fabrication steps are divided into two main stages: the creation of microbridges and the nanopatterning of the SQUID structures. The microbridge, including bond pads and markers, is precisely patterned onto the chip by optical lithography. As seen in the circuit diagram above, this results in a single grain boundary Josephson junction. Afterwards, the SQUID structure is defined within the microbridge using FIB milling. The circuit diagram above, shows a circle with two Josephson junctions, which is the basic structure of a SQUID, and the modulation line, acting as a coil to couple flux into the SQUID.

Micropatterning: Optical Lithography

In the second fabrication step, optical lithography is used to define a microbridge pattern, including bond pads and alignment markers, with micrometer precision. Subsequently, Ar ion milling is employed to etch the created pattern into the Au/YBCO bilayer. This fabrication approach enables the realisation of structures with line widths down to 2 µm.

The microbridges in our pattern have a width of 4 µm and a length of 20 µm. The primary challenge lies in aligning the lithography masks with ±10 µm precision relative to the grain boundary. The grain boundary is typically visible only under transmitted light microscopy, with illumination from underneath the bicrystal substrate. For STO substrates, the grain boundary is clearly visible using this technique, while for MgO substrates, the grain boundary is often only observable when focusing on the backside of the substrate. In some cases, anisotropic etching with Ga-FIB milling is necessary to make the grain boundary visible, as shown in Figure 4.4(b).

Due to this limited visibility, aligning the microbridge using the µMLA maskless aligner, which only illuminates from above, is particularly challenging. To address this, a novel alignment procedure was developed based on a ruler-marker design (Figure 4.2(a)). Each ruler consists of small triangles of 10 µm length, allowing precise localisation relative to the grain boundary. Only the marker system is patterned during the first lithography step. TechniEtch wet etching is used to transfer the markers into the gold layer, selectively removing gold where the markers are exposed. The exposed YBCO becomes clearly visible under the microscope, enabling accurate alignment in subsequent steps and ensuring the grain boundary does not need to be repeatedly identified. After etching the markers, the sample is cleaned, recoated with photoresist, and the microbridge mask is aligned to the markers with an accuracy of approximately ±5 µm. The lithography parameters are summarised in Table 4.1. The microbridge pattern is then transferred into the Au/YBCO bilayer via argon ion milling, as shown in Figure 4.3.

Nanopatterning: Focused Ion Beam Milling

The final fabrication step involves patterning the SQUID loop and the modulation line using either Ne[1] or Ga-FIB milling. This step requires both coarse and precise alignment techniques to achieve accurate nanostructuring.

---

[1] Ne-FIB milling was performed by Timur Weber

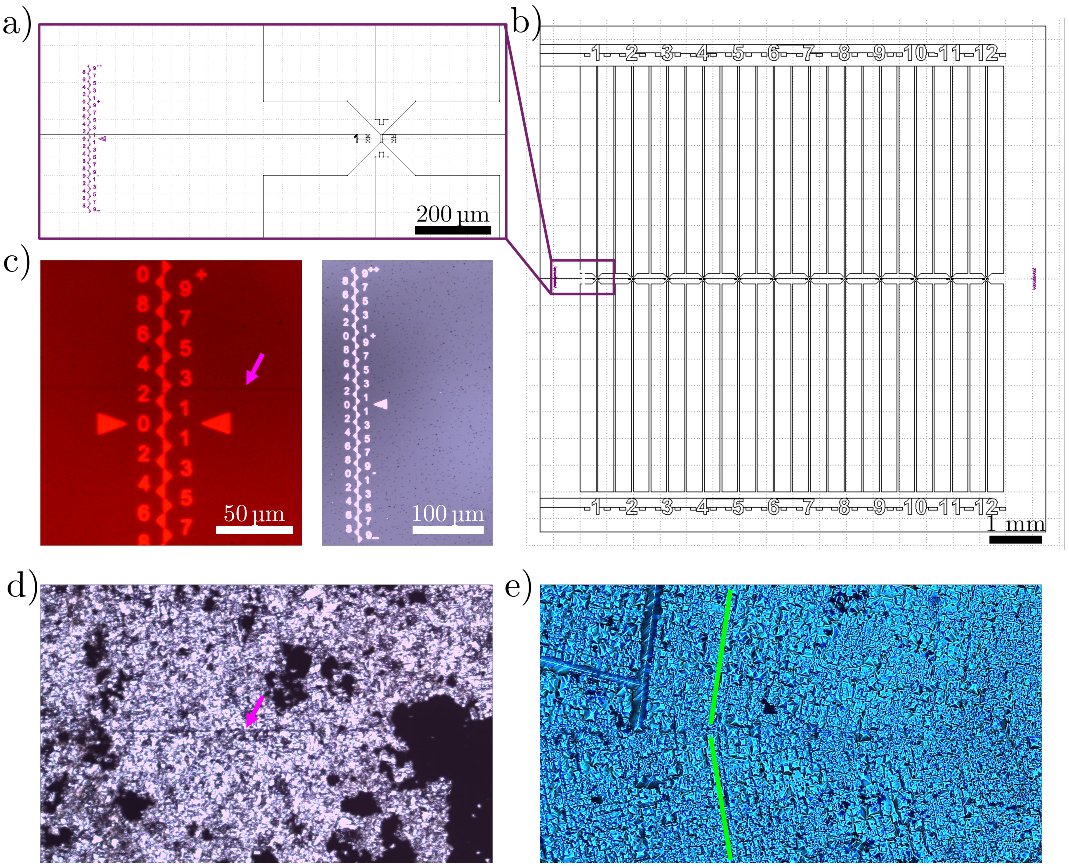

Figure 4.2.: Marker-based alignment strategy for microbridge fabrication. (a) Mask design for markers and microbridge. (b) Overview of the full lithography mask with 12 microbridges. The marker mask and microbridge are overlaid here. (c) Optical microscopy images of the marker system and grain boundary visibility for STO (left) and MgO (right) substrates, respectively. (d) Optical microscopy image focused on the rough backside of the bicrystal substrate. The grain boundary is marked by a magenta arrow. (e) Crystal orientation of an STO bicrystal visible from the backside. Green lines are added as visual aids to indicate the crystal orientation.

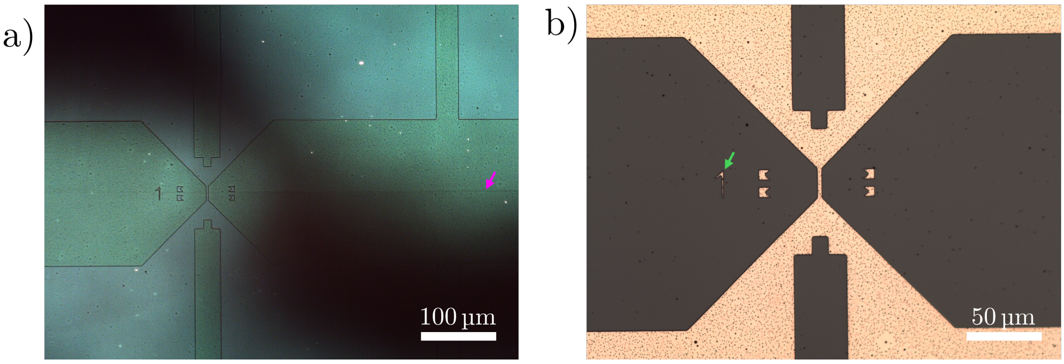

Figure 4.3.: Successful alignment of the mask with microbridges before and after the etching process. (a) Shows an STO bicrystal with patterned resist prior to the etching process. The grain boundary is indicated with a magenta arrow. (b) Displays the chip after the etching process and after removal of the mask. At position 1 (marked with a green arrow), slight overdevelopment of the resist can be observed. This step confirms the successful and precise transfer of the pattern into the Au/YBCO bilayer, critical for the precise alignment of the SQUID structure.

Table 4.1.: Lithography parameters for the CNT-Chip and EuS-Chip

	CNT-Chip	EuS-Chip
Resist	ma-P1215	ma-P1205
Spincoating	$v = 6000\,\mathrm{rpm}$, $t = 40\,\mathrm{s}$, ramp $10\,\mathrm{s}$	$v = 6000\,\mathrm{rpm}$, $t = 40\,\mathrm{s}$, ramp $10\,\mathrm{s}$
Soft-Bake	$T = 90\,°\mathrm{C}$, $t = 180\,\mathrm{s}$	$T = 90\,°\mathrm{C}$, $t = 180\,\mathrm{s}$
Exposure	Dose $190\,\mathrm{mJ}$, Defocus -4	Dose $180\,\mathrm{mJ}$, Defocus -4
developer	ma-D331/s, $t = 30 + 25 + 10 + 15\,\mathrm{s}$	ma-D331/s, $t = 15\,\mathrm{s}$

For coarse orientation in the FIB system, the combination of optical microscope data and lithographically etched markers near the microbridge is sufficient (Figure 4.4a).

For precise positioning, different approaches are used depending on the substrate material. On STO, the grain boundary is often associated with surface features, such as holes or contaminants, being visible at high resolution. However, the imaging resolution of the Ne-FIB system is not high enough to identify the these features of the grain boundary. Therefore, high resolution images from a SEM system need to be used as a reference to pinpoint the grain boundary during Ne-FIB milling. Alternatively, markers can be etched directly into the substrate surface using a dual SEM/Ga-FIB setup.

On MgO substrates, the grain boundary is generally not directly visible under normal imaging conditions. However, the anisotropic etching behaviour of Ga-FIB on MgO can be utilised to visualise the grain boundary. By etching rectangular trenches into the substrate at the estimated grain boundary location, the boundary can be effectively marked and identified (Figure 4.4b).

Once the grain boundary has been located or made visible, the SQUID design is patterned into the microbridge using either Ga- or Ne-FIB (Figure 4.4c, d).

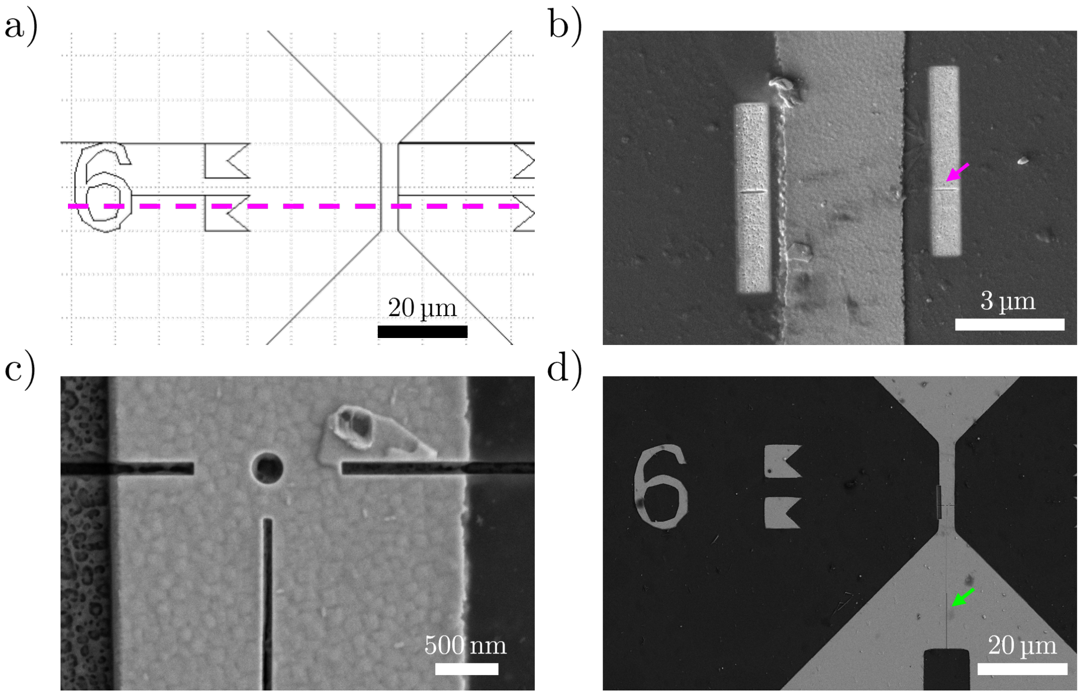

Figure 4.4.: Visualisation of the FIB nanopatterning process. (a) Lithography mask, with approximate location of the grain boundary indicated by a magenta dashed line. (b) SEM image of a prepatterned Au/YBCO microbridge (central vertical strip) on a MgO substrate of CNT-2. The bright two rectangles are etched by Ga-FIB. The position of the grain boundary is indicated by the magenta arrow. (c) SEM image of a nanostructured SQUID on MgO (CNT-6) patterned with Ne-FIB. (d) SEM image with overview of a successfully structured SQUID on MgO (CNT-6). The long cut for the modulation line is visible and highlighted with a green arrow.

Each ion source offers distinct advantages. Ne-FIB provides higher resolution, enabling precise patterning of smaller features critical to the SQUID design. Additionally, Ne-FIB avoids the implantation of Ga ions, which could degrade the superconducting properties of YBCO or potentially alter the substrate's properties. Ga-FIB, on the other hand, is more widely available due to the widespread use of dual SEM/Ga-FIB systems. It also offers a higher ablation rate, making it suitable for removing larger areas of material efficiently. However, Ga ion implantation and possible substrate damage need to be carefully managed.

A specific challenge encountered during this process is the potential swelling of the substrate when subjected to high ion doses, particularly in larger ablated areas when using Ne-FIB milling. Consequently, it is advised to use Ga-FIB for coarse structuring, while Ne-FIB is used for fine detailing to achieve optimal resolution and minimal damage.

4.1.2. Overview of SQUIDs used in this thesis

This subsection provides an overview of all SQUIDs used in this thesis, summarising their design parameters and key characteristics. The SQUIDs measured and presented in this thesis originate from two different YBCO thin films. To ensure traceability throughout the fabrication and measurement processes, the chips were named immediately after thin film deposition according to the convention *Crystal_ Substrate_ Year_ Number*, where the number increments sequentially with each new film produced in the corresponding year. Fe nanowire (CNT-1 to CNT-6) measurements were performed on the chip *Bi_ MgO_ 21_ 2*, with a YBCO thin film grown on a MgO 24° bi-crystal and 12 microbridges patterned into the thin film. EuS measurements were conducted on *Bi_ STO_ 22_ 1*, with a YBCO thin film grown on a STO 24° bicrystal and 14 microbridges patterned into the thin film. Each SQUID is identified by a label that combines the particle system under investigation and the microbridge number on the respective chip.

A comparison of the SQUIDs used in this thesis to other SQUIDs can be found in Chapter 4.1.6. Table 4.2 shows the overview of the SQUIDs used in this thesis. As expected the SQUID characteristics like I_c and R_n of similar sized SQUIDs on the same chip can vary $\approx 20\,\%$.[1]

Table 4.2.: Parameters of the SQUIDs used for Fe nanowire and EuS nanodisc measurements. The measurements corresponding to these data are shown in Fig. 4.11 to Fig. 4.20, where the specific measurement points and temperatures are described in more detail. Typically, measurements were conducted in liquid helium ($T = 4.2\,\mathrm{K}$), however the measurements of the SQUIDs with EuS discs were performed in a dilution refrigerator. Fe nanowire (CNT-1 to CNT-6) measurements were performed on the chip *Bi_MgO_21_2* with $T_\mathrm{c} = 87.8\,\mathrm{K}$, $d_\mathrm{YBCO} = 80\,\mathrm{nm}$, and $d_\mathrm{Au} = 20\,\mathrm{nm}$. EuS measurements were conducted on *Bi_STO_22_1* with $T_\mathrm{c} = 89\,\mathrm{K}$, $d_\mathrm{YBCO} = 90\,\mathrm{nm}$, and $d_\mathrm{Au} = 60\,\mathrm{nm}$.
*Modulation line incomplete.
**For theses SQUIDs the same recipe was used as for SQUID EuS-10.
***IVC was measured at zero external field, therefore it is not possible to give an exact value for $I_\mathrm{c,max}$ or $I_\mathrm{c,min}$.
****These values have a unknown uncertainty, since during these measurements the nanodiscs were already placed on top which will effect the external field due to the permeability of the discs.

SQUID	date of measurement	Hole ⌀ [nm]	$width_\mathrm{Jj}$ [nm]	$I_\mathrm{c,max}$ [µA]	$I_\mathrm{c,min}$ [µA]	R_n [Ω]	$Ic * R$ [V]	M_f [Φ_0/mA]	A_eff [µm^2]	r_eff [µm]	V_Φ [mV/Φ_0]
CNT-1	15.08.23	5000*	200	103	54	3.5	361		5	1.26	-
CNT-1	11.01.24	120	200	85	44	3.8	323	1.1	1.3	0.65	3.0
CNT-2	15.08.23	120	200	55	23	3.6	198	2.1	0.8	0.51	0.8
CNT-3	15.08.23	250	500	88	31	4.0	349	1.7	1.7	0.74	2.6
CNT-4	11.01.24	600	1000	262	167	2.6	692	2.4	5.9	1.37	4.2
CNT-6	22.06.23	250	500	194	86	2.1	407	1.6	2.5	0.89	3.1
EuS-5	12.06.23	**	**	138	66	2.4	325	1.0	1.1****	0.59	-0.6
EuS-10	01.06.23	500x300	600	378	287	3.6	1359	1.0	2.3****	0.86	-1.3
EuS-11	03.11.23	**	**	45***	***	7.0	315	2.8	2.2****	0.84	2.3
EuS-12	03.11.23	**	**	257***	***	4.3	1117	0.9	3.3****	1.02	3.0

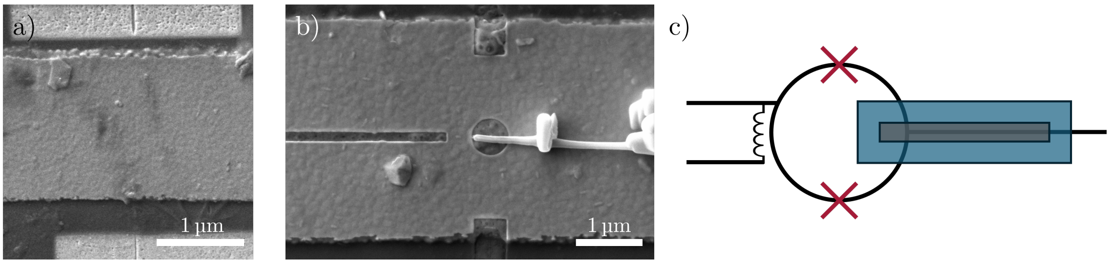

Figure 4.5.: Overview of the structures measured in the presented characterisations. (a) SEM image of an microbridge (CNT-2), representing a single grain boundary Josephson junction. This was the configuration for the measured microbridges shown in Figures 4.6 to 4.10. (b) A completed SQUID (CNT-4) with a placed Fe nanowire in a CNT. (c) A schematic of the SQUID with the Fe nanowire in place, illustrating the measurement configuration.

4.1.3. SQUIDs for Measuring Fe Nanowires

This subsection presents the results of the fabrication and characterisation of the sample *Bi_MgO_21_2*, designed for SQUIDs for the purpose of measuring Fe nanowires. The results of the Fe nanowire measurements are discussed in Chapter 4.3. As described in the previous section, the fabrication process involved optical lithography followed by FIB milling to define the SQUID structures.

Figure 4.5 provides an overview of the structures measured during the presented characterisations. Figure 4.5 a) shows an unprocessed microbridge, representing a single grain boundary Josephson junction. The microbridges measured in Figures 4.6 to 4.10 correspond to this configuration.

Figure 4.5 b) depicts a completed SQUID with a placed Fe nanowire. The SQUIDs characterised in Figures 4.11 to 4.15 follow a similar configuration.

Figure 4.5 c) illustrates a schematic of the SQUID with the Fe nanowire in place, showing the measurement configuration. The measurement setup and methodology are discussed in more detail in Chapter 3.1.6.

Characterisation of Microbridges

After patterning the Au/YBCO bilayer into 3.4 µm-wide microbridges, electrical characterisation was performed using four-point measurements in liquid helium. These measurements resulted in IVC curves and $I_c(B)$ curves. This approach checks whether the superconducting properties of the microbridge are sufficient to yield high-quality SQUIDs. Additionally, the spread of the I_c and I_cR products could provide insights into whether a patterned SQUID is particularly good or bad.

A magnetic field was applied perpendicular to the thin film plane using a coil integrated into the sample holder. Since the field was aligned parallel to the Josephson junction barrier plane and perpendicular to the long side of the Josephson junction, the suppression of I_c was relatively pronounced. All $I_c(B)$ measurements included a complete forward and backward field sweep.

Table 4.3.: Parameters of the microbridges measured at 4.2 K before Ne-FIB patterning. The microbridges are on chip *Bi_MgO_21_2* with $T_c = 87.8\,\mathrm{K}$, $d_{\mathrm{YBCO}} = 80\,\mathrm{nm}$, and $d_{\mathrm{Au}} = 20\,\mathrm{nm}$. Each bridge has a width of 3.4 µm. The measurements corresponding to these data are shown in Figures 4.6 to 4.10.

Microbridge	$I_{\mathrm{c,max}}$ [mA]	R_{n} [Ω]	$I_{\mathrm{c}}R$ [mV]
CNT-1	1.27	0.67	0.85
CNT-2	1.58	0.52	0.82
CNT-3	1.00	0.56	0.56
CNT-4	1.42	0.47	0.67
CNT-6	1.60	0.46	0.74

Additionally, IV curves were measured at fields where I_{c} was suppressed to determine the normal state resistance more accurately. These measurements provided a better understanding of the normal-conducting behaviour of the microbridges.

The extracted parameters for microbridges CNT-1, 2, 3, 4, and 6 are summarised in Table 4.3.

Figure 4.6 shows the transport characteristics of microbridge CNT-1. Similar to microbridge CNT-1, microbridge CNT-2 also exhibits good performance. The measurements are shown in Figure 4.7.

Figure 4.8 shows the transport characteristics of microbridge CNT-3, with a comparably low I_{c}. Whether the relatively low I_{c} is due to trapped flux cannot be determined with certainty, as no positive I_{c} values were recorded in the $I_{\mathrm{c}}(B)$ modulation curve. It is also well known that the characteristics of YBCO grain boundary Josephson junctions exhibit significant variation. Microbridge CNT-4 is shown in Figure 4.9. Microbridge CNT-6 is shown in Figure 4.10.

All the IV curves approach each other at higher currents and exhibit RCSJ-like behaviour without hysteresis. The $I_{\mathrm{c}}(B)$ curves are point-symmetric around 0 T (except for microbridge CNT-3 and CNT-6, where only one side was measured) and show I_{c} pattern typical for Josephson junctions in the intermediate range of short and long range Josephson junctions.[67] This indicates that the measurement is reliable and that the microbridges are in good condition and are suitable for further processing.

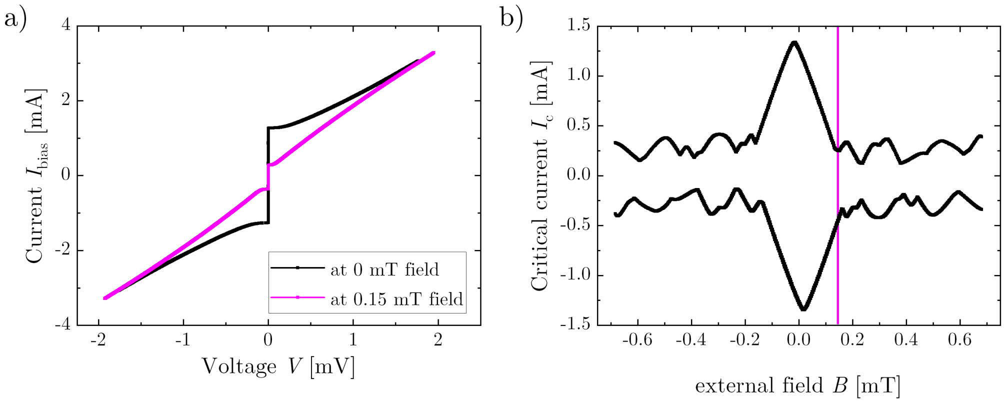

Figure 4.6.: Transport characteristics of microbridge CNT-1 measured at 4.2 K. (a) IVC measured at zero magnetic field and at a field where I_{c} is suppressed (indicated by the magenta line in b). (b) $I_{\mathrm{c}}(B)$ for both current polarities.

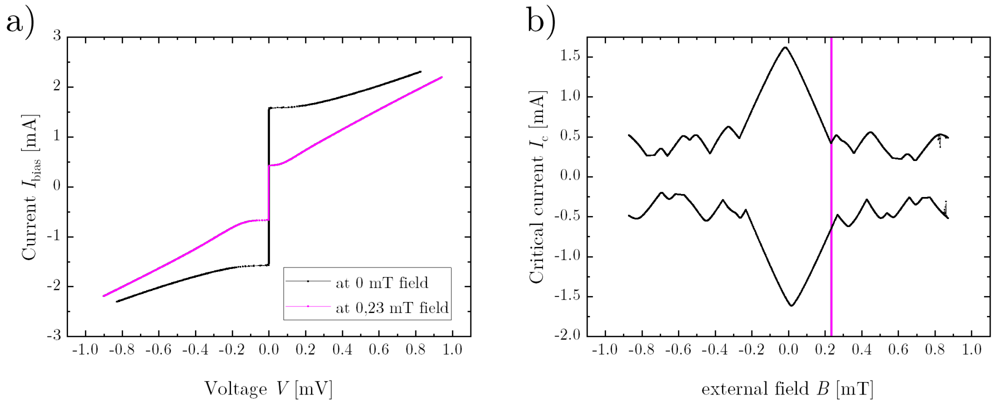

Figure 4.7.: Transport characteristics of microbridge CNT-2 measured at 4.2 K. (a) IVC measured at zero magnetic field and at a field where I_{c} is suppressed (indicated by the magenta line in b). (b) $I_{\mathrm{c}}(B)$ for both current polarities.

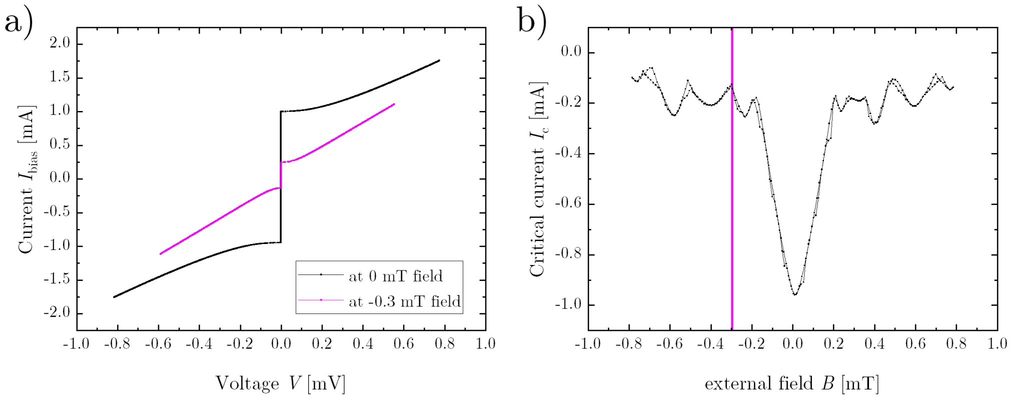

Figure 4.8.: Transport characteristics of microbridge CNT-3 measured at 4.2 K. (a) IVC measured at zero magnetic field and at a field where I_c is suppressed (indicated by the magenta line in b). (b) $I_c(B)$ for one current polarity.

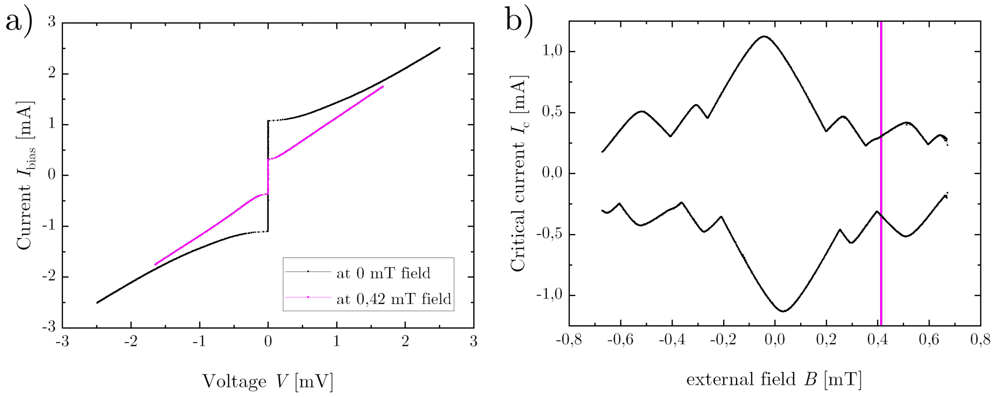

Figure 4.9.: Transport characteristics of microbridge CNT-4 measured at 4.2 K. (a) IVC measured at zero magnetic field and at a field where I_c is suppressed (indicated by the magenta line in b). (b) $I_c(B)$ for both current polarities.

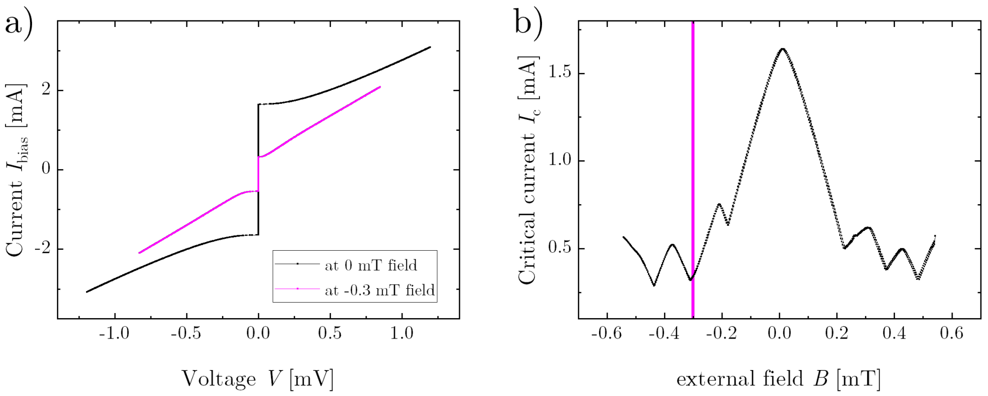

Figure 4.10.: Transport characteristics of microbridge CNT-6 measured at 4.2 K. (a) IVC measured at zero magnetic field and at a field where I_{c} is suppressed (indicated by the magenta line in b). (b) $I_{\mathrm{c}}(B)$ for both current polarities.

Characterisation of SQUIDs

This section presents the electrical characterisation of SQUIDs, which were fabricated from the microbridges described earlier. The SQUIDs were patterned using a Ne-FIB. These measurements serve as a reference for the later investigations involving Fe nanowires in Chapter 4.3. The suitability of the SQUIDs for these measurements, along with any associated limitations, is discussed in detail. A summary of the extracted parameters for all SQUIDs can be found in Table 4.2 provided earlier in this chapter.

SQUID CNT-1 Figure 4.11 illustrates the transport characteristics of SQUID CNT-1. The IVCs were recorded at two different points in time. Over five months, the critical current, I_c, decreased by approximately 15%, which is consistent with the expected ageing effects of the nanopatterned YBCO grain boundary Josephson junction due to oxygen loss.[68]

During the fabrication process in the Ne-FIB, a software crash resulted in an aborted cutting process midway. After the failure, the modulation line was not fully cut, as it was not evident that the SQUID would function correctly. As a result, a 3.6 µm long pickup loop was inadvertently formed adjacent to the SQUID. This effect is evident in the I_c vs. B measurements, which initially required an external magnetic field of 0.4 mT to couple one flux quantum Φ_0 into the SQUID. This corresponds to an effective area of 5 µm^2.

As the measurements confirmed that the SQUID was functional, the trench for the modulation line was completed in a subsequent Ne-FIB milling step. This modification reduced the effective area to 1.3 µm^2, requiring a field of 1.5 mT/Φ_0 for coupling in one flux quantum. The use of a pickup loop that is patterned directly beside the SQUID itself is an interesting concept that could be investigated further. These results suggest that the pickup loop and the SQUID behave like a SQUID with a larger loop size.

Figures 4.11(e) and (f) show the I_c vs. I_{mod} behaviour of SQUID CNT-1 across various current ranges. The mutual inductance, M_f, was determined to be 1.1 µA/Φ_0, meaning that this current is needed to couple one flux quantum into the SQUID. Exceeding a modulation current of approximately 0.7 mA resulted in flux jumps, which hindered measurements in the FLL modus. These flux jumps were likely caused by short circuits in the modulation line, a consequence of the fabrication failure. The modulation line near the SQUID was designed to be very narrow, and the software failure had more severe effects on this part compared to the SQUID itself, that is still functional.

Despite the defective modulation line, the remaining parameters, including $I_{\mathrm{c,max}} = 85\,\mu\mathrm{A}$, $R_n = 3.8\,\Omega$, and $I_cR = 323\,\mu\mathrm{V}$, are satisfactory. This indicates that SQUID CNT-1 is suitable for particle measurements but prevents operation in FLL mode.

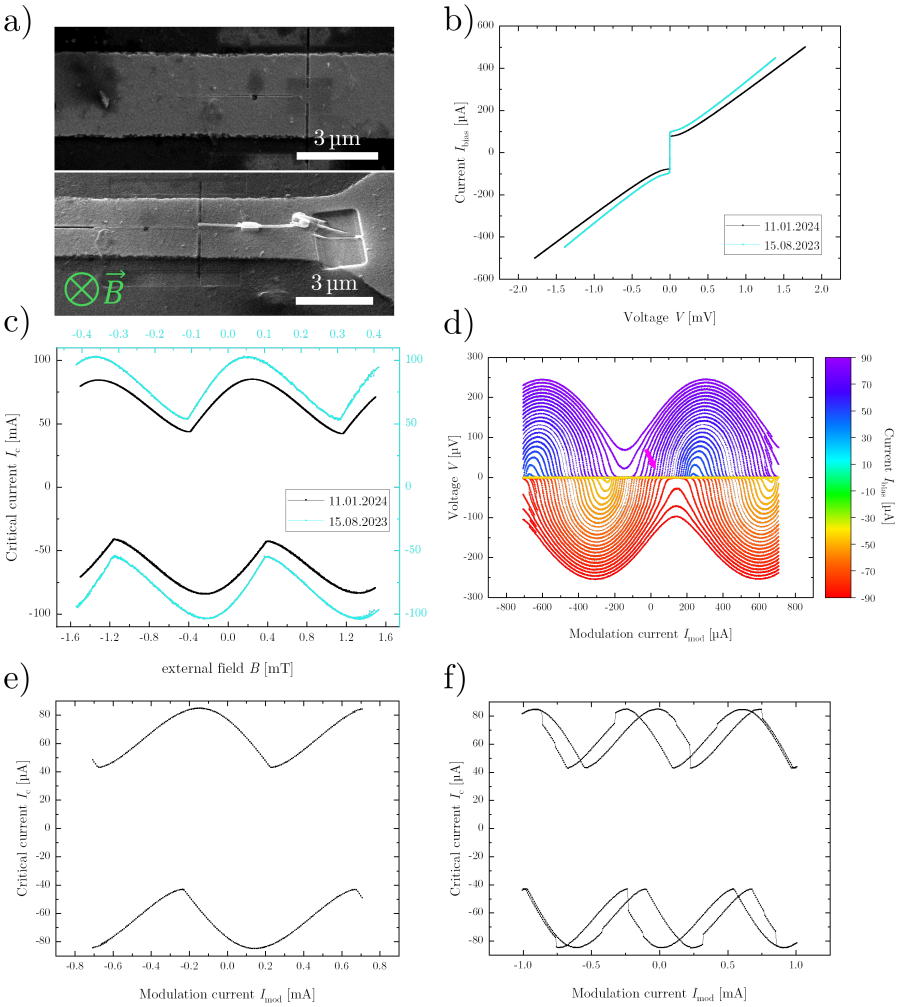

Figure 4.11.: Characterisation of SQUID CNT-1 measured at 4.2 K. (a) SEM images showing the modulation line during fabrication (top) and after completion (bottom) with the Fe nanowire in place. The direction of the external magnetic field B is indicated in green. (b) IVCs measured before (blue) and after (black) the completion of the modulation line and placement of the Fe nanowire. Over five months, I_c decreased by approximately 17%, likely due to oxygen loss from the grain boundary Josephson junctions. (c) $I_\mathrm{c}(B)$ before recutting the modulation trench (blue) and after recutting (black). (d) V vs. I_mod curves measured at different I_bias currents, with $V_\Phi = 3.0\,\mathrm{mV}/\Phi_0$ indicated by a magenta arrow. (e) and (f) I_c vs. I_mod. Modulation currents $> 0.7\,\mathrm{mA}$ lead to flux jumps.

SQUID CNT-2 Figure 4.12 illustrates the characterisation of SQUID CNT-2. The SEM image in Figure 4.12(a) shows the fabricated SQUID with the Fe nanowire in place, while the direction of the external magnetic field is indicated in green. The IVC, shown in Figure 4.12(b), displays a rounded transition near I_c, presumably due to a noise rounded transition. The maximum critical current, $I_{c,max}$, is approximately 35 % lower than that of SQUID CNT-1, despite having the same dimensions.

The reduced $I_{c,max}$ can be attributed to several factors. Firstly, during the FIB process, unavoidable edge damage occurs. Since SQUID CNT-2 underwent less intense ion beam exposure than SQUID CNT-1, the observed reduction in I_c could indicate reduced edge damage. Secondly, local variations in the grain boundary quality might play a role. Both factors are particularly significant for SQUIDs with such small Josephson junction widths.

Another potential explanation is the asymmetry observed in the I_c vs. B curve (Figure 4.12(c)). Unlike SQUID CNT-1, the $I_c(B)$ curve for CNT-2 does not exhibit point-symmetric behaviour around $B = 0$, suggesting the presence of trapped flux. Trapped flux can suppress the critical current and introduce asymmetries in the response to an external magnetic field, thereby distorting the measurements.

Figure 4.12(d) shows the V vs. I_{mod} curves for SQUID CNT-2. The voltage modulation amplitude, V_Φ, is very low at $0.1\,\mathrm{mV}/\Phi_0$, making this SQUID less suitable for particle measurements.

Despite these limitations, SQUID CNT-2 demonstrates functionality at very small dimensions. This highlights the potential utility of such small-scale SQUIDs in specific applications, such as operating under high external fields. Furthermore, the comparison of SQUID CNT-1 and CNT-2 characteristics suggests further investigation is required to determine whether significantly lower ion doses during the FIB process yield better-performing SQUIDs. At present, the dose is determined empirically by performing a test cut to visibly ablate the entire thin film, potentially using much higher doses than is necessary for fabricating a functional SQUID. Similar to the FIB cutting with helium ions reported by Müller et al. [69] this would leave a highly resistive area at the exposed part of the YBCO.

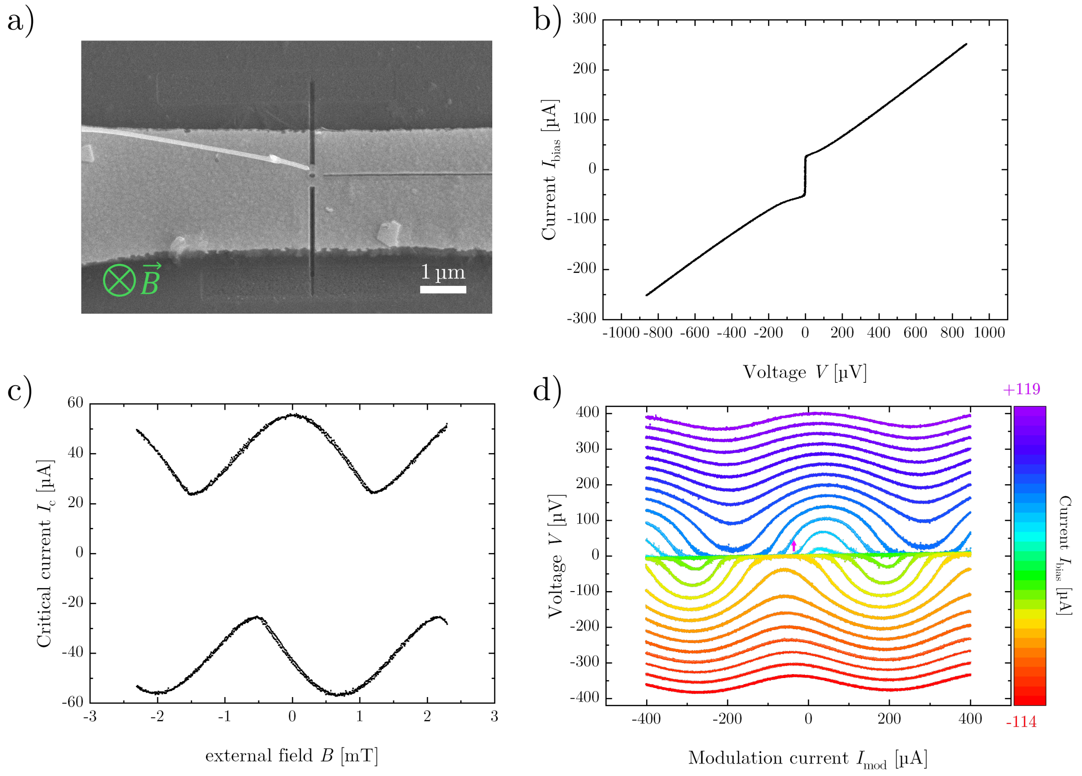

Figure 4.12.: Characterisation of SQUID CNT-2 measured at 4.2 K. (a) SEM image of the SQUID with the Fe nanowire in place. The direction of the external magnetic field B is indicated in green. (b) IVC measured without an external magnetic field. The curve shows a rounded transition near I_{c}. (c) $I_{\mathrm{c}}(B)$ curve does not exhibit point-symmetric behaviour around $B = 0$. (d) V vs. I_{mod} curves measured at different I_{bias} currents, with V_{Φ} indicated by a magenta arrow.

SQUID CNT-3 Figure 4.13 shows the characterisation data of SQUID CNT-3. The SEM image in Figure 4.13(a) displays the SQUID with a placed Fe nanowire. This device features a different geometry compared to the other SQUIDs, with rectangles cut out on both sides of the SQUID, leaving some superconducting material intact. The orientation of the external magnetic field B during the measurements is indicated by the green arrow. Key characterisation curves are presented in Figures 4.13(b)-(e).

The IVC measured at zero external magnetic field, shown in Figure 4.13(b), exhibits a comparably low I_c and a rounded transition near I_c. This rounded behaviour is caused by noise rounding.

In Figure 4.13(c), the I_c versus I_mod modulation demonstrates point-symmetric behaviour around $I_\mathrm{mod} = 0$, suggesting the absence of trapped flux. The V versus I_mod curves (Figure 4.13(d)) indicate a voltage modulation amplitude, V_Φ, of approximately $2.6\,\mathrm{mV}/\Phi_0$, which is a good value.

The I_c versus B data in Figure 4.13(e) is notably noisy. This noise can likely be attributed to the rounded I_c observed in the IVC. Furthermore, the possible influence of superconducting structures near the grain boundary Josephson junction may also affect the characteristics. This aspect requires further investigation to clarify its impact on device performance.

Overall, SQUID CNT-3 demonstrates good SQUID characteristics.

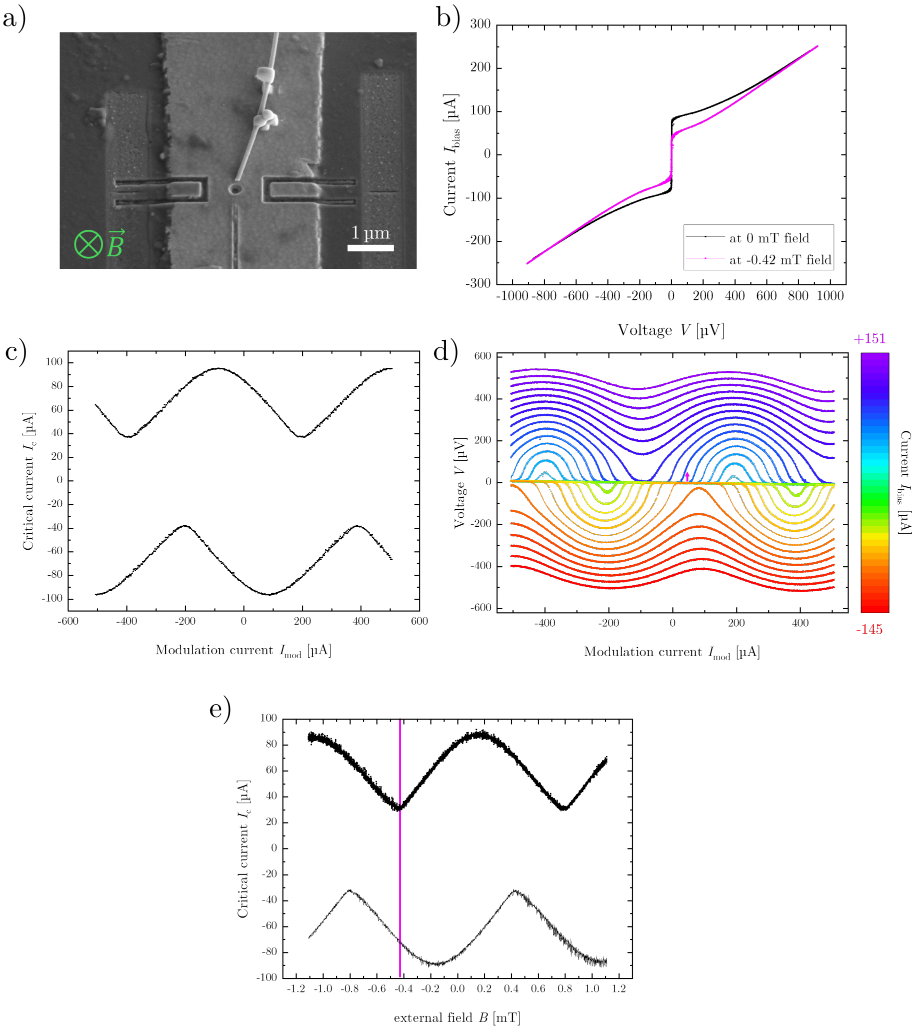

Figure 4.13.: Characterisation of SQUID CNT-3 measured at 4.2 K. (a) SEM image of the SQUID with the Fe nanowire in place. The direction of the external magnetic field B is indicated in green. (b) IVC measured without an external magnetic field (black) and with an applied field (magenta). The IVC shows a slightly rounded transition near I_c. The measurement point for the magenta curve is marked in (e) with a magenta line. (c) I_c vs. $I_{\rm mod}$ shows a point-symmetric behaviour around $I_{\rm mod} = 0$. (d) V vs. $I_{\rm mod}$ curves measured at different $I_{\rm bias}$ currents, with V_Φ indicated by a magenta arrow. (e) $I_c(B)$.

SQUID CNT-4 Figure 4.14 presents the characterisation data for SQUID CNT-4. The SEM image in Figure 4.14(a) shows the device, which features a significantly larger junction width compared to the other SQUIDs. The areas removed during the Ne-FIB processing appear swollen, likely due to the removal of a large area and the subsequent swelling of the substrate caused by the high ion dose. However, this does not appear to have negatively affected the SQUID's characteristics. The orientation of the external magnetic field B is indicated by the green arrow.

The IVC shown in Figure 4.14(b) exhibits a relatively high I_c value, a direct consequence of the larger junction width. The different coloured IVC curves correspond to three I_mod values, with measurement points marked in Figure 4.14(c) by lines. The inset highlights a unusual behaviour where the curves appear to intersect at different points instead of converging towards each other. This artefact requires further analysis, since it cannot be explained by the RCSJ model.

Figure 4.14(c) demonstrates the I_c versus I_mod modulation, which is point-symmetric around $I_\mathrm{mod} = 0$. However, the modulation appears strongly skewed, with maxima at positive bias currents aligning with minima at negative bias currents.

The V versus I_mod curves, shown in Figure 4.14(d), indicate a voltage modulation amplitude, V_Φ, of $4.2\,\mathrm{mV}/\Phi_0$, which is notably higher than that of the other SQUIDs characterised so far. This value is consistent with the larger junction area and improved voltage response.

Figures 4.14(e) and (f) display the I_c versus external field B data. At external fields exceeding $1\,\mathrm{mT}$, suppression of I_c is observed, which aligns with the expected behaviour for large junction widths. This suppression limits the usability of the SQUID in high-field measurements, despite its otherwise robust characteristics.

Key parameters of SQUID CNT-4 include $I_\mathrm{c,max} = 262\,\mu\mathrm{A}$, $R_\mathrm{n} = 2.6\,\Omega$, $I_\mathrm{c}R = 692\,\mu\mathrm{V}$, $A_\mathrm{eff} = 5.9\,\mu\mathrm{m}^2$, and $V_\Phi = 4.2\,\mathrm{mV}/\Phi_0$. These values highlight the influence of the larger junction width on the device's performance.

Overall, SQUID CNT-4 demonstrates excellent modulation and voltage characteristics under low-field conditions. However, its high-field performance is limited by the suppression of I_c, which restricts its suitability for operations in strong external fields.

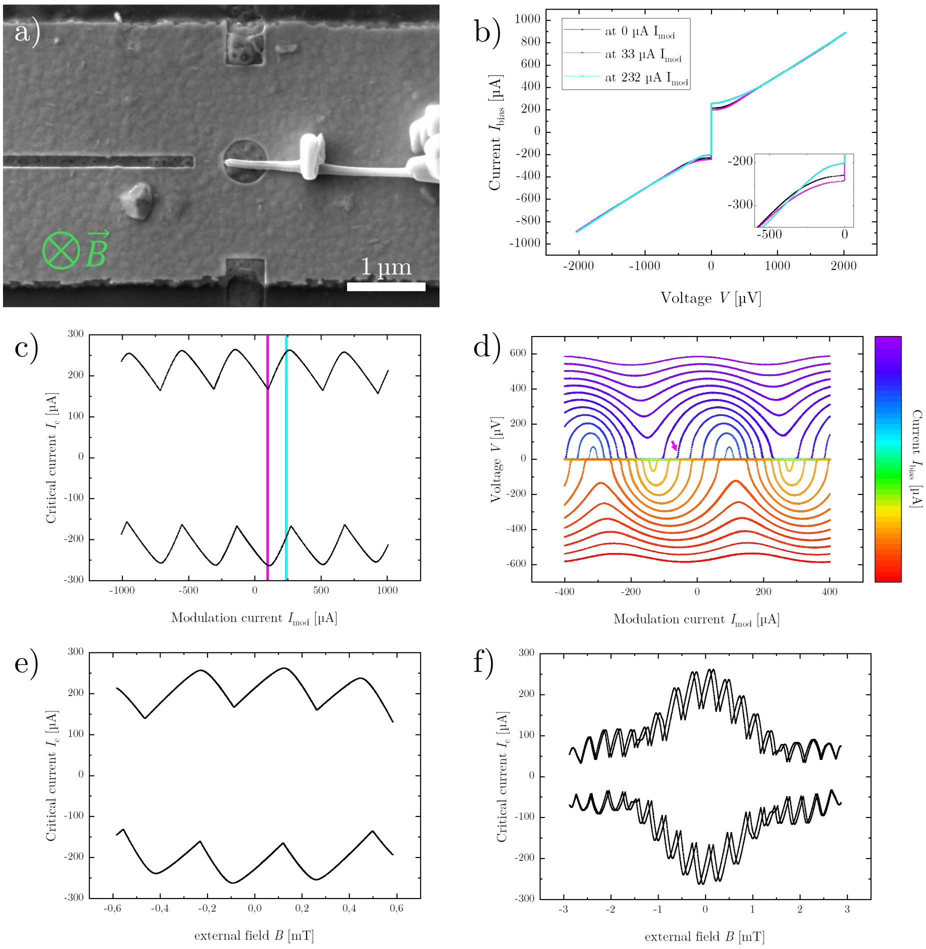

Figure 4.14.: Characterisation of SQUID CNT-4 measured at 4.2 K. (a) SEM image of the SQUID. Areas removed with Ne-FIB appear swollen. External magnetic field B is indicated in green. (b) IVC measured at different I_{mod} values marked in (c) by lines. The insert shows a magnified area of the IVCs where it can be seen that the curves seem to cut through each other at different points. (c) I_{c} vs. I_{mod} is point-symmetric around $I_{\mathrm{mod}} = 0$. (d) V vs. I_{mod} curves measured at different I_{bias} currents, with V_{Φ} indicated by a magenta arrow. (e) and (f) $I_{\mathrm{c}}(B)$ show suppression at fields greater than 1 mT.

SQUID CNT-6 Figure 4.15 presents the characterisation data for SQUID CNT-6. The SEM image in Figure 4.15(a) shows the device, where an unidentified fabrication residue is visible near the bridge. This residue appears to accumulate a charge under SEM imaging, contrasting with the non-charging gold surface. While the precise nature of this residue remains unclear, it raises concerns about potential interference during electrical measurements. However, the charging behaviour indicates, that the particle is an isolator, there for an interference is unlikely. The orientation of the external magnetic field B is indicated by the green arrow.

The IVC, displayed in Figure 4.15(b), demonstrates excellent behaviour consistent with the RCSJ model, indicating high-quality junctions. The magenta curve shows the IVC under an applied external magnetic field, with the corresponding measurement point marked by a magenta line in Figure 4.15(e).

In Figure 4.15(c), the I_c versus I_mod modulation exhibits point-symmetric behaviour around $I_\mathrm{mod} = 0$, slightly skewed.

The V versus I_mod curves shown in Figure 4.15(d) feature a voltage modulation amplitude, V_Φ, of $3.1\,\mathrm{mV}/\Phi_0$. This value, while slightly lower than that of SQUID CNT-4, remains within an acceptable range for sensitive measurements.

The I_c versus external field B data in Figure 4.15(e) exhibits clean and well-defined behaviour, with no significant abnormalities or noise. This suggests that the unidentified residue near the bridge might not have an impact on the SQUID's response to external magnetic fields. However, further investigations and stronger external fields are required to confirm this and to determine whether the residue influences other aspects of the device's performance, like the likelihood to trap flux.

Key parameters extracted from the characterisation are as follows: $I_\mathrm{c,max} = 194\,\mu\mathrm{A}$, $R_\mathrm{n} = 2.1\,\Omega$, $I_\mathrm{c}R = 407\,\mu\mathrm{V}$, $A_\mathrm{eff} = 2.5\,\mu\mathrm{m}^2$, and $V_\Phi = 3.1\,\mathrm{mV}/\Phi_0$. These parameters highlight the excellent electrical characteristics of SQUID CNT-6.

Overall, SQUID CNT-6 demonstrates good performance with well-defined modulation, and strong $I_\mathrm{c}R$ and V_Φ values. Nevertheless, the potential effects of the observed residue near the bridge require further exploration.

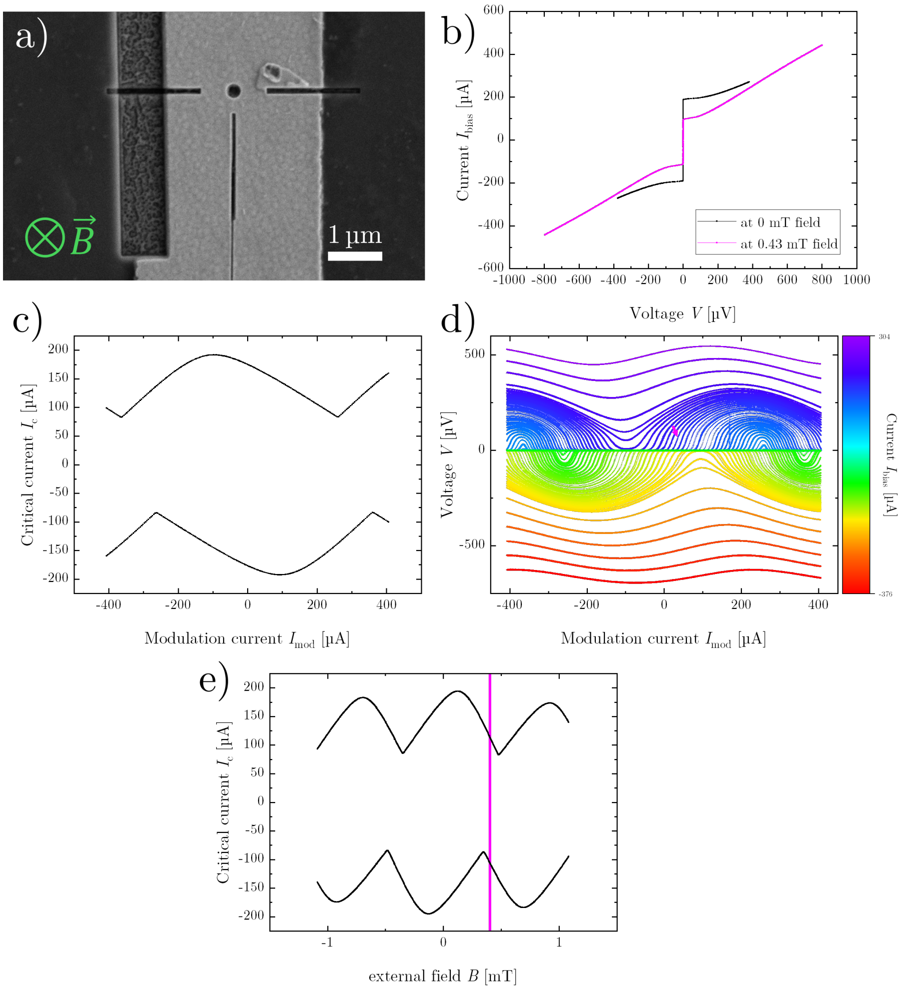

Figure 4.15.: Characterisation of SQUID CNT-6 measured at 4.2 K. (a) SEM image of the SQUID showing a fabrication residue near the bridge. The direction of the external magnetic field B is indicated in green. (b) IVC measured without an external magnetic field (black) and with an applied field (magenta). The measurement point for the magenta curve is marked in (e) with a magenta line. (c) I_c vs. I_mod is point-symmetric around $I_\text{mod} = 0$. (d) V vs. I_mod curves measured at different I_bias currents, with V_Φ indicated by a magenta arrow. (e) $I_\text{c}(B)$.

4.1.4. SQUIDs for Measuring EuS Nanodiscs

This subsection presents the fabrication and characterisation of SQUIDs for the sample *Bi_STO_22_1*, designed for measuring EuS nanodiscs in collaboration with María José (Pepa) Martínez-Pérez in Zaragoza, Spain. Microbridges were fabricated on an STO bicrystal substrate with a 90 nm YBCO layer and a 60 nm gold capping layer, following the optical lithography process described earlier in this chapter. Subsequent nanofabrication steps to transform the microbridges into functional SQUIDs, as well as the placement of the EuS nanodiscs, were performed by the collaborators in Spain. Using a FIB/SEM dual-beam microscope, the collaborators employed a Ga-FIB to nanopattern the SQUIDs and the EuS nanodiscs. An OmniProbe micromanipulator was then used to position the nanodiscs on top of the modulation lines, securing them with small platinum depositions.

Figure 4.16 provides an overview of the SQUIDs and their configurations for the EuS measurements. Figure 4.16 a) shows a SQUID without a nanodisc, highlighting the dimensions of the SQUIDs used in the experiments, including an elliptical SQUID hole with approximate dimensions of 500 × 300 nm and a junction width of 600 nm.

Figure 4.16 b) displays a SQUID with a placed EuS nanodisc. The nanodisc is positioned on a membrane, and its outline is visible in the SEM image due to the transparency of the Si_3N_4 membrane. Figure 4.16 c) illustrates a schematic representation of the SQUID with the EuS nanodisc in place, showing the measurement configuration.

The characterisation of these SQUIDs aimed to evaluate their suitability for detecting the magnetic properties of the EuS nanodiscs. The results of the EuS nanodisc measurements are discussed in more detail in Chapter 4.4. The measurement setup, including the dilution refrigerator used for these evaluations, is outlined in Chapter 3.1.6.

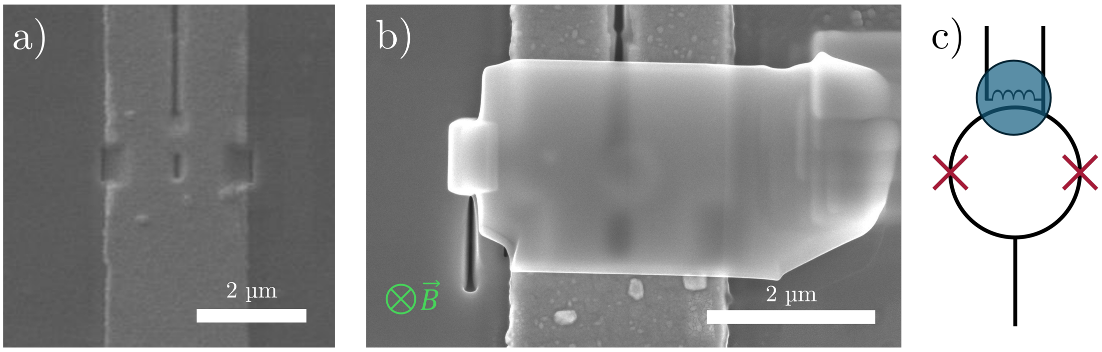

Figure 4.16.: SEM images the SQUID EuS-10 wtih an EuS nanodisc. (a) SQUID without a placed nanodisc. (b) SQUID with a placed EuS nanodisc. The nanodisc is located on a membrane, and its outline is visible in the SEM image due to the transparency of the Si_3N_4 membrane. (c) A schematic of the SQUID with the placed EuS nanodisc, illustrating the measurement configuration.

Characterisation of the SQUIDs with EuS Nanodiscs

Since the nanofabrication and particle placements was performed in Zaragoza, the characterisation of the SQUIDs was conducted simultaneously with the particle measurements inside the dilution refrigerator in Zaragoza. Details of the particle measurements are provided in Chapter 4.4.

In contrast to the previous characterisations, these measurements utilised `Magnicon` electronics alongside a National Instruments (NI) measurement card and a custom `LabVIEW` program developed in Zaragoza. This program was specifically designed to record multiple input signals while simultaneously controlling the applied magnetic field. However, measurements such as I_c versus I_mod or B could not be performed using this setup. Additionally, the maximal sampling rate of the `LabVIEW` program was limited to approximately 10 Hz, which imposed restrictions on the measurement speed, and the possibility of averaging of the measurements.

SQUID EuS-05 Figure 4.17 presents the characterisation data for SQUID EuS-05, with a 200 nm EuS nanodisc placed on the SQUID.

The IVC shown in Figure 4.17(a) exhibits a maximum critical current, $I_{c,max}$, of 138 µA. All IVC curves were extracted from the family of curves shown in Figure 4.17(b). Due to time constraints and the limited sampling rate, the bias current was not fully ramped to its maximum value. Instead, efforts were focused on obtaining higher resolution near the I_c transition.

Figure 4.17(b) shows a contour plot of multiple IVCs measured at different I_{mod} currents, with V represented as the colour scale. The contour line corresponding to 100 µV serves as an approximation for I_c versus B. The plot reveals multiple jumps and a lack of point symmetry around $I_{mod} = 0$, indicating the presence of trapped flux near the SQUID. This trapped flux could have influence the measurements and, due to the long cooling and warming times required in the dilution refrigerator, could not be removed by heating the SQUID above T_c. Care was taken during measurements to distinguish between hysteresis originating from trapped flux in the SQUID and hysteresis arising from the magnetic properties of the EuS nanodisc. These effects must not be confused, as certain hysteresis features were only observed in SQUIDs where precharacterisation indicated the presence of trapped flux.

Figure 4.17(c) shows the V versus I_{mod} curve at $I_{bias} = 124$ µA. The green arrow marks the working point used for FLL operation in the measurements discussed in Chapter 4.4. The V versus I_{mod} curve was adjusted with an additional applied V_{bias} to ensure that $V = 0$ at the FLL working point.

In Figure 4.17(d), the V versus B measurement at $I_{bias} = 120$ µA and $I_{mod} = -125$ µA shows that approximately 2 mT of external field is required to couple one flux quantum Φ_0 into the SQUID loop. This corresponds to an effective area, A_{eff}, of 1.09 µm^2. Notably these values are effected by the presence of the EuS nanodisc on the SQUID alters the external field distribution due to its magnetic permeability. The slight tilt observed in the V versus B curve is attributed to the suppression of I_c in the junctions.

The SQUID properties are adequate for particle measurements; however, the observed behaviour suggests the presence of trapped flux. Key parameters extracted from the characterisation include: $I_{c,max} = 138\,\mu\text{A}$, $R_n = 2.4\,\Omega$, $I_cR = 325\,\mu\text{V}$, $M_f = 1.0\,\mu\text{A}/\Phi_0$, $A_{eff} = 1.09\,\mu\text{m}^2$, and $V_\Phi = -0.6\,\text{mV}/\Phi_0$.

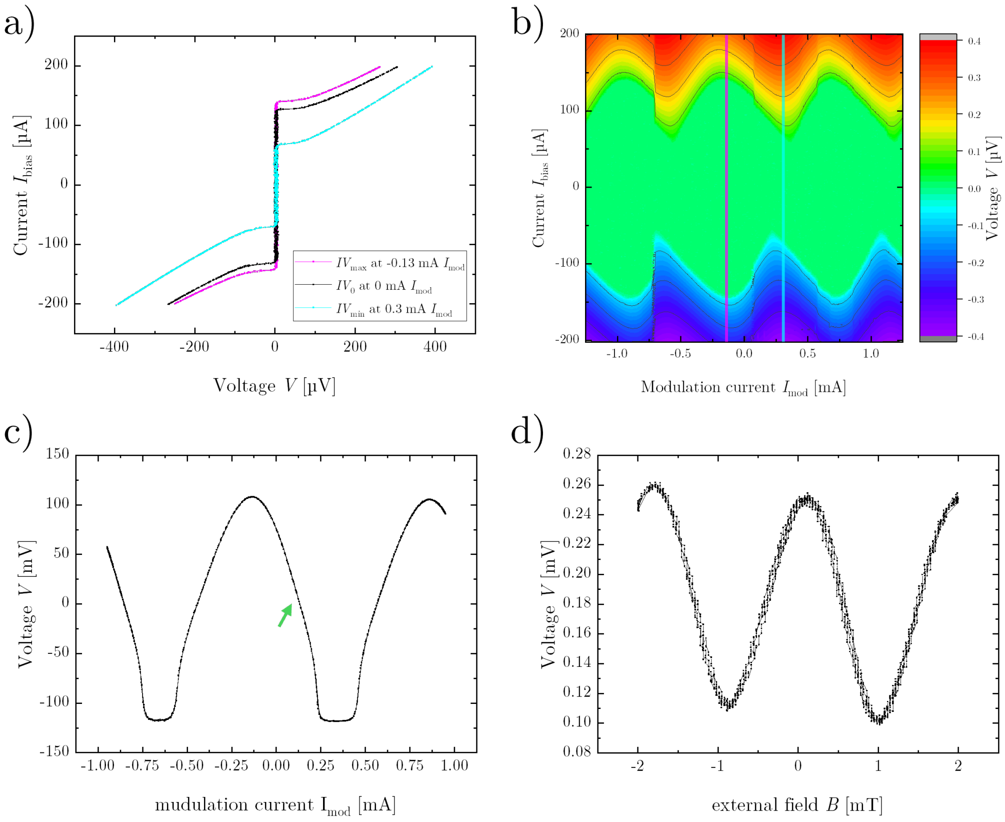

Figure 4.17.: Characterisation of SQUID EuS-05 with a 200 nm EuS nanodisc measured close to 4 K. (a) IVCs at different I_{mod}. The $I_{\mathrm{c,max}}$ curve (magenta) and $I_{\mathrm{c,min}}$ curve (blue) are shown, with their measuring point marked by a line in (b). (b) Contour plot of multiple IVCs at different I_{mod} currents. The plot shows I_{bias} vs. I_{mod} with V as the colour scale. Contour lines are marked on the colour bar. (c) V vs. I_{mod} at $I_{\mathrm{bias}} = 124\,\mu\mathrm{A}$. The measuring point for V_Φ is marked by a green arrow. (d) V vs. external field B at $I_{\mathrm{bias}} = 120\,\mu\mathrm{A}$ and $I_{\mathrm{mod}} = -125\,\mu\mathrm{A}$.

SQUID EuS-10 Figure 4.18 presents the characterisation data for SQUID EuS-10, with a 700 nm EuS nanodisc placed on the SQUID.

The IVCs shown in Figure 4.18(a) were recorded at two different I_{mod} values. The maximum critical current, $I_{\mathrm{c,max}}$, is quite high, reaching 378 µA.

Figure 4.18(b) provides a contour plot of multiple IVCs measured at different I_{mod} currents, with V represented as the colour scale. The contour line corresponding to 125 µV serves as an approximation for I_{c} versus B. The plot is symmetric around $I_{\mathrm{mod}} = 0$, indicating no significant evidence of trapped flux during these measurements.

Figure 4.18(c) shows the V versus I_{mod} curve at $I_{\mathrm{bias}} = 378\,\mu\mathrm{A}$. The green arrow marks the working point used for FLL operation in subsequent measurements. Notably, the minima and maxima of V decrease linearly, presumably due to a grounding problem.

Figures 4.18(d) and 4.18(e) display V versus external field B measurements at different bias currents. Figure 4.18(d) focuses on a smaller field range, while Figure 4.18(e) covers a larger range. At external fields greater than 1.5 mT, suppression of I_{c} becomes evident, consistent with the SQUID's junction size and geometry.

The SQUID demonstrates good overall properties for particle measurements. Key parameters extracted from the characterisation include: $I_{\mathrm{c,max}} = 378\,\mu\mathrm{A}$, $R_{\mathrm{n}} = 3.6\,\Omega$, $I_{\mathrm{c}}R = 1359\,\mu\mathrm{V}$, $M_f = 1.0\,\mu\mathrm{A}/\Phi_0$, $A_{\mathrm{eff}} = 2.32\,\mu\mathrm{m}^2$, and $V_\Phi = -1.3\,\mathrm{mV}/\Phi_0$.

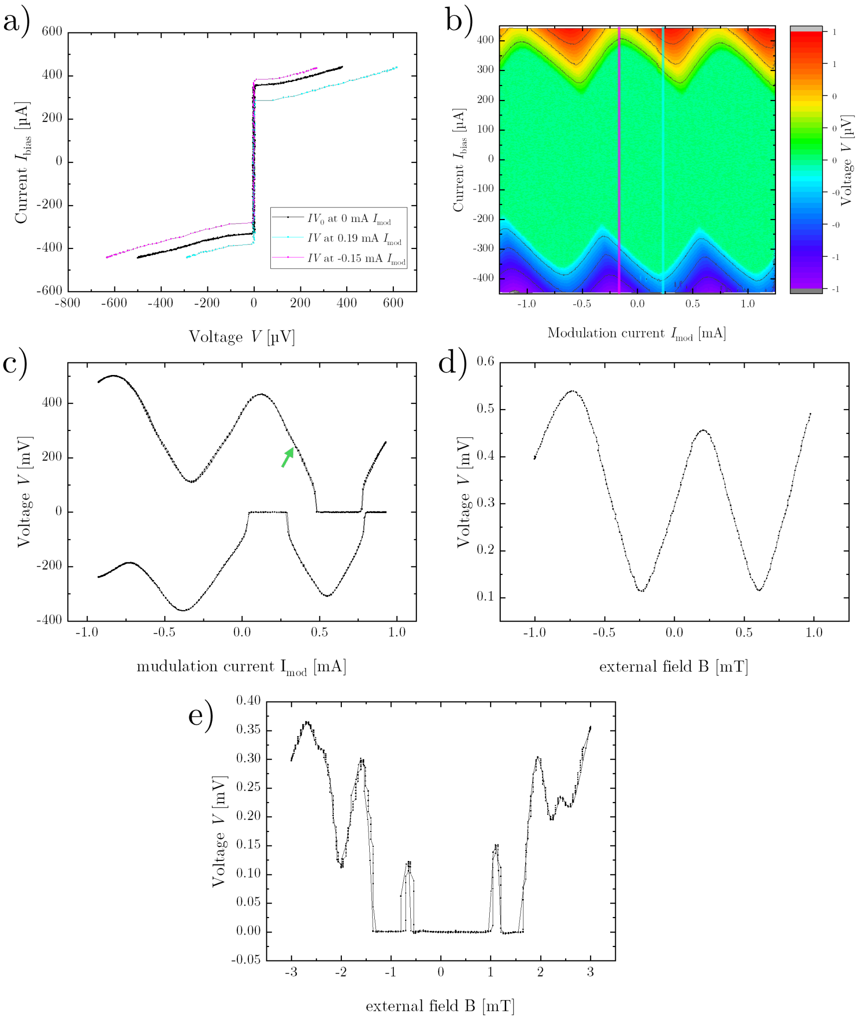

Figure 4.18.: Characterisation of SQUID EuS-10 with a 700 nm EuS nanodisc measured close to 4 K. (a) IVCs at different I_{mod}. The $I_{\mathrm{c,max}}$ curve (magenta) and $I_{\mathrm{c,min}}$ curve (blue) are shown, with their measuring point marked by a line in (b). (b) Contour plot of multiple IVCs at different I_{mod} currents. The plot shows I_{bias} vs. I_{mod} with V as the colour scale. Contour lines are 100 µV apart. The plot is symmetric around $I_{\mathrm{mod}} = 0$. (c) V vs. I_{mod} at $I_{\mathrm{bias}} = 378$ µA. The minima and maxima of V decrease linearly. The measuring point for V_{Φ} is marked by a green arrow. (d) V vs. external field B at $I_{\mathrm{bias}} = 388$ µA. (e) V vs. external field B at $I_{\mathrm{bias}} = 208$ µA over a larger field range.

SQUID EuS-11 Figure 4.19 presents the characterisation data for SQUID EuS-11, with a 600 nm EuS nanodisc placed on the SQUID.

Figure 4.19 a) shows the IVC measured at low I_{bias} currents, providing high resolution around I_{c}. The curve exhibits a step-like pattern rather than the typical RCSJ behaviour. Multiple transitions, marked by green arrows, are visible near I_{c}. These transitions could be caused by additional Josephson junctions in the SQUID ring, potentially originating from parasitic crystal orientations in the film, or by local variations in the YBCO film near the junctions. The relatively low critical current, $I_{\mathrm{c}} = 45\,\mu\mathrm{A}$, compared to other SQUIDs, supports the hypothesis that the Josephson junctions are of low quality.

Figure 4.19 b) displays the IVC measured at higher I_{bias} currents, which was used to determine the normal resistance, $R_{\mathrm{n}} = 7.0\,\Omega$. These measurements show that the SQUID has a relatively high resistance compared to the other characterised devices.

Figure 4.19 c) illustrates the V versus I_{mod} curve at $I_{\mathrm{bias}} = 48\,\mu\mathrm{A}$. This curve shows asymmetry, as it is not point-symmetric around $I_{\mathrm{mod}} = 0$. Additionally, the voltage increases unusually strongly with increasing I_{mod}. The observed behaviour suggests that the modulation line is also affected by the poor condition of the thin film.

Figure 4.19 d) shows the V versus external field B at $I_{\mathrm{bias}} = 102\,\mu\mathrm{A}$ and $I_{\mathrm{mod}} = 125\,\mu\mathrm{A}$. A voltage offset, $V_{\mathrm{b}} = 350\,\mu\mathrm{V}$, was applied to shift the curve such that $V = 0$ corresponds to the working point used later in FLL mode. The suppression of I_{c} at higher fields is pronounced, and towards negative fields, the minimum is missing. This further supports the hypothesis that the Josephson junctions of the SQUID are affected. This behaviour furthermore indicates significant challenges for reliable operation of the SQUID at higher fields.

It is worth to note that during pre-characterisation by the group of Martínez-Pérez (data not shown here), many microbridges exhibited similarly low I_{c} values and other anomalies, such as multiple transitions. These observations point to potential issues with the thin film, either during deposition or processing. As a result, most of the microbridges were deemed unsuitable for SQUID fabrication.

Although the transfer function slope appears excellent, the relatively low I_{c} and multiple transitions present challenges for reliable measurements. To mitigate these effects, the SQUID was operated at quite high I_{bias} currents during subsequent measurements. Key parameters extracted from the characterisation include: $I_{\mathrm{c}} = 45\,\mu\mathrm{A}$, $R_{\mathrm{n}} = 7.0\,\Omega$, $I_{\mathrm{c}}R = 315\,\mu\mathrm{V}$, $M_f = 2.9\,\mu\mathrm{A}/\Phi_0$, $A_{\mathrm{eff}} = 2.21\,\mu\mathrm{m}^2$, and $V_\Phi = 2.3\,\mathrm{mV}/\Phi_0$.

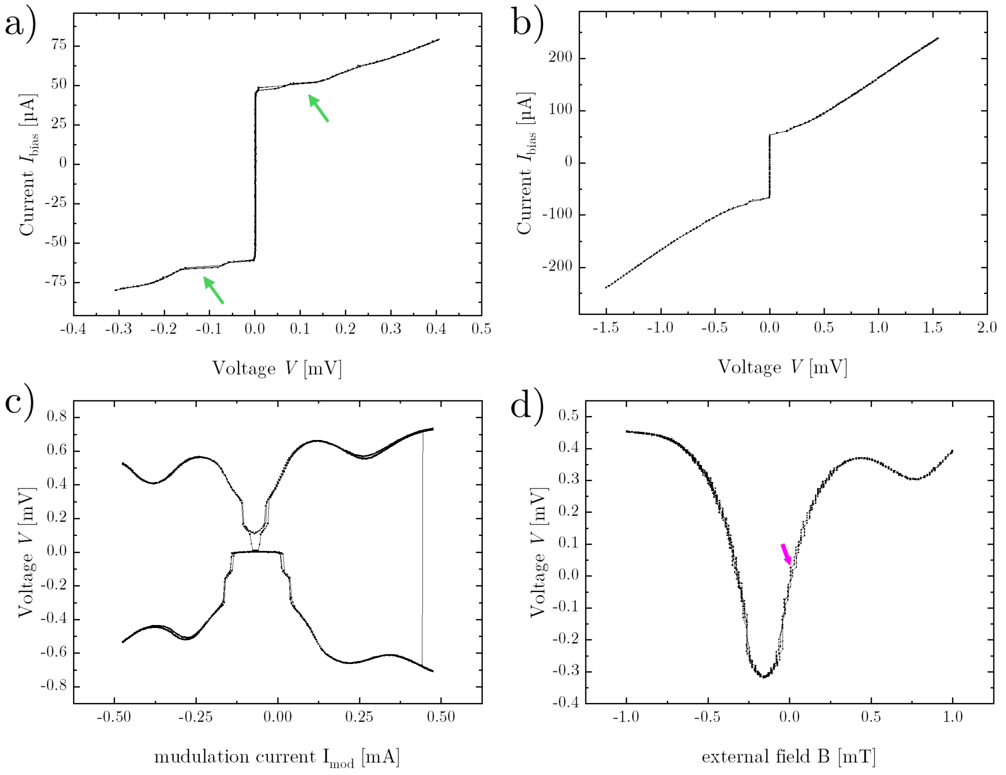

Figure 4.19.: Characterisation of SQUID EuS-11 with a 600 nm EuS nanodisc measured close to 4 K. (a) IVC measured at I_{bias} near I_{c}. (b) IVC measured at higher I_{bias} currents. (c) V vs. I_{mod} at $I_{\text{bias}} = 48\,\mu\text{A}$. (d) V vs. external field B at $I_{\text{bias}} = 102\,\mu\text{A}$, $I_{\text{mod}} = 125\,\mu\text{A}$, and a voltage offset $V_{\text{b}} = 350\,\mu\text{V}$. The point where V_{Φ} is measured is marked by a magenta arrow.

SQUID EuS-12 Figure 4.20 presents the characterisation data for SQUID EuS-12, with a 260 nm EuS nanodisc placed on the SQUID.

Figure 4.20 a) shows the IVC. The curve is symmetric and consistent with the expected RCSJ behaviour, and exhibits a good I_c.

Figure 4.20 b) illustrates the V versus I_mod curve measured at $I_\mathrm{bias} = 238\,\mu\mathrm{A}$ (black curve) and $I_\mathrm{bias} = 288\,\mu\mathrm{A}$ (magenta curve). The curve is symmetric around $I_\mathrm{mod} = 0$ but tilted, with a linear decrease in the minima and maxima of V. This tilting is similar to the behaviour observed in the V versus I_mod curve for SQUID EuS-11 and may indicate imperfections in the thin film, junction properties, or the modulation line.

Figure 4.20 c) displays the V versus external field B curve measured at $I_\mathrm{bias} = 262\,\mu\mathrm{A}$, $I_\mathrm{mod} = 39\,\mu\mathrm{A}$, and a voltage offset $V_\mathrm{b} = 398\,\mu\mathrm{V}$. The voltage offset was applied to shift the curve such that $V = 0$ corresponds to the working point used later in FLL mode. The curve is tilted, similar to the V versus I_mod curve but distinct from SQUID EuS-11. It appears that at fields below 0.5 mT, the I_c is less suppressed. This could be explained by a significant shift in the suppression of the I_c in the junctions or may indicate the presence of trapped flux. A jump near the measurement point for V_Φ, marked by the green bar, suggests the presence of multiple I_c transitions, though these are less pronounced compared to SQUID EuS-11.

For both SQUID EuS-11 and EuS-12, only a single IVC was measured at $I_\mathrm{mod} = 0$. As a result, precise values for $I_\mathrm{c,max}$ and $I_\mathrm{c,min}$ could not be determined. Since $I_\mathrm{c,max}$ was not used in the calculation, the reported $I_\mathrm{c}R$ product is likely an underestimate of the actual value.

Despite the observed tilting in both the V versus I_mod and V versus B curves, the SQUID demonstrates generally good properties for particle measurements. Key parameters extracted from the characterisation include: $I_\mathrm{c} = 257\,\mu\mathrm{A}$, $R_\mathrm{n} = 4.3\,\Omega$, $I_\mathrm{c}R = 1117\,\mu\mathrm{V}$, $M_f = 0.8\,\mu\mathrm{A}/\Phi_0$, $A_\mathrm{eff} = 3.30\,\mu\mathrm{m}^2$, and $V_\Phi = 3.0\,\mathrm{mV}/\Phi_0$.

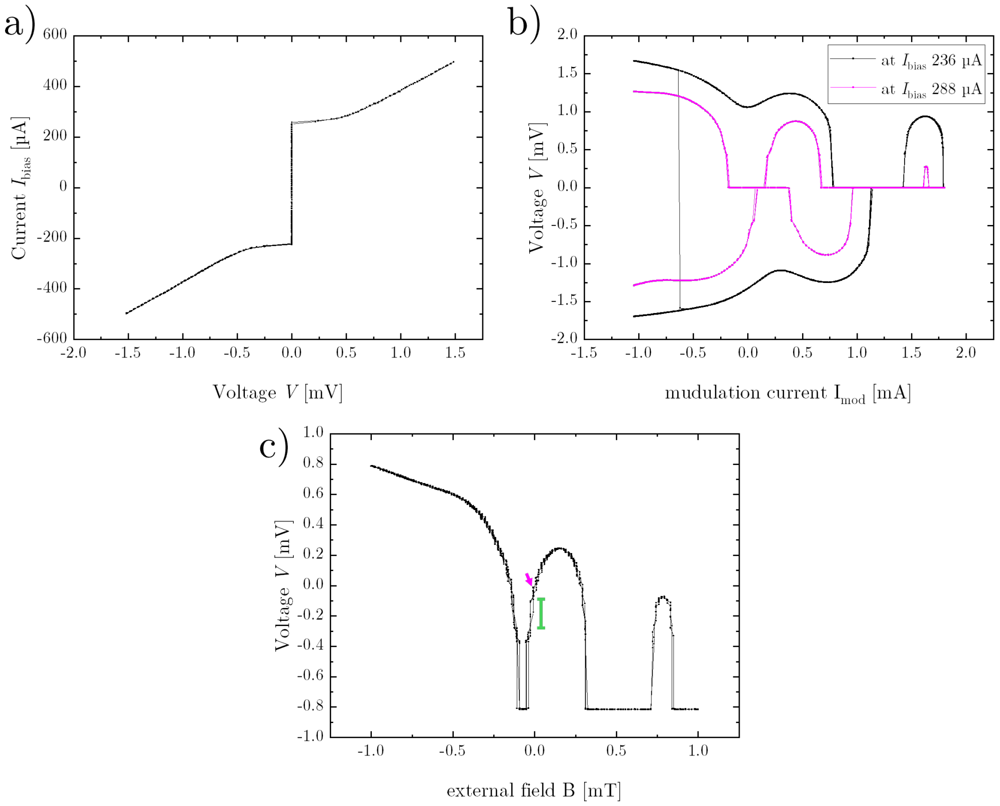

Figure 4.20.: Characterisation of SQUID EuS-12 with a 260 nm EuS nanodisc measured close to 4 K. (a) IVC measured at I_{bias}. (b) V vs. I_{mod} measured at $I_{\mathrm{bias}} = 238\,\mu\mathrm{A}$ (black curve) and $I_{\mathrm{bias}} = 288\,\mu\mathrm{A}$ (magenta curve). The curve is symmetric around $I_{\mathrm{mod}} = 0$ but tilted, with a linear decrease in the minima and maxima of V. (c) V vs. external field B measured at $I_{\mathrm{bias}} = 262\,\mu\mathrm{A}$, $I_{\mathrm{mod}} = 39\,\mu\mathrm{A}$, and a voltage offset $V_{\mathrm{b}} = 398\,\mu\mathrm{V}$.

4.1.5. Temperature Dependence of SQUID Characteristics

The high sensitivity and usability of YBCO SQUIDs at elevated fields and temperatures make them ideal sensors for particle measurements at various T and B. However, certain SQUID characteristics change with increasing temperature, making it essential to measure properties such as I_c and M_f across varying temperatures during experiments. Understanding these dependencies is crucial for ensuring accurate interpretations of measurements taken at different temperatures.

This subsection examines the behaviour of I_c and M_f for SQUID CNT-3 at temperatures between 19 K to 69 K. Additionally, the temperature dependence of M_f is presented for SQUID CNT-1 over the range from 4 mK to 31 K, and for the four EuS SQUIDs across temperatures between 15 mK and 30 K.

I_c and M_f of SQUID CNT-3 Near T_c

To evaluate whether SQUIDs CNT-1 to CNT-6 are suitable for measurements at relatively high temperatures, SQUID CNT-3 was characterised in an special dipstick setup at temperatures ranging from 19 K to 69 K. The special dipstick setup is similar to a regular dipstick for a dewar with liquid helium described in Chapter 3.1.6, but gives the opportunity to pump a vacuum between the sample and liquid helium, and has a heater system build in.

Figure 4.21(a) presents the IVCs across this temperature range. As the temperature increases, I_c decreases significantly, while R_n remains relatively consistent.

Ideally, the I_c of the SQUID should be measurable approximately up to the T_c of the material. For high-quality YBCO thin films, T_c is typically around 90 K. However, due to ageing effects, poor-quality films, or defects in the Josephson junctions, the disappearing of I_c can occur at lower temperatures. This is evident in Figure 4.21(b), where I_c disappears near 70 K. Above 60 K, I_c becomes too small for reliable measurements, suggesting that meaningful operation of the SQUID is limited to temperatures below approximately 60 K.

Figure 4.21(c) illustrates I_c versus I_mod at different temperatures. The curves remain point-symmetric around $I_\mathrm{mod} = 0$. In addition to the decrease in I_c, the modulation period changes with temperature, affecting the current required to couple one flux quantum, Φ_0, into the SQUID loop. This can be represented by the temperature dependence of the mutual inductance, M_f.

M_f is a characteristic that describes how much flux is coupled into the SQUID per milliampere (mA) of current flowing through the modulation line. It can be determined by measuring the period of the V versus I_mod curve. Specifically, the distance between two minima in the V versus I_mod curve corresponds to exactly one Φ_0 coupled into the SQUID via the modulation line.

To further investigate this behaviour, Figure 4.21(d) shows M_f as a function of temperature. Above 20 K, M_f changes significantly with increasing temperature, indicating that for reliable interpretation of FLL measurements, the temperature-dependent variation of M_f must be accounted for. As described by Martínez-Pérez et al. [70], M_f as a function of temperature can be modelled using the following equation:

$$\frac{M_f}{M_{f0}} = \frac{1}{\left(1 - \left(\frac{T}{T_c}\right)^2\right)^{2/3}} \tag{4.1.1}$$

where M_{f0} represents the mutual inductance at $T = 0\,\mathrm{K}$, and T_c is the critical temperature. This expression provides a theoretical framework for understanding the observed changes in M_f with temperature. A fit of this model at elevated temperatures is depicted in Figure 4.21 d).

These characterisations demonstrate that with an appropriate measurement setup, the SQUIDs CNT-1 to CNT-6 can be reliably used for Fe nanowire measurements at temperatures up to approximately 60 K.

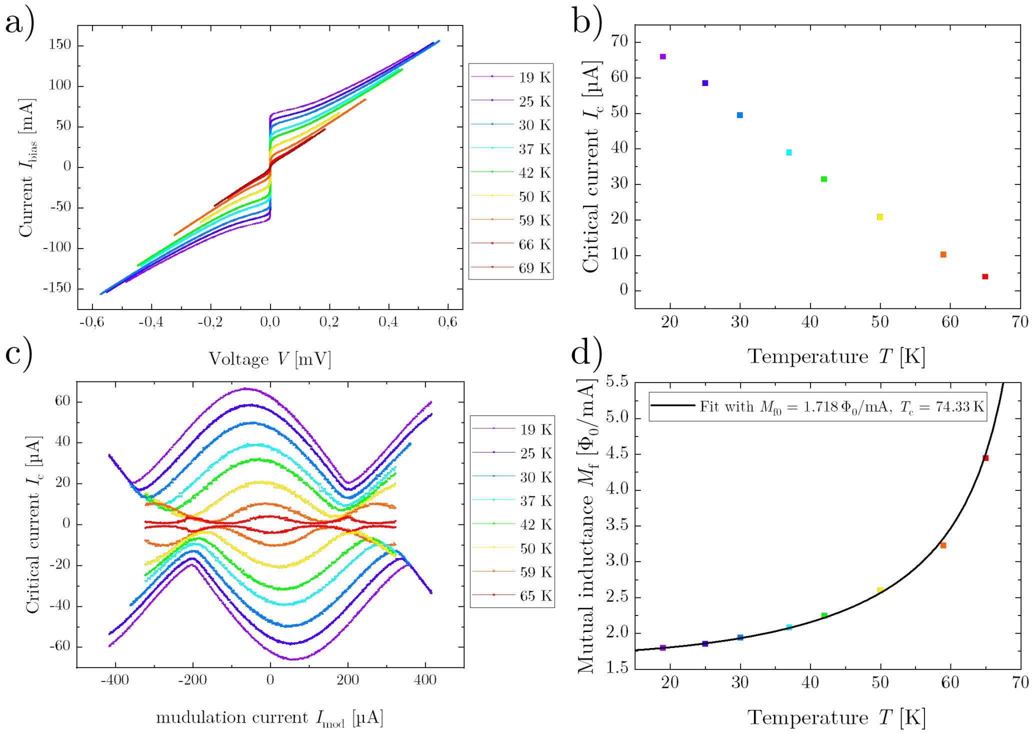

Figure 4.21.: Characterisation of SQUID CNT-3 at temperatures between 19 K and 69 K. (a) IVCs. As the temperature increases, I_{c} decreases significantly, while R_{n} remains relatively stable. (b) Temperature dependence of I_{c}. Above 60 K, I_{c} becomes too small for reliable measurements. (c) I_{c} versus I_{mod} at different temperatures. In addition to the reduction in I_{c}, the modulation period changes with temperature. (d) Mutual inductance M_f versus temperature.

M_f of SQUID CNT-1

V versus I_{mod} measurements were performed at temperatures of $T = 31, 21, 12, 7.5$, and 4 K. The modulation period, M_f, of the SQUID can be extracted from the V versus I_{mod} curves shown in Figure 4.22.

At low temperatures, M_f changes only slightly. The expected variation in M_f can be estimated using Equation (4.1.1), which predicts an increase of approximately 1.2% at $T = 12\,\mathrm{K}$, 2.2% at $T = 15\,\mathrm{K}$, and 3.5% at $T = 20\,\mathrm{K}$ for a critical temperature of $T_{\mathrm{c}} = 89\,\mathrm{K}$. However, in the presented measurements up to 12 K, the uncertainty of the experimental setup dominates over the expected temperature dependence of M_f, preventing a reliable resolution of these small changes. A temperature-induced change in M_f of approximately 3.5% is shown at $T = 21\,\mathrm{K}$.

These findings confirm the statement made in the previous subsection that, above a temperature of approximately 20 K, an adjustment of M_f is required for accurate data analysis.

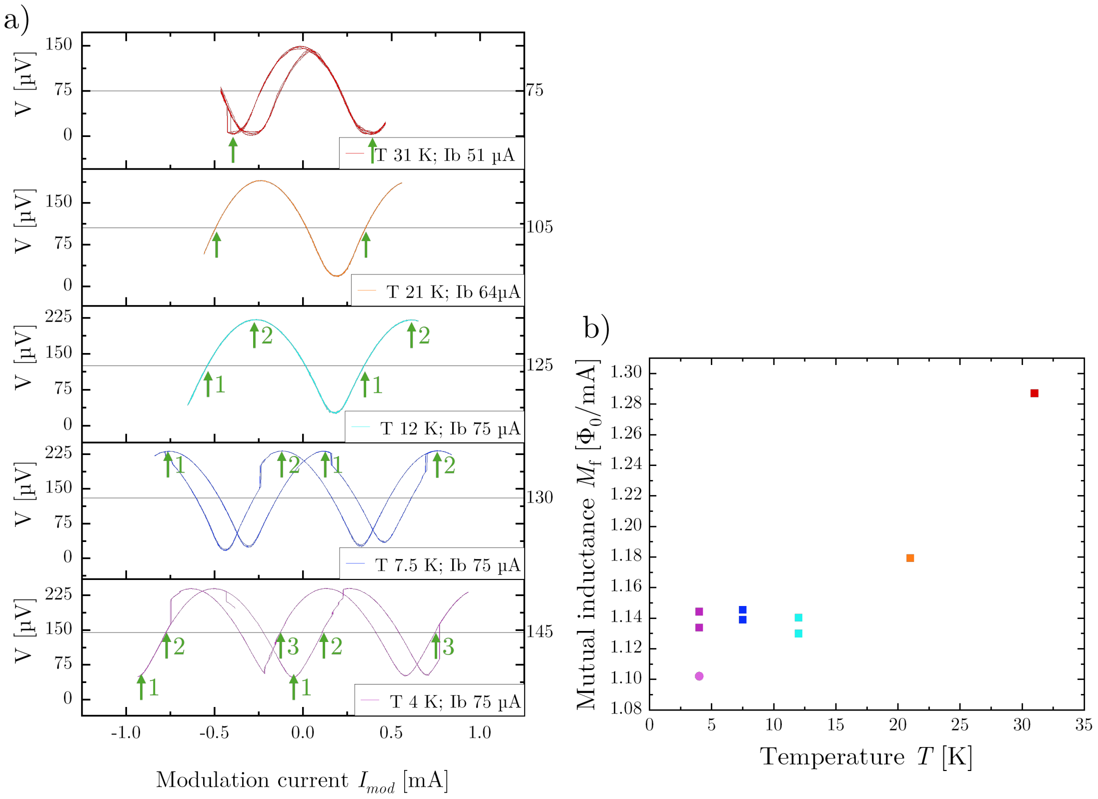

Figure 4.22.: Mutual inductance of SQUID CNT-1 at different temperatures with the Fe nanowire. (a) V vs. I_{mod} at $T = 31, 21, 12, 7.5, 4\,\mathrm{K}$ (from top to bottom). The modulation current was generated externally, with $R = 2000\,\Omega$ at the *Ext. Flux @ Amp* input of the `Magnicon` electronics. The horizontal black line indicates the center points between V_{max} and V_{min}, which serve as the measurement points for the mutual inductance M_f. Other potential measurement points for M_f include V_{max} and V_{min}. Green arrows in (a) indicate the measurement points for the mutual inductance values depicted in (b). (b) M_f vs. T shows the increase in mutual inductance at higher temperatures. The round data point at $4\,\mathrm{K}$ corresponds to the M_f value obtained from the pre-characterisation before the placement of the Fe nanowire.

M_f of EuS SQUIDs

To analyse the mutual inductance M_f of the EuS SQUIDs, V versus I_{mod} measurements were performed at different temperatures to evaluate the SQUID properties as a function of temperature.

During these measurements, a time-dependent voltage was applied using an external voltage source. Within the `Magnicon` electronics, an internal resistor was selected to precisely convert the applied voltage into a current through the modulation line. For the present measurements, the internal resistance of the `Magnicon` electronics was set to 2000 Ω, and the SQUID voltage was recorded as a function of the resulting modulation current.

The results of these measurements are presented in Figure 4.23, which illustrates the mutual inductance behaviour of the EuS SQUIDs at different temperatures.

Figure 4.23 a) shows the V versus I_{mod} characteristics for SQUID EuS-05 at 300 mK. Similarly, Figure 4.23 b) presents the corresponding measurement for SQUID EuS-11 at 1 K. In both cases, the green bars indicate the distance between two minima, which is used to determine $1/M_f$. From these measurements, M_f can be extracted by identifying the modulation period and calculating the reciprocal of the current change required to couple one flux quantum, Φ_0, into the SQUID loop.

Figure 4.23 c) depicts the mutual inductance M_f as a function of temperature for SQUIDs EuS-05, EuS-10, and EuS-12. The data exhibit significant variations, preventing a conclusive identification of a systematic increase in M_f at temperatures up to 20 K.

Figure 4.23 d) presents the temperature dependence of M_f for SQUID EuS-11. In comparison to the other SQUIDs, both the magnitude of M_f and its spread are significantly larger.

The strong variability observed in the measurements may be attributed to the lower quality of some of the EuS SQUIDs. In particular, SQUID EuS-11 exhibited multiple transitions in the IVC and a low critical current, I_{c}, which complicates the accurate determination of M_f.

Another potential source of variation in the measured values arises from the measurement setup and methodology. Applying the modulation current via an external voltage source, combined with the relatively low sampling rate of the measurement software, introduces additional variance of the measurement.

Despite these challenges, the values of M_f do not appear to exhibit a measurable increase below 20 K. This suggests that the SQUIDs maintain a relatively high T_c, supporting their suitability for the conducted measurements.

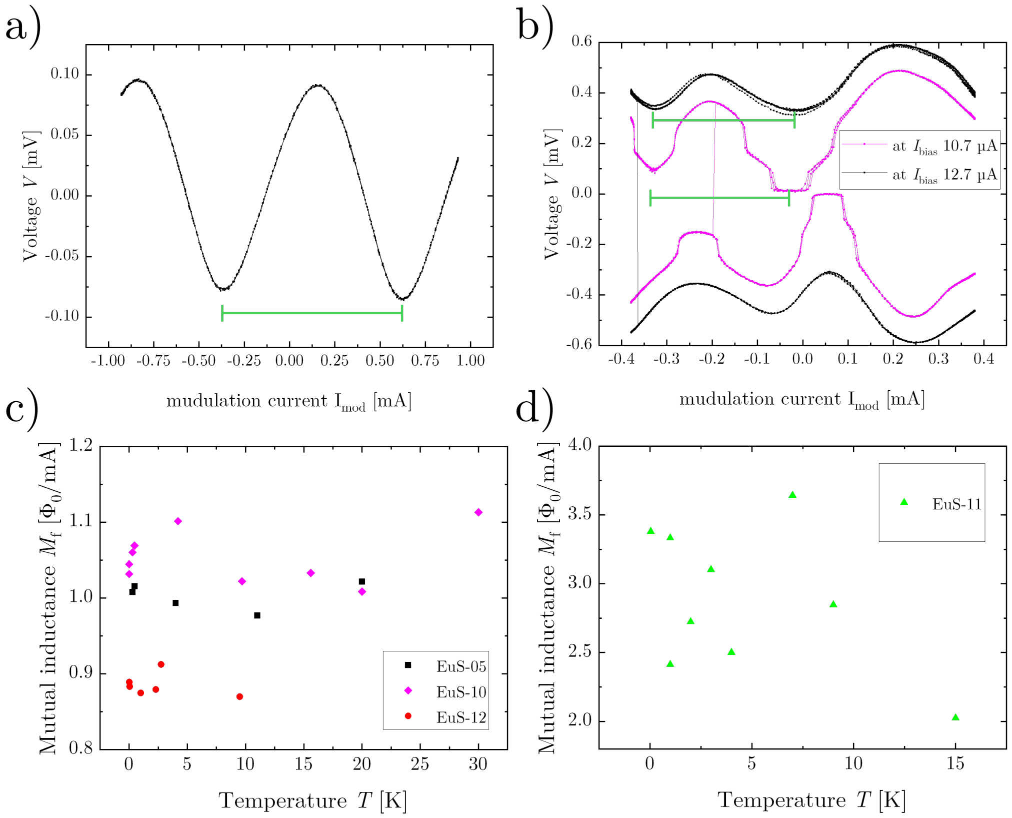

Figure 4.23.: Mutual inductance of the SQUIDs with EuS nanodiscs at different temperatures. (a) V vs. I_{mod} for SQUID EuS-05 at 300 mK and (b) for SQUID EuS-11 at 1 K. Green bars indicate the distance between two minima, used to determine $1/M_f$. (c) Mutual inductance M_f vs. T for SQUID EuS-05, EuS-10, and EuS-12. (d) Mutual inductance M_f vs. T for SQUID EuS-11.

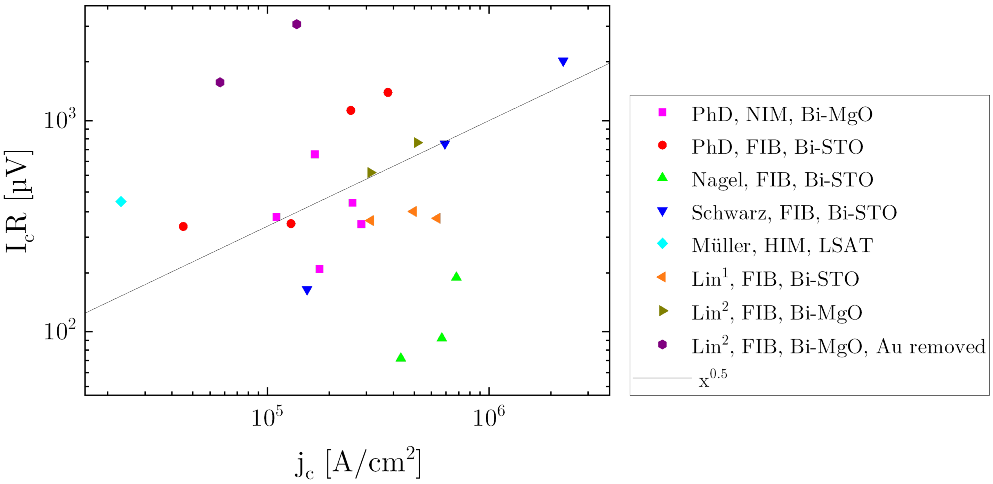

Figure 4.24.: I_cR product versus j_c. This figure displays the SQUIDs listed in Table 4.4. The solid line corresponds to $I_cR \propto j_c^{0.5\pm0.1}$, as previously reported in Gross et al. [72].

4.1.6. Comparison of Ne-FIB with Ga-FIB processed SQUIDs

The application of Ne-FIB technology for SQUID fabrication on YBCO bicrystals represents a novel approach to the structuring of Josephson junctions and SQUIDs. While Ga-FIB methods have been conventionally employed, this subsection compares the properties of SQUIDs fabricated using Ga-FIB, and Ne-FIB techniques. The comparison aims to assess whether Ne-FIB fabrication provides a reliable and reproducible method for fabricating these devices and to identify key features that require further investigation, including potential advantages of this new method.

Table 4.4 and Figure 4.24 illustrate that the properties of SQUIDs fabricated via Ne-FIB and Ga-FIB are comparable to those of other SQUIDs previously produced within the research group. The critical current density, j_c, as well as the I_cR products of Ne-FIB-structured SQUIDs, fall within the typical range observed for Ga-FIB-fabricated devices. The primary advantage of Ne-FIB lies in its ability to define significantly smaller structures with high precision. However, the limitations regarding the minimal feature sizes that can be reliably achieved with Ne-FIB require further investigation.

Particularly, the extent of edge damage in Josephson junctions remains an important open question. Since Ga-FIB processing introduces Ga ions into the material, potentially altering its conductivity, Ne-FIB structuring may yield junctions with reduced edge damage and improved superconducting properties.

When comparing the critical current density j_c of SQUIDs grown on MgO with a junction width of approximately 200 nm, the devices patterned using neon FIB appear to exhibit slightly better performance. However, the SQUIDs with a similar junction width reported by Lin^2 [36] underwent additional postprocessing, where parts of the gold shunt were removed. This additional processing step may have influenced their electrical characteristics and should be taken into account when comparing results.

Table 4.4.: Comparison of SQUIDs fabricated in this thesis with previously published SQUIDs from the research group of Kleiner and Kölle. For references, see Nagel [44], Schwarz [24], Müller [69], Lin^1 [71], and Lin^2 [36]. SQUIDs fabricated by Ne-FIB are marked by X^{Ne}, fabricated by He-FIB with X^{He}. Thin films grown on a MgO 24° bi-crystal are marked with ^{MgO}, on STO 24° bicrystal with ^{STO}, and on a LSAT substrate with ^{LSAT}. Josephson junction widths marked with * are the average width of both Josephson junctions measured in a SEM, widths without * corresponds to the designed fabrication target. **Au thickness after the gold layer was removed.

SQUID	YBCO + Au [nm]	w_{Jj} [nm]	$I_{\mathrm{c,max}}$ [µA]	j_{c} [$10^5\,\mathrm{A\,cm^{-2}}$]	R_{n} [Ω]	$I_{\mathrm{c}}R$ [mV]	V_{Φ} [mV/Φ_0]
CNT-1^{Ne}	80 + 20 ^{MgO}	200	85	2.7	3.8	0.32	3.0
CNT-2^{Ne}	80 + 20 ^{MgO}	200	55	1.7	3.6	0.20	0.1
CNT-3^{Ne}	80 + 20 ^{MgO}	500	88	1.1	4.0	0.35	0.3
CNT-4^{Ne}	80 + 20 ^{MgO}	1000	262	1.6	2.6	0.70	4.2
CNT-6^{Ne}	80 + 20 ^{MgO}	500	194	2.4	2.1	0.40	3.1
EuS-05	90 + 60 ^{STO}	600	138	1.3	2.4	0.33	0.6
EuS-10	90 + 60 ^{STO}	600	378	3.5	3.6	1.36	1.3
EuS-11	90 + 60 ^{STO}	600	45	0.4	7.0	0.32	2.3
EuS-12	90 + 60 ^{STO}	600	257	2.4	4.3	1.12	3.0
Nagel-1	50 + 60 ^{STO}	110	44	4.0	1.7	0.08	0.1
Nagel-2	50 + 60 ^{STO}	80	49	6.1	1.9	0.09	0.1
Nagel-3	50 + 60 ^{STO}	195	139	7.1	1.3	0.18	0.1
Schwarz-1	120 + 70 ^{STO}	185	960	21.6	2.0	1.92	4.4
Schwarz-2	120 + 70 ^{STO}	205	311	6.3	2.5	0.78	1.7
Schwarz-3	75 + 70 ^{STO}	305	69	1.5	2.3	0.16	0.7
Müller^{He}	50 + 0 ^{LSAT}	2000	44	0.2	9.5	0.41	2.1
Lin^1-14	120 + 65^{STO}	300	420	5.8	0.8	0.34	
Lin^1-15	120 + 65 ^{STO}	265	290	4.6	1.3	0.37	
Lin^1-SL	120 + 65 ^{STO}	285	200	2.9	1.7	0.34	
Lin^2-3-4	120 + 65 ^{MgO}	315	358	4.7	2.2	0.79	
Lin^2-1-5	120 + 65 ^{MgO}	270	189	2.9	3	0.57	
Lin^2-1-7	120 + 45** ^{MgO}	243	94	1.6	13.2	1.23	
Lin^2-1-10	120 + 20** ^{MgO}	205	64	1.3	28	1.78	
Lin^2-1-9	120 + 0** ^{MgO}	225	33	0.6	46	1.52	
Lin^2-2-S1	120 + 0** ^{MgO}	200	65	1.4	44	2.86	

In addition, SQUIDs patterned using neon FIB appear to remain relatively stable over extended periods of time. However, this observation has not yet been investigated systematically.

To perform a more comprehensive comparison, a larger dataset of SQUIDs is required. As a first step towards such an analysis, an attempt was made to fabricate simple Josephson junctions with progressively smaller widths to evaluate the resolution limits of Ne-FIB structuring.

To facilitate these studies, a new mask design was developed, as illustrated in Figure 4.25. This design was optimised to maximise the number of measurable structures on a single 10×10 mm YBCO bicrystal chip. Unlike previous designs, which typically include only 14 microbridges per chip for SQUID fabrication, the new layout incorporates:

- 24 individual microbridges,
- 10 SQUIDs with modulation lines,
- 3 experimental microbridges,
- 2 contact regions for measuring the thin film's specific resistance,
- A dedicated section for labelling the chip name and thin-film properties.

However, these fabrication attempts were unsuccessful due to significant degradation of superconducting properties during processing. It is likely that similar to the EuS-SQUID-chip an insufficiently thick photoresist layer failed to protect the thin film adequately during argon ion milling, leading to excessive damage.

A systematic approach employing YBCO thin films with varying thicknesses and a controlled reduction in Josephson junction width could provide valuable insights into the effects of Ne-FIB structuring on junction performance. Such a study would constitute an important future research direction, offering a systematic analysis of the interplay between junction width, ion milling parameters, and device characteristics.

These efforts represent a novel approach to fabricating SQUIDs using Ne-FIB technology. The initial measurements presented in this thesis demonstrate that the fabrication process is fundamentally viable and that the resulting SQUIDs exhibit electrical characteristics comparable to those produced by conventional Ga-FIB structuring. However, further studies are required to fully evaluate the potential advantages or limitations of this method. Open questions include long-term stability, noise performance, precise SQUID parameters such as β_L and β_C, as well as the extent of edge damage introduced during Ne-FIB processing. Addressing these aspects will be essential for establishing Ne-FIB structuring as a reliable method for high-performance nanoSQUID fabrication.

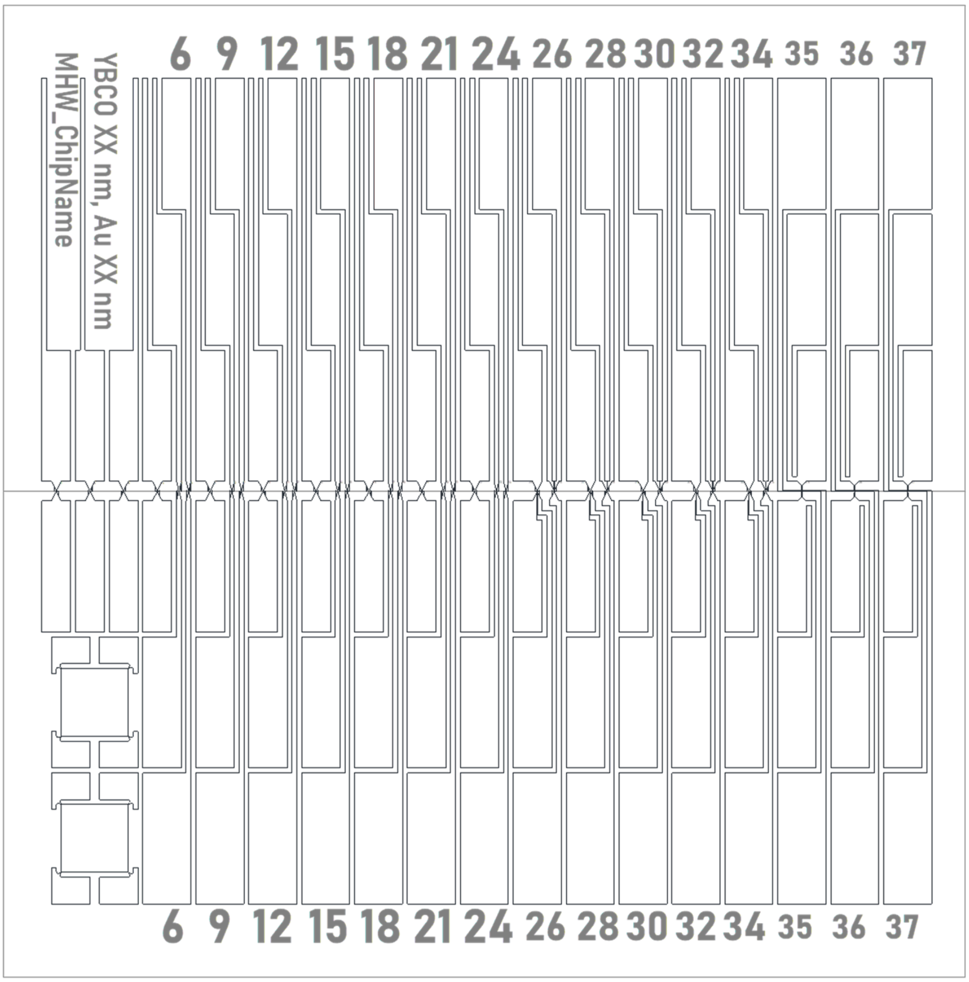

Figure 4.25.: Optimised mask design for fabricating SQUIDs using a maskless aligner on a single 10 × 10 mm YBCO bicrystal chip. The new design includes 24 individual microbridges, 10 SQUIDs with modulation lines, 3 experimental bridges, and 2 dedicated regions for measuring the thin film's specific resistance. Depending on the electrical wiring configuration, the 16×3 opposing bond pads can be selectively connected, allowing for either 48 independent microbridges or 32 bridges with modulation lines. In the upper portion of the chip, all bridges extend towards the top edge, enabling grounding via a continuous carbon tape strip to facilitate imaging in the SEM.

4.1.7. Final Discussion of Key Findings

This chapter has presented the fabrication and characterisation of the SQUIDs used for the particle measurements discussed in Chapters 4.3 and 4.4. The analysis has revealed several challenges in the fabrication process, as well as key insights into the suitability of different SQUID designs for specific measurement conditions.

Challenges in Fabrication

The fabrication of YBCO-based SQUIDs requires particular attention due to the sensitivity of the material. Exposure to moisture, as well as damage caused by ion milling, can significantly alter the crystal structure and degrade the superconducting properties of the thin films. To mitigate these effects, the following considerations must be taken into account:

- Minimising the exposure of YBCO thin films to moisture and ambient air or water during processing like repeated resist stripping and reapplication.
- Ensuring that an adequately thick resist layer is used during etching.
- Avoiding excessive heating due to prolonged ion milling.

Additionally, for grain boundary Josephson junction SQUIDs, precise alignment of the structures relative to the grain boundary is crucial. In this work, an integrated ruler-marker system was developed and successfully implemented to improve alignment accuracy to 5 µm in a maskless alignment system. Furthermore, an optimised lithography mask was designed, enabling a higher number of microbridges per chip and allowing for a more detailed analysis of thin-film properties.

Characterisation of SQUIDs for Fe Nanowires

The SQUIDs intended for Fe nanowire measurements were structured using Ne-FIB milling. A summary of their characteristics is as follows:

- **SQUID CNT-1** exhibits good SQUID characteristics; however, it shall be noted that a defect in the modulation line prevents operation in FLL mode.
- **SQUID CNT-2** was milled half way due to a software crash during milling. However, its properties are suitable for measurements, suggesting that completely milling away the visible thin film may not be necessary. This needs to be further investigated, giving the opportunity to minimise stress on the film due to processing.
- **SQUID CNT-3** demonstrates good overall SQUID properties.
- **SQUID CNT-4** was designed with an increased Josephson junction width, resulting in excellent SQUID performance. The larger Josephson junctions lead to a greater sensitivity to magnetic fields, making high-field measurements more challenging.

- **SQUID CNT-6** is well-suited for measurements but exhibits an unidentified residue near the SQUID, which may affect the particle placement.

Characterisation of SQUIDs for EuS Nanodiscs

The SQUIDs designed for EuS nanodisc measurements were fabricated using the established Ga-FIB technique. During fabrication, significant variability in the SQUID properties was observed, with several devices exhibiting multiple I_c transitions and tilted V vs. I_mod characteristics. These irregularities are likely due to damages induced during the fabrication of the microbridges during Ar-milling with too thin resist.

Additional challenges arise from the dilution refrigerator measurement setup, which introduced constraints such as:

- The inability to easily heat and cool the SQUIDs. This makes it impossible to remove trapped flux artifacts by cycling the temperature above T_c.
- A relatively low sampling rate of the measurement software, which may introduce uncertainty in the data and make it difficult to filter out noise.

The characterisation of individual EuS SQUIDs yielded the following observations:

- **SQUID EuS-05** is generally suitable for particle measurements. The potential of trapped flux shall be considered for the interpretation of results.
- **SQUID EuS-10** exhibits good SQUID characteristics. The origin of the tilt in the V vs. I_mod curve remains unclear, and it is uncertain whether it affects FLL-mode measurements.
- **SQUID EuS-11** has a relatively low I_c and multiple I_c transitions. To minimise measurement errors, it must be operated at relatively high I_bias currents to avoid false signals by transitions. The potential of trapped flux shall be considered for the interpretation of results.
- **SQUID EuS-12** demonstrates good SQUID characteristics. The remarks made for EuS-10 likewise apply to the tilt in the V vs. I_mod and V vs. B curves.

Comparison with Other SQUIDs

A comparison with previously fabricated SQUIDs (see Table 4.4 and Figure 4.24) reveals that the overall characteristics of the SQUIDs in this thesis fall within the typical range observed for YBCO grain boundary SQUIDs. The results confirm that Ne-FIB milled SQUIDs exhibit comparable properties to those fabricated using Ga-FIB techniques, with the additional advantage of enabling smaller structure sizes.

To exploit the full potential of Ne-FIB processing, further investigations might assess the junction performance, edge damage, and longevity of fabricated Josephson junctions. Future studies should include:

- A larger dataset of Ne-FIB-structured SQUIDs.
- Investigations into the minimum achievable junction size with Ne-FIB.
- A systematic comparison of edge damage between Ga-FIB and Ne-FIB structuring.
- Studies examining the influence of ion milling parameters on thin-film quality, such as the dose needed to sufficiently mill the thin film.
- Long-term studies about the performance of the Josephson junctions, as one of the possible reasons for junction performance could be the diffusion of Ga ions into the crystal structure of YBCO after Ga-FIB milling.

Conclusion

The results presented in this chapter demonstrate that the fabrication techniques used in this work are viable for producing high-quality SQUIDs for Fe nanowire and EuS nanodisc measurements. The development of improved lithography masks and alignment techniques represents a significant advancement in the fabrication process, enhancing precision and reproducibility. While challenges such as trapped flux, film degradation, and low-temperature measurement constraints remain, the characterisation confirms that the SQUIDs fabricated in this thesis are well-suited for the measurement of particles.

Studies focusing on the refinement of Ne-FIB structuring and systematic comparisons with Ga-FIB-fabricated devices promise to further improve the reliability and performance of SQUIDs.

4.2. Vector Substrates: A Novel Approach for Superconducting Josephson Junctions

The development of freestanding oxide membranes has become a rapidly advancing field of research, attracting significant interest from physics institutes worldwide.[45], [46], [73]–[86] The introduction of an epitaxial sacrificial layer in 2018 enabled researchers to fabricate freestanding oxide membranes, paving the way for novel applications, including new two-dimensional material research in oxides and the heterointegration of oxides onto alternative substrates.

Previously, materials such as YBCO, along with other oxides exhibiting intriguing physical properties—such as superconductivity governed by their crystalline structure—could only be grown on lattice-matched substrates. However, recent work by Varun Harbola and Yu-Jung Wu in Jochen Mannhart's research group marked a key milestone, as they used a sacrificial layer to facilitate the vector substrate approach. [2], [87] They successfully transferred a membrane of bi-crystalline STO onto a sapphire substrate and demonstrated the growth of high-quality crystalline YBCO on top.

Leveraging my expertise in microfabrication from other YBCO-based devices, I was able to process these novel films, fabricate functional Josephson junctions, and conduct measurements on these structures.

The paper resulting from this collaboration with Varun Harbola is presented in Chapter 4.2.3, as published in [2]. The supplementary materials associated with the publication are included in Appendix A.

4.2.1. Contributions

Vector-substrate-based Josephson junctions

> For this paper, I performed the microfabrication of the YBCO thin film grown on a vector substrate and performed electric transport measurements. Varun Harbola was responsible for guiding the research. Yu-Jung Wu performed the growth and transfer of a $SrTiO_3$ membrane on a sapphire substrate, therefore creating the vector substrate, growing of the YBCO thin film, annealing, and AFM measurements. Katja Wurster and Simon Koch assisted with growing the YBCO thin film, electric transport measurements and measurement evaluation. Reinhold Kleiner, Dieter Kölle and Jochen Mannhart were responsible to support the writing process and helped with research questions. I contributed the figures of the electrical transport measurements and supported the writing of the text about transport properties. The rest of the paper was co-written by Varun Harbola and Yo-Jung Wu.

4.2.2. Introduction to the Paper

The production of high-quality YBCO requires epitaxial growth on lattice-matched substrates. The selection of substrates for grain boundary YBCO thin films is limited due to the inherent limitations of epitaxial growth. The choice of substrate also affects the measurement, with STO, for example, having a high dielectric constant. The advent of the perovskite sacrificial layer in 2018[45] has opened up new avenues for the fabrication of freestanding oxide membranes. The utilisation of a water-soluble sacrificial layer to release the YBCO membrane from its growth substrate has the potential to compromise the quality of the YBCO thin film (see Katja Wurster's thesis[37] for further details). Consequently, a highly sophisticated encapsulation process is required to safeguard the YBCO from the water during the release process. An alternative approach is to grow only the STO on a sacrificial layer and then transfer a thin membrane of STO, which is not affected by the water, onto the new substrate. The next step is the deposition of the YBCO thin film on the heterostructure. This allows the use of different substrates under a $\sim 10\,\mathrm{nm}$ thick STO membrane and the reuse of expensive bicrystal substrates. Furthermore, the approach offers additional possibilities, including the production of LSAT or MgO substrates using an STO bicrystal, as well as other experimental modifications of the vector membrane.

This alternative approach was successfully demonstrated by Varun Harbola and Yu Wu at the Max Planck Institute for Solid State Research in Stuttgart. The successful transfer of grain boundary STO membranes on sapphire, including the epitaxial growth of superconducting YBCO on top, was achieved. Subsequent lithographic processing and measurement of Josephson junctions in this heterostructure were conducted within this work.

4.2.3. Vector-substrate-based Josephson junctions - Applied Physics Letters

The following pages contain the publication *Yu-Jung Wu, Martin Hack, Katja Wurster, Simon Koch, Reinhold Kleiner, Dieter Koelle, Jochen Mannhart & Varun Harbola, "Vector-substrate-based Josephson junctions", Applied Physics Letters, vol. 125, no. 3, 2004 DOI:* `https://doi.org/10.1063/5.0217861`*; licensed under a Creative Commons Attribution (CC BY) license*[2]. Here, the general concept of this approach is described, and the obtained electronic transport measurements are presented, along with a discussion and outlook on this novel approach.

Applied Physics Letters ARTICLE pubs.aip.org/aip/apl

Vector substrate-based Josephson junctions

Cite as: Appl. Phys. Lett. **125**, 032601 (2024); doi: 10.1063/5.0217861
Submitted: 7 May 2024 · Accepted: 27 June 2024 ·
Published Online: 15 July 2024

Yu-Jung Wu,[1] Martin Hack,[2] Katja Wurster,[2] Simon Koch,[2] Reinhold Kleiner,[2] Dieter Koelle,[2] Jochen Mannhart,[1] and Varun Harbola[1,a)]

AFFILIATIONS

[1] Max Planck Institute for Solid State Research Heisenbergstrasse 1, 70569 Stuttgart, Germany
[2] Physikalisches Institut, Center for Quantum Science (CQ) and LISA$^+$ Universität Tübingen, auf der Morgenstelle 14, 72076 Tübingen, Germany

[a)] Author to whom correspondence should be addressed: v.harbola@fkf.mpg.de

ABSTRACT

We present a way to fabricate bicrystal Josephson junctions of high-T_c cuprate superconductors that are not grown on bulk bicrystalline substrates. Based on vector substrate technology, this approach makes use of a few tens-of-nanometer-thick bicrystalline membranes transferred onto conventional substrates. We demonstrate 24° [001]-tilt $YBa_2Cu_3O_{7-x}$ Josephson junctions fabricated on sapphire single crystals by utilizing 10-nm-thick bicrystalline $SrTiO_3$ membranes. This technique allows one to manufacture bicrystalline Josephson junctions of high-T_c superconductors on a large variety of bulk substrate materials, providing distinctive degrees of freedom in designing the junctions and their electronic properties. Furthermore, it offers the capability to replace the fabrication of bulk bicrystalline substrates with thin-film growth methods.

Bicrystal Josephson junctions of high-transition temperature (high-T_c) cuprate superconductors[1–4] have found many uses in fundamental science and applications.[2,5–7] For example, bicrystal and the related tricrystal junctions have been instrumental in identifying the *d*-wave order parameter symmetry of high-T_c cuprates.[8,9] Studies of their critical currents as a function of the grain boundary angle revealed the necessity of aligning the grains in high-T_c cables and/or utilizing large grain boundary areas[6] to achieve high critical currents, as is now done in coated conductor technologies (see, e.g., Refs. 10 and 11).

Bicrystal Josephson junctions rely on bulk bicrystalline substrates for the epitaxial growth of bicrystalline high-T_c superconducting thin films. However, such substrates are expensive to fabricate, are only available with a limited range of materials, and may have properties detrimental to desired applications. Sapphire, for example, features a low dielectric loss tangent of $<10^{-4}$ at 10^{10} Hz and 300 K, high thermal conductivity of $\approx$35 W/mK at 300 K, and a moderate dielectric constant of $\approx$10. It, therefore, appears to be a desirable material for substrates of high-T_c Josephson junctions.[12] However, because of its hexagonal crystal lattice symmetry, its poor lattice match, and its contamination of high-T_c films by Al diffusion, sapphire is not generally considered a useful material for bicrystals.

Recently, an approach called vector substrate technology[13] was presented, that builds on advances based on the fabrication[14–20] and application[21–28] of freestanding oxide membranes and offers unique degrees of freedom in choosing substrates for the epitaxial growth of thin films.[13,28] One particular advantage provided by this concept is the possibility of versatile heterogeneous integration, which offers flexibility in choosing materials for functional devices, and the concept of vector substrates can also be incorporated into processes such as transfer printing.[29] With vector substrate technology, membranes as thin as ten nanometers placed on carrier substrates are used as templates for the epitaxial film growth of further films. Importantly, only the membrane has to have the properties required for further epitaxial film growth, whereas the materials of the carriers are constrained by far fewer restrictions. For example, a carrier may be an unrefined, low-cost compound or a material with properties that offer advantages for a desired application. This technology is versatile and allows the epitaxial growth of single-crystalline films on curved surfaces, among many other uses.

Given its many advantages, vector substrate technology has been proposed as an alternative to bicrystalline bulk substrates by making use of bicrystalline membranes[13] as illustrated in Fig. 1(a). Here, we report on the realization of this concept by demonstrating excellent bicrystalline $YBa_2Cu_3O_{7-x}$ Josephson junctions fabricated on standard *c*-plane sapphire single crystals. In this demonstration, the surfaces of the sapphire substrates are coated by 10-nm-thick $SrTiO_3$ membranes.

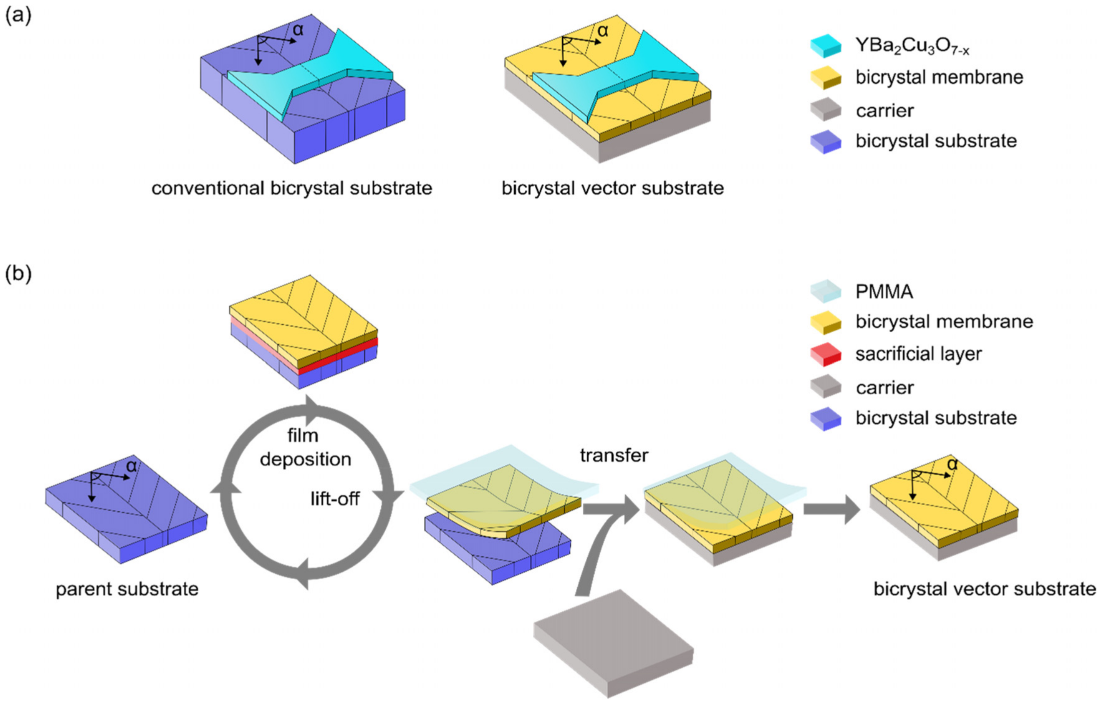

FIG. 1. (a) Illustration of the main idea of this work. Left: sketch of an arrangement of a bicrystalline Josephson junction fabricated by epitaxial growth on a conventional bicrystalline bulk substrate. Right: sketch of a bicrystal arrangement that utilizes a vector substrate. The vector substrate, which consists of a bulk substrate of almost unrestricted choice, carries a bicrystalline thin-film membrane sintered to its surface. In this case, it is a sapphire single crystal and a 10-nm-thick, 24° $SrTiO_3$ bicrystalline film. High-T_c superconducting films grown on either substrate yield Josephson junctions at the bicrystal grain boundary. (b) Fabrication process of the vector substrates. Note that the parent substrates can be recycled many times. Here, α equals ~24°.

These membranes are obtained by thin-film growth on bicrystalline substrates, called parent substrates, which can be recycled for growing numerous additional membranes.

To fabricate bicrystalline $YBa_2Cu_3O_{7-x}$ Josephson junctions on sapphire single crystals, we used $SrTiO_3$ bicrystals[30] as parent substrates. On such a parent substrate, a water-soluble, sacrificial $Sr_2CaAl_2O_6$ layer[23,31] and a $SrTiO_3$ layer were epitaxially deposited by pulsed laser deposition (PLD), such that the bicrystal structure was transferred through the sacrificial layer to the final $SrTiO_3$ membrane. By dissolving the sacrificial layer in water, the bicrystal $SrTiO_3$ membrane was then lifted off and transferred onto a carrier substrate, in our case, a sapphire single crystal, yielding a vector substrate. In this process, illustrated in Fig. 1(b), the surface structure of the bicrystal parent substrate remains unscathed. The parent substrates are therefore reusable, such that numerous membranes can be derived from one parent substrate (Fig. S2). Furthermore, vector substrates fabricated in this way may also be used as parent substrates, reducing the overall need for bulk bicrystals.

In detail, the samples were fabricated by first thermally preparing 24° [001]-tilt $SrTiO_3$ bicrystals[30] by an *in situ* anneal in $pO_2 = 0.1$ mbar at 825 °C for 40 min such that their surfaces exhibited standard step-terrace patterns and well visible boundaries between the two constituent crystals. Following the layer-by-layer growth of $Sr_2CaAl_2O_6$—this material having been selected for its lattice match to $SrTiO_3$—by PLD, $SrTiO_3$ layers were also grown layer-by-layer by PLD (Fig. S1, see the supplementary material). Both the $Sr_2CaAl_2O_6$ layer and the $SrTiO_3$ membranes were 10 nm thick, optimized for large-area membrane lift-off and practical dissolving time. To provide structural support for the subsequent transfer of the membranes, these samples were spin-coated with ~600-nm-thick PMMA layers. Upon dissolving the sacrificial layers in water, the PMMA-covered bicrystalline $SrTiO_3$ membranes were transferred in air onto thermally prepared sapphire substrates [Fig. 1(b), see the supplementary material].

The surfaces of the parent substrates were restored by cleaning and annealing to again reveal the distinct step-terrace features (see the supplementary material, Fig. S2). We reused the parent substrates up to five times without encountering the end of their lifetime. Note, however, that although the surfaces of the parent bicrystal substrate can be completely restored, the bicrystal grain boundaries may experience some reconstruction due to the high temperatures used for film growth and annealing, resulting in a sub-nanometer trench that develops along the boundary during subsequent preparations (see the supplementary material, Fig. S2).

Although the fragile grain boundary sections of the membranes remained intact after the transfer, the outer parts of the membranes always became fragmented. As a result, the bicrystal membranes had variable shapes with areas of several millimeters per square (see the supplementary material, Fig. S4).

To prepare the vector substrate surface and remove the contaminants still present between the sapphire substrates and the $SrTiO_3$

membranes and to enhance the bonding between the membranes and the sapphires, a 825 °C, 40-min anneal in $pO_2 = 0.1$ mbar was also performed on these samples.[13,32] The membrane surfaces smoothly bulged upward by ∼20 nm over a length perpendicular to the boundary of ∼2 × 200 nm^2, which we attribute to relaxation of strain present between the two $SrTiO_3$ grains. Otherwise we found the surfaces to be flat and smooth, well suited for subsequent epitaxial growth. We observed bulging each time a bicrystal membrane was transferred, and found it to persist after annealing. The amplitude of the bulging was so small, that it never interfered with subsequent epitaxial deposition. Figure 2 provides a series of atomic force micrographs (AFM) that illustrate the evolution of the sample surface during its fabrication.

These results reveal that it is possible to grow heterostructures consisting of a bicrystalline substrate and several layers of thin films, in which the grain boundary is copied from the substrate into each layer. Furthermore, the results show that bicrystalline membranes are sufficiently robust to allow them to be lifted-off and transferred.

In the next step, ∼100-nm-thick $YBa_2Cu_3O_{7-x}$ films were epitaxially grown by PLD on the bicrystalline $SrTiO_3$ surface using standard growth parameters (see the supplementary material). The bulge at the

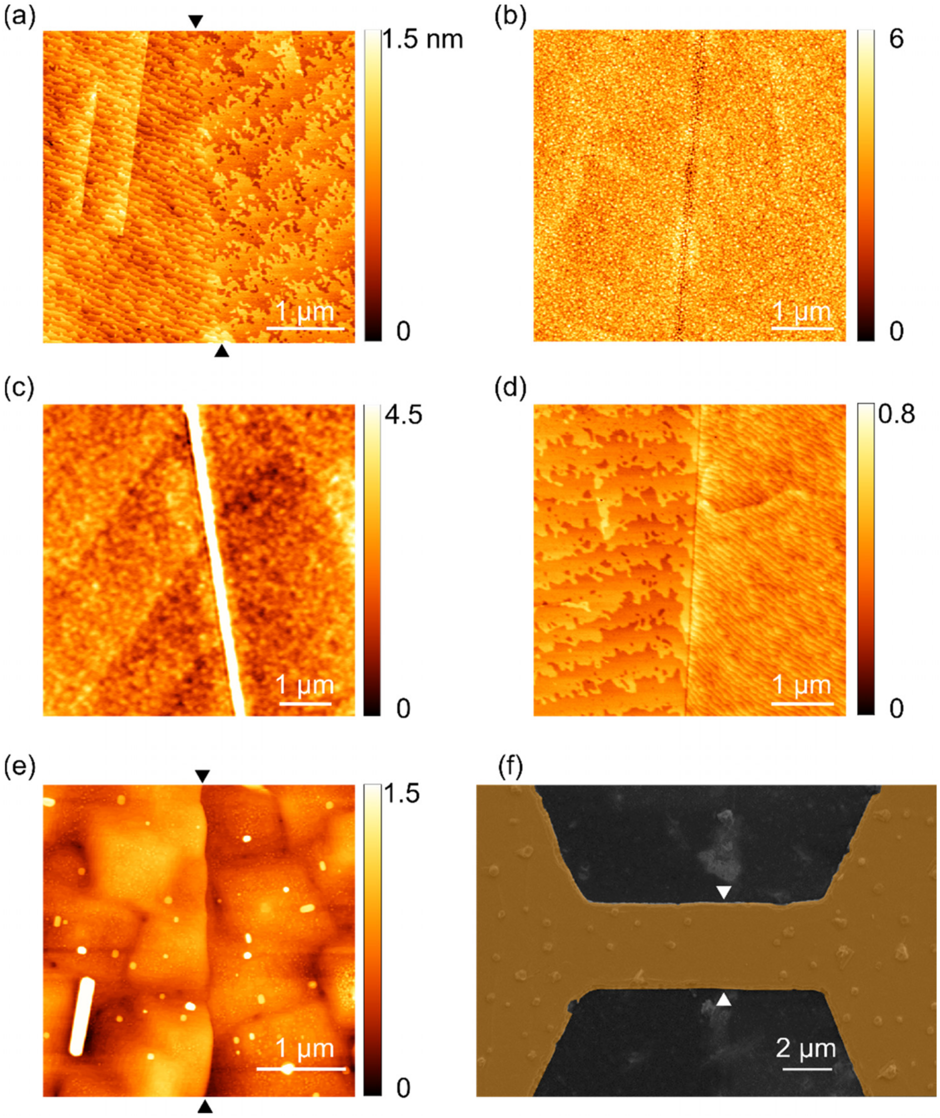

FIG. 2. (a)–(e) AFM micrographs of sample surfaces imaged during various stages of sample preparation. (a) Surface of a bicrystal parent substrate after termination at 825 °C for 40 min. (b) Surface morphology after the growth of $Sr_2CaAl_2O_6$ layers with a $SrTiO_3$ membrane at top. (c) The same bicrystal $SrTiO_3$ membrane after transfer onto a *c*-plane sapphire and post-annealing at 825 °C for 40 min. (d) Surface morphology of the parent bicrystal substrate after membrane lift-off, cleaning and preparation for reuse. (e) Grain boundary after deposition of $YBa_2Cu_3O_{7-x}$ on a bicrystal vector substrate. (f) Scanning electron microscopy image of a $YBa_2Cu_3O_{7-x}$ microbridge crossing the 24° [001]-tilt bicrystal boundary of the vector substrate, which forms a Josephson junction. Grain boundary positions in (a), (e), and (f) are marked by arrows.

grain boundary became unnoticeable after the YBa$_2$Cu$_3$O$_{7-x}$ deposition. The film surfaces were decorated by precipitates [Fig. 2(e)] attributed to a non-stoichiometric material transfer from the PLD target to the growing film. X-ray diffraction revealed the films to be otherwise single-phase and c-axis oriented consistent with YBa$_2$Cu$_3$O$_{7-x}$ films grown on standard SrTiO$_3$ single-crystalline substrates.[33] Their intragrain superconducting $T_{c,0}$ equaled $\sim$88 K. To define $\sim$3–4-μm-wide superconducting bridges crossing the grain boundary as desired to fabricate the Josephson junctions, the samples were patterned by optical lithography. The patterning called for the deposition of an $\sim$20-nm-thick Au film on the sample as well as that lithography, gold etching, and Ar ion milling be performed. The samples were resilient through each stage of the fabrication process. A scanning electron microscopy image of a typical sample is shown in Fig. 2(f).

The transport properties of the bridges were obtained from 4-point measurements performed at 4.2 K in an electrically and magnetically shielded environment with an external magnetic field applied perpendicular to the substrate plane. Figure 3 provides the current–voltage $I(V)$ characteristics for two nominally identical bridges under the influence of the magnetic field. Both bridges show textbook-like I (V) characteristics, as described by the resistively and capacitively shunted junction (RCSJ) model.[34,35] The critical currents I_c at $H = 0$ equal $\sim$116 and 159 μA, corresponding to critical current densities J_c $\sim 5 \times 10^4$ A/cm^2, respectively. These I_c values were obtained after keeping the samples at 300 K for several months. Immediately after fabrication, they were a factor of about 3–5 smaller (see the supplementary material, Fig. S6). We attribute this enhancement to relaxation of oxygen ions at the grain boundary,[2] a phenomenon also observed in Josephson junctions fabricated on bulk bicrystalline substrates.[36] The normal state resistance R_n of the junctions shunted by the 18-nm-thick Au layer were calculated to equal 7.1 and 5.4 Ω. The calculated I_cR_n products for the two bridges are 820 and 850 μV, in agreement with literature values of $\sim$300 μV of comparably shunted 24° junctions.[37,38] The fit of the $I(V)$ characteristics by the RCSJ model yields a Stewart–McCumber parameter of $\beta_c \sim 1.7$, which agrees with the expected value of $\beta_c \sim 2.5$ resulting from a stray capacity of $\sim$0.15 pF possibly caused by the huge low-temperature dielectric permittivity of SrTiO$_3$.[39] The $I_c(H)$ characteristics (Fig. 4) reveal a notably homogeneous current density and high-quality junctions.

In summary, we have demonstrated the viability of fabricating bicrystalline high-T_c Josephson junctions on bulk single-crystalline sapphire substrates by using vector substrate technology. This process utilizes membranes of bicrystalline films, which are deposited

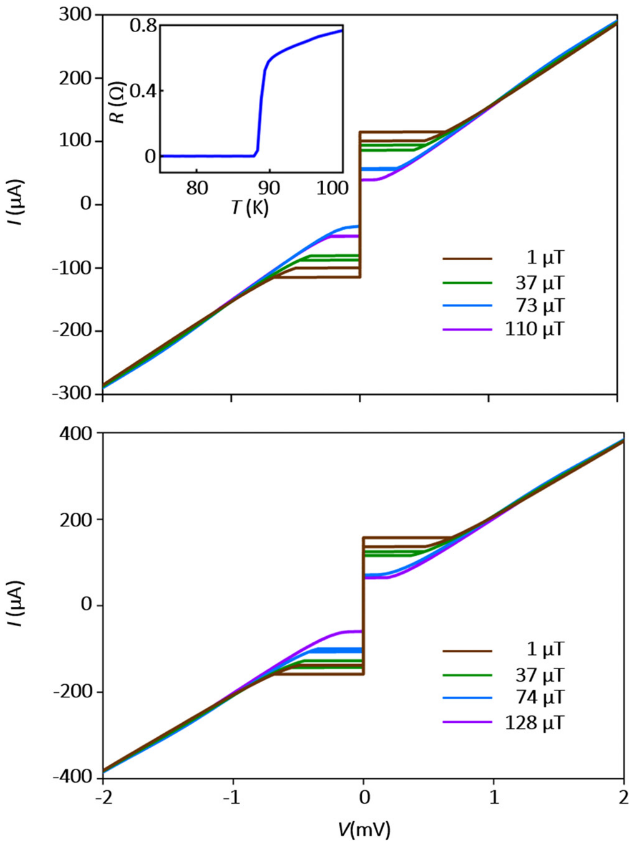

FIG. 3. Current–voltage characteristics of two nominally identical 24° bicrystal Josephson junctions fabricated with vector substrate technology. The data were taken at 4.2 K with a magnetic field H applied perpendicular to the sample surfaces as described. The characteristics follow RCSJ behavior (see the supplementary material, Fig. S8). Inset in the upper graph: Intragrain $R(T)$ characteristic of a nominally identical sister sample.

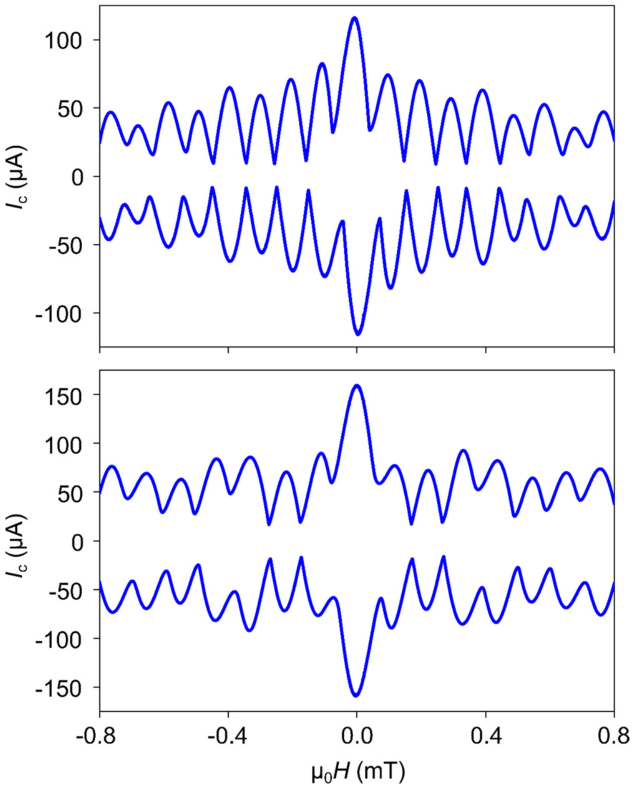

FIG. 4. $I_c(H)$ characteristics of the two Josephson junctions shown in Fig. 3 measured at 4.2 K. The magnetic field H is applied perpendicular to the sample surface.

by thin-film growth methods and transferred onto substrates of choice. We have demonstrated the viability of this technique by fabricating high-quality, 24° YBa$_2$Cu$_3$O$_{7-x}$ bicrystalline Josephson junctions. This technique minimizes the need for bicrystalline substrates to grow bicrystal Josephson junctions, and it allows the growth of such junctions on bulk substrates of choice, which are only covered by a $\sim$10-nm-thick bicrystalline layer suitable for epitaxial growth. This technology can be readily extended (i) to fabricate further vector substrates, such as tricrystalline or polycrystalline substrates, (ii) to grow bicrystalline films of other, possibly non-superconducting materials, and (iii) to deposit heterostructures that comprise single-crystalline films on top of bicrystal layers.

See the supplementary material for details on bicrystal membranes and Josephson junction fabrication.

This project was partially supported by the EU FLAG-ERA Project To2Dox, the European Commission under H2020 FET Open Grant "FIBsuperProbes" (Grant No. 892427), the COST action SUPERQUMAP (No. CA2114), and the German Science Foundation (DFG). We thank S. Goeres for technical support and L. Pavka for editorial support.

AUTHOR DECLARATIONS

Conflict of Interest

The authors have no conflicts to disclose.

Author Contributions

Yu-Jung Wu: Conceptualization (equal); Data curation (equal); Formal analysis (equal); Writing – original draft (equal); Writing – review & editing (equal). **Martin Hack:** Conceptualization (equal); Data curation (equal); Formal analysis (equal); Writing – original draft (equal); Writing – review & editing (equal). **Katja Wurster:** Data curation (equal); Writing – review & editing (equal). **Simon Koch:** Data curation (equal); Writing – review & editing (equal). **Reinhold Kleiner:** Data curation (equal); Funding acquisition (equal); Supervision (equal); Writing – review & editing (equal). **Dieter Koelle:** Funding acquisition (equal); Supervision (equal); Writing – review & editing (equal). **Jochen Mannhart:** Funding acquisition (equal); Supervision (equal); Writing – original draft (equal); Writing – review & editing (equal). **Varun Harbola:** Conceptualization (equal); Data curation (equal); Formal analysis (equal); Funding acquisition (equal); Supervision (equal); Writing – original draft (equal); Writing – review & editing (equal).

DATA AVAILABILITY

The data that support the findings of this study are available from the corresponding author upon reasonable request.

REFERENCES

[1] D. Dimos, P. Chaudhari, and J. Mannhart, Phys. Rev. B **41**(7), 4038 (1990).

[2] H. Hilgenkamp and J. Mannhart, Rev. Mod. Phys. **74**(2), 485 (2002).

[3] F. Tafuri, D. Massarotti, L. Galletti, D. Stornaiuolo, D. Montemurro, L. Longobardi, P. Lucignano, G. Rotoli, G. P. Pepe, A. Tagliacozzo, and F. Lombardi, J. Supercond. Nov. Magn. **26**(1), 21 (2013).

[4] R. Kleiner and W. Buckel, *Superconductivity: An Introduction* (John Wiley & Sons, 2016).

[5] D. Koelle, R. Kleiner, F. Ludwig, E. Dantsker, and J. Clarke, Rev. Mod. Phys. **71**(3), 631 (1999).

[6] J. Mannhart and P. Chaudhari, Phys. Today **54**(11), 48 (2001).

[7] M. J. Martínez-Pérez and D. Koelle, Phys. Sci. Rev. **2**(8), 20175001 (2017).

[8] C. C. Tsuei, J. R. Kirtley, C. C. Chi, L. S. Yu-Jahnes, A. Gupta, T. Shaw, J. Z. Sun, and M. B. Ketchen, Phys. Rev. Lett. **73**(4), 593 (1994).

[9] H. Hilgenkamp, J. Mannhart, and B. Mayer, Phys. Rev. B **53**(21), 14586 (1996).

[10] A. Palau, T. Puig, X. Obradors, R. Feenstra, and A. A. Gapud, Appl. Phys. Lett. **88**(12), 122502 (2006).

[11] J. L. MacManus-Driscoll and S. C. Wimbush, Nat. Rev. Mater. **6**(7), 587 (2021).

[12] D. Stornaiuolo, G. Papari, N. Cennamo, F. Carillo, L. Longobardi, D. Massarotti, A. Barone, and F. Tafuri, Supercond. Sci. Technol. **24**(4), 045008 (2011).

[13] V. Harbola, Y.-J. Wu, F. V. E. Hensling, H. Wang, P. A. van Aken, and J. Mannhart, Adv. Funct. Mater. **34**(4), 2306289 (2024).

[14] S. R. Bakaul, C. R. Serrao, M. Lee, C. W. Yeung, A. Sarker, S. L. Hsu, A. K. Yadav, L. Dedon, L. You, A. I. Khan, J. D. Clarkson, C. Hu, R. Ramesh, and S. Salahuddin, Nat. Commun. **7**, 10547 (2016).

[15] D. Lu, D. J. Baek, S. S. Hong, L. F. Kourkoutis, Y. Hikita, and H. Y. Hwang, Nat. Mater. **15**(12), 1255 (2016).

[16] D. M. Paskiewicz, R. Sichel-Tissot, E. Karapetrova, L. Stan, and D. D. Fong, Nano Lett. **16**(1), 534 (2016).

[17] P. Singh, A. Swartz, D. Lu, S. S. Hong, K. Lee, A. F. Marshall, K. Nishio, Y. Hikita, and H. Y. Hwang, ACS Appl. Electron. Mater. **1**(7), 1269 (2019).

[18] S. S. Hong, M. Gu, M. Verma, V. Harbola, B. Y. Wang, D. Lu, A. Vailionis, Y. Hikita, R. Pentcheva, J. M. Rondinelli, and H. Y. Hwang, Science **368**(6486), 71 (2020).

[19] F. M. Chiabrera, S. Yun, Y. Li, R. T. Dahm, H. Zhang, C. K. R. Kirchert, D. V. Christensen, F. Trier, T. S. Jespersen, and N. Pryds, Ann. Phys. **534**(9), 2200084 (2022).

[20] D. Pesquera, A. Fernández, E. Khestanova, and L. W. Martin, J. Phys.: Condens. Matter **34**(38), 383001 (2022).

[21] G. Dong, S. Li, M. Yao, Z. Zhou, Y. Q. Zhang, X. Han, Z. Luo, J. Yao, B. Peng, Z. Hu, H. Huang, T. Jia, J. Li, W. Ren, Z. G. Ye, X. Ding, J. Sun, C. W. Nan, L. Q. Chen, J. Li, and M. Liu, Science **366**(6464), 475 (2019).

[22] H. S. Kum, H. Lee, S. Kim, S. Lindemann, W. Kong, K. Qiao, P. Chen, J. Irwin, J. H. Lee, S. Xie, S. Subramanian, J. Shim, S.-h. Bae, C. Choi, L. Ranno, S. Seo, S. Lee, J. Bauer, H. Li, K. Lee, J. A. Robinson, C. A. Ross, D. G. Schlom, M. S. Rzchowski, C.-B. Eom, and J. Kim, Nature **578**, 75 (2020).

[23] R. Xu, J. Huang, E. S. Barnard, S. S. Hong, P. Singh, E. K. Wong, T. Jansen, V. Harbola, J. Xiao, B. Y. Wang, S. Crossley, D. Lu, S. Liu, and H. Y. Hwang, Nat. Commun. **11**(1), 3141 (2020).

[24] Y. Li, C. Xiang, F. M. Chiabrera, S. Yun, H. Zhang, D. J. Kelly, R. T. Dahm, C. K. R. Kirchert, T. E. Le Cozannet, F. Trier, D. V. Christensen, T. J. Booth, S. B. Simonsen, S. Kadkhodazadeh, T. S. Jespersen, and N. Pryds, Adv. Mater. **34**(38), 2203187 (2022).

[25] J.-K. Huang, Y. Wan, J. Shi, J. Zhang, Z. Wang, W. Wang, N. Yang, Y. Liu, C.-H. Lin, X. Guan, L. Hu, Z.-L. Yang, B.-C. Huang, Y.-P. Chiu, J. Yang, V. Tung, D. Wang, K. Kalantar-Zadeh, T. Wu, X. Zu, L. Qiao, L.-J. Li, and S. Li, Nature **605**(7909), 262 (2022).

[26] V. Harbola, Y.-J. Wu, H. Wang, S. Smink, S. C. Parks, P. A. van Aken, and J. Mannhart, Adv. Mater. **35**(10), 2210989 (2023).

[27] G. Sánchez-Santolino, V. Rouco, S. Puebla, H. Aramberri, V. Zamora, M. Cabero, F. A. Cuellar, C. Munuera, F. Mompean, M. Garcia-Hernandez, A. Castellanos-Gomez, J. Íñiguez, C. Leon, and J. Santamaria, Nature **626**(7999), 529 (2024).

[28] H. Li, S. Yun, A. Chikina, V. Rosendal, T. Tran, E. Brand, C. H. Christoffersen, N. C. Plumb, M. Shi, N. Pryds, and M. Radovic, Adv. Funct. Mater. **34**(26), 2313236 (2024).

[29] A. Carlson, A. M. Bowen, Y. Huang, R. G. Nuzzo, and J. A. Rogers, Adv. Mater. **24**(39), 5284 (2012).

[30] MTI Corporation, see https://www.mtixtl.com/bi-crystalsrtio3substrate10x5x05 mm1sp24deg-1.aspx for "Bi-crystal SrTiO$_3$ substrate (100) 10x10x1.0 mm, 1sp, 24 Deg."

[31] S. Yun, T. E. le Cozannet, C. Høgfeldt Christoffersen, E. Brand, T. S. Jespersen, and N. Pryds, Small 2310782 (2024).

[32]H. Wang, V. Harbola, Y.-J. Wu, P. A. van Aken, and J. Mannhart, arXiv:2403.08736 (2024).
[33]D. Dijkkamp, T. Venkatesan, X. D. Wu, S. A. Shaheen, N. Jisrawi, Y. H. Min-Lee, W. L. McLean, and M. Croft, Appl. Phys. Lett. **51**(8), 619 (1987).
[34]W. C. Stewart, Appl. Phys. Lett. **12**(8), 277 (1968).
[35]D. E. McCumber, J. Appl. Phys. **39**(7), 3113 (1968).
[36]L. R. Vale, R. H. Ono, J. Talvacchio, M. G. Forrester, B. D. Hunt, M. S. Dilorio, K. Y. Yang, and S. Yoshizumi, IEEE Trans. Appl. Supercond. **9**(2), 3382 (1999).
[37]A. Klushin, A. Golubov, W. Prusseit, and H. Kohlstedt, J. Low Temp. Phys. **106**(3), 265 (1997).
[38]J. Nagel, K. B. Konovalenko, M. Kemmler, M. Turad, R. Werner, E. Kleisz, S. Menzel, R. Klingeler, B. Büchner, R. Kleiner, and D. Koelle, Supercond. Sci. Technol. **24**(1), 015015 (2011).
[39]B. Müller, M. Karrer, F. Limberger, M. Becker, B. Schröppel, C. J. Burkhardt, R. Kleiner, E. Goldobin, and D. Koelle, Phys. Rev. Appl. **11**(4), 044082 (2019).

4.3. Fe nanowires measured with SQUIDs at Various Temperatures

This section presents the SQUID measurements of the magnetic properties of Fe nanowires embedded in CNTs at various temperatures. The primary objective was to measure flux signals during the magnetisation reversal of the Fe nanowires at different temperatures. This study aims to investigate whether the switching field, as well as the coercive field are temperature-dependent and to gain further insights into the magnetisation reversal mechanism of the nanowires.

Our measurements are based on the methodology described by Schwarz et al. [24], who measured similar Fe nanowires in CNTs. Schwarz et al. measured the Fe nanowires at 4 K with switching of the magnetisation at $\mu_0 H_n = \pm 101\,\mathrm{mT}$ and a saturation magnetisation of $M = \pm 1500\,\mathrm{kA/m}$. They suggest a magnetisation reversal via curling mode (see Chapter 2.5). Similar to the approach taken by Martínez-Pérez et al. [48], [49], who studied Co particles and wires, Fe nanowires were measured at various temperatures.

For the measurement, different layout approaches were used. The layouts of the YBCO-based SQUID are presented in Chapter 3.1.5. The microstructuring of the YBCO films followed the methodology described in Chapter 3.1. The subsequent nanostructuring of the SQUID structure for this experimental series was performed with Ne-FIB milling (see Chapter 3.1.4).

To assess the magnetic characterisation of the Fe nanowires, the SQUIDs were first pre-characterised without the placed Fe nanowire. The results of the pre-characterisation are shown in Chapter 4.1.3.

After successful pre-characterisation, the Fe nanowires were placed on the SQUID devices. The placement was carried out at the IFW Dresden under the supervision of Thomas Mühl. The experimental setup and placement of the Fe nanowires onto the SQUIDs are described in Chapter 3.2.1.

All measurements for the magnetic characterisation were conducted in the high-field setup using the 300 mK dipstick and the `Magnicon` electronics for readout (see Chapter 3.1.6). This experimental setup was chosen to achieve temperature, as well as field-dependent characterisation of the Fe nanowires.

Chapter 4.3.1 focuses on the challenges of measuring SQUID devices in the high-field setup and improvements to ensure the integrity of the devices. The critical steps are discussed, and additional optimisations are presented, which led to the successful measurement of SQUID devices with Fe nanowires at 4 K (see Chapter 4.3.2). The additional characterisation of the electrical transport and magnetic response of the Fe nanowires using SQUIDs during field sweeps at various temperatures is described in detail in Chapter 4.3.3.

A final overview of the obtained results and their implications are presented in Chapter 4.3.4. Based on the findings presented, an improved approach for further experiments with Fe nanowires is suggested.

The temperature dependence of the switching of the nanowire is planned to be used in a publication.

4.3.1. Optimisation of the measuring procedure

To ensure accurate and reliable measurements of the magnetic properties of Fe nanowires, several optimisations were added to the measurement procedure. For the first run of the experiments CNT-2, CNT-3 and CNT-6 were fabricated, and pre-characterised. CNT-2 has an $I_\mathrm{c} = 55\,\mu\mathrm{A}$, CNT-3 has an $I_\mathrm{c} = 88\,\mu\mathrm{A}$ and CNT-6 has an $I_\mathrm{c} = 194\,\mu\mathrm{A}$ at $4.2\,\mathrm{K}$. Further details to the SQUIDs can be found in Table 4.2 in Chapter 4.1.2. These I_c values are comparable to previous SQUID data and seemed sufficient for a first analysis of the Fe nanowires. However, since I_c decreases with increasing T and a higher value of I_c might increase the performance of the SQUID at higher T, SQUID CNT-4 was designed with a larger Josephson junction width. The increased width of the Josephson junction increases I_c, as well as the influence of the external field on the Josephson junction. Therefore, both effects must be balanced against each other and a compromise between high I_c and low influence of the external field must be found. A detailed analysis of the SQUID data can be seen in Chapter 4.1.3.

The placement of the Fe nanowires was performed by Thomas Wiek at the IFW Dresden. During the placement of the Fe nanowire on SQUID CNT-6, an electric discharge occurred at the moment the Fe nanowire touched the surface of the SQUID. This discharge destroyed the SQUID, as shown in Figure 4.26(b). The different charges on the SQUID and the Fe nanowire arose because the SQUIDs were not properly grounded to the setup. Additionally, the particle near the SQUID might have caused some local charges on the surface. Following this incident, the SQUIDs were carefully grounded using electrically conducting carbon tape before the placement, which resolved the issue. Figures 4.26(c) and (e) depict the SQUID devices after the successful placement of the Fe nanowires.

Afterwards, the measurements were conducted in the high-field setup in Tübingen. During this attempt, the SQUIDs behaved like an open circuit, as the V measurement went into overload even without an applied current. This indicates a loss of the superconductive properties of the SQUID device. SEM imaging confirmed the destruction of the SQUIDs as shown in Figure 4.26 b), d) and f). Both SQUID devices show structural damages, no current permeability, and surface alterations. The damage is characteristic for too high currents applied through a Josephson junction of a SQUID. High currents can be caused by equipment malfunction or an electrostatic discharge (ESD) event. ESD events are a common cause to damage sensitive electronics.As the human body can accumulate up to several kV of electrostatic potential due to the triboelectric effect, often experienced as a spark when touching something on ground potential after walking over a carpet, direct and even indirect contact to sensitive devices can be destructive. Connecting a device can also lead to its destruction, if the device and connected equipment have different potentials.

To minimise the likelihood of an ESD in the following measurements, several precautions were implemented. The precautions can be divided in handling of the devices, measurement setup improvements and the procedure for connecting the devices to the dipstick or measuring devices. The device was only handled with an antistatic wristband attached, to prevent the build-up of electrostatic potential.

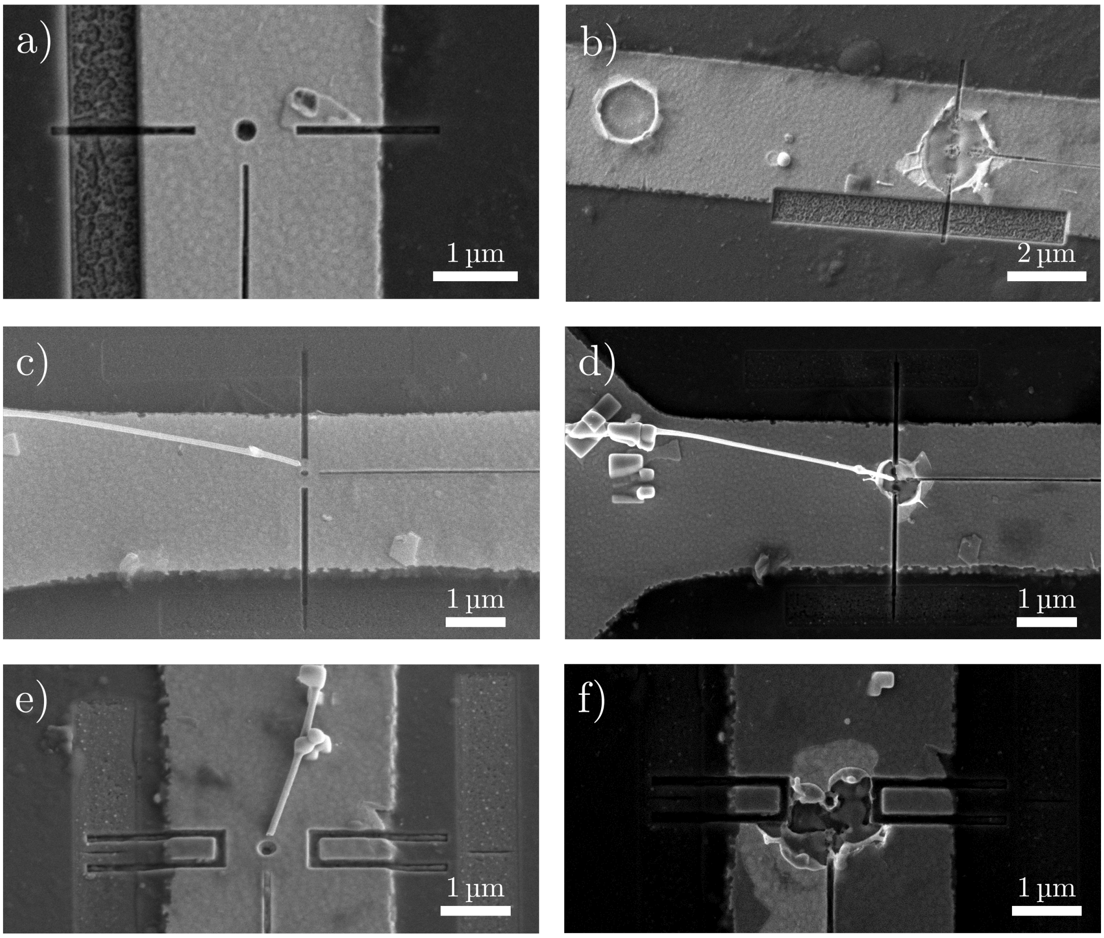

Figure 4.26.: SEM images of SQUIDs from the first run of measurements. (a) SQUID CNT-6 before the placement of a Fe nanowire. (b) SQUID CNT-6 after an electrical discharge that occurred during the attempted placement of a Fe nanowire. (c) and (e) show the SQUID devices CNT-2 and CNT-3, respectively, with Fe nanowires successfully placed on top. (d) and (f) depict the same SQUIDs after being destroyed, likely due to an ESD incident. In (f), the Fe nanowire is no longer positioned on the SQUID. SEM images (c)-(f) were taken at a tilt angle.

Additionally the sample was only touched with rubber gloves to avoid unintentional contact with wires, especially after the devices were bonded to the sample holder.

The entire highfield measurement setup was re-grounded by stripping all grounds and rechecking for residual ground connections to avoid ground loops.[2] New grounds were then connected in a star-like manner, enabling an improved connection and ensuring the cryostat and dipstick setups were continuously connected with a clamp to avoid potential differences. The clamps can be disconnected, once the dipstick is mounted on the cryostat, to avoid ground loops.

Furthermore, the 300 mK dipstick has a custom made connector box that can cause problems during the connecting and measuring of the devices. The connector box works as an adapter between the outlet of the dipstick and the `Magnicon` electronic. However, the electrical lines are not directly connected between the plugs, since the electric lines are connected to a switch. The switch optionally connects different electric lines of the dipstick to the channel 1 of the `Magnicon` electronic. Therefore, during the connecting of the chip only one SQUID is connected and grounded through the `Magnicon` electronic. In addition, great care has been taken during the measurement to ensure that no currents flow in the electronics when switching to another SQUID. To minimise this potential risk of failure and avoid switching during measurements, new plugs were build in. The improved connector box should directly connect the electric lines of the dipstick to the electric lines of the `Magnicon` electronic. This improvement ensures that the system remains connected throughout the connecting of the device and the measurement process.

Based on the recommendations of Martínez-Pérez, the following precautions were implemented. During the connection of the devices to the dipstick, grounding was ensured between the dipstick and the cryostat. An important step is to connect the `Magnicon` electronics to the dipstick without a power source. This precaution was necessary, because the `Magnicon` electronics connects the electric lines, connected to the device, to ground with high resistance in the MΩ range.

With these precautions the second attempt to measure the Fe nanowires was successful.

---

[2] The re-grounding was performed by Robin Hutt

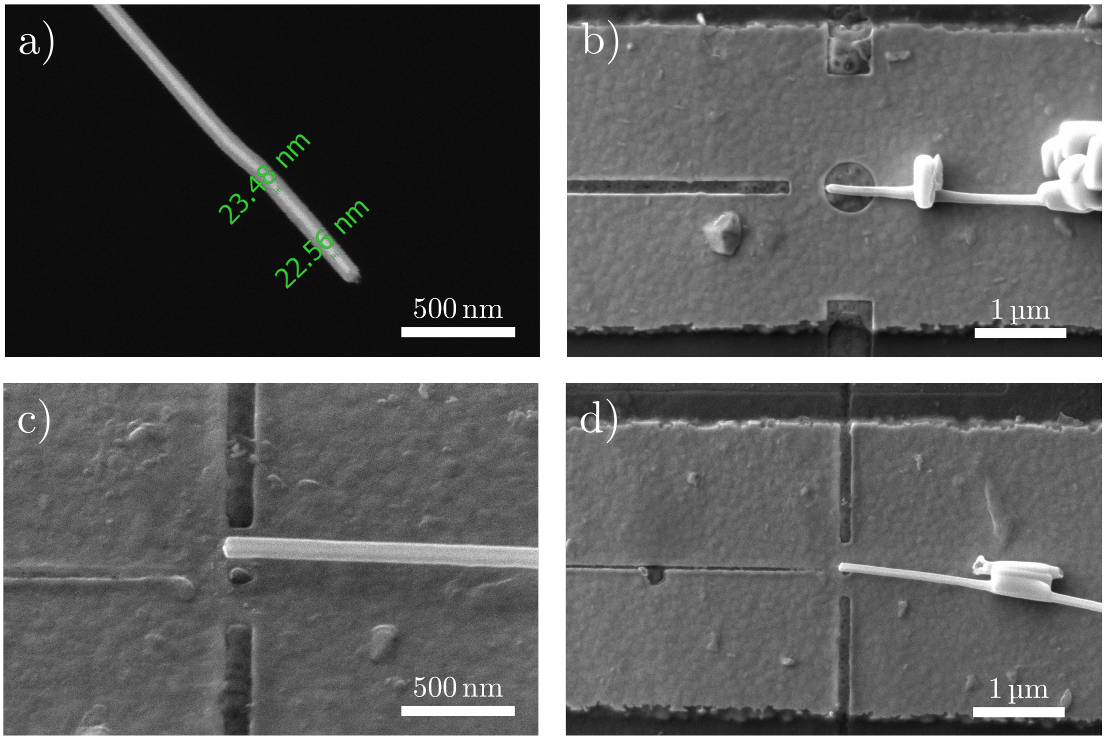

Figure 4.27.: SEM images of (a) Fe nanowire that has been placed on top of SQUID CNT-4, (b) SQUID CNT-4 with a Fe nanowire, (c) SQUID CNT-1 close up at an angle of 35° and (d) SQUID CNT-1 overview. In (a) and (c) the nanowire can be seen inside of the CNT.

4.3.2. Fe nanowire measurements at 4 K

This section presents measurements in the highfield setup at 4 K, including a re-characterisation of the SQUID devices, and SQUID measurement with different B sweeps. Details about the measurement procedure and setup are described in Chapter 3.1.6. For the second run of the experiments SQUID CNT-1 and SQUID CNT-4 were fabricated and pre-characterised. A detailed pre-characterisation can be seen in Chapter 4.1.3. At the time of the pre-characterisation SQUID CNT-1 showed an $I_c = 100\,\mu$A and, SQUID CNT-4 showed an $I_c = 250\,\mu$A. These relatively high I_cs are good preconditions for measurements at high temperatures, since I_c decreases with increasing temperatures. It should be noted, that in the pre-characterisation V of SQUID CNT-1 jumps at several points if $I_{\mathrm{mod}} > 1\,$mA, indicating problems with the modulation line of the SQUID device.

The placement of the Fe nanowires was performed by Thomas Wiek at the IFW Dresden, as seen in Figure 4.27. This time all the precautions described in section 4.3.1 were applied and both SQUID devices were measured in the highfield setup.

Characterisation measurements in the highfield setup

Both SQUIDs were re-characterised. It is important to fully characterise the SQUID devices with Fe nanowires in the measurement setup, to verify that the placement of the Fe nanowires did not change the characteristics of the SQUID. To measure a current-voltage-characteristic (IVC) the generator of the `Magnicon` electronic is used to modulate I. V vs I_{mod} can be measured by applying an external V to the external feed line of the `Magnicon` electronic. The feed line translates into an external Flux at normal amplification mode and is coupled to a variable R in the `Magnicon` electronic. In this case $2\,\mathrm{k}\Omega$ were used, resulting in approximately $0.5\,\mathrm{mA}$ for $1\,\mathrm{V}$ applied to the modulation line, if the resistance of connecting lines to the SQUID device is neglected. IVC and V vs I_{mod} data were gathered with `GoldExi`[3] as a V measurement over time. The re-characterisation can be seen in Figure 4.28 for SQUID CNT-1 and in Figure 4.29 for SQUID CNT-4. The measured IVC of SQUID CNT-1 has an $I_{\mathrm{c}} = 72\,\mu\mathrm{A}$, and SQUID CNT-4 has an $I_{\mathrm{c}} = 82\,\mu\mathrm{A}$. It should be mentioned, that the IVCs seem to be tilted, however the cause could not be determined. The modulation period for SQUID CNT-1 is $1/M_f = 0.88\,\mathrm{mA}/\Phi_0$ and for SQUID CNT-4 is $1/M_f = 0.41\,\mathrm{mA}/\Phi_0$. The I_{c} values are decreased compared to the pre-characterisation, which can be explained by ageing processes of the SQUID devices. Nevertheless, these characteristics justified further measurements with these SQUID devices. In the future, the characterisation of SQUIDs in the highfield setup could be improved by modulating the SQUID with an external field perpendicular to the loop by a vector magnet of the setup and a configuration of the `Magnicon` electronic that allows to measure negative I_{bias} as well. This could help to determine if the SQUIDs have trapped flux.

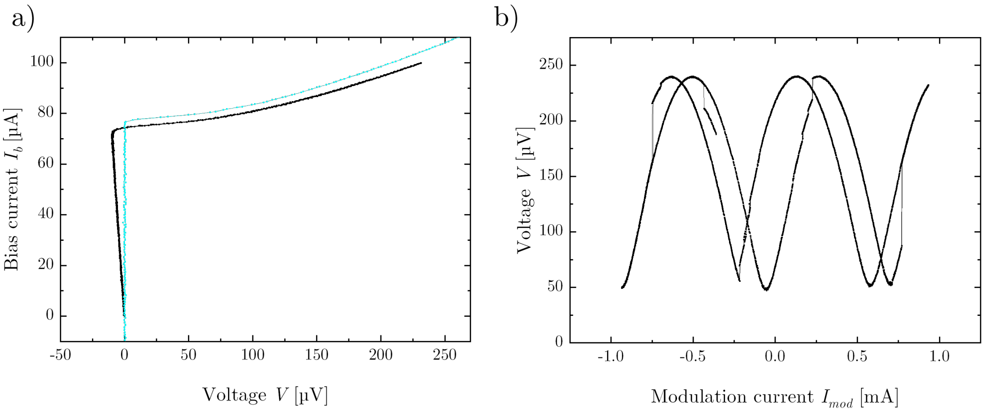

Figure 4.28.: Characteristics after Fe nanowire placement on SQUID CNT-1 at 4.2 K. (a) IVC of SQUID CNT-1. The black curve was measured inside of the high-field cryostat with a Fe nanowire and in comparison the blue curve before the placement of the Fe nanowire. The critical current of black curve was found to be here $I_{\mathrm{c}} = 72\,\mu\mathrm{A}$. (b) V vs I_{mod} with a modulation period of $1/M_f = 0.88\,\mathrm{mA}/\Phi_0$.

---

[3] Program written by Edward Goldobin. Further details are available at `https://www.geocities.ws/goldexi/links.htm` [Accessed 06.04.2025]

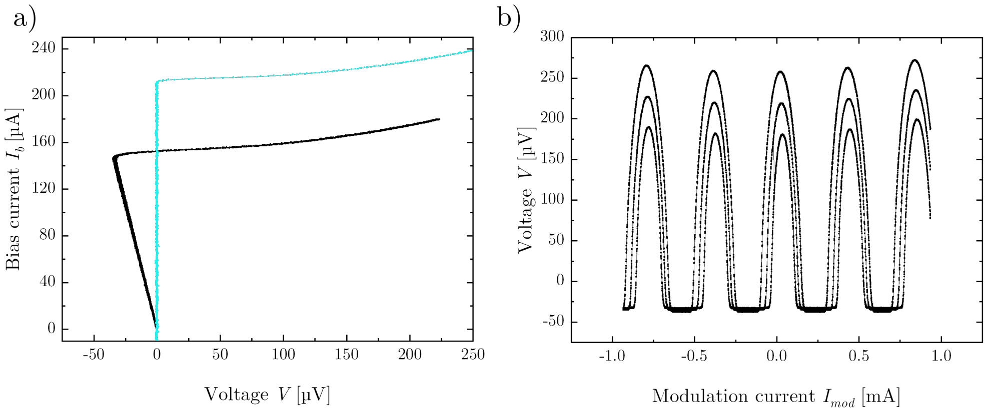

Figure 4.29.: Characteristics after Fe nanowire placement on SQUID CNT-4 at 4.2 K. (a) IVC of SQUID CNT-4. The black curve was measured inside of the high-field cryostat with a Fe nanowire and in comparison the blue curve before the placement of the Fe nanowire. The critical current of black curve was found to be here $I_c = 82\,\mu$A. (b) V vs I_{mod} with a modulation period of $1/M_f = 0.41\,\mathrm{mA}/\Phi_0$.

Field sweeps

The expected switching field of the Fe nanowires is approximately ±200 mT.[24] Therefore, both SQUIDs were measured while applying fields up to 240 mT parallel to the Fe nanowire. Figure 4.30 shows the open loop and FLL response of V versus B of SQUID CNT-1. Due to a small misalignment of the the SQUID loop in respect to the external field, the field has a small out-of-plane component. The sweep of ±90 mT results in ±1 full oscillation of V, with one oscillation corresponding to one Φ_0 of flux coupled into the SQUID. This out-of-plane field caused by the misalignment results in two issues. The first issue is that the currents applied through the modulation line in FLL mode should not exceed a few mA to avoid damaging the SQUID device. In this case $1\,\Phi_0$ with the modulation period of $1/M_f = 0.88\,\mathrm{mA}/\Phi_0$ cause 0.88 mA of compensation current through the modulation line. The second issue is that the out-of-plane field gets added or subtracted from the signal of the Fe nanowire, making it difficult to distinguish the signal of the nanowire and the out-of-plane field. At the time of the measurement, the loop was aligned to the field, utilising the limited means being accessible. A recommendation for future measurements would be to measure with compensation coils to allow better alignment of the direction of B in the plane of the SQUID loop. In the I_{mod} vs B curves in FLL mode several signal jumps are measured, even though the open loop curves measure no jumps in the same region. These jumps correspond to the jumps seen in the pre-characterisation in I_c vs I_{mod} (see Figure 4.11). Since these signal jumps do not carry information about the Fe nanowires, measurements in FLL mode were considered not reasonably applicable. Figure 4.31 shows the open loop signal at B sweeps of 240 mT and 500 mT. The two distinct jumps at −193 mT and 197 mT could correspond to a magnetisation reversal of the Fe nanowire. Therefore, similar measurements at various T with SQUID CNT-1 were conducted.

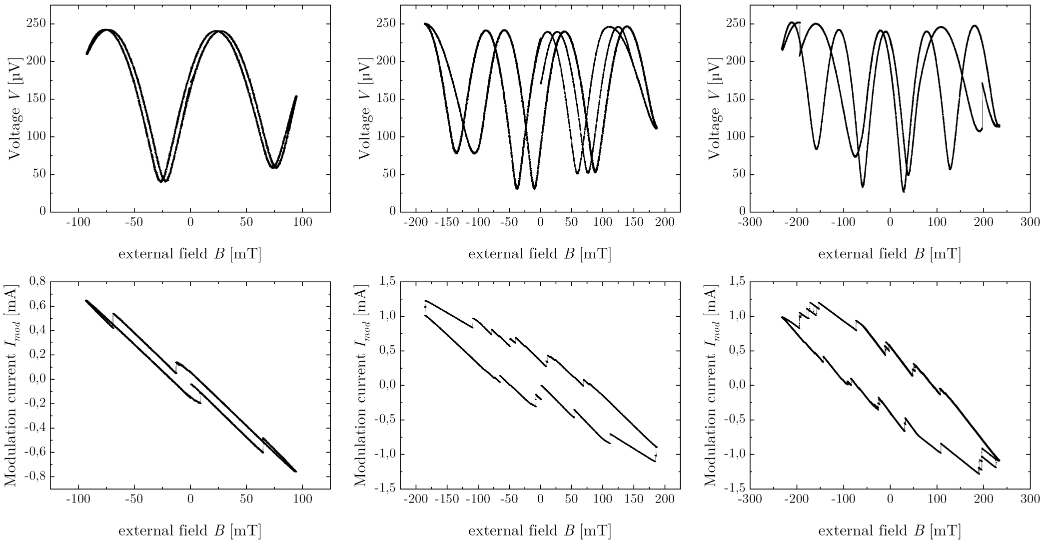

Figure 4.30.: Field sweep measurements with SQUID CNT-1 with an Fe nanowire at 4.2 K and B field parallel to the nanowire. The top row represents open-loop measurements, while the bottom row depicts FLL measurements of SQUID CNT-1 with field sweeps of 95, 187 and 234 mT, respectively.

Figure 4.32 shows the open loop response of V versus B of SQUID CNT-4. The sweep of ±90 mT results in ±4 full oscillations of V. Each oscillation corresponds to one Φ_0 flux coupled into the SQUID loop. This out-of-plane field field leads to the same issues with FLL mode and signal distortion as observed with SQUID CNT-1. The difficulties of SQUID CNT-4 arising from misalignment in FLL mode are even higher, since $4\,\Phi_0$ and the modulation period of $1/M_f = 0.41\,\mathrm{mA}/\Phi_0$ need 1.64 mA of compensation current through the modulation line. Another observation seen in Figure 4.32 a) is that B suppresses I_c significantly, leading to three undesired side effects. The signal will be weak in the region of the expected switching field. The suppressed I_c might also reduce the capability of the SQUID device to measure at high T, since the increase of T also suppresses I_c. Since the working point of the FLL gets shifted, the signal of the FLL becomes nonlinear, difficult to interpret, and sometimes the `Magnicon` electronic looses the working point. To ensure reliable measurements with SQUID CNT-4 it is suggested to reduce the width of the Josephson junctions with the Ne-FIB or Ga-FIB to decrease the suppression of I_c.

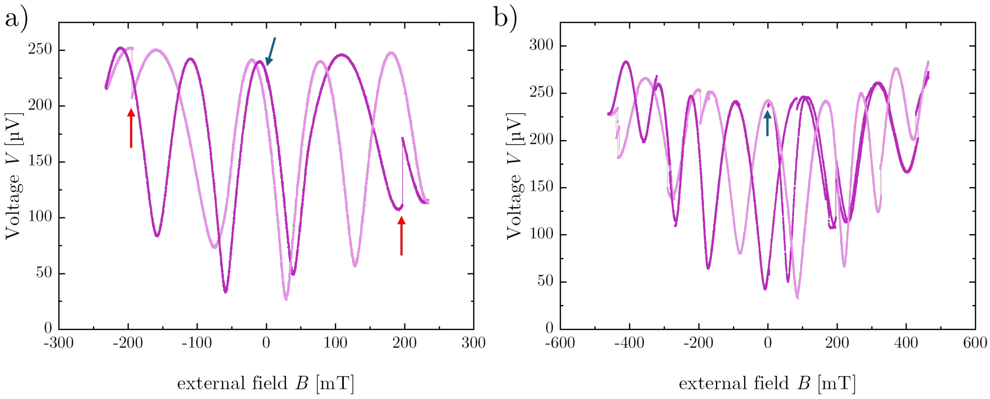

Figure 4.31.: Open loop measurements of SQUID CNT-1 with an Fe nanowire at 4.2 K and B field parallel to the nanowire. Field sweeps of (a) 234 mT and (b) 462 mT. The start of the measurement is indicated by a blue arrow, field sweeps in the positive field direction are shown in a darker shade, while sweeps in the negative field direction are depicted in a lighter shade. The field was swept twice in both measurements. In (a), two distinct jumps in the voltage are visible, indicated by red arrows, while in (b), several jumps can be seen.

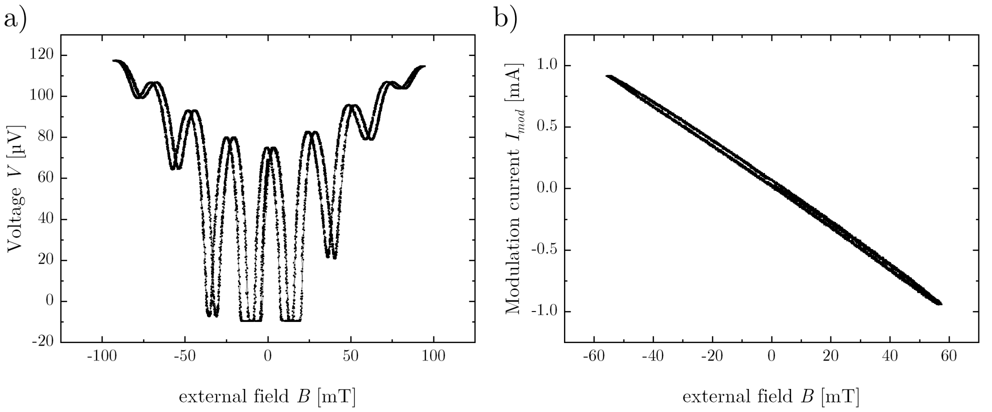

Figure 4.32.: Field sweep measurements with SQUID CNT-4 at 4.2 K and B field parallel to the nanowire. (a) The open-loop measurement of the voltage during an external field sweep of ±93 mT demonstrates an increase in voltage with increasing field, indicating a significant suppression of I_c. (b) The FLL measurements of SQUID CNT-4, depicting the modulation current during an external field sweep of ±55 mT.

4.3.3. Investigation of the temperature dependence of the switching field

This section presents electric transport measurements at various temperatures and shows the temperature dependence of the switching fields of a Fe nanowire. All measurements of this section were performed by SQUID CNT-1. Open loop measurements were performed for the temperatures $T = 31, 21, 12, 7.5$ and $4\,\mathrm{K}$.

Figure 4.33 shows the main result of the open loop field sweeps at different temperatures. Three observations were made: As expected, the flux coupled into the SQUID leads to a modulation of the voltage across the SQUID. This flux is most likely caused by a misalignment between the magnetic field direction and the SQUID leading to a field component perpendicular to the chip surface. At external fields of $\approx 200\,\mathrm{mT}$, all curves show a clear jump in the voltage. This voltage jump is attributed to a switching of the magnetic domains in the Fe nanowire. It can also be seen that the modulation of the voltage caused by the external field depends on both the temperature and the changes prior to a switching event. The change in periodicity at different T can be attributed to the same changes as in Figure 4.22. Even though, the underlying mechanism for the change in periodicity prior to the switching event is not fully understood. Visible kinks in the periodicity curve could be observed. Such kinks become evident for $4\,\mathrm{K}$ at $\sim 60\,\mathrm{mT}$, for $7.5\,\mathrm{K}$ at $\sim 45\,\mathrm{mT}$ and at higher T the kink is closer to zero external field before the switching event.

Figure 4.34 shows the temperature dependence of the switching fields extracted from the field sweep measurements. The temperature dependence of the switching field indicates a thermally activated process over an energy barrier, which is well-described by the Kurkijärvi model. The model is described in Chapter 2.5 with the equation 2.5.6 which is repeated below for clarity.

$$H_{sw} = H_{sw}^0 \left\{ 1 - \left[\frac{k_B T}{U_0} \ln \frac{k_B T H_{sw}^0}{\alpha \tau_0 U_0 v \left(1 - \frac{H_{sw}}{H_{sw}^0}\right)} \right]^{1/\alpha} \right\} \tag{4.3.1}$$

Given that the external field is applied approximately parallel to the axis of the wire and the diameter is $> 24\,\mathrm{nm}$, it can be assumed that the switching mechanism is curling mode, and that the parameter α can be taken to be 2. The remaining parameters are $k_B = 1.38 \times 10^{-23}\,\mathrm{J/K}$, $\tau_0 = 1 \times 10^{-10}\,\mathrm{s}$, $v = 1\,\mathrm{mT/s}$. The fit results in an energy barrier of $U_0 = 8.5 \times 10^{-18}\,\mathrm{J} = 53\,\mathrm{eV}$ and switching field $H_{sw}^0 = 197.1\,\mathrm{mT}$. According to Thomas Mühl this energy barrier is in the same order of magnitude as the energy that is theoretically needed to insert a domain wall into the Fe nanowire. Therefore, the calculation of the energy barrier measured for this thesis is an interesting experimental result. However, the connection of the energy of a domain wall and the energy barrier deserves further theoretical investigation.

In open loop measurements the $V(\Phi)$ follows a nonlinear relation. One approach is the fit of the flux-voltage relation with an appropriate model and extract the amount of flux coupled into the SQUID. However, this can be arbitrarily complicated and the suppression of I_c with increasing B makes an accurate fit increasingly difficult.

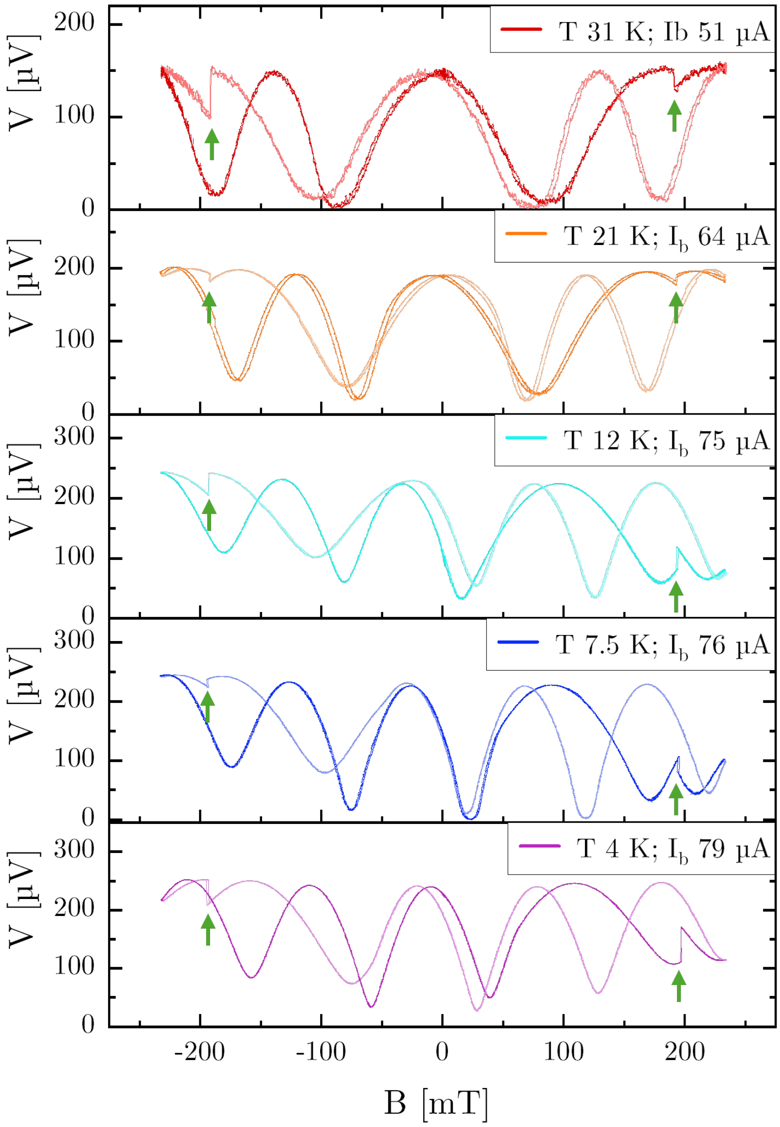

Figure 4.33.: Open-loop measurements of SQUID CNT-1 with an Fe nanowire at various T and B field parallel to the nanowire. Measurements were conducted with field sweeps of $B = \pm 233\,\mathrm{mT}$ and $T = 31, 21, 12, 7.5$, and $4\,\mathrm{K}$. Field sweeps in the positive field direction are shown in a darker shade, while sweeps in the negative field direction are depicted in a lighter shade. The occurrence of a jumps in V at approximately $B = \pm 195\,\mathrm{mT}$, marked by green arrows, suggests a sudden flux change in the SQUID loop, indicating a switching of the particle. The values of the fields are depicted in Figure 4.34. The modulation of the voltage oscillation during the sweep is caused by a small misalignment of the external field out of the SQUID loop plane.

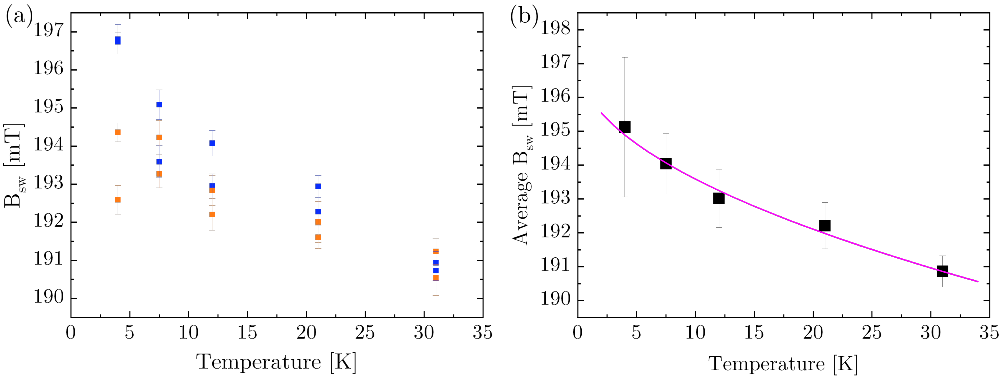

Figure 4.34.: Magnetic switching fields B_{SW} of the Fe nanowire vs T. (a) shows all values for the switching fields depicted in Figure 4.33. Switching events depicted with blue points correspond to positive field values and orange to negative field values. To reduce the influence of the noise of the external field, the mean of the five field values before the jump is taken, the standard deviation is shown as an error bar. (b) shows the average of the absolute difference of the switching field as a function of temperature. The pink line is a fit according to the Kurkijärvi model that describes a thermal process with an energy barrier.

Furthermore, it is not possible to say exactly in which direction flux is coupled in and whether one or more flux quanta have been coupled in. Nevertheless, an attempt was made to provide an initial estimate of the flux that can be seen in Figure 4.35. In this case the misalignment of the SQUID towards the external field is used, to attribute a difference of the external field to one flux quantum 1 Φ_0 that is coupled into the SQUID. If the misalignment couples linearly into the SQUID, the readout of the signals measured is also linear. Due to the variance in the periodicity $\mathrm{d}B$ equal to 1 Φ_0 has a relatively large error bar. To interpret a flux signal, the voltage after the jump can be compared with the preceding curve. Here, the suppression of I_c must be taken into account by comparing minima or maxima in the vicinity and adding the respective suppression of the voltage to the voltage at the jump. Now the distance of the external field at the voltage before and after the jump can be determined. To calculate the amount of flux in units of Φ_0 coupled into the SQUID, $\mathrm{d}B$ (green arrow) was divided by the field B needed to couple in 1 Φ_0 (blue distance). The large error bars prevents an exact statement about the signal of the Fe nanowire.

Nevertheless, Thomas Mühl provided the following estimate of the saturation magnetisation of the Fe nanowire, and subsequently calculated the expected flux coupled into the SQUID. The magnetic stray field of a Fe nanowire in a single-domain configuration in the vicinity of one of the nanowire poles at a distance of r to this pole can be approximated by a radial monopole field, $|\mathbf{B}| = \frac{\mu_0 q}{4\pi r^2}$, where the magnetic monopole moment q is used. In the case of a 23 nm diameter single domain Fe nanowire and assuming a single domain magnetisation along the nanowire axis with a bulk-like Fe magnetisation of 1710 kA/m, the monopole moment is $q = 7.1 \times 10^{-10}$ Am. The analysis of SEM images taken at different tilt angles revealed a height of the magnetic pole above the center plane of the SQUID of 224 nm. Integrating the z-component of the magnetic monopole stray field over the effective SQUID area (1.33 $\mu\mathrm{m}^2$) results in a magnetic flux of $3 \times 10^{-16}\,\mathrm{Wb} = 0.145\,\Phi_0$. The flux change associated with a complete Fe nanowire magnetisation reversal is twice as large, i.e. $0.29\,\Phi_0$. This estimation agrees well to the experimental magnetic flux change associated with the voltage jumps (Figure 4.35) supporting the interpretation that these jumps are caused by Fe nanowire magnetisation switching.

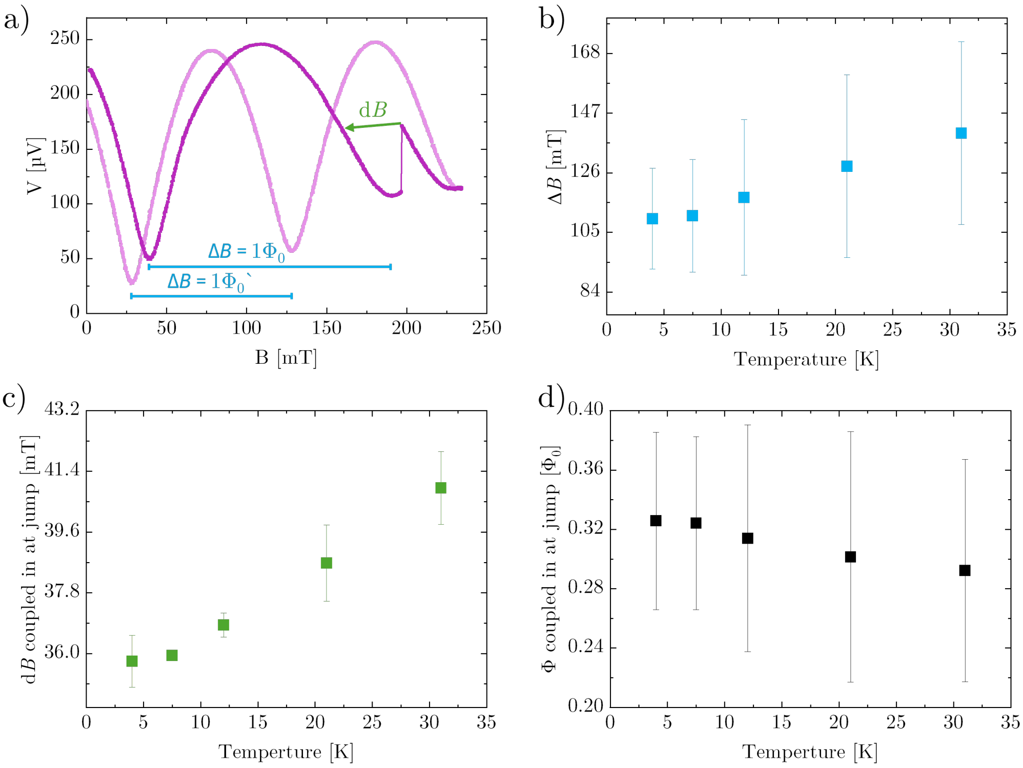

Figure 4.35.: Temperature dependence of the flux coupled into the SQUID at the point of switching of the nanowire. (a) The open-loop measurement at 4 K. The external field ΔB necessary to couple in one flux quantum 1 Φ_0 due to misalignment is illustrated by the blue intervals. The green arrow indicated the field change dB at the jump. (b) ΔB vs T. (c) dB vs T. (d) T dependence of the flux coupled into the SQUID at the jump ($dB/\Delta B$).

4.3.4. Discussion and Outlook

After optimising the measurement procedure, it was possible to successfully measure Fe nanowires for temperatures $T = 31, 21, 12, 7.5$, and 4 K. The temperature dependence of the switching behavior of the Fe nanowire appears to follow Kurkijärvi's model. Additionally, the switching events and the measured curves show a high degree of consistency across the different temperatures and during two measurement cycles. Thomas Mühls' estimate for the saturation magnetisation also aligns well with our data. As a result, alternative explanations for the voltage jump, such as trapped flux, are less likely, reinforcing the interpretation that the voltage jumps are indeed caused by the switching of the Fe nanowires.

To validate the hypothesis that the energy of a domain wall is connected to the energy calculated by the thermally activated process observed in the temperature dependence of the switching event, it would be valuable to measure Fe nanowires with various diameters. In Fe nanowires, different types of domain walls can emerge depending on the nanowire's diameter. By combining simulations of the various domain wall types with temperature-dependent measurements, it would be possible to experimentally validate the energies associated with these domain walls and correlate them to the different diameters of the Fe nanowires. If the simulations and measurements yield consistent energy values across various diameters, this would strongly suggest a connection between the two. Moreover, the conclusion that different diameters give rise to specific domain walls would be experimentally verified.

To draw reliable conclusions, the measurements need to be repeated. Several improvements are proposed to further increase the accuracy and quality of the experiments. In general, the geometric dimensions of the Josephson Junctions of the SQUIDs should be small enough to avoid interference from the magnetic field (both in width and height), while large enough to ensure that the critical current I_c is sufficient for measurements at higher temperatures. Depending on the quality of the junctions before nano-patterning, the final I_c should not be $\geq 70\,\mu\mathrm{A}$ and for a layer thickness of 80 nm the width of each junction should be $\leq 500\,\mathrm{nm}$.

FLL measurements can provide a more accurate insight into the saturation magnetisation. To achieve this, the modulation line of SQUID CNT-1 should be re-cut to avoid potential short circuits. In addition, the bridge-width in SQUID CNT-4 should be narrowed to reduce the influence of external magnetic fields and to ensure reliable measurements in FLL mode.

The temperature range can also be extended by increasing the isolation vacuum between the measurement chamber and the sample. In addition, the use of new measurement software such as `Terra3`[4] will automate field sweeps and enable measurements such as $I_\mathrm{c}(H)$. The use of compensation coils and the program `vectorramp`[5] can also be used to compensate for any misalignment during the experiments.

---

[4] Program written by Simon Koch, ideal to measure IV families, extended by Jan Ullmann to make it communicate with the high-field magnet

[5] Program written by Carsten Spanheimer, details in his Bachelor thesis[65]

4.4. EuS Nanodiscs: Comparison of Simulation and Measurement

As described in Chapter 2.5 Europium sulfide (EuS) is an especially promising material for integration with superconductors in hybrid devices because it simultaneously enables two essential functionalities at cryogenic temperatures: spin splitting of the superconducting density of states (via the magnetic proximity effect) and spin filtering of tunneling electrons.[57]–[61] This makes it a crucial component in creating non-reciprocal superconducting electronics such as tunnel diodes and thermoelectric detectors. These properties make it particularly suitable for superconducting spintronic applications at zero external field.

The goal is to fabricate EuS nanodiscs with stable magnetic vortex states, which can be coupled to superconducting resonators. To explore the suitability of such nanodiscs for future hybrid quantum devices, it is essential to compare their magnetic behaviour to theoretical expectations. This enables a deeper understanding of both the nanofabrication limits and the intrinsic physical properties of the resulting structures.

In this study, EuS nanodiscs with varying diameters were patterned using FIB techniques and positioned on YBCO SQUIDs. The magnetic response of each nanodisc was investigated by sweeping an external magnetic field parallel to the substrate surface, while monitoring the coupled flux signal through the SQUID. Measurements were performed over a wide temperature range, from 15 mK to 20 K, and compared to micromagnetic simulations carried out using `mumax`^{3}.

From the flux-versus-field measurements, key temperature-dependent properties—such as the saturation magnetisation—were extracted. At low temperatures, distinct hysteretic features emerged, consistent with the formation of magnetic vortex states in the EuS nanodiscs. The overall shape and temperature evolution of the measured curves are in good agreement with the simulation results.

For these experiments, a YBCO thin film (Bi_STO_22_1) was initially patterned into twelve microbridges. Subsequent SQUID fabrication was carried out by the group of María José Martínez-Pérez, including pre-characterisation and nanopatterning of the junctions. A EuS thin film was grown on a Si_3N_4 membrane by collaborators from the Materials Physics Center in San Sebastián. The nanodiscs were fabricated and precisely placed on the SQUIDs by Isabel Rivas and Carolina del Río, as detailed in Chapter 3.2.2. Final device integration and measurements were conducted in a dilution refrigerator, described in Chapter 3.1.6, with support from María José (Pepa) Martínez-Pérez, David García Pons, Alex Francisco Estupiñán López, and Jorge Pérez Bailón.

Figure 4.36(a) presents an SEM image of a SQUID with an aligned EuS nanodisc. The nanodisc is positioned on a thin Si_3N_4 membrane suspended above the SQUID. Owing to the membrane's thinness, the underlying SQUID structure remains partially visible in the SEM. Figure 4.36 b) illustrates the measurement configuration schematically. Figure 4.36 c) shows a cross-sectional diagram of the SQUID and EuS nanodisc. Magnetic flux lines, generated by magnetisation aligned along the y-axis, are partially closed through the SQUID loop, resulting in a measurable signal.

This chapter is organised as follows:

- Section 4.4.1 provides a brief summary of the SQUID characterisation results from Chapter 4.1.4.
- Section 4.4.2 presents micromagnetic simulations in `mumax`^{3} of the nanodisc magnetisation and coupling.
- Section 4.4.3 describes the temperature-dependent measurements and discusses the extraction of magnetic properties.
- Section 4.4.4 compares experimental data with simulations and outlines implications for nanodisc fabrication and future studies.

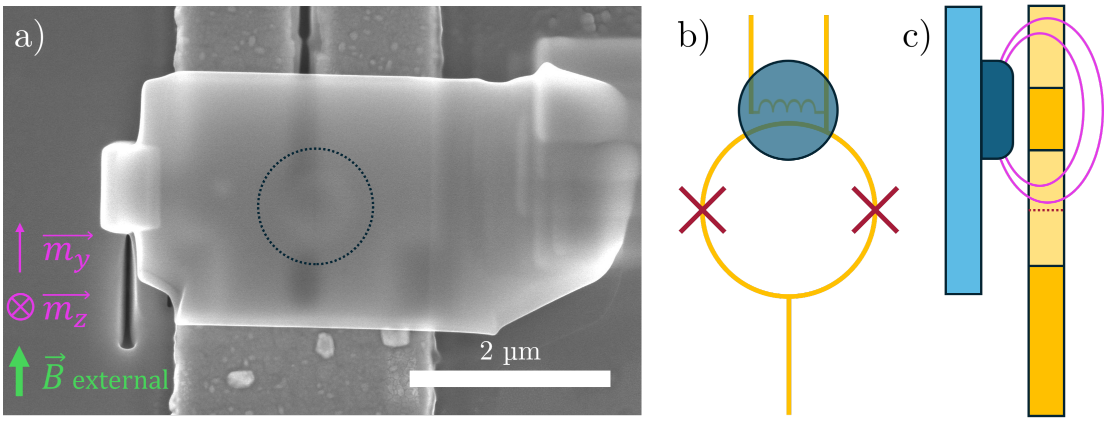

Figure 4.36.: Overview of a EuS nanodisc placed on a SQUID. (a) SEM image of a SQUID with a placed EuS nanodisc. The disc is located on a Si_3N_4 membrane and is highlighted by a dotted circle. The orientation of the external field B is shown in green, while the in-plane magnetisation direction (m_y), used in simulations, is indicated in magenta. (b) Schematic diagram of the measurement configuration. (c) Cross-section through the SQUID and EuS nanodisc. The SQUID is shown in gold, with the grain boundary Josephson junction represented by a red dashed line. The EuS nanodisc (dark blue) and Si_3N_4 membrane (light blue) are suspended above the SQUID loop. Magnetic flux lines (magenta), arising from m_y magnetisation, couple into the SQUID loop.

4.4.1. Overview of the Characteristics of the Measured Samples

The detailed characterisation of the SQUIDs used for the EuS nanodisc measurements is presented in Chapter 4.1.4. This section provides a brief summary of the key findings relevant for the analysis presented in this chapter.

An overview from the main SQUID parameters is provided in Table 4.5. All devices were fabricated on the same thin film, Bi_STO_22_1, with a critical temperature of $T_c = 89\,\mathrm{K}$, a YBCO thickness of 90 nm, and a gold capping layer of 60 nm. The SQUIDs were patterned using FIB milling to have identical geometries, including a SQUID hole of $500 \times 300\,\mathrm{nm}$ and Josephson junction widths of 600 nm. Due to the placed EuS nanodiscs, the values of the effective area A_{eff} are subject to some uncertainty, as the magnetic permeability of the discs alters the external field distribution.

The characterisation of the individual SQUIDs yielded the following observations:

- **SQUID EuS-05** shows generally suitable performance for particle measurements; however, trapped flux near the SQUID may distort the measurement signal.
- **SQUID EuS-10** exhibits good SQUID characteristics, although a notable tilt in the V versus I_{mod} curve is observed. The origin of this tilt remains unclear, and its influence on FLL-mode measurements could not be fully assessed.
- **SQUID EuS-11** has a relatively low I_c and multiple I_c transitions. To minimise measurement errors, it must be operated at relatively high I_{bias} currents to avoid false signals by transitions. Possible presence of trapped flux.
- **SQUID EuS-12** demonstrates good SQUID characteristics but, similar to EuS-10, exhibits tilted V vs. I_{mod} and V vs. B curves.

Table 4.5.: Characteristics of the SQUIDs used for EuS nanodisc measurements. All SQUIDs were patterned with identical dimensions and fabricated on the same YBCO/Au film (Bi_STO_22_1). Values for the effective area A_{eff} are affected by the presence of the EuS nanodiscs, which modify the field distribution due to their magnetic permeability. *IVCs were measured at zero external field; thus, precise values for $I_{\text{c,max}}$ and $I_{\text{c,min}}$ could not be determined.

SQUID	$I_{\text{c,max}}$ [µA]	$I_{\text{c,min}}$ [µA]	R_n [Ω]	I_cR [µV]	M_f [Φ_0/mA]	A_{eff} [µm^2]	r_{eff} [µm]	V_Φ [mV/Φ_0]
EuS-05	138	66	2.4	325	1.0	1.1	0.59	-0.6
EuS-10	378	287	3.6	1359	1.0	2.3	0.86	-1.3
EuS-11	45*	*	7.0	315	2.8	2.2	0.84	2.3
EuS-12	257*	*	4.3	1117	0.9	3.3	1.02	3.0

4.4.2. Simulations

To estimate the expected signal of the EuS nanodiscs in the SQUID measurements, the magnetic response to in-plane magnetic field sweeps was simulated using a micromagnetic simulation program.[6] The simulations were performed with `mumax`^{3}, a GPU-accelerated micromagnetic simulation tool developed by the DyNaMat group at Ghent University. Key references for the simulation framework include Vansteenkiste et al. [88] and Exl et al. [89]. The scripts used in this work are provided in Appendix B.

The primary goal of the simulations is to model how the magnetisation within EuS nanodiscs responds to varying magnetic fields, and how this response couples into the SQUID loop. As the SQUID detects flux changes in the SQUID loop, the key coupling

---

[6] Available at mumax.github.io, accessed on 06.03.2025

mechanism is the increase or decrease of magnetic flux lines through the SQUID loop, particularly those originating from magnetisation components aligned along the y-axis of the nanodisc. This coupling geometry is discussed schematically in Figure 4.36(c).

General Simulation Parameters

The following guidelines were used to ensure the stability and physical accuracy of the simulations:

- The total number of simulation cells should ideally be a power of two (e.g. 64, 128, 256, ...), optimising performance on the GPU.
- The cell size must be smaller than 0.75 times the exchange length l_{ex} to resolve magnetic domain structures and interactions accurately. If GPU memory is limited, slightly larger cells still yield qualitatively useful results.
- For reference, 16×10^6 cells occupy approximately 2 GB of GPU RAM.
- The parameter `EdgeSmooth = 8` specifies that 8^3 subcells are sampled per cell to better approximate edge volumes, reducing discretisation artifacts near geometric surfaces.
- The initial vortex state was defined using `vortex(1,1)`, which sets the circulation and core polarity.
- The function `relax()` minimises the total energy of a possibly unstable initial configuration but was omitted in this work due to excessive computation times. The vortex configuration was sufficiently close to the ground state.
- Instead, `minimize()` was used during the magnetic field sweeps, as it is computationally more efficient and suited for tracing continuous hysteresis curves.
- Large steps in the applied field can result in longer convergence times or failure to track the local energy minimum accurately.

Material Parameters

The following material parameters were used in the simulations:

- Saturation magnetisation: $M_{\mathrm{sat}} = 1163 \times 10^3\,\mathrm{A\,m^{-1}}$ (from Aguilar-Pujol et al. [50]).
- Landau-Lifshitz damping constant: $\alpha = 0.04$ (derived from the Gilbert damping coefficient used in [50]).
- Exchange stiffness: $A_{\mathrm{ex}} = 0.16 \times 10^{-12}\,\mathrm{J\,m^{-1}}$ (based on Kuz'Min et al. [56]).

From these parameters, the exchange length was calculated using:

$$l_{\mathrm{ex}} = \sqrt{\frac{2A_{\mathrm{ex}}}{\mu_0 M_{\mathrm{sat}}^2}}, \tag{4.4.1}$$

with $\mu_0 = 1.257 \times 10^{-6}\,\mathrm{N\,A^{-2}}$ yields $l_{\mathrm{ex}} \approx 0.43\,\mathrm{nm}$. This implies that the cell size in the simulations should be smaller than 0.32 nm for high-fidelity resolution of magnetic features. Due to limited graphics card resources the here presented simulations were made with cell sizes ranging from $1.56 \times 1.25\,\mathrm{nm}$ to $2.73 \times 1.25\,\mathrm{nm}$.

Simulation Protocol

The EuS nanodiscs were modelled as cylinders with a thickness of 40 nm, matching the EuS film thickness, as grown on the $\mathrm{Si_3N_4}$ membrane. In order to account for possible damage at the disc edges or reduced thickness during fabrication, each structure was also simulated with a reduced thickness of 20 nm. The external field was applied in the disc plane and swept in three stages: initial ramp-up to the maximum field, followed by a ramp-down to the minimum field, and a return to the maximum value. This sweep protocol allowed the observation of hysteretic behaviour, vortex formation, and saturation effects.

The results of these simulations, including visualisations of the magnetisation configurations and corresponding field maps, are discussed in the following subsection.

Response of the Magnetic Vortex to the External Magnetic Field

Figure 4.37 shows the output of a micromagnetic simulation for a EuS nanodisc with a diameter 600 nm, and 40 nm thickness. While smaller discs exhibit a similar domain structure qualitatively, the magnetic field strengths required to reach comparable magnetisation states vary with particle size. A detailed comparison of different disc diameters is presented in Figure 4.38 and 4.39.

The ground state of the EuS nanodisc is a magnetic vortex configuration, where the magnetic domains curl circularly around the centre of the disc. At the core, the domains align perpendicular to the plane, pointing either upwards or downwards, resulting in a small net polarisation along the z-axis. When an external magnetic field is applied parallel to the disc surface, more and more domains begin to align with the field, displacing the vortex towards the edge of the disc.

At an applied field of approximately 50 mT, the vortex reaches a metastable configuration at the disc edge. Beyond a field of around 90 mT, the single vortex splits into two smaller vortices at the upper and lower edges of the disc. At a field of around 100 mT, the majority of magnetic moments are aligned with the external field.

When the magnetic field is reduced again, the system initially remains in the two-vortex configuration. Only below a field of about 50 mT it is energetically favourable for the vortices to recombine into a single central vortex. This switching behaviour leads to a hysteresis in the magnetic response of the nanodisc, which is observable in the reduced magnetisation along the y-axis, m_y.

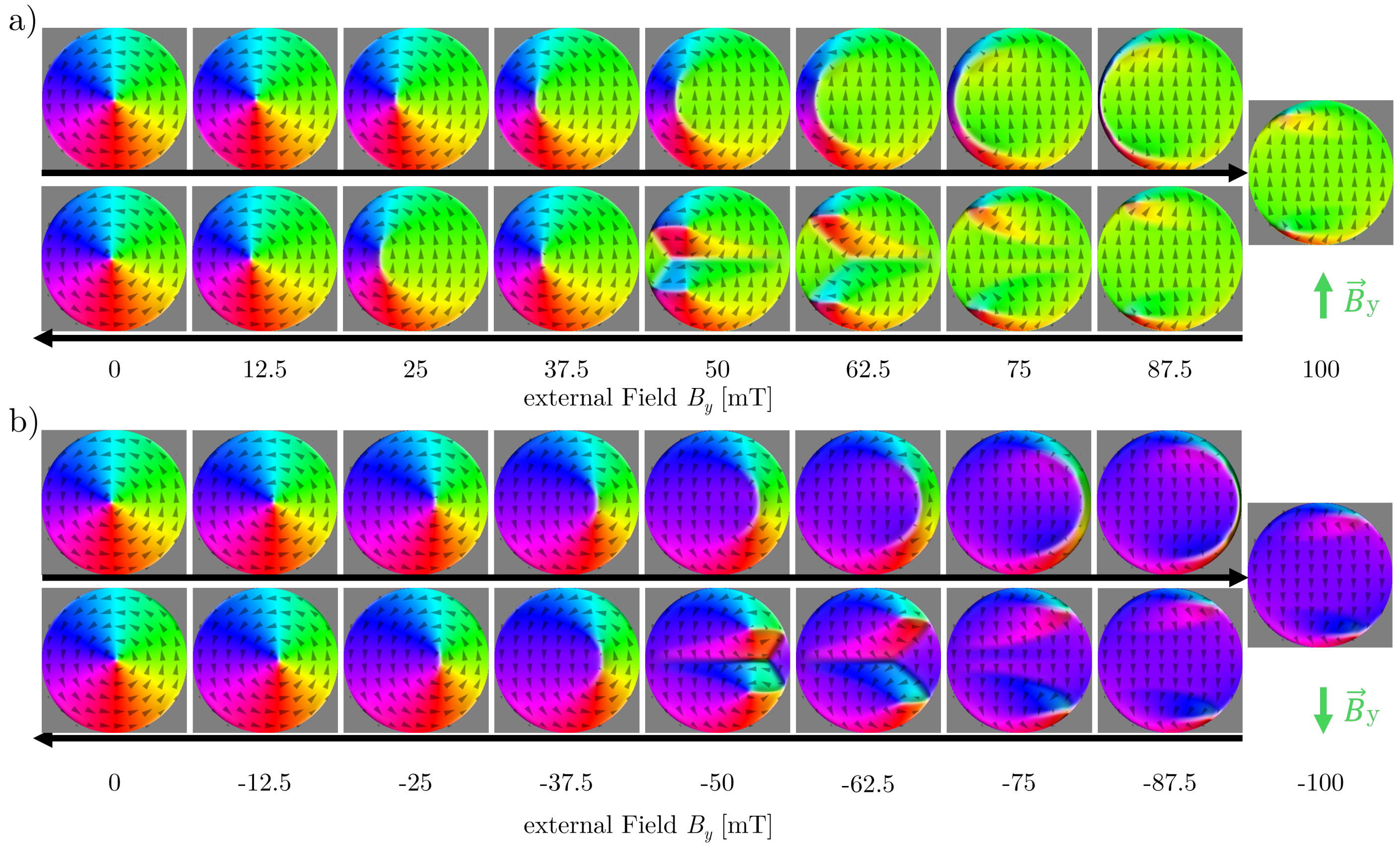

Figure 4.37.: `mumax`^{3} simulations of a 600 nm diameter, 40 nm thick EuS nanodisc during a magnetic field sweep. The domain orientations are indicated by colour and small arrows. The direction of the external field B is shown with a green arrow. Simulations of other nanodisc sizes yield similar pictures.

This hysteresis and the size-dependent vortex dynamics are illustrated in the reduced magnetisation m_y versus external field B_y plots shown in Figures 4.38 and 4.39. All simulated discs exhibit hysteretic behaviour, although the transition fields and saturation values differ significantly. Smaller discs require larger magnetic fields to reach saturation, and the metastable vortex configuration appears less stable. This leads to earlier vortex splitting during the sweep compared to larger discs, resulting in a narrower hysteresis.

For instance, saturation occurs at approximately:

- 200 mT for a 200 nm disc,
- 175 mT for a 260 nm disc,
- 100 mT for a 600 nm disc, and
- 75 mT for a 700 nm disc.

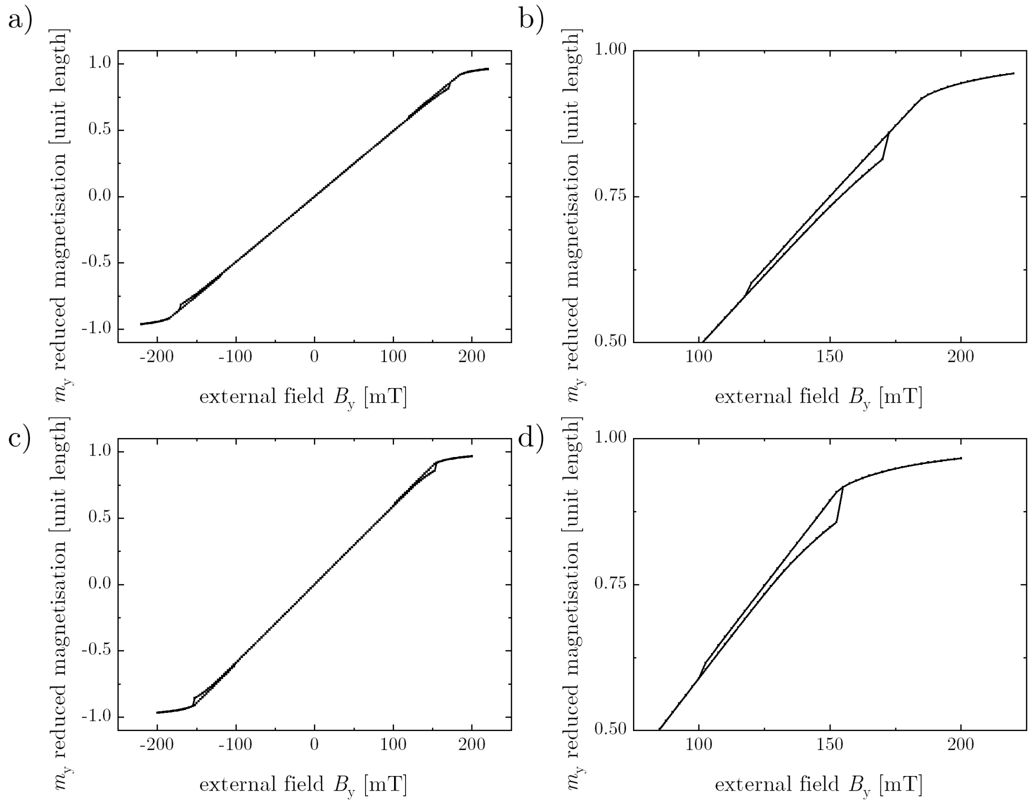

Figure 4.38.: Reduced magnetisation in the y-direction, m_y, versus external field B_y. (a) Simulation for a 200 nm disc. (b) Zoom into the hysteresis region. Saturation occurs around 200 mT. (c) Simulation for a 260 nm disc. (d) Zoom into the hysteresis region. Saturation occurs around 175 mT.

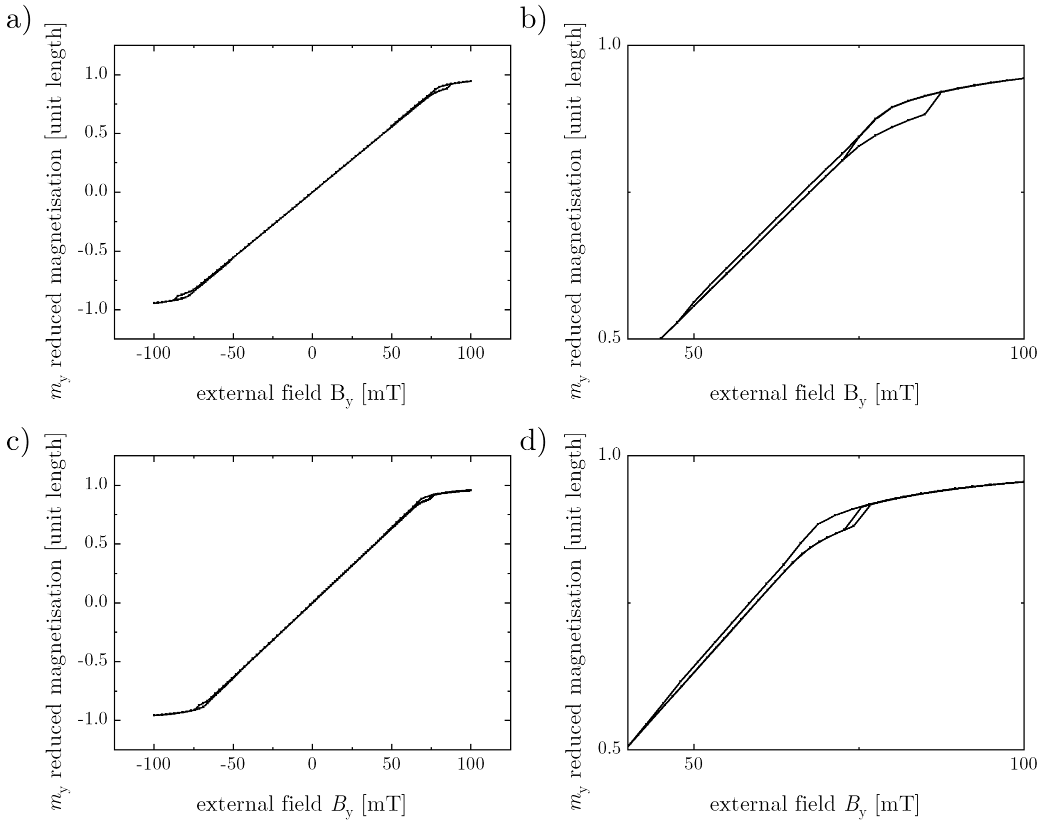

Figure 4.39.: Reduced magnetisation in the y-direction, m_y, versus external field B_y. (a) Simulation for a 600 nm disc. (b) Zoom into the hysteresis region. Saturation occurs around 100 mT. (c) Simulation for a 700 nm disc. (d) Zoom into the hysteresis region. Saturation occurs around 90 mT.

In addition to m_y, the out-of-plane magnetisation m_z was also analysed, as shown in Figure 4.40. This component mainly reflects the vortex core polarisation. However, the magnitude of m_z is approximately three orders of magnitude smaller than m_y, making its contribution to the overall SQUID signal negligible. Interestingly, smaller discs exhibit slightly higher m_z components and exhibit a symmetric response to the external field, while the larger disc appears to transition between different metastable polarised vortex states. A detailed simulation of how different regions of the nanodisc couple into the SQUID loop could further refine the understanding of the observed signals. Such analysis would help quantify spatial contributions more accurately, particularly from regions near the junction. Nonetheless, the m_y versus B response serves as a reliable approximation of the expected flux signal, as it dominates the field coupling into the SQUID loop.

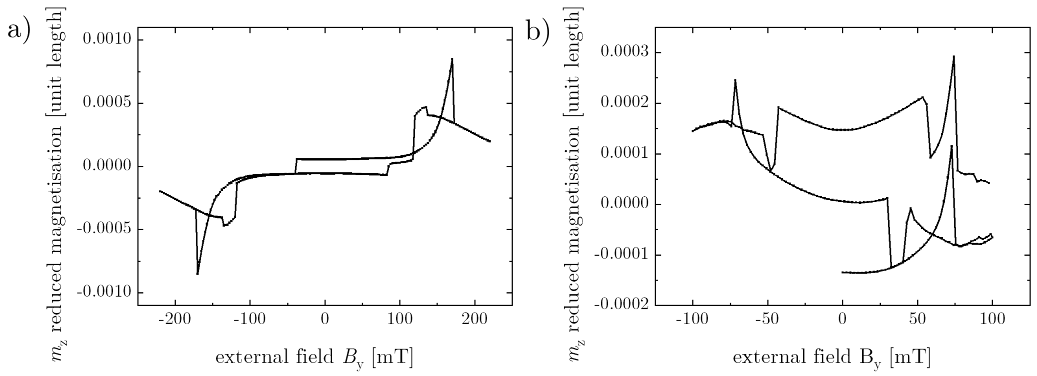

Figure 4.40.: Reduced magnetisation in the z-direction, m_z, versus external field B_y. (a) Simulation for a 200 nm disc. (b) Simulation for a 700 nm disc. The m_z signal is three orders of magnitude smaller than m_y.

4.4.3. Measurements of EuS Nanodiscs at Various Temperatures

The aim of these measurements is to investigate the temperature-dependent magnetic behaviour of the EuS nanodiscs and determine whether the expected hysteresis can be observed.

The Curie temperature of the EuS thin film, as reported by Aguilar-Pujol et al. [50], is approximately 18 K, above which the nanodisc is expected to lose its ferromagnetic behaviour and thus becomes undetectable in the SQUID signal.

Since the exact coupling factor of the nanodisc to the SQUID loop is unknown, we cannot extract a precise value for the saturation magnetisation M_{sat}. However, the flux coupled into the SQUID once the nanodisc magnetisation saturates is directly proportional to M_{sat} and can therefore be used as a relative measure.

Furthermore, the saturation field of the nanodisc is compared to micromagnetic simulations to estimate fabrication-related limitations.

200 nm EuS Nanodisc – SQUID EuS-05

The 200 nm EuS nanodisc on SQUID EuS-05 was measured at $T = 0.3$, 1, 1.4, 4, 11, and 20 K. Figure 4.41 displays SEM images of the nanodisc following Ga-FIB processing, and the SQUID with the positioned disc. To minimise edge damage, an initially larger disc was patterned, followed by a second milling step to define the final disc shape. The remaining shadow-like outline from the first milling step is still visible around the nanodisc.

The resulting FLL measurements at various temperature are shown in Figure 4.42. As the signal saturates at ±100 mT the flux difference between +100 and −100 mT is taken as an estimate for M_{sat}. Apart from an anomaly at 20 K, M_{sat} decreases with increasing temperature, suggesting a reduced magnetic response at elevated T. The signal magnitude is relatively small and declines sharply well below the expected Curie temperature of about 18 K, which may indicate significant edge damage.

An unexpected artefact is observed in the asymmetric tilt of the FLL curves: At low temperatures (0.3 to 1.4 K), the curves are steeper at negative fields and tilted upwards at positive fields. Above 4 K, the trend reverses. This behaviour persists at 20 K, where the EuS nanodisc should no longer contribute due to the loss of ferromagnetism. Although similar features were observed in measurements of other nanodiscs, the reversal of tilt direction between temperature regimes appears unique to this SQUID. This suggests that the feature may originate from the SQUID itself, the nanodisc, or the membrane. It may be associated with the SQUID's known issues, such as the tilted V vs. I_{mod} curves reported in their characterisation.

At 300 mK, a hysteresis can be observed. The measurements started at +150 mT, with four full magnetic field sweeps between −125 and +125 mT. A discrete jump in the FLL signal appears at approximately −60 mT, while no corresponding jump is seen on the positive side. This asymmetry could again be caused by trapped flux. Trapped flux was already detected in the pre-characterisation of this SQUID (see Chapter 4.1.4). A similar hysteresis and flux trapping were observed in SQUID EuS-11. Further measurements would be needed to determine the origin of this behaviour.

A comparison with simulation results (Figure 4.42c) shows that the measured nanodisc reaches saturation at around 100 mT, while the simulated 40 nm-thick disc saturates near 200 mT. A simulation of a disc with only 20 nm thickness (half of the expected value) aligns more closely with the measured response. This suggests that edge damage may have significantly reduced the effective magnetic height, or that the nanodisc surface became degraded during fabrication or handling. The observation that even a simulated disc with half the nominal thickness saturates at similar fields but behaves differently than the measured disc implies that fabricating EuS nanodiscs as small as 200 nm may already be too small for reliable performance.

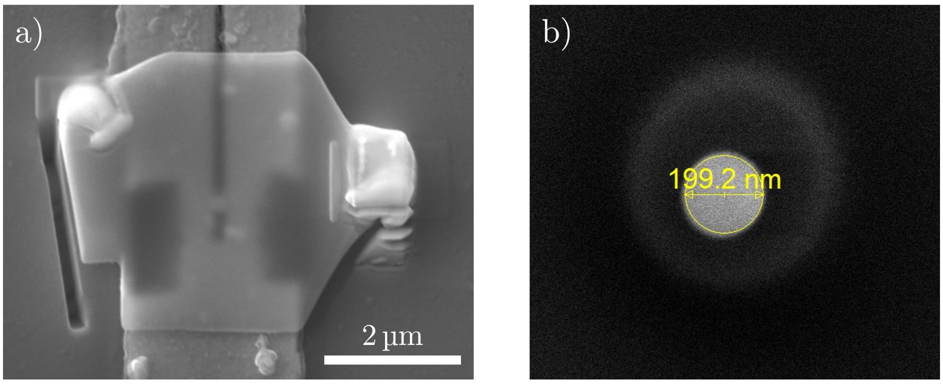

Figure 4.41.: SEM images of SQUID EuS-05 and the 200 nm EuS nanodisc. (a) SQUID EuS-05 with a placed EuS nanodisc on a Si_3N_4 membrane. (b) SEM image during Ga-FIB fabrication. To reduce edge damage, a larger disc was milled first, followed by fine patterning of the final shape. The outer shadow indicates the area of the first milling step.

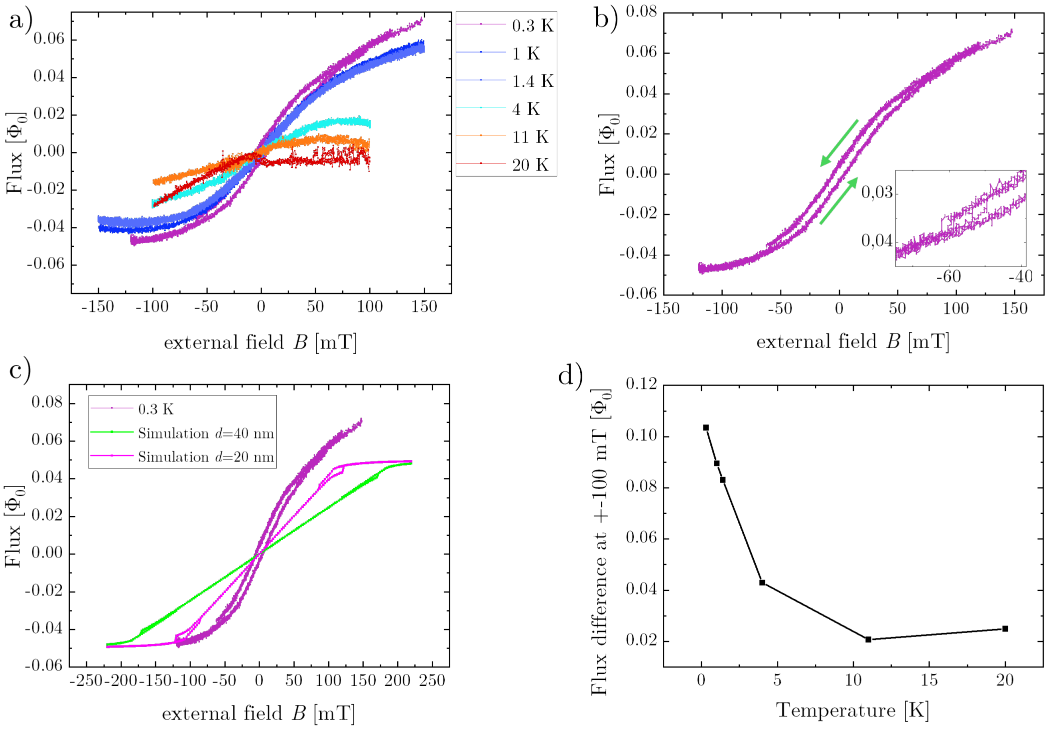

Figure 4.42.: FLL measurements of SQUID EuS-05 with a 200 nm EuS nanodisc. (a) FLL curves at various temperatures. At $T = 0.3$ to 1.4 K, the curves are tilted upwards at high fields; at $T = 4$ to 20 K the tilt reverses. (b) Hysteresis measurement at 300 mK. A jump occurs near −60 mT, but no jump is observed at positive fields. (c) Comparison between measurements and simulations. The measured disc saturates near 100 mT; the simulated 40 nm-thick disc (green) saturates at 200 mT, while the simulated 20 nm-thick disc (magenta) saturates at 100 mT. (d) Temperature-dependent flux difference between ±100 mT as a measure of M_{sat}. The response vanishes between 4 and 11 K. FLL curves are offset to zero, with $M_f = 1\,\Phi_0/\mathrm{mA}$ and were measured with feedback resistor R_f between 10 and 100 kΩ.

260 nm EuS Nanodisc – SQUID EuS-12

The 260 nm EuS nanodisc on SQUID EuS-12 was measured at multiple temperatures between 20 mK and 15 K. The results are shown in Figure 4.43. Compared to the 200 nm disc on SQUID EuS-05, the signal amplitude at low temperatures is roughly twice as large. This may be due not only to the larger volume of the disc but also to its positioning and possible differences in the resulting coupling factor, or could already indicate better quality of the nanodisc.

Figure 4.43 a) shows the raw FLL curves at various temperatures. A tilt resulting from misalignement towards the external field—similar in magnitude to the magnetisation signal itself—is observed. To account for this misalignment, a linear background (taken from the high-temperature trace) was subtracted, as shown in Figure 4.43 b).

No hysteresis could be resolved during the field sweeps. This supports the hypothesis that the hysteresis observed in SQUID EuS-05 was likely not caused by the nanodisc itself, but rather by trapped flux or other SQUID-related artifacts. It should be noted, however, that the external field in measurements below 1K was limited to ±100 mT, which might be insufficient to lead to a hysteresis related to a switching event.

Figure 4.43 c) compares the measurement at 20 mK with the corresponding micromagnetic simulation. Although no clear hysteresis is observed, the saturation magnetisation agrees better with the simulated curve compared to the 200 nm disc. The measured signal begins to saturate around 100 mT, whereas the simulated 260 nm disc saturates at approximately 175 mT. The simulation for a nanodisc with $d = 20$ nm matches the measured response remarkably well, suggesting that the effective thickness of the disc might be reduced due to surface degradation or edge damage, while maintaining the magnetic properties of a EuS nanodisc.

Figure 4.43 d) shows the temperature dependence of the signal, using the flux difference between ±100 mT as an approximation for M_{sat}. A clear temperature dependence is observed. The signal decreases steadily and vanishes between 9 and 15 K, which is more consistent with the Curie temperature reported for EuS thin films.

Compared to the 200 nm disc, this nanodisc exhibits a significantly stronger signal and a magnetic response that aligns more closely with simulation. This suggests that the 260 nm disc retains better magnetic properties, and that the edge damage is substantially smaller in this case.

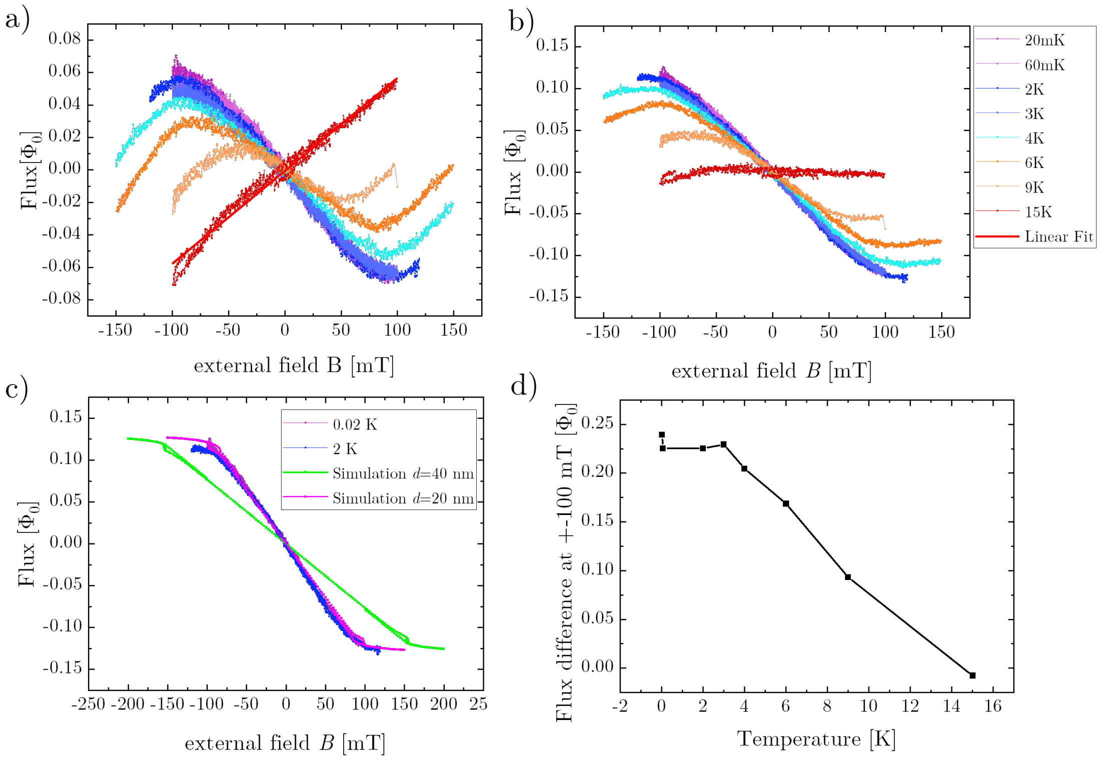

Figure 4.43.: FLL measurements of SQUID EuS-12 with a 260 nm EuS nanodisc at various temperatures. (a) FLL curves before tilt correction. The linear misalignment is comparable in magnitude to the saturation signal. (b) Background tilt (0.57 Φ_0/T) subtracted using the high-temperature trace. (c) Comparison of the 20 mK measurement with simulation. The measured curve saturates around 100 mT; the simulated 40 nm-thick disc (green) saturates at 175 mT, while the simulated 20 nm-thick disc (magenta) saturates at 100 mT, fitting well to the measured curve. (d) Temperature-dependent flux difference between ±100 mT as an approximation for M_{sat}. The signal declines to zero between 9 and 15 K. FLL curves are offset to zero. Measurements were taken with $M_f = 0.9\,\Phi_0$/mA and R_f between 30 and 100 kΩ.

600 nm EuS Nanodisc – SQUID EuS-11

The 600 nm EuS nanodisc placed on SQUID EuS-11 was measured at temperatures ranging between 45 mK and 18 K, with the results shown in Figure 4.44. The flux signal is clearly stronger than in previous measurements, consistent with the increased volume of the nanodisc. Figure 4.44 a) presents the raw FLL curves across different temperatures. Even at 18 K, a slight misalignment of the SQUID response with respect to the applied field is visible, yet the nanodisc signal remains well distinguishable.

Figure 4.44 b) shows a measurement at $T = 20\,\mathrm{mK}$, where a small hysteresis can be observed. This could be attributed to trapped flux, as previously suggested by the characterisation data for this SQUID. Similar behaviour was seen in SQUID EuS-05 and discussed in detail.

Figure 4.44 c) compares the experimental curve at 1 K with the micromagnetic simulation. The measured signal saturates at around 60 mT, while the simulation for a 40 nm-thick disc saturates close to 100 mT, and the simulated 20 nm-thick disc saturates at 50 mT. This is comparable to the behaviour observed for the 260 nm disc and may again be attributed to edge degradation or a reduced effective thickness somewhere between 20 and 40 nm.

Figure 4.44 d) displays the flux difference between ±75 mT as a function of temperature, serving as an approximation for M_{sat}. The response decreases steadily with increasing temperature and vanishes between 9 and 18 K, in line with the expected Curie temperature for EuS.

Despite the known limitations of SQUID EuS-11—such as its relatively low critical current and irregular IVCs—the measurements themselves exhibit reliable and interpretable behaviour. Taken together, the data from the 600 nm and 260 nm nanodiscs show consistent trends, reinforcing the validity of the observed magnetic responses.

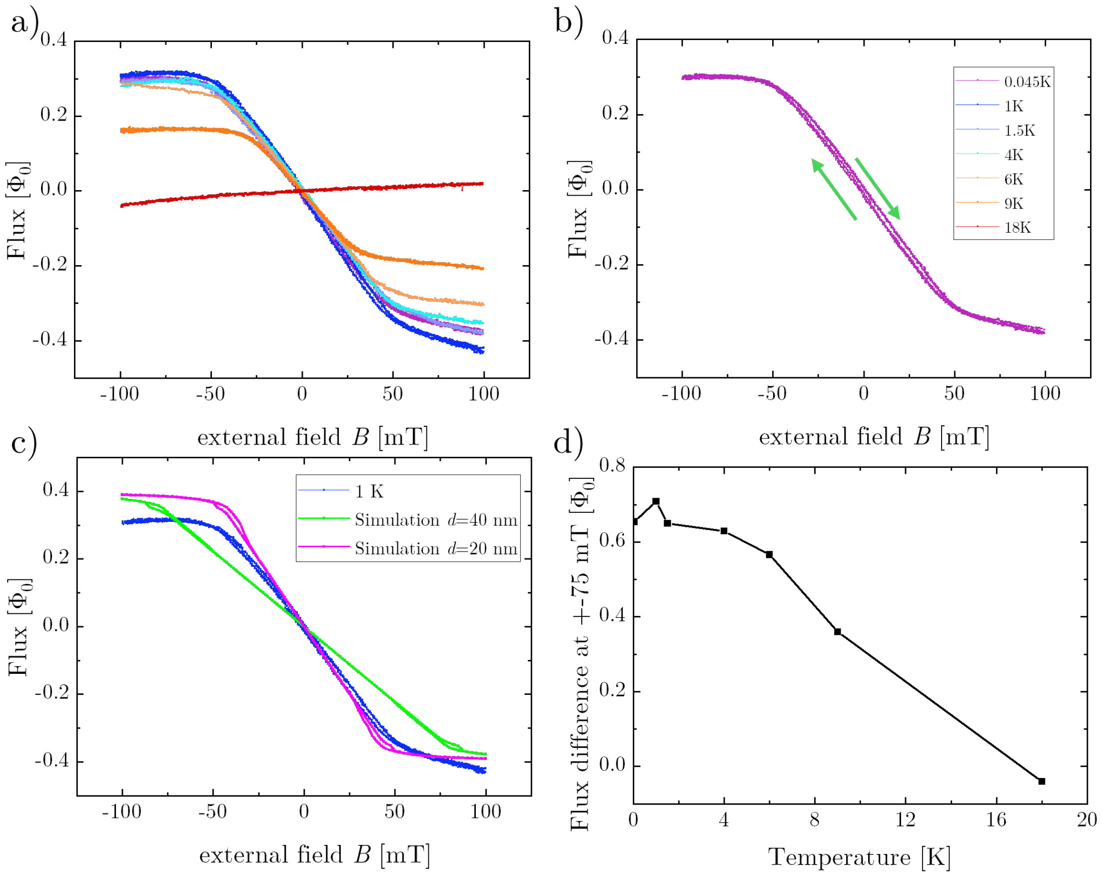

Figure 4.44.: FLL measurements of SQUID EuS-11 with a 600 nm EuS nanodisc at various temperatures. (a) FLL curves at different temperatures. A minor misalignment remains visible at 18 K, but the nanodisc signal is clearly distinguishable. (b) Measurement at 20 mK shows a small hysteresis, likely caused by trapped flux. The legend also applies for a). (c) Comparison of measurement at 1 K with simulation. The measured curve saturates near 60 mT; the simulated 40 nm-thick disc (green) saturates at 100 mT, and the 20 nm-thick disc (magenta) saturates at 50 mT. (d) Flux difference between ±75 mT at each temperature, used as an approximation for M_{sat}. The signal disappears between 9 and 18 K. All FLL curves are offset to zero. Measurements were performed with $M_f = 2.9\,\Phi_0/\mathrm{mA}$ and R_f between 7 and 30 kΩ.

700 nm EuS Nanodisc – SQUID EuS-10

The 700 nm EuS nanodisc placed on SQUID EuS-10 is the largest particle measured in this study. SEM images of the SQUID and nanodisc are shown in Figure 4.45.

The FLL measurements at various temperatures are presented in Figure 4.46 a). All curves except the one at 4 K were corrected for misalignment towards the external field using a linear background subtraction of $-1.51\,\Phi_0/\mathrm{T}$. The 4 K measurement was taken without magnetic field compensation and required a different correction of $+3\,\Phi_0/\mathrm{T}$. The curves from 9 to 19 K were recorded continuously while gradually increasing the temperature, allowing for a detailed observation of the magnetic response near the Curie temperature.

Figure 4.46 b) displays the temperature dependence of the flux difference between ±75 mT, serving as an approximation for M_{sat}. The signal decreases linearly between 10 and 19 K, approaching 0 at ≈ 19 K. This is in good agreement with the Curie temperature of $T_{\mathrm{c}} \approx 18$ K reported by Aguilar-Pujol et al. [50].

Figure 4.46 c) compares the low-temperature measurement at 13 mK with micromagnetic simulations. The saturation field of the measured curve is around 60 mT. The simulated 40 nm-thick disc (green) saturates at 80 mT, while the 20 nm-thick disc (magenta) saturates at 40 mT. This result is comparable to the findings from the 600 nm nanodisc.

A clear hysteresis is visible in the measurement, consistent with expectations from the simulations. The hysteresis is analysed in more detail in Figure 4.47. Figure 4.47 a) shows 30 consecutive field sweeps from +100 to −100 mT and back. Figure 4.47 b), the data are sorted by sweep direction and smoothed using local polynomial regression (loess, span = 0.1). Figure 4.47 c) and (d) show the hysteresis at positive and negative fields, respectively. At positive fields, the measured behaviour closely follows simulation predictions. At negative fields, the hysteresis agrees well between −50 and 0 mT, but deviates for larger fields: the magnetisation crosses over at −50 mT and returns only when the sweep direction changes. This jump behaviour at the turning point of the sweep is highlighted in the inset of Figure 4.47 a) and may point to a metastable states in the vortex structure that is influenced by the sweep direction.

These results confirm that the 700 nm disc behaves similarly to a thin film, exhibiting clear hysteresis, a well-defined Curie temperature, and close agreement with micromagnetic simulations. This further supports the notion that at this size scale, edge degradation plays a minor role, and the disc retains nanodisc magnetic properties with the vortex behaviour expected from the simulations.

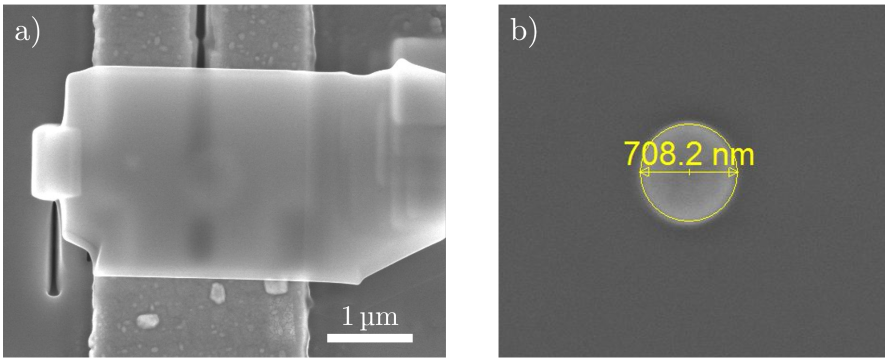

Figure 4.45.: SEM images of SQUID EuS-10 and the 700 nm EuS nanodisc. (a) SQUID with placed nanodisc on a Si_3N_4 membrane. (b) SEM image after Ga-FIB fabrication of the EuS nanodisc.

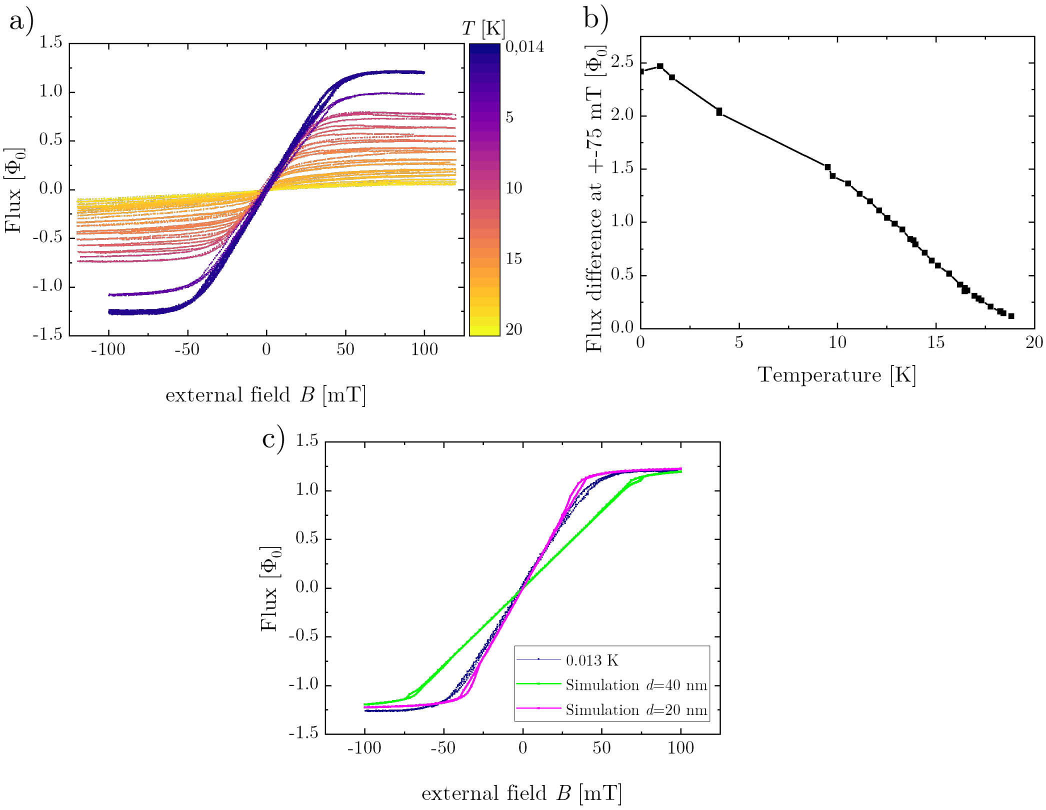

Figure 4.46.: FLL measurements of SQUID EuS-10 with a 700 nm EuS nanodisc at various temperatures. (a) FLL curves at different T. Misalignment corrected by subtracting $-1.51\,\Phi_0/\mathrm{T}$ from all traces, except the 4 K curve, which required a correction of $+3\,\Phi_0/\mathrm{T}$. (b) Flux difference between ±75 mT as a measure of M_{sat}. The signal declines linearly from 10 to 19 K approaching 0 at the expected Curie temperature of $\approx$ 18 K. (c) Comparison with simulation at 13 mK. The measured disc saturates at 60 mT, the simulated 40 nm-thick disc (green) saturates at 80 mT, and the 20 nm-thick disc (magenta) saturates at 40 mT.. Measurements were taken with $M_f = 1\,\Phi_0/\mathrm{mA}$ and R_f between 3 and 7 kΩ.

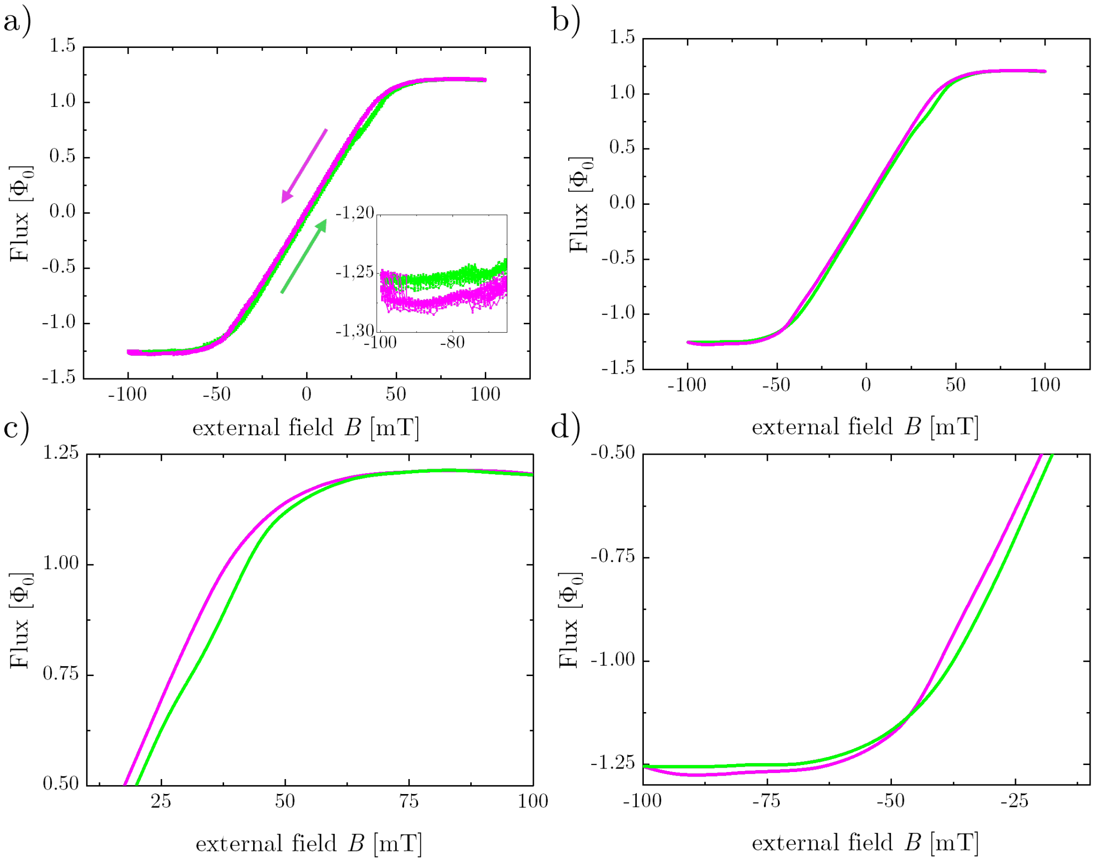

Figure 4.47.: Hysteresis of the 700 nm EuS nanodisc at 1 K. (a) Thirty consecutive field sweeps from +100 to −100 mT (magenta) and back (green). (b) Data sorted by sweep direction and smoothed using local polynomial regression (loess, span = 0.1). (c) Hysteresis at positive fields shows excellent agreement with simulation. (d) Hysteresis at negative fields deviates at −50 mT, returning only when the sweep direction is reversed, as highlighted in the inset of (a). All curves are offset to zero, measured with $M_f = 1\,\Phi_0/\text{mA}$ and $R_f = 3\,\text{k}\Omega$. Correction factor: $-1.51\,\Phi_0/\text{T}$.

Comparison of Nanodiscs with Different Diameters

To assist a cross-sample comparison of the temperature-dependent magnetic response, the extracted saturation magnetisation M_{sat} values for all four nanodiscs are shown in Figure 4.48. The flux difference between $\pm B$ at each temperature was used as an approximation for M_{sat}, providing a comparative measure of signal strength and temperature dependence across particle sizes.

As expected, M_{sat} increases with increasing nanodisc diameter, reflecting the larger magnetic volume of the particles. The 700 nm nanodisc exhibits by far the strongest magnetic signal, with a well-defined Curie temperature near 19 K. Its hysteretic magnetic behaviour matches closely with micromagnetic simulations and shows minimal deviation, suggesting that at this scale the intrinsic magnetic properties of the EuS thin film are well preserved.

The 600 nm and 260 nm nanodiscs show intermediate signal strengths, with M_{sat} vanishing between approximately 9 and 18 K (for the 600 nm disc) and 9 to 15 K (for the 260 nm disc). Their behaviour also agrees reasonably well with the simulations, though some deviation in saturation field and amplitude suggests moderate edge degradation.

In contrast, the 200 nm nanodisc exhibits the weakest response. The signal drops sharply with increasing temperature, vanishing between 4 and 11 K, significantly below the thin-film Curie temperature. This indicates that fabrication-related damage, particularly at the edges, likely compromises the magnetic properties of discs below 260 nm more severely.

These observations confirm a consistent trend: as the disc diameter decreases, both the absolute signal strength and the apparent Curie temperature are reduced. This highlights the fabrication-induced limits for producing small EuS nanodiscs with well-preserved magnetic behaviour.

4.4.4. Discussion and Outlook

This chapter presents the micromagnetic simulation and experimental characterisation of FIB patterned EuS nanodiscs of various diameters, placed on high-temperature YBCO SQUIDs and measured across a broad temperature range. The results show that the magnetic response of the nanodiscs agrees qualitatively with micromagnetic simulations, especially for larger particles, and confirm that the nanodisc fabrication was successful.

The 700 nm nanodisc exhibited a magnetic hysteresis and a Curie temperature of approximately 18–19 K, matching the values reported for thin EuS films. This strongly suggests that at this size, the disc retains the intrinsic material properties of the EuS thin film. The hysteresis was consistent with expectations from vortex dynamics simulations and confirms the formation of stable vortex states in this geometry.

In contrast, the 200 nm disc showed a significantly reduced signal and a Curie temperature well below 11 K. This behaviour points to strong edge damage or surface degradation, likely introduced during fabrication. The results indicate that discs with diameters below 260 nm suffer from substantial loss of magnetic properties, whereas discs above 600 nm are sufficiently robust to preserve the expected magnetisation behaviour.

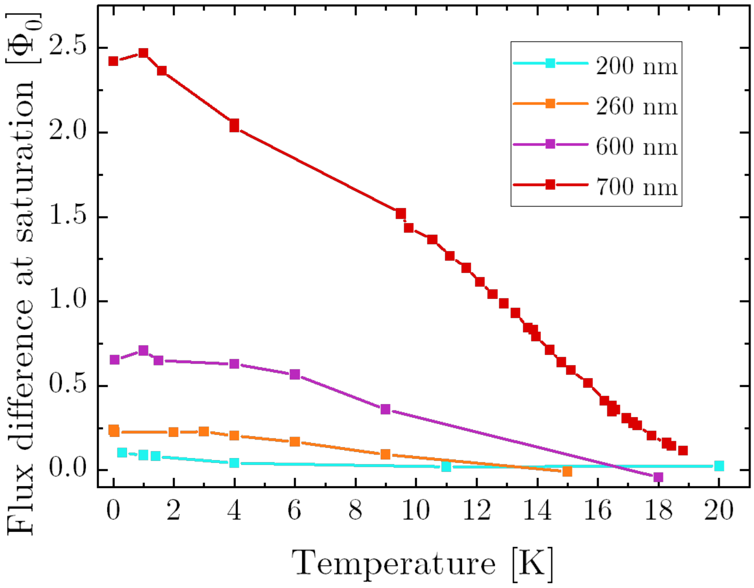

Figure 4.48.: Comparison of M_{sat} between the different nanodisc sizes. The 700 nm nanodisc shows the strongest signal and highest Curie temperature. The 600 and 260 nm discs exhibit intermediate responses, while the 200 nm disc shows significantly reduced magnetic behaviour and a lower Curie temperature. These results suggest that larger discs retain the intrinsic properties of the EuS thin film more effectively during fabrication.

The comparison between the measurements and simulations with 40 nm and 20 nm disc thickness suggests that the effective thickness of the fabricated discs may be reduced. One possible reason for a reduced effective thickness of the disc might be due to surface degradation or edge damage. This reduced effective thickness should be considered when designing and fabricating future EuS nanodiscs.

All nanodiscs provided a clear signal with a temperature dependent trend that is conclusive. However, several factors may contribute to variation in the measured signals and complicate the interpretation of results, which will be listed below:

- The nanodiscs may have been positioned at different locations, distances or orientations towards the constriction of the modulation line, resulting in varying coupling factors to the SQUID loop.
- Residual misalignment between the external magnetic field and the sample can alter both the SQUID response and the effective field acting on the nanodisc.
- The local quality of the EuS and YBCO thin films may vary across the chip, influencing the properties of individual SQUIDs and nanodiscs.
- Some SQUIDs exhibited artifacts such as multiple I_c transitions or tilted V vs. I_{mod} curves, which may introduce false signals or distort the measured flux response.

To further improve nanodisc fabrication and measurements, several strategies are suggested for future work:

- Protective capping of the EuS thin film during FIB structuring, e.g. with a thin platinum layer, may reduce surface degradation and edge damage.
- A two-step structuring method using rough milling with Ga-FIB followed by fine structuring with Ne-FIB, analogous to the method proposed for SQUIDs in Chapter 4.1.6,could further reduce edge artifacts and improve magnetic quality.
- To exclude the possibility that artifacts originate from faulty SQUIDs, it would be beneficial to repeat measurements with new chips using SQUIDs with better characteristics.
- The coupling between SQUIDs and nanodiscs could be simulated in more detail, taking into account the full 3D geometry of the setup and accurately calculate the coupling factor.

In summary, the successful fabrication and measurement of magnetic signals from EuS nanodiscs demonstrate the feasibility of creating stable, super-ferromagnetic nanodiscs that retain vortex-state behaviour. These results pave the way for future integration of such nanodiscs into hybrid quantum systems, where they could be coupled to superconducting resonators or used as well-defined nanoscale magnetic elements.

Chapter 5.

Conclusion

This dissertation presents advancements in the development and application of nanoSQUIDs for the investigation of individual magnetic nanoparticles. The goal was to establish highly sensitive, cryogenic single-particle magnetometry, which required both cutting-edge sensor technology and precise control over particle placement on the nanoscale. To achieve this, YBCO-based nanoSQUIDs were fabricated and successfully operated at magnetic fields up to 300 mT and temperatures as high as 31 K, demonstrating robust functionality and maintained flux sensitivity in challenging conditions.

A range of nanopositioning techniques was developed and adapted to the specific requirements of different magnetic nanoparticle systems, enabling reliable placement of individual particles in close proximity to the SQUID loop. From a technological perspective, novel fabrication strategies were established: a Ne-FIB was used to pattern nanoSQUIDs in YBCO, providing high-resolution structuring with minimal material damage. Additionally, Josephson junctions on superconducting YBCO on Sapphire were realised using a novel oxide membrane transfer method, overcoming conventional limitations of epitaxial growth and expanding the scope of compatible substrate materials.

The nanoSQUIDs were then employed for the magnetic characterisation of two magnetic nanoparticle systems: Fe nanowires encapsulated in CNTs, and EuS nanodiscs. Fe-nanowires exhibited magnetisation switching in the curling mode, from which domain wall energy barriers could be indirectly extracted.

The EuS nanodiscs demonstrated temperature-dependent magnetisation behaviour in close agreement with micromagnetic simulations, confirming the presence of magnetic vortex states and the successful realisation of high-quality nanodiscs through FIB structuring. Both systems are of interest for quantum technologies, particularly for their potential coupling to superconducting resonators, which are key components in quantum information processing.

Taken together, these results demonstrate the feasibility and utility of advanced YBCO-based nanoSQUID magnetometry, establishing a versatile platform for fundamental studies of magnetic nanostructures and their integration into future quantum devices.

Acknowledgements

Fides, du hattest recht, als du meintest, ich soll mich doch einfach mal hinsetzen und die Doktorarbeit fertig schreiben. Aber selbst mit ChatGPT schreibt sich so eine Doktorarbeit nicht von alleine. Deshalb möchte ich mich an dieser Stelle bei allen bedanken, die mich auf diesem Weg begleitet haben und durch Korrekturen, Beistand und Ablenkung zu diesem Buchstabensalat beigetragen haben.

Mein Dank gilt meinen Betreuern Dieter und Reinhold. Dank Euch durfte ich mich mit SQUIDs (Nobelpreis 2025) auseinandersetzen. Die starken Wechselwirkungen mit Euch und Eurer Arbeitsgruppe haben mir bei diesem Phasenübergang geholfen. Ihr seid immer zur Stelle gewesen mit guten Ratschlägen und auch im Kopenhagener Exil blieben ein paar unserer Quanten verschränkt.

Ohne Christoph, Luise-Marie, Susanne, Ronny, Markus, Manuel, Roy und Martin hätte ich weder Probenstäbe, noch Helium oder SQUIDs gehabt. Danke für Eure tolle Arbeit und Unterstützung!

Danke and Pepa, Varun und Thomas für spannenden Kollaborationen. Eure Proben, Partikel und Pinchos haben diese Arbeit bereichert.

Dem D6 danke ich für die feuchtfröhlichen Kurvendiskussionen und die schönen Freundschaften. Robin, trotz vieler dornigen Chancen ist nix aus dem Ruder gelaufen und ich genoss unser soziales Büro. Ich möchte mich bei den FOXes und Prof Nini Pryds in Kopenhagen bedanken, die mir neuen Schwung gegeben haben.

Meiner Familie möchte ich für Ihre stets große und liebevolle Unterstützung danken. Egal ob in Tübingen oder Kopenhagen, ich bin meinen Freunden dankbar für ihre Unterstützung.

Ohne die Expertise und Geduld von Johann, wäre diese Arbeit ein Rohrkrepierer geblieben. Danke für Deine Hilfe und Geduld mit mir! Familie Hattermann und Wurster Danke ich für die Schreibexils und Diskussionen. Bei Statistik fragen - Schwiegervater fragen.

Ich stimme Prof Oettel zu, als er meinte, dass ohne Frauen sich die Welt nicht drehen würde. Ich danke meiner Frau, dass ich diese Arbeit endlich fertig bekommen habe und freue mich auf unsere nächsten Abenteuer.

Appendices

Appendix A.

Supplementary Material for the paper "Vector-substrate-based Josephson junctions"

The following pages contain the supplementary of the publication *Yu-Jung Wu, Martin Hack, Katja Wurster, Simon Koch, Reinhold Kleiner, Dieter Koelle, Jochen Mannhart & Varun Harbola, "Vector-substrate-based Josephson junctions", Applied Physics Letters, vol. 125, no. 3, 2004 DOI:* `https://doi.org/10.1063/5.0217861`*; licensed under a Creative Commons Attribution (CC BY) license*[2].

Supplementary Material for

Vector-substrate-based Josephson junctions

Yu-Jung Wu[1], Martin Hack[2], Katja Wurster[2], Simon Koch[2], Reinhold Kleiner[2], Dieter Koelle[2], Jochen Mannhart[1] & Varun Harbola[1]*

[1]Max Planck Institute for Solid State Research
Heisenbergstrasse 1, 70569 Stuttgart, Germany

[2]Physikalisches Institut, Center for Quantum Science (CQ) and LISA$^+$
Universität Tübingen, auf der Morgenstelle 14, 72076 Tübingen, Germany

*v.harbola@fkf.mpg.de

Supplementary note S1:

Epitaxial Film Growth: Prior to growth, the $SrTiO_3$ bicrystal substrates were pre-annealed in pO_2= 0.1 mbar at 825°C for 40 minutes using a CO_2 laser to attain a smooth step-terrace surface. Subsequently, the $Sr_2CaAl_2O_6$ sacrificial layer and $SrTiO_3$ top membrane were deposited via pulsed laser deposition, utilizing an excimer laser with 248 nm wavelength. The $Sr_2CaAl_2O_6$ sacrificial layer was deposited at a substrate temperature of 825°C and pO_2= 1 x 10^{-5} mbar, with a laser fluence of 1.76 Jcm^{-2}. The $SrTiO_3$ membrane was grown at a substrate temperature of 825°C and pO_2= 1 x 10^{-5} mbar, with a laser fluence of 1.21 Jcm^{-2}. The films were grown in the layer-by-layer mode, with film thickness monitored via RHEED oscillations (see Fig. S1). $YBa_2Cu_3O_{7-x}$ films were grown at 720°C and pO_2= 0.25 mbar, 2 J cm^{-2} laser fluence, followed by post-annealing at 450°C and pO_2= 450 mbar for 1 hr. All the targets were commercial targets from Kurt J. Lesker.

Transfer and Characterization of Freestanding Membranes: PMMA layers were spin-coated onto the $SrTiO_3$- $Sr_2CaAl_2O_6$- $SrTiO_3$ stacks. The stacks were immersed in room-temperature deionized water to dissolve the $Sr_2CaAl_2O_6$ sacrificial layers. Following lift-off with PMMA support, the resulting freestanding membranes were affixed onto annealed Al_2O_3 substrate by heating them to 80°C on a hot plate. The Al_2O_3 had been prepared by annealing at 1615°C in vacuum to achieve a smooth, well-defined step-and-terrace surface. The membranes remained on the substrate subsequent to the dissolution of the PMMA layers with acetone. All the AFM images were captured using an Asylum Cypher AFM in tapping mode. The X-ray diffraction data were obtained utilizing a monochromatic Cu-$K_{\alpha 1}$ source on a Panalytical Empyrean machine.

Substrates Reprepare and Reuse: Following dissolution and lift-off, the bicrystal parent substrate underwent a cleaning process with deionized water, acetone, and isopropanol in a ultrasonic bath for 10 minutes each. After cleaning, the substrates were then annealed at pO_2= 7.5 x 10^{-2} mbar at 825°C for 8 minutes. As a result of the treatment, the surface of the reused substrate then regained cleanliness and exhibited clear step-terrace surface.

Josephson Junction Fabrication and Measurement: 18 nm of gold (Au) were thermally evaporated onto $YBa_2Cu_3O_{7-x}$ at room temperature, serving as a resistive shunt and protection layer during the fabrication of the bridges. The both 3–4 μm wide bridges straddling the grain boundary were fabricated via photolithography and Ar ion milling. The bridges were characterized at T = 4.2 K in an electrically and magnetically shielded environment. For the measurement of current-voltage characteristics, $I_c(H)$ and $V(H)$, a four-point arrangement with a room temperature voltage amplifier was employed.

Supplementary figures:

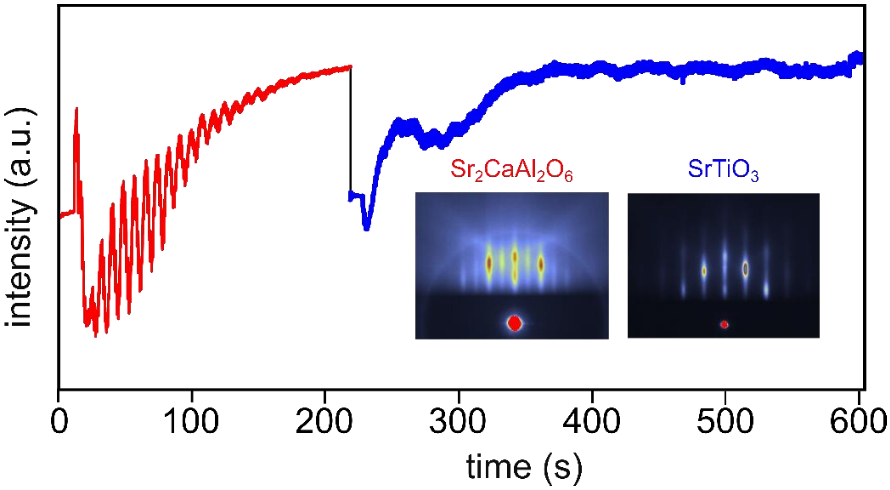

FIG. S1. Layer-by-layer growth of bicrystal substrate, aluminate sacrificial layer and $SrTiO_3$ heterostructure monitored via *in-situ* RHEED.

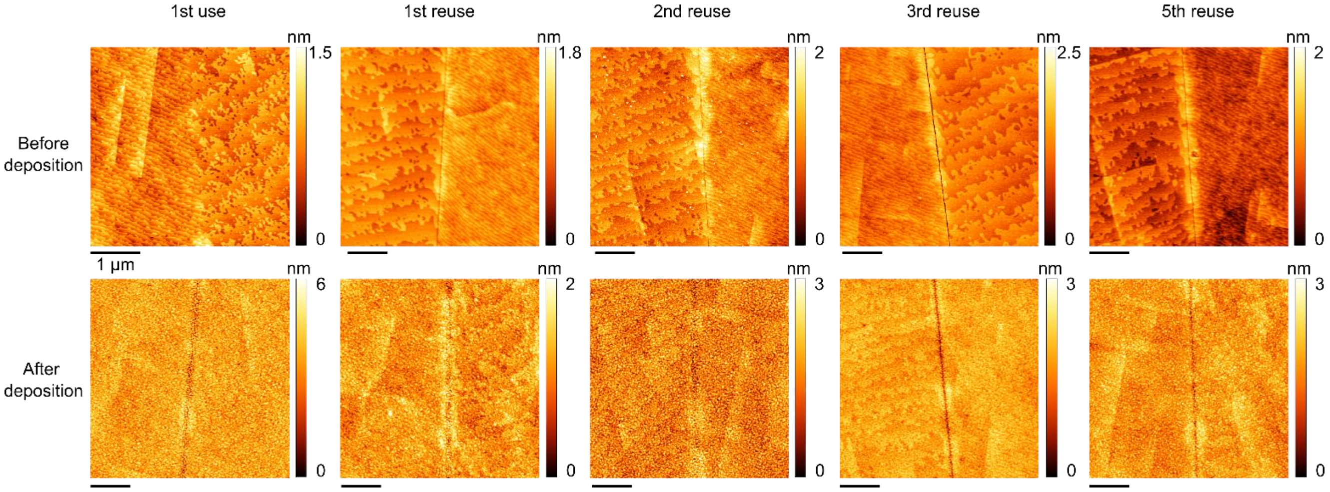

FIG. S2. Evolution of the surface morphology upon reusing the parent $SrTiO_3$ bicrystal substrate. A clear preservation of the bicrystal grain boundary upon substrate reusage after membrane lift off can be seen here. There is a slightly more pronounced diffusion of material near and at the grain boundary resulting in a sub-nanometer trench appearing even after the first reuse and evolving with subsequent reusage (top row). Bottom row shows how the surface looks after deposition of the sacrificial layer and thin film on top of the parent substrate. Note that even after the 5th reuse, the substrate surface is still viable for epitaxial growth.

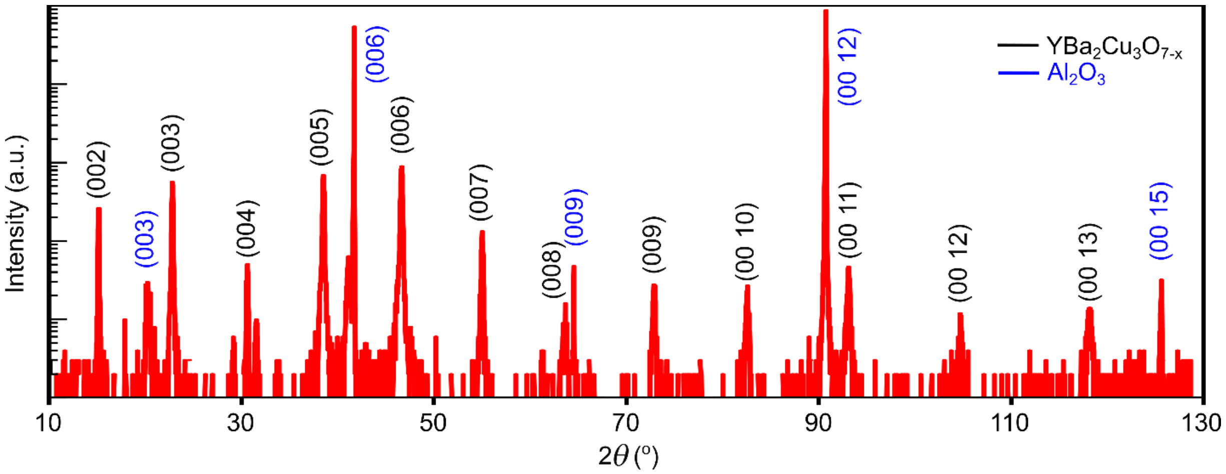

FIG. S3. A 2θ-ω X-ray diffraction scan of $YBa_2Cu_3O_{7-x}$ deposited on a bicrystal $SrTiO_3$-on-sapphire vector substrate. A single-phase growth of $YBa_2Cu_3O_{7-x}$ occurs with peaks corresponding to $YBa_2Cu_3O_{7-x}$ on $SrTiO_3$ (001) identified explicitly here. The $SrTiO_3$ peaks are not perceptible here owing to the 10 nm thickness of this layer, compared to ~100 nm of the $YBa_2Cu_3O_{7-x}$ layer.

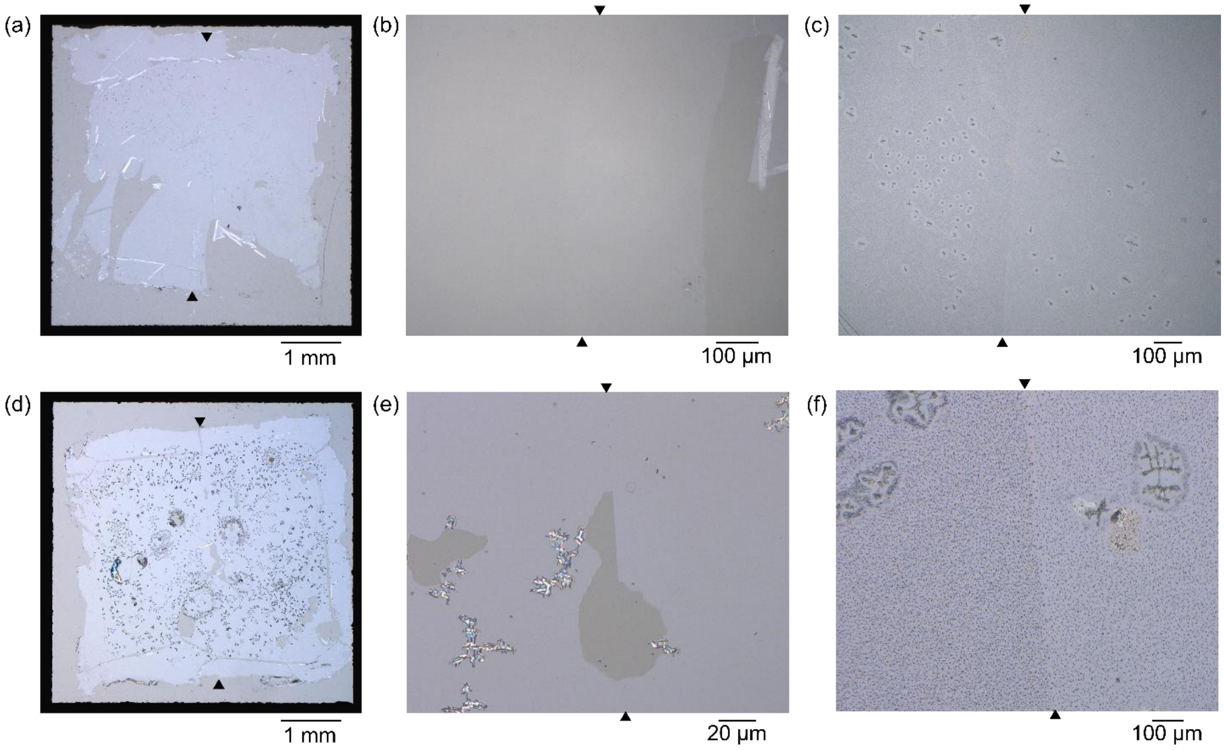

FIG. S4. Optical microscopy images of two different bicrystal $SrTiO_3$ on sapphire vector substrates made from the same parent substrate. (a) and (d) are images of the full vector substrates on 5x5 mm^2 sapphire carriers. (b) and (e) are images zooming into the grain boundary area of the vector substrates, where the grain boundary is optically not visible, but in (e), the fracture of the membrane can be seen to happen right at the grain boundary, indicating its position. By comparison of (d) and (e), what looks like dirt in (d) is actually wrinkling of the bicrystal membrane upon this transfer, as apparent in (e). (c) and (f) are images taken after deposition of ~ 100 nm $YBa_2Cu_3O_{7-x}$ on these vector substrates, and now the bicrystal boundary is perceptibly visible. The arrows mark the position of the grain boundaries in all the images.

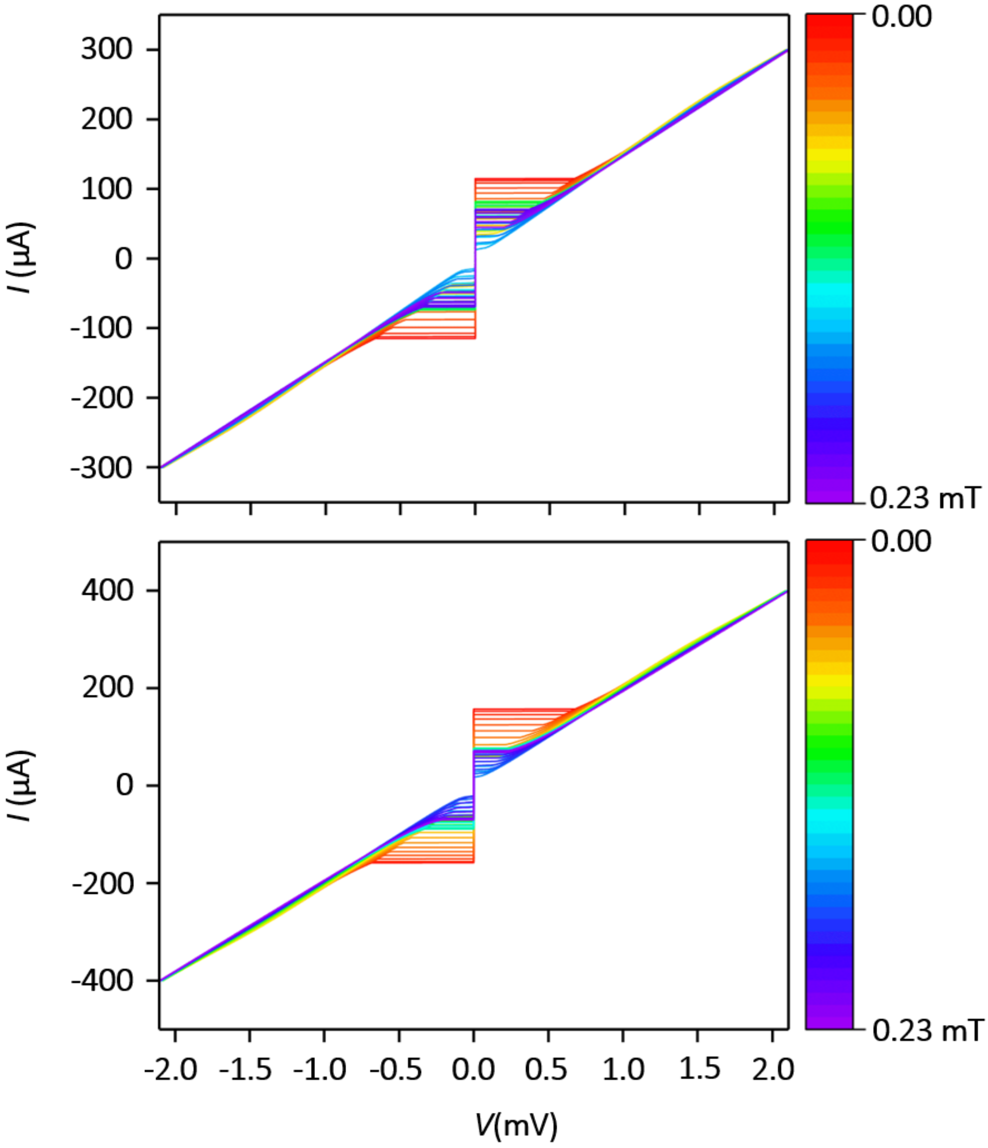

FIG. S5. The complete and extended dataset of the Josephson junction characteristics shown in Fig. 3 of the main text. Electric-transport characteristics of $YBa_2Cu_3O_{7-x}$ grain boundary Josephson Junctions fabricated with the vector substrate technology. Shown are several Current vs Voltage measurements at different external fields ranging from 0 to 0.23 mT. Only one direction of the current sweep is shown here for clarity.

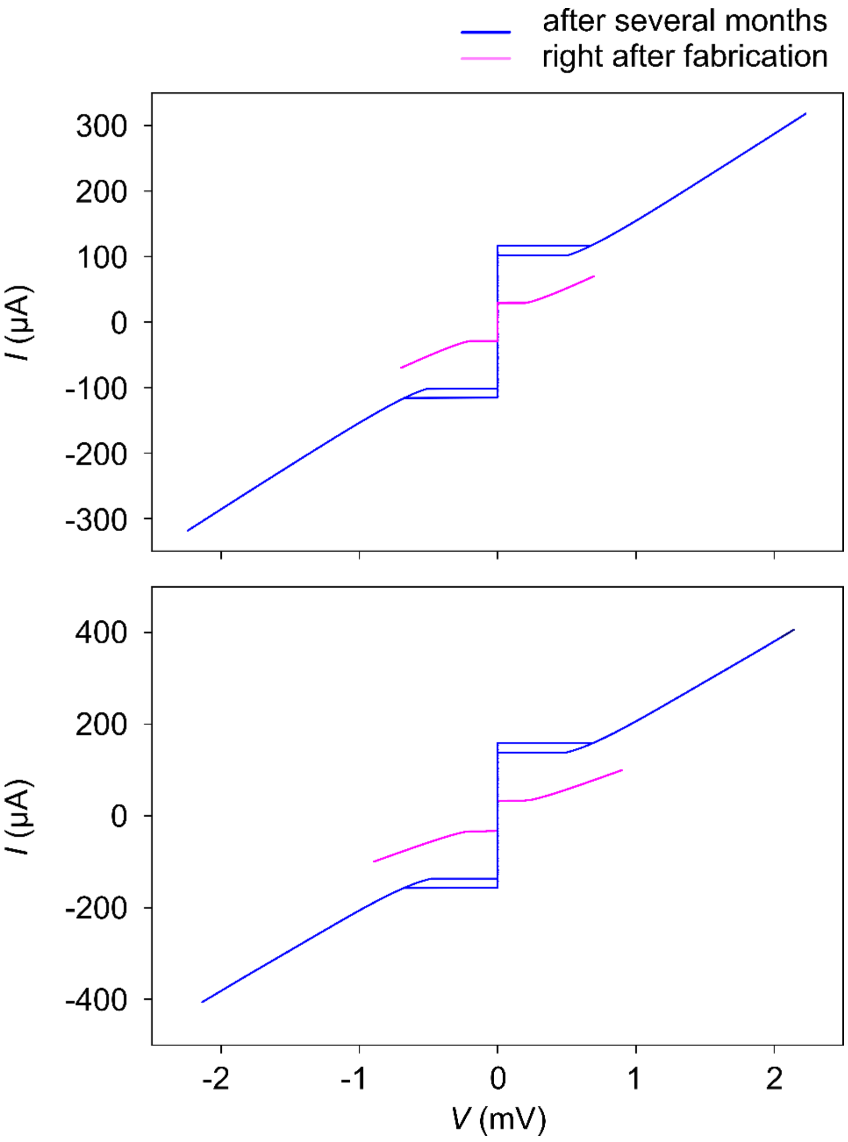

FIG. S6. Temporal evolution of the $I(V)$ characteristics of two Josephson junctions shown in Fig. 3. Both junctions were measured right after fabricating them and after several months of storage in a nitrogen atmosphere. An improvement in the I_c is evident, by a factor of about five in both junctions characterized, along with a more pronounced hysteresis during the I-V sweep, owing to the increased Stewart-McCumber parameter. This "healing" of the Josephson junction can be attributed to the oxygen ion relaxation at the grain boundary with time.

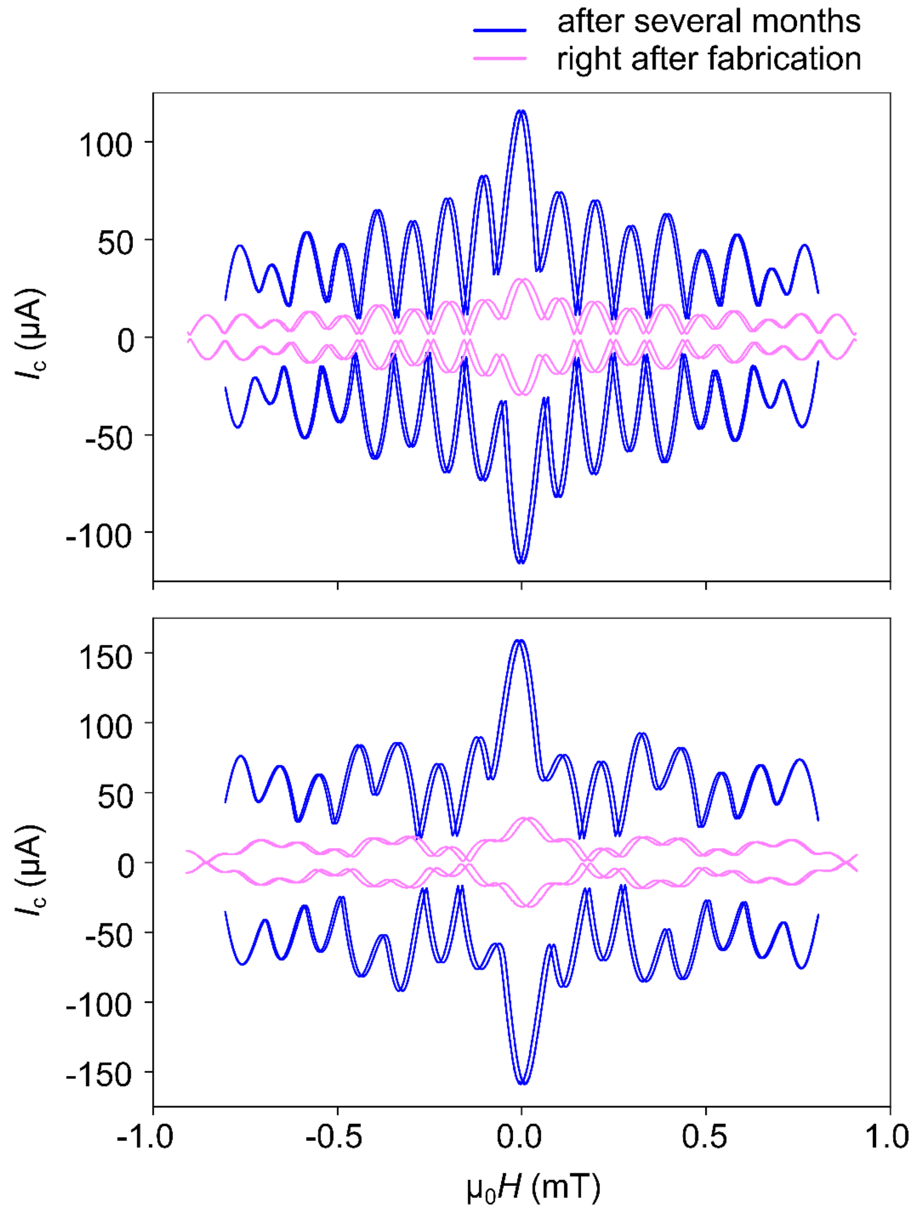

FIG. S7. Temporal evolution of $I_c(H)$ of the same two Josephson junctions as in Fig. S6. The shape of the I_c oscillations is retained over time but an overall increase in I_c by about a factor of five applies also for the small magnetic fields under which the Josephson junctions were characterized after a span of several months.

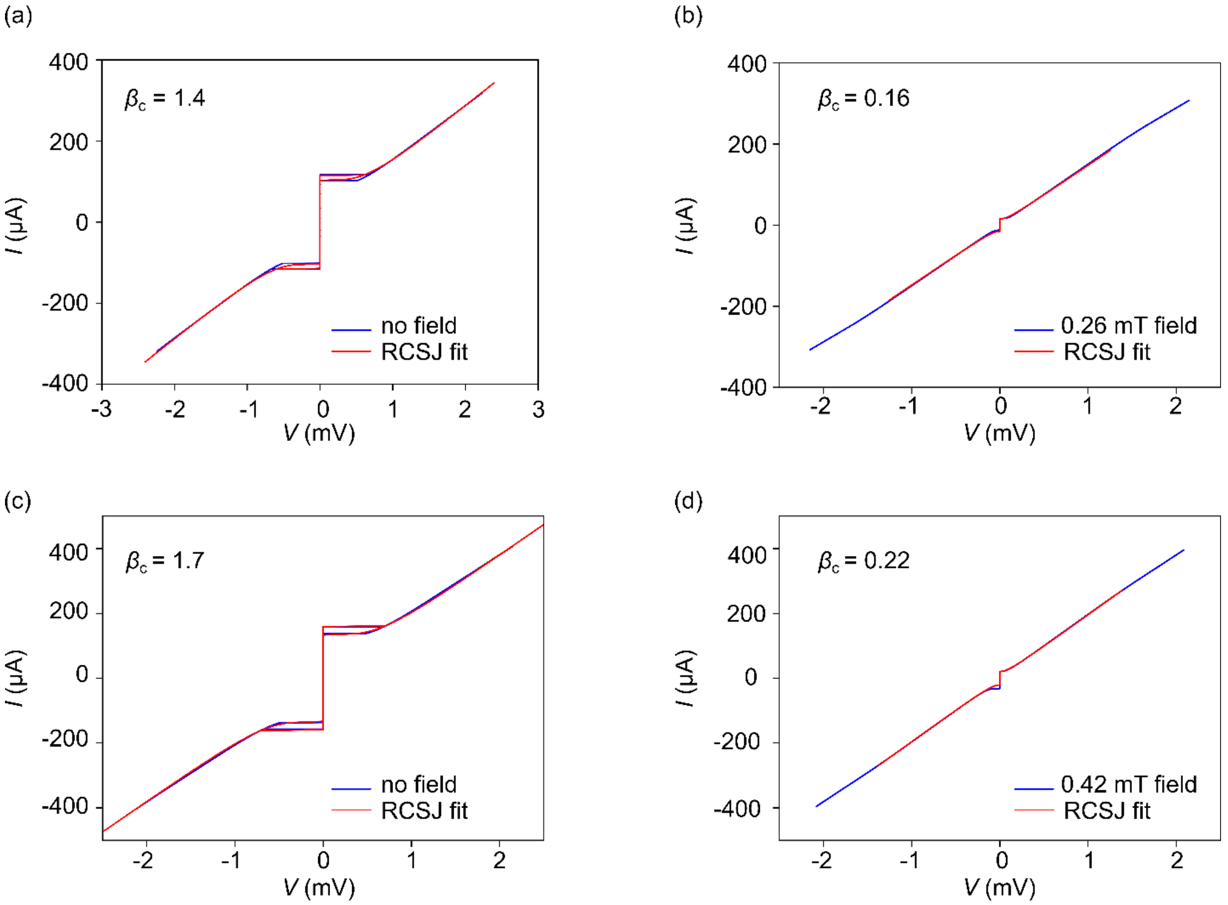

FIG. S8. Electric-transport characteristics of the two Josephson junctions shown in Fig. 3. Shown are current (*I*) vs voltage (*V*) measurements compared to RCSJ fits to determine β_c of the Josephson junctions. (a), (b) *I*-*V* characteristics of the bridge shown in Fig. 3(a) at 0 and 0.26 mT external field, respectively. The comparison with the fit results in a β_c of 1.4 and 0.16, respectively. (c), (d) *I*-*V* characteristics of the other bridge shown in Fig. 3(b) at 0 and 0.42 mT external field, respectively. The comparison with the fit results in β_c of 1.7 and 0.22, respectively.

Appendix B.

mumax^3 Scripts

EuS, 200 nm diameter, 40 nm thickness, 220 mT fieldsweep

```
//powers of two: 1 2 4 8 16 32 64 128 256 512 1024 2048(number of cells is a power of two)
//small prime numbers: 2 3 5 7
// exch length 0.43 nm, cells not larger than 0.75 exchange lengths -> 0.32 nm
//changed vortex 1,-1, added smoothness

Nx := 128
Ny := 128
Nz := 32
sizeX := 200e-9  // cell=200/1024=0.2   cell=200/512=0.39
sizeY := 200e-9
sizeZ := 40e-9  // cell=40/128=0.31
SetGridSize(Nx, Ny, Nz)
SetCellSize(sizeX/Nx, sizeY/Ny, sizeZ/Nz)

EdgeSmooth = 8

SetGeom(Cylinder(200e-09, 40e-09))


Msat    = 1163e3
Aex     = 0.16e-12
alpha   = 0.04

Temp = 0

m = Vortex(1, 1)
save(m)

//autosave(m, 100e-12)

Bmax  := 220.0e-3
Bstep :=  2.5e-3
MinimizerStop = 1e-6
TableAdd(B_ext)
TableAdd(E_total)
TableAdd(E_anis)
TableAdd(E_demag)
TableAdd(E_exch)
```

```
TableAdd(E_therm)
TableAdd(Edens_demag)
TableAdd(Edens_anis)
TableAdd(Edens_exch)
TableAdd(Edens_Zeeman)

for B:=0.0; B<=Bmax; B+=Bstep{
    B_ext = vector(0, B, 0) // was vector(B, B*0.0001, B*0.01)
    minimize()   // small changes best minimized by minimize()
    tablesave()
    save(m)
}

for B:=Bmax; B>=-Bmax; B-=Bstep{
    B_ext = vector(0, B, 0)
    minimize()   // small changes best minimized by minimize()
    tablesave()
    save(m)
}

for B:=-Bmax; B<=Bmax; B+=Bstep{
    B_ext = vector(0, B, 0)
    minimize()   // small changes best minimized by minimize()
    tablesave()
    save(m)
}
```

EuS, 200 nm diameter, 20 nm thickness, 220 mT fieldsweep

```
//powers of two: 1 2 4 8 16 32 64 128 256 512 1024 2048(number of cells
    is a power of two)
//small prime numbers: 2 3 5 7
// exch length 0.43 nm, cells not larger than 0.75 exchange lengths ->
    0.32 nm
//changed vortex 1,-1, added smoothness

Nx := 128
Ny := 128
Nz := 16
sizeX := 200e-9  // cell=200/1024=0.2   cell=200/512=0.39
sizeY := 200e-9
sizeZ := 20e-9  // cell=20/64=0.31
SetGridSize(Nx, Ny, Nz)
SetCellSize(sizeX/Nx, sizeY/Ny, sizeZ/Nz)

EdgeSmooth = 8

SetGeom(Cylinder(200e-09, 40e-09))


Msat    = 1163e3
Aex     = 0.16e-12
alpha   = 0.04

Temp = 0

m = Vortex(1, 1)
save(m)

//autosave(m, 100e-12)

Bmax  := 220.0e-3
Bstep :=  2.5e-3
MinimizerStop = 1e-6
TableAdd(B_ext)
TableAdd(E_total)
TableAdd(E_anis)
TableAdd(E_demag)
TableAdd(E_exch)
TableAdd(E_therm)
TableAdd(Edens_demag)
TableAdd(Edens_anis)
TableAdd(Edens_exch)
TableAdd(Edens_Zeeman)

for B:=0.0; B<=Bmax; B+=Bstep{
    B_ext = vector(0, B, 0) // was vector(B, B*0.0001, B*0.01)
    minimize()   // small changes best minimized by minimize()
    tablesave()
    save(m)
}
```

```

for B:=Bmax; B>=-Bmax; B-=Bstep{
    B_ext = vector(0, B, 0)
    minimize()   // small changes best minimized by minimize()
    tablesave()
    save(m)
}

for B:=-Bmax; B<=Bmax; B+=Bstep{
    B_ext = vector(0, B, 0)
    minimize()   // small changes best minimized by minimize()
    tablesave()
    save(m)
}
```

EuS, 260 nm diameter, 40 nm thickness, 200 mT fieldsweep

```
//powers of two: 1 2 4 8 16 32 64 128 256 512 1024 2048(number of cells is a power of two)
//small prime numbers: 2 3 5 7
// exch length 0.43 nm, cells not larger than 0.75 exchange lengths -> 0.32 nm
//changed vortex 1,-1, added smoothness

Nx := 128
Ny := 128
Nz := 32
sizeX := 260e-9  // cell=260/1024=0.25  cell=200/512=0.5
sizeY := 260e-9
sizeZ := 40e-9  // cell=40/128=0.31
SetGridSize(Nx, Ny, Nz)
SetCellSize(sizeX/Nx, sizeY/Ny, sizeZ/Nz)

EdgeSmooth = 8

SetGeom(Cylinder(260e-09, 40e-09))


Msat    = 1163e3
Aex     = 0.16e-12
alpha   = 0.04

Temp = 0

m = Vortex(1, 1)
save(m)    // relaxed state

//autosave(m, 100e-12)

Bmax  := 200.0e-3
Bstep :=  2.5e-3
MinimizerStop = 1e-6
TableAdd(B_ext)
TableAdd(E_total)
TableAdd(E_anis)
TableAdd(E_demag)
TableAdd(E_exch)
TableAdd(E_therm)
TableAdd(Edens_demag)
TableAdd(Edens_anis)
TableAdd(Edens_exch)
TableAdd(Edens_Zeeman)

for B:=0.0; B<=Bmax; B+=Bstep{
    B_ext = vector(0, B, 0) // was vector(B, B*0.0001, B*0.01)
    minimize()   // small changes best minimized by minimize()
    tablesave()
    save(m)
}
```

```

for B:=Bmax; B>=-Bmax; B-=Bstep{
    B_ext = vector(0, B, 0)
    minimize()   // small changes best minimized by minimize()
    tablesave()
    save(m)
}

for B:=-Bmax; B<=Bmax; B+=Bstep{
    B_ext = vector(0, B, 0)
    minimize()   // small changes best minimized by minimize()
    tablesave()
    save(m)
}
```

EuS, 260 nm diameter, 20 nm thickness, 150 mT fieldsweep

```
//powers of two: 1 2 4 8 16 32 64 128 256 512 1024 2048(number of cells is a power of two)
//small prime numbers: 2 3 5 7
// exch length 0.43 nm, cells not larger than 0.75 exchange lengths -> 0.32 nm
//changed vortex 1,-1, added smoothness

Nx := 128
Ny := 128
Nz := 16
sizeX := 260e-9  // cell=260/1024=0.25  cell=200/512=0.5
sizeY := 260e-9
sizeZ := 20e-9  // cell=40/128=0.31
SetGridSize(Nx, Ny, Nz)
SetCellSize(sizeX/Nx, sizeY/Ny, sizeZ/Nz)

EdgeSmooth = 8

SetGeom(Cylinder(260e-09, 40e-09))


Msat    = 1163e3
Aex     = 0.16e-12
alpha   = 0.04

Temp = 0

m = Vortex(1, 1)
save(m)    // relaxed state

//autosave(m, 100e-12)

Bmax  := 150.0e-3
Bstep :=  2.5e-3
MinimizerStop = 1e-6
TableAdd(B_ext)
TableAdd(E_total)
TableAdd(E_anis)
TableAdd(E_demag)
TableAdd(E_exch)
TableAdd(E_therm)
TableAdd(Edens_demag)
TableAdd(Edens_anis)
TableAdd(Edens_exch)
TableAdd(Edens_Zeeman)

for B:=0.0; B<=Bmax; B+=Bstep{
    B_ext = vector(0, B, 0) // was vector(B, B*0.0001, B*0.01)
    minimize()   // small changes best minimized by minimize()
    tablesave()
    save(m)
}
```

```

for B:=Bmax; B>=-Bmax; B-=Bstep{
    B_ext = vector(0, B, 0)
    minimize()   // small changes best minimized by minimize()
    tablesave()
    save(m)
}

for B:=-Bmax; B<=Bmax; B+=Bstep{
    B_ext = vector(0, B, 0)
    minimize()   // small changes best minimized by minimize()
    tablesave()
    save(m)
}
```

EuS, 600 nm diameter, 40 nm thickness, 100 mT fieldsweep

```
//powers of two: 1 2 4 8 16 32 64 128 256 512 1024 2048(number of cells is a power of two)
//small prime numbers: 2 3 5 7
// exch length 0.43 nm, cells not larger than 0.75 exchange lengths -> 0.32 nm
//changed vortex 1,-1, added smoothness

Nx := 256
Ny := 256
Nz := 32
sizeX := 600e-9  // cell=600/2048=0.3  cell=600/1024=0.59
sizeY := 600e-9
sizeZ := 40e-9  // cell=40/128=0.31
SetGridSize(Nx, Ny, Nz)
SetCellSize(sizeX/Nx, sizeY/Ny, sizeZ/Nz)

EdgeSmooth = 8

SetGeom(Cylinder(600e-09, 40e-09))


Msat    = 1163e3
Aex     = 0.16e-12
alpha   = 0.04

Temp = 0

m = Vortex(1, 1)
save(m)    // relaxed state

//autosave(m, 100e-12)

Bmax  := 100.0e-3
Bstep :=  2.5e-3
MinimizerStop = 1e-6
TableAdd(B_ext)
TableAdd(E_total)
TableAdd(E_anis)
TableAdd(E_demag)
TableAdd(E_exch)
TableAdd(E_therm)
TableAdd(Edens_demag)
TableAdd(Edens_anis)
TableAdd(Edens_exch)
TableAdd(Edens_Zeeman)

for B:=0.0; B<=Bmax; B+=Bstep{
    B_ext = vector(0, B, 0) // was vector(B, B*0.0001, B*0.01)
    minimize()   // small changes best minimized by minimize()
    tablesave()
    save(m)
}
```

```

for B:=Bmax; B>=-Bmax; B-=Bstep{
    B_ext = vector(0, B, 0)
    minimize()   // small changes best minimized by minimize()
    tablesave()
    save(m)
}

for B:=-Bmax; B<=Bmax; B+=Bstep{
    B_ext = vector(0, B, 0)
    minimize()   // small changes best minimized by minimize()
    tablesave()
    save(m)
}
```

EuS, 600 nm diameter, 20 nm thickness, 100 mT fieldsweep

```
//powers of two: 1 2 4 8 16 32 64 128 256 512 1024 2048(number of cells is a power of two)
//small prime numbers: 2 3 5 7
// exch length 0.43 nm, cells not larger than 0.75 exchange lengths -> 0.32 nm
//changed vortex 1,-1, added smoothness

Nx := 256
Ny := 256
Nz := 16
sizeX := 600e-9  // cell=600/2048=0.3  cell=600/1024=0.59
sizeY := 600e-9
sizeZ := 20e-9  // cell=40/128=0.31
SetGridSize(Nx, Ny, Nz)
SetCellSize(sizeX/Nx, sizeY/Ny, sizeZ/Nz)

EdgeSmooth = 8

SetGeom(Cylinder(600e-09, 40e-09))


Msat    = 1163e3
Aex     = 0.16e-12
alpha   = 0.04

Temp = 0

m = Vortex(1, 1)
save(m)    // relaxed state

//autosave(m, 100e-12)

Bmax  := 100.0e-3
Bstep :=  2.5e-3
MinimizerStop = 1e-6
TableAdd(B_ext)
TableAdd(E_total)
TableAdd(E_anis)
TableAdd(E_demag)
TableAdd(E_exch)
TableAdd(E_therm)
TableAdd(Edens_demag)
TableAdd(Edens_anis)
TableAdd(Edens_exch)
TableAdd(Edens_Zeeman)

for B:=0.0; B<=Bmax; B+=Bstep{
    B_ext = vector(0, B, 0) // was vector(B, B*0.0001, B*0.01)
    minimize()   // small changes best minimized by minimize()
    tablesave()
    save(m)
}
```

```

for B:=Bmax; B>=-Bmax; B-=Bstep{
    B_ext = vector(0, B, 0)
    minimize()   // small changes best minimized by minimize()
    tablesave()
    save(m)
}

for B:=-Bmax; B<=Bmax; B+=Bstep{
    B_ext = vector(0, B, 0)
    minimize()   // small changes best minimized by minimize()
    tablesave()
    save(m)
}
```

EuS, 700 nm diameter, 40 nm thickness, 100 mT fieldsweep

```
//powers of two: 1 2 4 8 16 32 64 128 256 512 1024 2048(number of cells is a power of two)
//small prime numbers: 2 3 5 7
// exch length 0.43 nm, cells not larger than 0.75 exchange lengths -> 0.32 nm
//changed vortex 1,-1, added smoothness

Nx := 256
Ny := 256
Nz := 32
sizeX := 700e-9  // cell=700/2048=0.34 cell=700/1024=0.68
sizeY := 700e-9
sizeZ := 40e-9  // cell=40/128=0.31
SetGridSize(Nx, Ny, Nz)
SetCellSize(sizeX/Nx, sizeY/Ny, sizeZ/Nz)

EdgeSmooth = 8

SetGeom(Cylinder(700e-09, 40e-09))


Msat    = 1163e3
Aex     = 0.16e-12
alpha   = 0.04

Temp = 0

m = Vortex(1, 1)
save(m)    // relaxed state

//autosave(m, 100e-12)

Bmax   := 100.0e-3
Bstep :=  2.6e-3
MinimizerStop = 1e-6
TableAdd(B_ext)
TableAdd(E_total)
TableAdd(E_anis)
TableAdd(E_demag)
TableAdd(E_exch)
TableAdd(E_therm)
TableAdd(Edens_demag)
TableAdd(Edens_anis)
TableAdd(Edens_exch)
TableAdd(Edens_Zeeman)

for B:=0.0; B<=Bmax; B+=Bstep{
    B_ext = vector(0, B, 0) // was vector(B, B*0.0001, B*0.01)
    minimize()   // small changes best minimized by minimize()
    tablesave()
    save(m)
}
```

```

for B:=Bmax; B>=-Bmax; B-=Bstep{
    B_ext = vector(0, B, 0)
    minimize()   // small changes best minimized by minimize()
    tablesave()
    save(m)
}

for B:=-Bmax; B<=Bmax; B+=Bstep{
    B_ext = vector(0, B, 0)
    minimize()   // small changes best minimized by minimize()
    tablesave()
    save(m)
}
```

EuS, 700 nm diameter, 20 nm thickness, 100 mT fieldsweep

```
//powers of two: 1 2 4 8 16 32 64 128 256 512 1024 2048(number of cells is a power of two)
//small prime numbers: 2 3 5 7
// exch length 0.43 nm, cells not larger than 0.75 exchange lengths -> 0.32 nm
//changed vortex 1,-1, added smoothness

Nx := 256
Ny := 256
Nz := 16
sizeX := 700e-9  // cell=700/2048=0.34 cell=700/1024=0.68
sizeY := 700e-9
sizeZ := 20e-9  // cell=40/128=0.31
SetGridSize(Nx, Ny, Nz)
SetCellSize(sizeX/Nx, sizeY/Ny, sizeZ/Nz)

EdgeSmooth = 8

SetGeom(Cylinder(700e-09, 40e-09))


Msat    = 1163e3
Aex     = 0.16e-12
alpha   = 0.04

Temp = 0

m = Vortex(1, 1)
save(m)    // relaxed state

//autosave(m, 100e-12)

Bmax  := 100.0e-3
Bstep :=  2.5e-3
MinimizerStop = 1e-6
TableAdd(B_ext)
TableAdd(E_total)
TableAdd(E_anis)
TableAdd(E_demag)
TableAdd(E_exch)
TableAdd(E_therm)
TableAdd(Edens_demag)
TableAdd(Edens_anis)
TableAdd(Edens_exch)
TableAdd(Edens_Zeeman)

for B:=0.0; B<=Bmax; B+=Bstep{
    B_ext = vector(0, B, 0) // was vector(B, B*0.0001, B*0.01)
    minimize()   // small changes best minimized by minimize()
    tablesave()
    save(m)
}
```

```

for B:=Bmax; B>=-Bmax; B-=Bstep{
    B_ext = vector(0, B, 0)
    minimize()   // small changes best minimized by minimize()
    tablesave()
    save(m)
}

for B:=-Bmax; B<=Bmax; B+=Bstep{
    B_ext = vector(0, B, 0)
    minimize()   // small changes best minimized by minimize()
    tablesave()
    save(m)
}
```

Bibliography

[1] D. Koelle, R. Kleiner, F. Ludwig, E. Dantsker, and J. Clarke, "High-transition-temperature superconducting quantum interference devices," *Reviews of Modern Physics*, vol. 71, pp. 631–686, 1999. DOI: 10.1103/revmodphys.71.631.

[2] Y.-J. Wu, M. Hack, K. Wurster, S. Koch, R. Kleiner, D. Koelle, J. Mannhart, and V. Harbola, "Vector substrate-based Josephson junctions," *Applied Physics Letters*, vol. 125, p. 032 601, 2024. DOI: 10.1063/5.0217861.

[3] J. Clarke and A. I. Braginski, *The SQUID handbook Vol. I Fundamentals and Technology of SQUIDs and SQUID Systems.* John Wiley & Sons, 2004, ISBN: 9783527603640.

[4] J. Clarke and A. I. Braginski, *The SQUID handbook Vol. II Applications of SQUIDs and SQUID Systems.* John Wiley & Sons, 2006, ISBN: 9783527609956.

[5] R. Kleiner, D. Koelle, F. Ludwig, and J. Clarke, "Superconducting QUantum Interference Devices: State-of-the-Art and Applications," *Proceedings of the IEEE*, vol. 92, pp. 1534–1548, 2004. DOI: 10.1109/JPROC.2004.833655.

[6] J. Gallop, "SQUIDs: Some limits to measurement," *Superconductor Science and Technology*, vol. 16, pp. 1575–1582, 2003.

[7] R. L. Fagaly, "Superconducting Quantum Interference Device Instruments and Applications," *Review of Scientific Instruments*, vol. 77, p. 101 101, 2006.

[8] D. Koelle, "Magnetic sensors: A tip for better sensing," *Nature Nanotechnology*, vol. 8, pp. 617–618, 2013. DOI: 10.1038/nnano.2013.179.

[9] D. Vasyukov, Y. Anahory, L. Embon, D. Halbertal, J. Cuppens, L. Ne'eman, A. Finkler, Y. Segev, Y. Myasoedov, M. L. Rappaport, M. E. Huber, and E. Zeldov, "A scanning superconducting quantum interference device with single electron spin sensitivity," *Nature Nanotechnology*, vol. 8, pp. 639–644, 2013. DOI: 10.1038/nnano.2013.169.

[10] C. Granata and A. Vettoliere, "Nano Superconducting Quantum Interference device: A powerful tool for nanoscale investigations," *Physics Reports*, vol. 614, pp. 1–69, 2016. DOI: 10.1016/j.physrep.2015.12.001.

[11] M. José Martínez-Pérez and D. Koelle, "NanoSQUIDs: Basics & recent advances," *Physical Sciences Reviews*, vol. 2, p. 20 175 001, 2017. DOI: 10.1515/psr-2017-5001.

[12] D. D. Awschalom, D. P. DiVincenzo, and J. F. Smyth, "Macroscopic Quantum Effects in Nanometer-Scale Magnets," *Science*, vol. 258, pp. 414–421, 1992. DOI: 10.1126/science.258.5081.414.

[13] L. Thomas, F. Lionti, R. Ballou, D. Gatteschi, R. Sessoli, and B. Barbara, "Macroscopic quantum tunnelling of magnetization in a single crystal of nanomagnets," *Nature*, vol. 383, pp. 145–147, 1996. DOI: 10.1038/383145a0.

[14] A. P. Guimarães, *Principles of Nanomagnetism.* Springer, 2017, ISBN: 9783319594095.

[15] J. Bartolomé, *Molecular Magnets: Physics and Applications*, F. Luis and J. F. Fernández, Eds. Springer, 2014, ISBN: 9783642406096.

[16] S. A. Majetich, T. Wen, and O. T. Mefford, "Magnetic nanoparticles," *MRS Bulletin*, vol. 38, pp. 899–903, 2013. DOI: 10.1557/mrs.2013.230.

[17] A. Hirohata and K. Takanashi, "Future perspectives for spintronic devices," *Journal of Physics D: Applied Physics*, vol. 47, p. 193 001, 2014. DOI: 10.1088/0022-3727/47/19/193001.

[18] C. L. Degen, M. Poggio, H. J. Mamin, C. T. Rettner, and D. Rugar, "Nanoscale magnetic resonance imaging," *PNAS*, vol. 106, pp. 1313–1317, 2009. DOI: 10 . 1073^pnas.0812068106.

[19] E. Schäfer-Nolte, F. Reinhard, M. Ternes, J. Wrachtrup, and K. Kern, "A diamond-based scanning probe spin sensor operating at low temperature in ultra-high vacuum," *Review of Scientific Instruments*, vol. 85, p. 013 701, 2014. DOI: 10.1063/1.4858835.

[20] E. Schäfer-Nolte, L. Schlipf, M. Ternes, F. Reinhard, K. Kern, and J. Wrachtrup, "Tracking Temperature-Dependent Relaxation Times of Ferritin Nanomagnets with a Wideband Quantum Spectrometer," *Physical Review Letters*, vol. 113, p. 217 204, 2014. DOI: 10.1103/PhysRevLett.113.217204.

[21] L. Thiel, D. Rohner, M. Ganzhorn, P.Appel, E. Neu, B. Müller, R. Kleiner, D. Koelle, and P. Maletinsky, "Quantitative nanoscale vortex imaging using a cryogenic quantum magnetometer," *Nature Nanotechnology*, vol. 11, pp. 677–681, 2016. DOI: 10.1038/nnano.2016.63.

[22] M. Ganzhorn, S. Klyatskaya, M. Ruben, and W. Wernsdorfer, "Carbon Nanotube Nanoelectromechanical Systems as Magnetometers for Single-Molecule Magnets," *ACS Nano*, vol. 7, pp. 6225–6236, 2013. DOI: 10.1021/nn402968k.

[23] K. Lipert, S. Bahr, F. Wolny, P. Atkinson, U. Weißker, T. Mühl, O. G. Schmidt, B. Büchner, and R. Klingeler, "An individual iron nanowire-filled carbon nanotube probed by micro-Hall magnetometry," *Applied Physics Letters*, vol. 97, p. 212 503, 2010. DOI: 10.1063/1.3520146.

[24] T. Schwarz, R. Wölbing, C. F. Reiche, B. Müller, M. J. Martínez-Pérez, T. Mühl, B. Büchner, R. Kleiner, and D. Koelle, "Low-Noise $YBa_2Cu_3O_7$ Nano-SQUIDs for Performing Magnetization-Reversal Measurements on Magnetic Nanoparticles," *Physical Review Applied*, vol. 3, p. 044 011, 2015. DOI: 10.1103/physrevapplied.3.044011.

[25] W. Wernsdorfer, K. Hasselbach, D. Mailly, B. Barbara, A. Benoit, L. Thomas, and G. Suran, “DC-SQUID magnetization measurements of single magnetic particles,” *Journal of Magnetism and Magnetic Materials*, vol. 145, pp. 33–39, 1995. DOI: 10.1016/0304-8853(94)01621-6.

[26] W. Wernsdorfer and R. Sessoli, “Quantum Phase Interference and Parity Effects in Magnetic Molecular Clusters,” *Science*, vol. 284, pp. 133–135, 1999. DOI: 10.1126/science.284.5411.133.

[27] W. Wernsdorfer, “Classical and quantum magnetization reversal studied in nanometersized particles and clusters,” *Advances in Chemical Physics*, vol. 118, pp. 99–190, 2001.

[28] M. Jamet, W. Wernsdorfer, C. Thirion, D. Mailly, V. Dupuis, P. Mélinon, and A. Pérez, “Magnetic Anisotropy of a Single Cobalt Nanocluster,” *Physical Review Letters*, vol. 86, pp. 4676–4679, 2001. DOI: 10.1103/PhysRevLett.86.4676.

[29] W. Wernsdorfer, “From micro- to nano-SQUIDs: Applications to nanomagnetism,” *Superconductor Science and Technology*, vol. 22, p. 064 013, 2009. DOI: 10.1088/0953-2048/22/6/064013.

[30] R. Gross and A. Marx, *Festkörperphysik*. Oldenbourg Wissenschaftsverlag, 2012, ISBN: 9783486714869.

[31] R. Kleiner and W. Buckel, *Superconductivity: An Introduction*. John Wiley & Sons, 2016, ISBN: 9783527686544.

[32] J. Bardeen, L. N. Cooper, and J. R. Schrieffer, “Theory of Superconductivity,” *Physical Review*, vol. 108, pp. 1175–1204, 1957. DOI: 10.1103/physrev.108.1175.

[33] J. Bardeen, L. N. Cooper, and J. R. Schrieffer, “Microscopic Theory of Superconductivity,” *Physical Review*, vol. 106, pp. 162–164, 1957. DOI: 10.1103/physrev.106.162.

[34] B. Josephson, “Possible new effects in superconductive tunnelling,” *Physics Letters*, vol. 1, pp. 251–253, 1962. DOI: 10.1016/0031-9163(62)91369-0.

[35] R. Behr, O. Kieler, J. Kohlmann, F. Müller, and L. Palafox, “Development and metrological applications of Josephson arrays at PTB,” *Measurement Science and Technology*, vol. 23, p. 124 002, 2012. DOI: 10.1088/0957-0233/23/12/124002.

[36] J. Lin, B. Müller, J. Linek, M. Karrer, M. Wenzel, M. J. Martínez-Pérez, R. Kleiner, and D. Koelle, “$YBa_2Cu_3O_7$ nano superconducting quantum interference devices on MgO bicrystal substrates,” *Nanoscale*, vol. 12, pp. 5658–5668, 2020. DOI: 10.1039/c9nr10506a.

[37] K. I. Wurster, “Herstellung und Transfer von Nanometerdünnen YBCO Membranen,” Dissertation, Eberhard Karls University Tübingen, 2023.

[38] D. R. Harshman and A. P. Mills, “Concerning the nature of high-T_c superconductivity: Survey of experimental properties and implications for interlayer coupling,” *Physical Review B*, vol. 45, pp. 10 684–10 712, 1992. DOI: 10.1103/physrevb.45.10684.

[39] R. K. Singh and D. Kumar, “Pulsed laser deposition and characterization of high-Tc $YBa_2Ca_3O_{7-x}$ superconducting thin films,” *Materials Science and Engineering: R: Reports*, vol. 22, pp. 113–185, 1998. DOI: 10.1016/s0927-796x(97)00019-3.

[40] R. Wördenweber, “Growth of High-T_c Thin Films,” *Superconductor Science and Technology*, vol. 12, R86–R102, 1999.

[41] H. Y. Zhai and W. K. Chu, “Effect of interfacial strain on critical temperature of $YBa_2Ca_3O_{7-x}$ thin films,” *Applied Physics Letters*, vol. 76, pp. 3469–3471, 2000.

[42] Crystec, *Datenblätter*, http://www.crystec.de/datasheets-e.html, Accessed: 2025-05-05.

[43] H. Hilgenkamp and J. Mannhart, “Grain boundaries in high-T_c superconductors,” *Reviews of Modern Physics*, vol. 74, pp. 485–549, 2002. DOI: 10.1103/revmodphys.74.485.

[44] J. Nagel, K. B. Konovalenko, M. Kemmler, M. Turad, R. Werner, E. Kleisz, S. Menzel, R. Klingeler, B. Büchner, R. Kleiner, and D. Koelle, “Resistively shunted $YBa_2Cu_3O_7$ grain boundary junctions and low-noise SQUIDs patterned by a focused ion beam down to 80 nm linewidth,” *Superconductor Science and Technology*, vol. 24, p. 015 015, 2010. DOI: 10.1088/0953-2048/24/1/015015.

[45] D. Lu, D. J. Baek, S. S. Hong, L. F. Kourkoutis, Y. Hikita, and H. Y. Hwang, “Synthesis of freestanding single-crystal perovskite films and heterostructures by etching of sacrificial water-soluble layers,” *Nature Materials*, vol. 15, pp. 1255–1260, 2016. DOI: 10.1038/nmat4749.

[46] H. Wang, V. Harbola, Y.-J. Wu, P. A. van Aken, and J. Mannhart, “Interface Design beyond Epitaxy: Oxide Heterostructures Comprising Symmetry-Forbidden Interfaces,” *Advanced Materials*, vol. 36, 2024. DOI: 10.1002/adma.202405065.

[47] Y.-J. Wu, “Opening New Perspectives in Nanotechnology: Symmetry Forbidden Interfaces, Vector Substrates, and Self-assembled Nanocrystals,” Dissertation, Eberhard Karls University Tübingen, 2025.

[48] M. J. Martínez-Pérez, J. Pablo-Navarro, B. Müller, R. Kleiner, C. Magén, D. Koelle, J. M. de Teresa, and J. Sesé, “NanoSQUID Magnetometry on Individual As-grown and Annealed Co Nanowires at Variable Temperature,” *Nano Letters*, vol. 18, pp. 7674–7682, 2018. DOI: 10.1021/acs.nanolett.8b03329.

[49] M. J. Martínez-Pérez, B. Müller, J. Lin, L. A. Rodriguez, E. Snoeck, R. Kleiner, J. Sesé, and D. Koelle, “Magnetic vortex nucleation and annihilation in bi-stable ultra-small ferromagnetic particles,” *Nanoscale*, vol. 12, pp. 2587–2595, 2020. DOI: 10.1039/c9nr08557b.

[50] M. X. Aguilar-Pujol, S. Catalano, C. González-Orellana, W. Skowroński, J. M. Gomez-Perez, M. Ilyn, C. Rogero, M. Gobbi, L. E. Hueso, and F. Casanova, “Magnon currents excited by the spin Seebeck effect in ferromagnetic EuS thin films,” *Physical Review B*, vol. 108, p. 224 420, 2023. DOI: 10.1103/physrevb.108.224420.

[51] D. García-Pons, J. Pérez-Bailón, A. Méndiz, V. Júlvez, M. Hack, K. Wurster, R. Kleiner, D. Koelle, and M. J. Martínez-Pérez, *Metastability in individual magnetic vortices*, arXiv:2410.14344 [cond-mat.mes-hall], 2024.

[52] R. Skomski, *Simple Models of Magnetism.* Oxford University Press, 2012, ISBN: 9780199655397.

[53] W. Wernsdorfer, K. Hasselbach, A. Benoit, B. Barbara, B. Doudin, J. Meier, J.-P. Ansermet, and D. Mailly, "Measurements of magnetization switching in individual nickel nanowires," *Physical Review B*, vol. 55, pp. 11 552–11 559, 1997. DOI: 10.1103/physrevb.55.11552.

[54] J. Kurkijärvi, "Intrinsic Fluctuations in a Superconducting Ring Closed with a Josephson Junction," *Physical Review B*, vol. 6, pp. 832–835, 1972. DOI: 10.1103/PhysRevB.6.832.

[55] P. Banerjee, F. Wolny, D. V. Pelekhov, M. R. Herman, K. C. Fong, U. Weissker, T. Mühl, Y. Obukhov, A. Leonhardt, B. Büchner, and P. C. Hammel, "Magnetization reversal in an individual 25 nm iron-filled carbon nanotube," *Applied Physics Letters*, vol. 96, p. 252 505, 2010. DOI: 10.1063/1.3440951.

[56] M. D. Kuz'min, K. P. Skokov, L. V. B. Diop, I. A. Radulov, and O. Gutfleisch, "Exchange stiffness of ferromagnets," *The European Physical Journal Plus*, vol. 135, 2020. DOI: 10.1140/epjp/s13360-020-00294-y.

[57] K. Lahabi, M. Amundsen, J. A. Ouassou, E. Beukers, M. Pleijster, J. Linder, P. Alkemade, and J. Aarts, "Controlling supercurrents and their spatial distribution in ferromagnets," *Nature Communications*, vol. 8, p. 2056, 2017. DOI: 10.1038/s41467-017-02236-2.

[58] G. De Simoni, E. Strambini, J. S. Moodera, F. S. Bergeret, and F. Giazotto, "Toward the Absolute Spin-Valve Effect in Superconducting Tunnel Junctions," *Nano Letters*, vol. 18, pp. 6369–6374, 2018. DOI: 10.1021/acs.nanolett.8b02723.

[59] T. T. Heikkilä, R. Ojajärvi, I. J. Maasilta, E. Strambini, F. Giazotto, and F. S. Bergeret, "Thermoelectric Radiation Detector Based on Superconductor-Ferromagnet Systems," *Physical Review Applied*, vol. 10, p. 034 053, 2018. DOI: 10.1103/physrevapplied.10.034053.

[60] M. Zeer, D. Go, J. P. Carbone, T. G. Saunderson, M. Redies, M. Kläui, J. Ghabboun, W. Wulfhekel, S. Blügel, and Y. Mokrousov, "Spin and orbital transport in rare-earth dichalcogenides: The case of EuS2," *Physical Review Materials*, vol. 6, p. 074 004, 2022. DOI: 10.1103/physrevmaterials.6.074004.

[61] Z. Geng, A. Hijano, S. Ilić, M. Ilyn, I. Maasilta, A. Monfardini, M. Spies, E. Strambini, P. Virtanen, M. Calvo, C. González-Orellána, A. P. Helenius, S. Khorshidian, C. I. L. de Araujo, F. Levy-Bertrand, C. Rogero, F. Giazotto, F. S. Bergeret, and T. T. Heikkilä, "Superconductor-ferromagnet hybrids for non-reciprocal electronics and detectors," *Superconductor Science and Technology*, vol. 36, p. 123 001, 2023. DOI: 10.1088/1361-6668/ad01e9.

[62] T. Weber, “nanoSQUIDs für die Rastersondenmikroskopie,” M.S. thesis, Eberhard Karls University Tübingen, 2025.

[63] R. M. Hutt, “Bestimmung der Spinsensitivität $S_\mu^{1/2}$ von Vector-Nano-SQUIDs,” M.S. thesis, Eberhard Karls University Tübingen, 2021.

[64] J. Linek, “Elektrische Eigenschaften von nanostrukturierten Nb-HfTi-Nb-Josephson-Kontakten und SQUIDs,” M.S. thesis, Eberhard Karls University Tübingen, 2018.

[65] C. Spanheimer, *Optimierung des Betriebs von Nano-SQUIDs in starken Magnetfeldern.* Bachelor’s Thesis, Universität Tübingen, Tübingen, 2023.

[66] L. Koch, “Positionierung individueller magnetischer Nanopartikel mit Wolfram-Spitzen annanoSQUIDs,” M.S. thesis, Eberhard Karls University Tübingen, 2020.

[67] K. K. Likharev, *Dynamics of Josephson junctions and circuits.* Gordon and Breach, 1996, ISBN: 2881240429.

[68] K. Meyer, *Degradationseffekte in* $YBa_2Cu_3O_7$ *nanoSQUIDs*, Bachelor’s Thesis, Universität Tübingen, Tübingen, 2015.

[69] B. Müller, M. Karrer, F. Limberger, M. Becker, B. Schröppel, C. Burkhardt, R. Kleiner, E. Goldobin, and D. Koelle, “Josephson Junctions and SQUIDs Created by Focused Helium-Ion-Beam Irradiation of $YBa_2Cu_3O_7$,” *Physical Review Applied*, vol. 11, p. 044 082, 2019. DOI: 10.1103/physrevapplied.11.044082.

[70] M. J. Martínez-Pérez, B. Müller, D. Schwebius, D. Korinski, R. Kleiner, J. Sesé, and D. Koelle, “NanoSQUID magnetometry of individual cobalt nanoparticles grown by focused electron beam induced deposition,” *Superconductor Science and Technology*, vol. 30, p. 024 003, 2016. DOI: 10.1088/0953-2048/30/2/024003.

[71] J. Lin, J. Linek, R. Kleiner, and D. Koelle, “NanoSQUIDs from $YBa_2Cu_3O_7/SrTiO_3$ superlattices with bicrystal grain boundary Josephson junctions,” *Nanoscale*, vol. 12, pp. 20 016–20 024, 2020. DOI: 10.1039/d0nr05446a.

[72] R. Gross, L. Alff, A. Beck, O. Froehlich, D. Koelle, and A. Marx, “Physics and Technology of High Temperature Superconducting Josephson Junctions,” *IEEE Transactions on Appiled Superconductivity*, vol. 7, pp. 2929–2935, 1997. DOI: 10.1109/77.621919.

[73] S. R. Bakaul, C. R. Serrao, M. Lee, C. W. Yeung, A. Sarker, S.-L. Hsu, A. K. Yadav, L. Dedon, L. You, A. I. Khan, J. D. Clarkson, C. Hu, R. Ramesh, and S. Salahuddin, “Single crystal functional oxides on silicon,” *Nature Communications*, vol. 7, p. 10 547, 2016. DOI: 10.1038/ncomms10547.

[74] D. M. Paskiewicz, R. Sichel-Tissot, E. Karapetrova, L. Stan, and D. D. Fong, “Single-Crystalline $SrRuO_3$ Nanomembranes: A Platform for Flexible Oxide Electronics,” *Nano Letters*, vol. 16, pp. 534–542, 2015. DOI: 10.1021/acs.nanolett.5b04176.

[75] P. Singh, A. Swartz, D. Lu, S. S. Hong, K. Lee, A. F. Marshall, K. Nishio, Y. Hikita, and H. Y. Hwang, "Large-Area Crystalline $BaSnO_3$ Membranes with High Electron Mobilities," *ACS Applied Electronic Materials*, vol. 1, pp. 1269–1274, 2019. DOI: 10.1021/acsaelm.9b00215.

[76] S. S. Hong, M. Gu, M. Verma, V. Harbola, B. Y. Wang, D. Lu, A. Vailionis, Y. Hikita, R. Pentcheva, J. M. Rondinelli, and H. Y. Hwang, "Extreme tensile strain states in $La_{0.7}Ca_{0.3}MnO_3$ membranes," *Science*, vol. 368, pp. 71–76, 2020. DOI: 10.1126/science.aax9753.

[77] F. M. Chiabrera, S. Yun, Y. Li, R. T. Dahm, H. Zhang, C. K. R. Kirchert, D. V. Christensen, F. Trier, T. S. Jespersen, and N. Pryds, "Freestanding Perovskite Oxide Films: Synthesis, Challenges, and Properties," *Annalen der Physik*, vol. 534, p. 2 200 084, 2022. DOI: 10.1002/andp.202200084.

[78] D. Pesquera, A. Fernández, E. Khestanova, and L. W. Martin, "Freestanding complex-oxide membranes," *Journal of Physics: Condensed Matter*, vol. 34, p. 383 001, 2022. DOI: 10.1088/1361-648x/ac7dd5.

[79] G. Dong, S. Li, M. Yao, Z. Zhou, Y.-Q. Zhang, X. Han, Z. Luo, J. Yao, B. Peng, Z. Hu, H. Huang, T. Jia, J. Li, W. Ren, Z.-G. Ye, X. Ding, J. Sun, C.-W. Nan, L.-Q. Chen, J. Li, and M. Liu, "Super-elastic ferroelectric single-crystal membrane with continuous electric dipole rotation," *Science*, vol. 366, pp. 475–479, 2019. DOI: 10.1126/science.aay7221.

[80] H. S. Kum, H. Lee, S. Kim, S. Lindemann, W. Kong, K. Qiao, P. Chen, J. Irwin, J. H. Lee, S. Xie, S. Subramanian, J. Shim, S.-H. Bae, C. Choi, L. Ranno, S. Seo, S. Lee, J. Bauer, H. Li, K. Lee, J. A. Robinson, C. A. Ross, D. G. Schlom, M. S. Rzchowski, C.-B. Eom, and J. Kim, "Heterogeneous integration of single-crystalline complex-oxide membranes," *Nature*, vol. 578, pp. 75–81, 2020. DOI: 10.1038/s41586-020-1939-z.

[81] R. Xu, J. Huang, E. S. Barnard, S. S. Hong, P. Singh, E. K. Wong, T. Jansen, V. Harbola, J. Xiao, B. Y. Wang, S. Crossley, D. Lu, S. Liu, and H. Y. Hwang, "Strain-induced room-temperature ferroelectricity in $SrTiO_3$ membranes," *Nature Communications*, vol. 11, p. 3141, 2020. DOI: 10.1038/s41467-020-16912-3.

[82] Y. Li, C. Xiang, F. M. Chiabrera, S. Yun, H. Zhang, D. J. Kelly, R. T. Dahm, C. K. R. Kirchert, T. E. L. Cozannet, F. Trier, D. V. Christensen, T. J. Booth, S. B. Simonsen, S. Kadkhodazadeh, T. S. Jespersen, and N. Pryds, "Stacking and Twisting of Freestanding Complex Oxide Thin Films," *Advanced Materials*, vol. 34, p. 2 203 187, 2022. DOI: 10.1002/adma.202203187.

[83] J.-K. Huang, Y. Wan, J. Shi, J. Zhang, Z. Wang, W. Wang, N. Yang, Y. Liu, C.-H. Lin, X. Guan, L. Hu, Z.-L. Yang, B.-C. Huang, Y.-P. Chiu, J. Yang, V. Tung, D. Wang, K. Kalantar-Zadeh, T. Wu, X. Zu, L. Qiao, L.-J. Li, and S. Li, "High-κ perovskite membranes as insulators for two-dimensional transistors," *Nature*, vol. 605, pp. 262–267, 2022. DOI: 10.1038/s41586-022-04588-2.

[84] V. Harbola, Y.-J. Wu, H. Wang, S. Smink, S. C. Parks, P. A. van Aken, and J. Mannhart, "Self-Assembly of Nanocrystalline Structures from Freestanding Oxide Membranes," *Advanced Materials*, vol. 35, p. 2 210 989, 2023. DOI: 10.1002/adma.202210989.

[85] G. Sánchez-Santolino, V. Rouco, S. Puebla, H. Aramberri, V. Zamora, M. Cabero, F. A. Cuellar, C. Munuera, F. Mompean, M. Garcia-Hernandez, A. Castellanos-Gomez, J. Íñiguez, C. Leon, and J. Santamaria, "A 2D ferroelectric vortex pattern in twisted $BaTiO_3$ freestanding layers," *Nature*, vol. 626, pp. 529–534, 2024. DOI: 10.1038/s41586-023-06978-6.

[86] H. Li, S. Yun, A. Chikina, V. Rosendal, T. Tran, E. Brand, C. H. Christoffersen, N. C. Plumb, M. Shi, N. Pryds, and M. Radovic, "Transition Metal-Oxide Nanomembranes Assembly by Direct Heteroepitaxial Growth," *Advanced Functional Materials*, vol. 34, p. 2 313 236, 2024. DOI: 10.1002/adfm.202313236.

[87] V. Harbola, Y.-J. Wu, F. V. E. Hensling, H. Wang, P. A. van Aken, and J. Mannhart, "Vector Substrates: Idea, Design, and Realization," *Advanced Functional Materials*, vol. 34, p. 2 306 289, 2023. DOI: 10.1002/adfm.202306289.

[88] A. Vansteenkiste, J. Leliaert, M. Dvornik, M. Helsen, F. Garcia-Sanchez, and B. Van Waeyenberge, "The design and verification of Mumax3," *AIP Advances*, vol. 4, p. 107 133, 2014. DOI: 10.1063/1.4899186.

[89] L. Exl, S. Bance, F. Reichel, T. Schrefl, H. Peter Stimming, and N. J. Mauser, "LaBonte's method revisited: An effective steepest descent method for micromagnetic energy minimization," *Journal of Applied Physics*, vol. 115, p. 17D118, 2014. DOI: 10.1063/1.4862839.